A NOVEL TECHNIQUE FOR THE SYNTHESIS OF PURE AND DOPED ZINC OXIDE NANOSTRUCTURES USING THERMAL CHEMICAL VAPOR DEPOSITION METHOD

TAMIL MANY K.THANDAVAN

FACULTY OF SCIENCE
UNIVERSITY OF MALAYA
KUALA LUMPUR

2016

A NOVEL TECHNIQUE FOR THE SYNTHESIS OF PURE AND DOPED ZINC OXIDE NANOSTRUCTURES USING THERMAL CHEMICAL VAPOR DEPOSITION METHOD

TAMIL MANY K.THANDAVAN

THESIS SUBMITTED IN FULFILMENT OF THE REQUIREMENTS FOR THE DEGREE OF DOCTOR OF PHILOSOPHY

FACULTY OF SCIENCE
UNIVERSITY OF MALAYA
KUALA LUMPUR

2016

UNIVERSITY of MALAYA

ORIGINAL LITERARY WORK DECLARATION

ABSTRACT

A novel technique for the synthesis of ZnO nanostructures utilizing solid brass as the Zn source and alcohol as the oxygen source is described. Zn vapor obtained from solid brass due to the dezincification process aided by a hotwire were carried to the substrates using Ar gas in an evacuated reaction chamber. Also, crucial for the formation of ZnO nanostructures is the presence of alcohol vapor which seemed to provide the oxygen required. Here, the alcohol molecules dissociated on the hotwire surface to produce radical species for the oxidation of Zn produced from the solid brass source. Doping of the ZnO nanostructures with Mn or Al at different concentration was demonstrated by mixing Mn or Al salts in the alcohol to be carried in the reaction chamber by flowing Ar gas. A study on the deposition time on the synthesis of pure ZnO using methanol has yielded ZnO nanostructures of very good crystal structure with changes in morphology from button-liked mushroom to nanorods and to nanoneedles. Using ethanol, ZnO nanorods with larger diameters were produced. Lower values of strain, stress and energy density were observed for samples produced using methanol compared to ethanol which can be related to the formation of low energy sites of ZnO for higher rate of condensation of more energised particle in ZnO using methanol. ZnO nanostructures synthesised using methanol is suitable for field electron emission applications based on their smaller geometrical structures. Photoluminescence spectroscopy results revealed the existence of defects such as zinc interstitials (Zn_i), oxygen interstitials (O_i), zinc vacancy (V_{zn}), singly charged zinc vacancy (V_{Zn}^-), oxygen vacancy (V_o), singly charged oxygen vacancy (V_o^+) and oxygen anti-site defects (O_{Zn}) in the grown nanostructures. The Raman scattering results also provided evidence of Mn and Al doping due to peak shift from 145 cm^{-1} in pure ZnO to an anomalous peak at 140 and 138 cm^{-1} respectively. Field electron emission studies were performed on pure and Mn doped ZnO nanostructures. The best field electron emission properties were obtained with Mn-

doped ZnO nanostructures with a threshold electric field of 2.06 $V\mu m^{-1}$, and field enhancement factor of 4548. In summary, the pure and doped ZnO nanostructures that have been synthesized using a novel technique utilizing a solid Zn source in thermal CVD system were analyzed. This technique has the potential for simple and economical patterned growth of ZnO nanostructures and films.

ABSTRAK

Teknik novel untuk mensintesis ZnO nanostruktur menggunakan tembaga pepejal sebagai sumber Zn dan alkohol sebagai sumber oksigen telah diterangkan. Wap Zn yang diperolehi daripada tembaga pepejal telah melalui proses zinkfikasi yang dibantu oleh filamen panas telah dibawa kepada substrat menggunakan gas Ar ke dalam kebuk tindak-balas. Selain itu, yang penting bagi pembentukan ZnO nanostruktur adalah kehadiran wap alkohol yang seolah-olah memberi oksigen yang diperlukan. Di sini, molekul alkohol bercerai di permukaan filamen panas untuk menghasilkan radikal spesies yang sesuai untuk pengoksidaan Zn yang dihasilkan daripada sumber tembaga pepejal. Pendopan ZnO nanostruktur menggunakan Mn atau Al pada kepekatan yang berbeza disempurnakan dengan mencampurkan garam Mn atau Al ke dalam alkohol yang dibawa ke dalam kebuk tindak balas oleh aliran gas Ar. Satu kajian mengenai kesan pemendapan masa sintesis ZnO tulen menggunakan metanol telah menghasilkan hablur ZnO nanostruktur yang sangat baik berdasarkan analisis XRD. Perubahan morfologi dari bentuk cendawan berbutang ke bentuk nanorod dan akhirnya ke bentuk nanoneedles telah diperhatikan. Pengunaan etanol telah menghasilkan ZnO nanorod dengan diameter yang lebih besar. Nilai-nilai keputusan yang lebih rendah berdasarkan ketegangan, tekanan dan ketumpatan tenaga telah diperhatikan pada sampel yang dihasilkan menggunakan metanol berbanding etanol yang boleh yang dikaitan dengan penubuhan tapak tenaga ZnO dan kadar pemeluwapan zarah bertenaga yang lebih tinggi di dalam ZnO berasaskan metanol. ZnO nanostruktur berasaskan methanol adalah sesuai untuk aplikasi pancaran elektron berdasarkan struktur Geometri yang lebih kecil. Keputusan Spektroskopi Photoluminescence mendedahkan terdapatnya kecacatan seperti zink interstitials (Zn_i), interstitials oksigen (O_i), zink kekosongan (V_{zn}), secara berseorangan dikenakan zink kekosongan kekosongan (V_{Zn}^-), oksigen (V_o), dikenakan secara berseorangan kekosongan oksigen (V_o^+) dan sebarang kecacatan anti oksigen

(O_{Zn}) di nanostruktur ini berkembang. Analisis Raman juga telah membuktikan kewujudan mineral Mn dan Al disebabkan oleh peralihan puncak dari 145 cm^{-1} di ZnO tulen ke sebuah puncak anomali 140 dan 138 cm^{-1} masing-masing. Kajian pancaran elektron yang dilakukan ke atas ZnO tulen dan yang didopkan dengan Mn telah mempertikaikan bahawa ZnO yang telah didopkan dengan ciri 2.06 $V\mu m^{-1}$ dan field enhancement factor 4548 boleh digunakan dalam bidang pancaran electron.

ACKNOWLEDGEMENT

First and foremost I would like to thank my supervisor Assoc. Prof. Dr. Roslan Md Nor and co-supervisor, Assoc. Prof. Dr. Siti Meriam Ad Gani for their overall support, guidance, patience, and constant positive attitude in facing various problems and surprises in this project till the end. Their knowledge and guidance has helped me in publishing 5 papers and a book chapter. I would also like to express my deepest appreciation and thanks to Prof. Dr. Wong Chiow San for his continuous tolerance of me while conducting the entire experimental work in the Low Temperature Plasma Laboratory. The analytical laboratory technicians, Ms. Zurina Marzuki, Mr. Mohd Aruf and Mr. Jasbir Singh are not forgotten for their guidance in obtaining relevant results in FESEM, XRD, Raman and Photoluminescence. I want to express my gratitude to other academic staff, Assoc. Prof. Dr. Vengadesh, Prof. Dr. Siti Vinayagam Muniandy, Prof. Dr. Ramesh Subramaniam, Dr. Ramesh Kasi and Prof. Datin Dr. Saadah for their support and motivation in completing my research. Besides that, the tension and obstacles that I have faced were ended cheerfully in a very conducive research environment with two buddies, Dr. Zubahir Kahn and Mr. Naresh Nitturi. Partial monetary support from Peruntukan Penyelidikan Pascasiswazah (PPP) of UM grant no.: PS212/2009A, PG068-2013A, UMRG grant no.: RG247-12AFR and RP008-13AFR are acknowledged with thankfulness. I would like to thank my family members (OHANA), relatives and friends for their unconditional love, undoubting belief, understanding and moral support for the completion of the first Degree of Doctor of Philosophy in my family. Special thanks go to my wife, Theanmolzhi and my mom, Chandra Dewie for their care and financial assistance during my hard time paying the fee. Unlimited thanks to my spiritual master, Sri Harold Klemp, for his external and inner guidance from the first day of registration. Finally, I would like to dedicate this hard work to my son, Resshmehn.

….TAMIL MANY K.THANDAVAN

TABLE OF CONTENT

CHAPTER 3: METHODOLOGY

CHAPTER 4: ANALYTICAL TECHNIQUE

CHAPTER 5: RESULTS AND DISCUSSION

LIST OF FIGURES

LIST OF TABLES

LIST OF SYMBOLS AND ABBREVIATIONS

NSs	Nanostructures
NWs	Nanowires
NCs	Nanocapsules
ZnO	Zinc oxide
ZnO:Al	Aluminium doped zinc oxide
ZnO:Mn	Manganese doped zinc oxide
UV	Ultraviolet
NBE	Near band emission
NIR	Near Infrared
Al	Aluminium
Mn	Mangan
CVD	Chemical vapor deposition
PL	Photoluminescence
FESEM	Field emission scanning electron microscopy
XRD	X-ray diffraction
TEM	Transmission electron microscopy
EDAX	Energy dispersive ananlysis of x-ray
Cu	Copper
Zn	Zinc
CuZn	Brass
ZnO/methanol	Zinc oxide prepared using methanol
ZnO/ethanol	Zinc oxide prepared using ethanol
STM	Scanning tunnelling microscope
AFM	Atomic force microscope

VPT	Vapor phase transport
Si	Silicon
W-H	Williamson-Hall
UDM	Uniform deformation model
UDSM	Uniform deformation stress model
UDEDM	Uniform deformation energy density model
SSP	Size-strain plot
D	Crystallite size
D_v	Volume averaged crystallite size
u	Energy per unit volume
B_{DS}	Debye-Scherer size broadening
B_ε	Strain broadening

LIST OF APPENDICES

CHAPTER 1: INTRODUCTION

1.1 The revolution of ZnO nanotechnology

The concept of nanotechnology had been first introduced by Nobel Laureate Richard Feynman in 1959, stating that *"The principles of physics as far as I can see do not speak against the possibility of manoeuvring things atom by atom."* Almost twenty one years after the statement, the first nanotech paper (Drexler, 1981) had been published and had motivated many researchers to develop various characterizing instruments namely Field electron microscope (FEM) scanning tunnelling microscope (STM) and atomic force microscope (AFM). The popular term nanotechnology has been used by many researchers to describe the characteristic dimensions that are less than about thousand nanometres. For example, continued improvements in lithography (Sen et al., 2013) have resulted sub-micron lithography which has allowed building semiconductor devices in which individual dopants are located at specific lattice sites. The field of nanotechnology, including advanced materials holds a vast potential as it promises paradigm shift in almost all technology that pervade everyday life in computing, communications, drug delivery, structural material and energy storage.

However, the revolution of zinc oxide (ZnO) technology started in the early thirties of the nineteenth century. The early research was driven by the availability of good bulk single crystals and first epitaxial layers (Dodson & Savage, 1968) with investigations of ion radii and crystal structure, the specific heat at low temperatures, its density or optical properties (Schneck & Helbig, 1975). But a slow decline in the interest in ZnO was observed in the mid-80s due to ambipolar doping of ZnO. The nature of ZnO as a n-type semiconductor which easily can be n-type doped by aluminium (Al), gallium (Ga) or indium (In) (Cimitan et al., 2009)to the range of $n \approx 10^{20}$ cm^{-3} had sustained the work in optoelectronics until the absence of p-type doping

had destroyed the hope of obtaining ZnO semiconductor laser-diodes in the blue, violet or near ultraviolet (UV) spectral ranges. Besides that III-V compounds, especially GaAs/$Al_{1-y}Ga_yAs$ came more into focus in the field of light emitting diode (LED) and optoelectronics.

Now a revival has been encountered in the mid-90s where more than 2000 ZnO related articles were published in 2005, compared to only ~100 articles in 1970s. This was due to an evident that ZnO and its alloys with magnesium oxide (MgO), beryllium oxide (BeO) and cadmium oxide (CdO) have partially similar properties as GaN such as band gap, crystal structure, carrier mobility and heat conductivity. Nevertheless, ZnO being cheaper, not poisonous and insensitive to radiation damage had opened the patenting field. ZnO also has strong tendency for self-organized growth of nanostructures (NSs) in one dimensional (1D) NSs as nanotubes (Guo et al., 2004; Mishra et al., 2014), nanowires (NWs) (Piner et al., 1999), nanorods (Lockman et al., 2010; Yi et al., 2005), nanobelts (Lao et al., 2006), nanocables (Kim et al., 2006) and nanoribbons (Wang et al., 2010a).

1.2 The objective of the research

This dissertation was prepared to give optimization information and facts on producing ZnO NSs using a combination of vapor phase transport (VPT) and thermal dissociation method assisted with hot wire technique to study the properties of pure and doped ZnO NSs. In order to achieve that, the following anticipated steps have been taken into consideration;

(a) Development of new ZnO NS synthesis technique utilizing a solid brass as the Zn source and alcohol as the oxygen (O) source in a thermal CVD reactor.

(b) The effect of Mn and Al doping on the ZnO NS synthesized using the technique in (a).

(c) Application of ZnO NS synthesized as field electron emission cathodes.

1.3 The layout of the thesis

The thesis consists of six chapters including Chapter 1. Chapter 2 presents a brief discussion on the literature review about ZnO nanomaterial. Mainly the physical properties of ZnO are discussed. Importance is focused on electrical, mechanical and optical properties due to its exceptional application in the field of bio medicals, electronics, light emitting diodes and sensors. Various growth technique and methods are reviewed in contrast of the developed technique, particularly the VPT and thermal evaporation methods used to synthesize ZnO NSs.

The development of experimental setup is explained in Chapter 3. This chapter covers a detailed step by step protocol in obtaining pure and doped ZnO NSs. A selection of Zn and O source material is discussed. Initial optimization procedure to obtain a polycrystalline Zn layer and further conversion to ZnO NSs is detailed.

Chapter 4 is about instrumentation and analytical technique used in characterizing the samples. All the films prepared in the laboratory were characterized using energy dispersive analysis x-ray (EDAX), field emission scanning electron microscopy (FESEM), X-ray diffraction (XRD), photoluminescence (PL), micro Raman spectroscopy and field electron emission (FEE).

Chapter 5 consist of details of spectroscopic and structural characterization studies about the synthesized ZnO NSs using methanol and ethanol. The imaging characterization shows fabrication of hexagonal and nanoneedle like growth of ZnO NSs. Williamson-Hall method was applied to determine strain and stress distribution in pure ZnO NSs. The time dependence growth for both ZnO produced using methanol

and ethanol further proposed that methanol is better source material to obtain nanosized ZnO NWs. The discussion is further extended to Mn and Al doped ZnO NSs. The possibility of functionalization on the wall of ZnO NWs is also discussed based on PL and Raman scattering results.

Finally, Chapter 6 gives some general conclusions and suggestions for future work in developing functionalized and hybrid ZnO NWs using the newly developed technique.

CHAPTER 2: LITERATURE REVIEW

2.1 ZnO nanostructures

ZnO is a II-VI inorganic compound which can be found in one dimension (1D) less than 100 nm (Lieber, 1998), typically including NWs, nanobelts, nanorods, nanolayer film, nanoparticles, nanocables, nanoribbons and nanotubes. It has stable wurtzite hexagonal structure as shown in Figure 2.1(a) which has the characteristics of non-central symmetry and polar surface as in Figure 2.1(b). The wurtzite ZnO belongs to the space group $P6_3mc$ that has a lattice spacing a = b = 0.3249 nm and c = 0.5204 nm. Ideal wurtzite ZnO crystal has axial ratio $c/a = (8/3)^{3/2}$ and u parameter equals to 3/8 which are correlated by the relationship $uc/a = (3/8)^{1/2}$.

The ZnO crystal consists of two interconnecting sublattices of Zn^{2+} and O^{2-} ions that form tetrahedral coordination involving sp^3 hybridization of electron states, leading to four equivalent orbitals. The tetrahedrally coordinated bonding structures of one Zn^{2+} and four O^{2-} and vice versa are stacked alternately along the c-axis giving rise to polar symmetry (Özgür et al., 2005; Zhang et al., 2005). The polar symmetry in ZnO is responsible for a number of properties including piezoelectricity and pyroelectricity. Spontaneous polarization in ZnO believed to be a key factor in crystal growth, etching and defect generation.

Four most common face termination of the wurtzite ZnO has equal number of Zn and O atoms. They are positively charged Zn-(0001) and negatively charged O-(0001) faces which are polar terminated, oriented along c-axis and non-polar (1120) along a-axis and (1010) faces. The non-polar faces have lower energy than the basal plane, (0001) face. However, the bond polarity in ZnO is caused by a very strong electronegativity of the oxygen and very low electronegativity of zinc that leads to an iconicity of fi = 0.616 on the Philips scale (Phillips, 2012). Thus, ZnO lies in the border

line between a covalent and ionic compound known as semiconductor. Further, each ion has twelve next-nearest neighbours of the same type of ions. The O-Zn distance of the nearest neighbours is 1.992 Å in the direction parallel to the *c*-axis of the hexagonal unit cell and 1.973 Å in three directions $\langle 0001 \rangle, \langle 1120 \rangle$ and $\langle 1100 \rangle$ of the tetrahedral arrangement as shown in Figure 2.2. The tetrahedral arrangement between the nearest neighbours indicates the covalent bond between the zinc and oxygen atoms. The covalent radii of zinc and oxygen are reported to be 1.31 Å and 0.66 Å, respectively (Yogamalar & Bose, 2013). As the semiconductor undergoes shrinkage of lattice parameters or changes from 1D nanometer to zero dimensions, this would lead to an increase in band gap energy of ZnO.

Few typical growth morphologies for 1D NSs of ZnO are shown in Figure 2.3. These growth structures 2.3(a) - (c) are lean to minimize the areas of the (2110) and (0110) facets due to the nature of energy minimization. Some growth morphology is dominated by polar surfaces as shown in Figure 2.3(d) due to planar defects along the polar surface. Planar defects and twins are observed occasionally parallel to the (0001) plane but dislocations are rarely seen (Nishii et al., 2003; Wang, 2004a; Wang & Kang, 1998). The three surfaces (0001), (1120) and (1100) are preferred growth directions which are desirable in furthering studies into applications. In the low processing temperature and full compatibility with large scale integrated circuit fabrication, ZnO NSs has already been recognized as a promising material for improving nanoscale optoelectronic devices such as bandgap engineered solar cells, organic light emitting diodes (OLED's), ultraviolet (UV) laser diodes and etc (Morkoç et al., 2010; Özgür et al., 2005).

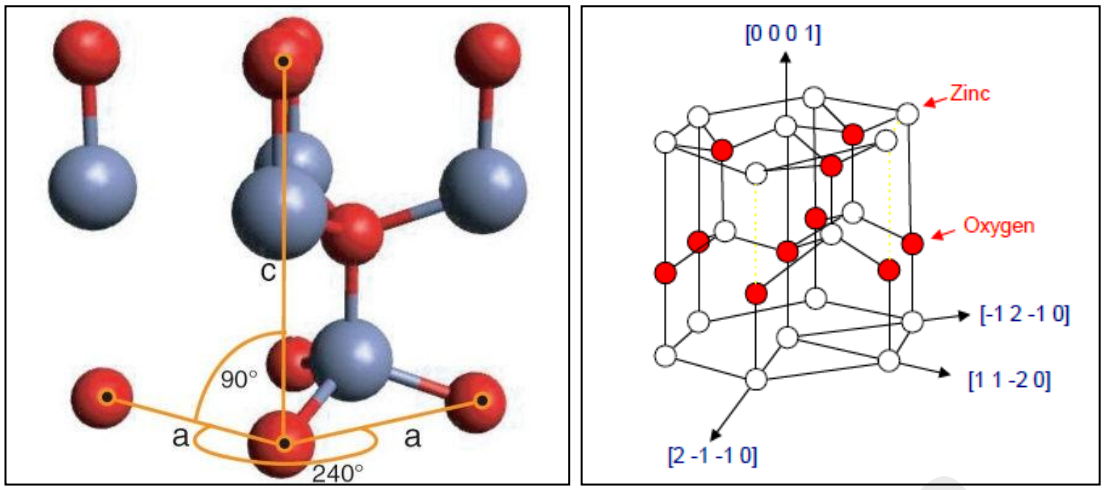

(a) (b)

Figure 2.1: Wurtzite unit cell of ZnO with (a) tetrahedral coordination (b) polar surfaces (Yogamalar & Bose, 2013).

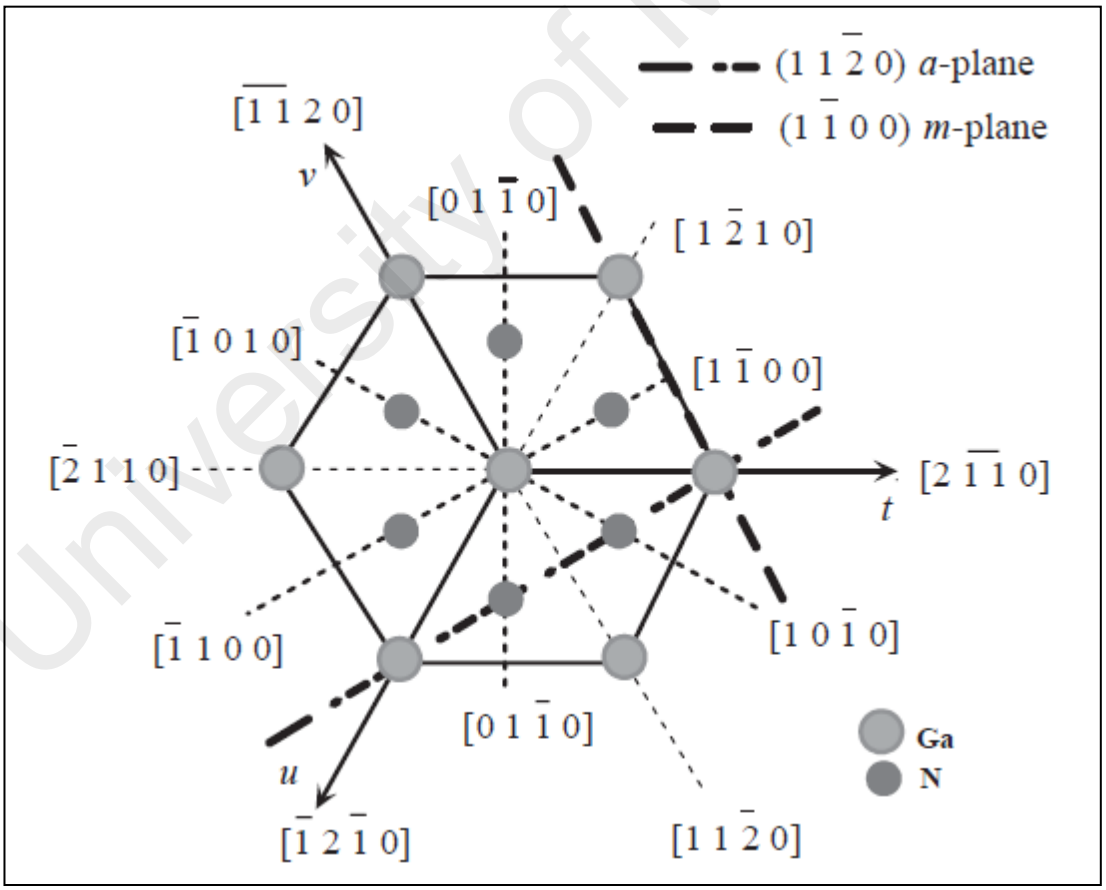

Figure 2.2: Orientations that are commonly used in wurtzite phase, namely, the (1 1 20) and (1 1 0 0) planes and associated directions are shown as projections on the (0 0 0 1) basal plane (Morkoç & Özgür, 2009).

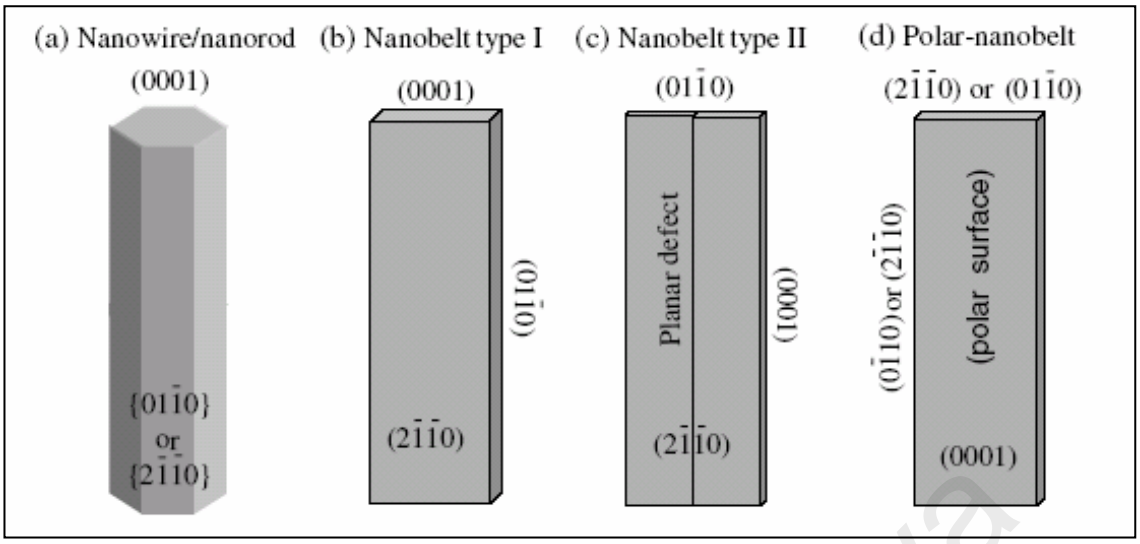

Figure 2.3: Typical growth morphologies of one-dimensional ZnO nanostructures and the corresponding facets (Wang, 2004a).

2.2 Physical properties of ZnO

The basic physical properties of ZnO are listed in Table 2.1 (Subramanyam et al., 2000; Wang, 2004a). Quantum size confinement effect on some of the physical properties may show interest if there are continuous shrinkage from nanometer to smaller dimension (Baruah & Dutta, 2009). The surface and quantum size confinement including the well-established fundamental physics of ZnO are believed to have stimulated considerable interest for scientific researchers in determining the novel electrical, mechanical, optical and chemical properties of ZnO.

Table 2.1: Physical properties of wurtzite ZnO.

Properties	Values
Appearance	Amorphous white or yellowish white powder
Odour	Odourless
a (Lattice constants at 300 K)	0.32469 nm
c (Lattice constants at 300 K)	0.52069 nm
a/c	1.602 (ideal hexagonal structure shows 1.633)
Molar mass	81.4084 g/mol
Density	5.606 g/cm^3
Stable phase at 300K	Wurtzite
Melting point	2248 K (1975 °C)
Boiling point	2633 K (2360 °C)
Solubility in water	0.16 mg/100 ml
Thermal conductivity	0.6 $Wcm^{-1}K^{-1}$
Relative dielectric constant	8.66
Refractive index	2.008, 2.029
Energy gap	3.4 eV direct
Intrinsic carrier concentration	$< 10^6$ cm^{-3}
Exciton binding Energy	60 meV
Electron effective mass	$0.24m_o$
Electron mobility (T = 300 K)	200 cm^2/Vs
Hole effective mass	$0.59m_o$
Hole mobility (T = 300 K)	5-50 cm^2/Vs

2.2.1 Electrical properties

The native nature of ZnO as an intrinsic n-type semiconductor has embarked several favourable properties, high electron mobility 2000 cm^2/(Gu et al.) (Wagner & Helbig, 1977) wide direct band gap (3.37 eV) and a relatively large excitation binding energy (60 meV) at room and high temperatures. These attractive properties have made ZnO a potential utility (Wang, 2004a) as UV photonics, transparent high power electronics solar cells, piezoelectric transducers and gas sensing devices (Raju & Rao, 1991). Presence of point, ionic and electronic defects in the lattices of ZnO, has made it a good n-type semiconductor (Fan & Lu, 2005; Subramanyam et al., 2000). Point defect is related to deviation of perfect atomic arrangement. Ionic defects which occupy the lattice atomic positions including vacancies and interstitials also known as point defects (Seghier & Gislason, 2008). Electronic defects can be related to deviation of ground state electron orbital configuration of a crystal. Excitation of electron from the valence orbital to higher energy level orbital may create an electron in the conduction band or electron hole in the valence band of the ZnO crystal.

Özgür et al. (2005) have reported that electron mobility in ZnO NSs is approximately 120 – 440 cm^2/Vs at room temperature which depends on the growth method. Doped ZnO has been reported with lower mobility compared to undoped ZnO. The electrical resistivity of undoped ZnO NSs has been reported in the range of 0.15 MΩcm (Lupan et al., 2008). They also found out that a doped ZnO tremendously decreases the electrical resistivity to 70 Ωcm. In an effort to decrease the electrical resistivity, Mal et al. (2010) had showed resistivity as low as 0.2 Ωcm with an n-type carrier concentration of $1.1x10^{19}$ cm^{-3} for ZnO prepared at 750 °C in an oxygen (O_2) pressure of 100 mTorr and exposed to laser irradiation. This shows that point defects such as vacancies and interstitials in the crystal have played an important role in modifying the electrical properties (Mal et al., 2010).

Recently a group work from Raja Ramana Centre for Advanced Technology from India have achieved remarkable electrical properties in ZnO film produced using atomic layer deposition technique. They presented the lowest value of room temperature resistivity ~ 3.6 x 10^{-3} Ωcm was achieved for the film deposited at ~200 °C, which had an estimated carrier concentration ~5.7x10^{19} cm^{-3} and mobility ~30 cm^2/V s. However the films deposited both below and above ~200 °C showed increased resistivity and decreased mobility presumably due to the intensified defects and deteriorated crystalline quality of these films (Saha et al., 2013).

However the major roadblock of ZnO for widespread applications in electronics and photonics is its problems with p-type doping. Quite a few p-type doping efforts have been reported like Ga and N co-doping method which resulted in the formation of low resistivity (0.5 Ωcm) p-type ZnO thin films. Successful p-type doping for ZnO NSs will give a boost to their future prospects in nanoscale electronics and in the field of optoelectronics devices and detectors (Van et al., 2008; Zhang et al., 2010). P-type and n-type ZnO NSs can serve as p-n junction diodes and light emitting diodes (Wang et al., 2011). Field effect transistors (FETs) fabricated from them can be used to make complementary logic circuits (Derycke et al., 2001).

2.2.2 Mechanical properties

Among the tetrahedrally bonded semiconductors, ZnO has the highest piezoelectric tensor or at least one that comparable to GaN and AlN due to lack of center of symmetry. This property makes it a technologically important material for many piezoelectrical applications, which requires a large electromechanical coupling. By using the piezoelectric effect in ZnO, mechanical stress or strain can be converted into electrical power. For this Xu et al. (2010) have investigated ZnO NWs. They have demonstrated vertical and lateral integration of 700 rows of ZnO NWs capable of

producing a peak voltage of 1.26 V at a low strain of 0.19 %. This is potentially sufficient to recharge an AA battery. Nevertheless, a peak power density 2.7 $mWcm^{-1}$ also has been noticed from vertical integration of three layers of ZnO NWs arrays (Xu et al., 2010). ZnO is a relatively soft material with approximate hardness of 4.5 on the Mohs scale. Its elastic constants are smaller than those of relevant III-V semiconductors, such as GaN. The high heat capacity, heat conductivity, low thermal expansion and high melting temperature of ZnO are beneficial in ceramics productions.

2.2.3 Photoluminescence properties

The extrinsic and intrinsic defects in the crystal structure contribute a lot in understanding the optical properties of semiconductor (Liu et al., 2006b; Willander et al., 2009). Extrinsic properties can be related to impurities and/or point defects that create electronic states in the bandgap, and therefore influences the optical properties of a semiconductor. The intrinsic optical transitions take place between the electrons in the conduction band and holes in the valence band including excitonic effects due to the Coulomb interaction. In 1960s Thomas had done early investigation in the optical properties of ZnO (Thomas, 1960).

ZnO became a very attractive material compare to other potential materials like GaN due to its wide band gap (3.37 eV) and large exciton energy about 60 meV at room temperatures (Jagadish & Pearton, 2006). The wide band gap which lies in the ultraviolet (UV) region and alternating stacking layers of Zn and O has made ZnO a unique candidate for UV light lasers and detectors working in the range of 368 - 390 nm (Fang et al., 2009; Mishra et al., 2014). The strong exciton binding energy which is larger than the GaN (25meV), and the thermal energy about 25 meV can ensure an efficient emission at room temperature under low excitation energy. Thus many efforts have been taken to study the optical transition in bulk and nanostructured ZnO using

variety of analytical techniques such as photoluminescence (Xiang et al., 2007), optical absorption, transmission, photoreflection, spectroscopic ellipsometry, reflection, calorimetric spectroscopy and cathodoluminescence. Among these, the well-known technique, PL at room temperature exhibits a spectrum of good crystallinity ZnO typically consist of only UV emission band as shown in Figure 2.4. On the other hand, Figure 2.5 shows both UV emission band and broad emission band which indicate defect orientation in ZnO NSs.

Typical ZnO nanorods exhibits fairly strong UV emission peak at 380 nm (3.26 eV). This UV emission is attributed by transition recombination of free exciton (FE) in the near band edge (3.37 eV) of ZnO. An exciton is a pair of excited electron and a hole that are bound together by their Coulomb attraction. There are two classes of excitons. The excitons can be free to move through the crystal or can be bound to neutral or charged donors and accepters (Alvi et al., 2011). The broad emission band is also called deep level emission (DLE) band which literally attributes in the visible region between 420 and 750 nm (Ahn et al., 2009). DLE band can be attributed to several native defect levels within the band gap in the crystal structure such as O-vacancy (V_o) (Kasai, 1963; Vanheusden et al., 1996a; Yamauchi et al., 2004), Zn-vacancy (V_{Zn}) (Bylander, 1978; Liu et al., 1992; Yang et al., 2003), O-interstitial (O_i) (Zhong et al., 1993), Zn-interstitial (Zn_i) (Liu et al., 2010) and extrinsic impurities such as substitutional Cu (Dingle, 1969). The DLE band also had been identified at two different defect origins V_O and V_{Zn} and different optical characteristics were claimed to contribute to this DLE band (Børseth et al., 2006; Klason et al., 2008; Zhao et al., 2005).

Figure 2.6 shows a typical PL spectrum of *n*-type bulk ZnO NS measured at 4.2 K (Meyer et al., 2004). The ZnO exhibits PL spectrum from the band edge to green/orange band. A broad band centred at about 2.45 eV is extending from blue into green range. The lines are dominating the spectrum originated from bound exciton (BE)

recombinations (excitons bound to neutral donors (D_0X) and/or acceptors (A_0X)) followed by longitudinal optical (LO) phonon replicas with an energy separation of 72 meV. The FE emission with the A-valence band (FXA) positioned at 3.375 eV already is seen. And a donor-acceptor-pair transition around 3.22 eV is found, which is again followed by phonon replicas (Xiang et al., 2007).

PL spectra of ZnO NSs have been extensively studied in early 2000s. PL spectrum of ZnO film obtained by Studenikin et al. (2000) revealed a complicated multi-line structure. They described that the origin of near UV emission lines were identified in terms of bound exciton complexes and the phonon replicas as in Figure 2.7. Mendelsberg et al. (2008) have reported that incorporation of carbon impurities in the lattices of ZnO has enhanced blue/violet emission band. The carbon appeared to inhibit the green band by typing up oxygen atoms in the plume that would otherwise become interstitial in the film.

D. Li et al. (2004) found that ZnO NSs prepared using chemical and thermal evaporation method exhibited yellow and green luminescence respectively. The yellow luminescence has been reported not sensitive to the surface modification of the NSs hence it is originated from the defects in the bulk ZnO. Hatch et al. (2013) have reported the excitonic emissions from the PL spectra of ZnO nanorods synthesised using an aqueous pH 11 solution. It showed strong green luminescence which can be linked to zinc vacancies due to annealing conditions in oxygen atmosphere. The transition responsible for the "green band" often observed in ZnO is seems to be related to free holes (Gu et al., 2004). A stronger green luminescence is related to the existence of more singly ionized V_O whereas many have reported red luminescence is contributed by the doubly ionized V_O. The intensity of green emission also influence by the diameter of ZnO nanorods. Quantum confinement effect of one dimensional (1D) ZnO NSs showed that the binding energy of excitons in nanorods is significantly enhanced by 1D

confinement. Size reduction has contributed more atoms to be closer to the surface and hence increased the intensity of green emission. This is due to larger surface to volume ratio favours higher level of defects and surface recombination (Shalish et al., 2004). Further decrease in the size may produce ZnO nanobelts that give a blue shift near the UV emission band (Wang, 2004b). Zhou et al. (2006) reported that the near UV emission and green emission properties depended on heating temperature and annealing time. Increment in the annealing temperature has decreased the size of ZnO nanoparticles and caused an increase in the green emission intensity (Zhou et al., 2006).

The research on ZnO has been extended by employing polymer based materials to investigate the PL properties. ZnO NWs covered with polymethyl methacrylate (PMMA) has exhibited significant improvement in the excitonic emission whereby NBE increased about three times due to the decrease in non-radiative process by surface recombination compared to the uncovered ZnO NWs (Liu et al., 2010). Terasako et al. (2010) found that orange band emission at ~600 nm is attributed to interstitial oxygen atoms. The domination of orange band with increasing deposition temperature has been reported by (Han et al., 2010).

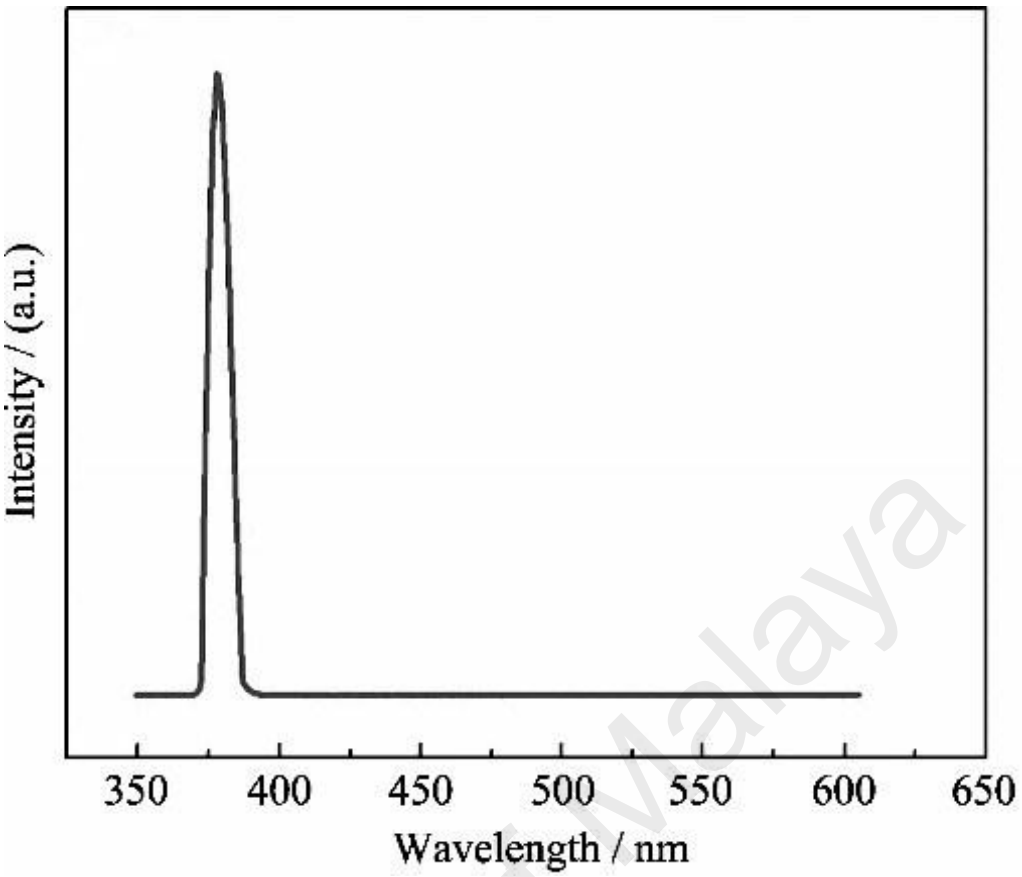

Figure 2.4: Photoluminescence spectrum of ZnO nanorods grown on a Si (100) substrate. The strong ultraviolet emission at around 381 nm is attributed to the near band edge emission of the wide bandgap ZnO. No broad defect-related green peak is observed indicating good crystallinity of the ZnO material (Zhang et al., 2014).

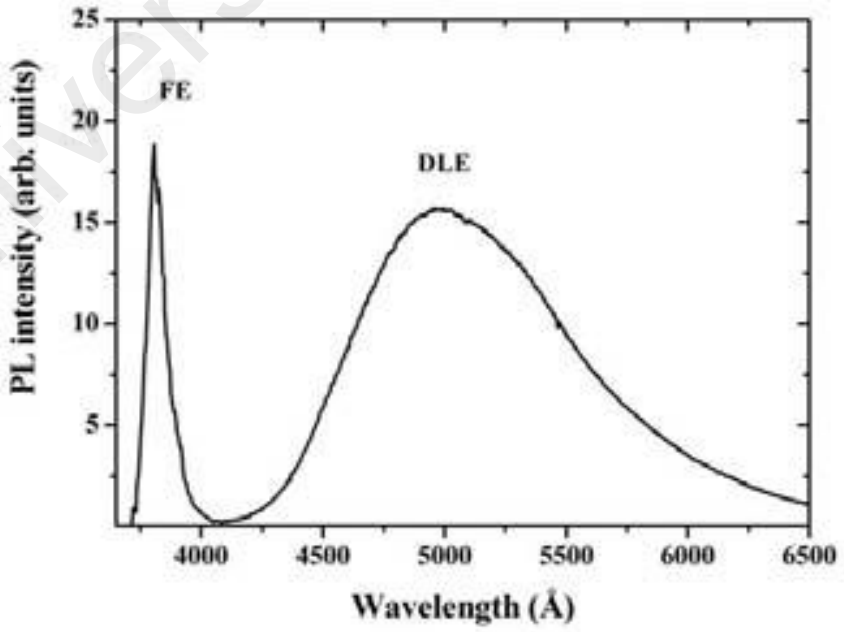

Figure 2.5: PL spectrum of ZnO nanorods grown on Au-layer deposited on Si (001) substrate at 890 °C, measured at room temperature (Zheng, 2012).

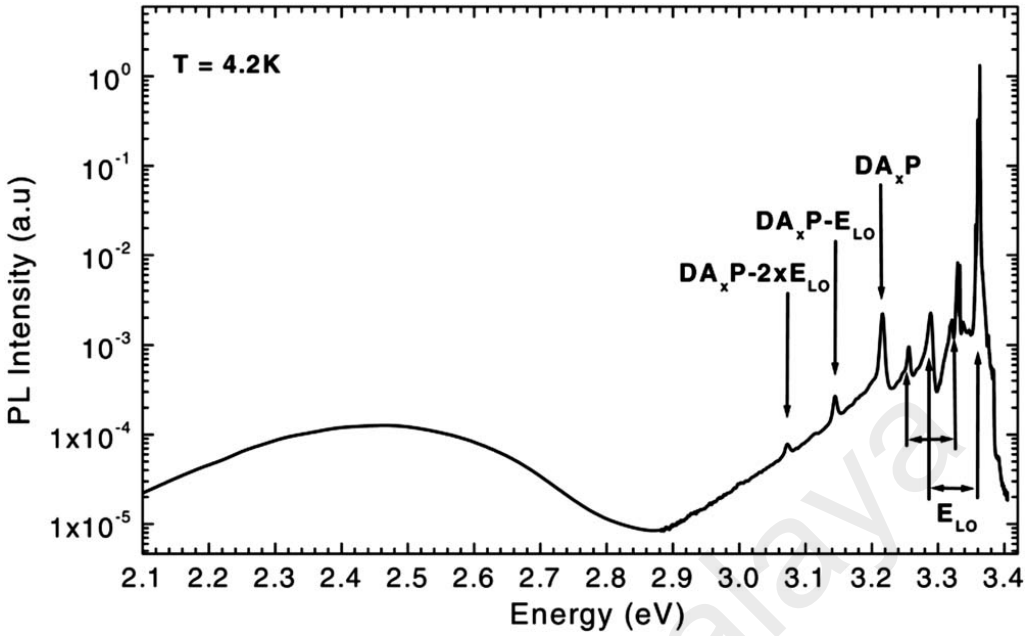

Figure 2.6: Typical PL spectrum of n-type ZnO measured at 4.2 K, showing exciton lines, donor acceptor pair transitions and their phonon replicas. The broad "green luminescence" is centered at ~2.45 eV (Meyer et al., 2004).

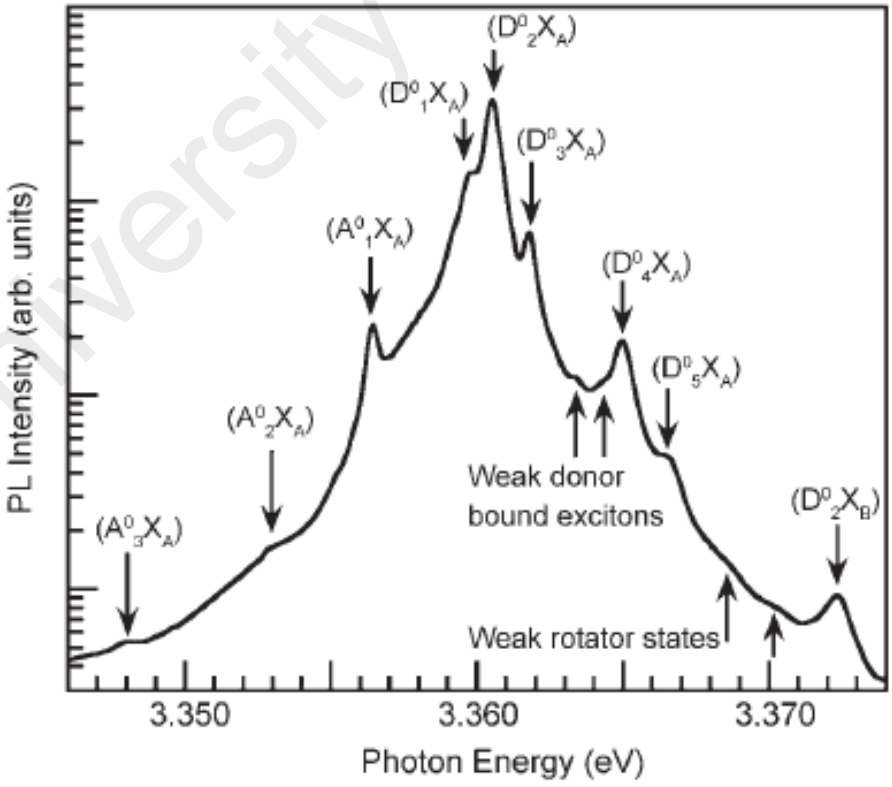

Figure 2.7: PL spectrum of donor-bound excitons in ZnO at 10 K (Teke et al., 2004).

2.3 Raman scattering effect in ZnO

Raman scattering is a fundamental form of molecular spectroscopy. Together with infrared (IR) absorption, Raman scattering is used to obtained information about the structure and properties of molecules from their vibrational modes. Infrared absorption arises from a direct resonance between the frequency of the IR radiation and the vibrational frequency of a particular normal mode of vibration. When the IR photon encounters molecule, the photon disappears and the molecule is elevated in vibrational energy if the property of molecule involved in the resonant interaction between the dipole moment of the molecule and its vibrational motion. In contrast, Raman scattering is a two-photon event. In this case, the property involved is the change in the polarizability of the molecule with respect to its vibrational motion. The interaction of the polarizability with the incoming radiation creates an induced dipole moment in the molecule, and the radiation emitted by this induced dipole moment contains the observed Raman scattering. The light scattered by the induced dipole of the molecule consists both Rayleigh scattering and Raman scattering. Rayleigh scattering corresponds to the light scattered at the frequency of the incident radiation, whereas the Raman radiation is shifted in frequency, and hence energy, from the frequency of the incident radiation by the vibrational energy that is gained (Stokes Raman) or lost (anti-Stokes Raman) in the molecule as shown in Figure 2.8.

In 1966, Damen et al. (1966) did the first experimental observation of the ZnO Raman spectrum followed by Arguello et al. (1969) enabled phonon modes of ZnO. Four atoms per unit cell of wurtzite hexagonal structures of ZnO leading to 12 phonon branches. They are 1 longitudinal acoustic (LA), 2 transverse acoustic (TA), 3 longitudinal optical (LO), and 6 transverse optical (TO) branches. The phonon modes were classified according to the following irreducible representations: $\Gamma = 2A_1 + 2B_1 + 2E_1 + 2E_2$, where A and B modes present one-fold degeneracy and E are twofold. One

A_1 mode and one E_1 pair are the acoustic phonons. The 9 optical phonons are divided into one A_1 branch (both Raman and IR active), one doubly degenerate E_1 branch (both Raman and IR active), two doubly degenerate E_2 branches (Raman active only) and two inactive B_1 branches. Therefore there are 4 Raman active phonons at the centre of the Brillouin zone (Damen et al., 1966). Complete phonon dispersion relations calculated at zero pressure and temperature has been reported by Serrano et al. (2004) together with Inelastic Neutron Scattering experimental data.

Raman scattering of ZnO has been studied extensively using various laser excitation but very few has been reported based on 532 nm green laser. Vempati et al. (2012a) used 532 nm on ZnO NSs. ZnO NSs peaks corresponding to E_2(high) at 439 cm^{-1} and $2E_2$ (low) at 329 cm^{-1} were annotated. In addition, multiple peaks attributable to defects such as V_o and Z_{ni} has been noticed spanning the range from 470 to 670 cm^{-1}. Specifically, the A_1(LO) peak at 545 cm^{-1} known to be due to lattice V_o. Earlier in 2011, Vempati et al. (2012b) investigated Raman spectrum using 532.5 nm green laser from a lab-built based on a Jobin-Yvon HR640 spectrometer with the CCD attached on ZnO grainy films. They found quite prominent peak at 242 cm^{-1} which has not been identified in the literature. Some have done comparison studies on ZnO using different laser excitation of 325 and 532 nm. In this case, a research group from Max-Planck Institution of Germany showed dominant peak at 578 cm^{-1} that attributes to LO phonon of ZnO when excited with 325 nm. While major peak at ~555 cm^{-1}, shoulder at ~440 cm^{-1} and a peak with low intensity at ~370 cm^{-1} were collected after excited with 532 nm laser source. The 440 cm^{-1} and 380 cm^{-1} were related to E2 mode of wurtzite lattice of ZnO and A1 –TO phonon modes respectively (Chen et al., 2013).

The doping effect on ZnO also has been studied using Raman spectrum. Shift position in ZnO modes often observed due to the effect of doping (Abaira et al., 2015). Jang et al. (2009) has compared Al doped and Ga doped ZnO with ZnO single crystal as

a reference. The unpolarized Raman spectra of ZnO single crystal exhibited peaks at E_2 optical mode at 101 cm^{-1} and 441 cm^{-1}, $A_1(z)(TO)$, $E_1(x)(TO)$, and $E_1(x)(LO)$ modes at 381 cm^{-1}, 413 cm^{-1} and 588 cm^{-1} respectively. They have concluded that high-order Raman peaks are more strongly related to y(Zhang et al.)y geometry than of y(Zhang et al.)y geometry which agreed with Arguello et al. (1969), Calleja and Cardona (1977) and Serrano et al. (2004). The Al and Ga doped ZnO, attributed more effect on the Raman spectra of the multi-phonon mode near 208 cm^{-1}, 336 cm^{-1}, and 1162 cm^{-1} than on those of the one-phonon modes. Strong Raman signal been reported depends on the size of ZnO nanorods . This is also similar to the findings of that related to several oxygen deficiencies in the ZnO NSs which influences intensity of Raman peak.

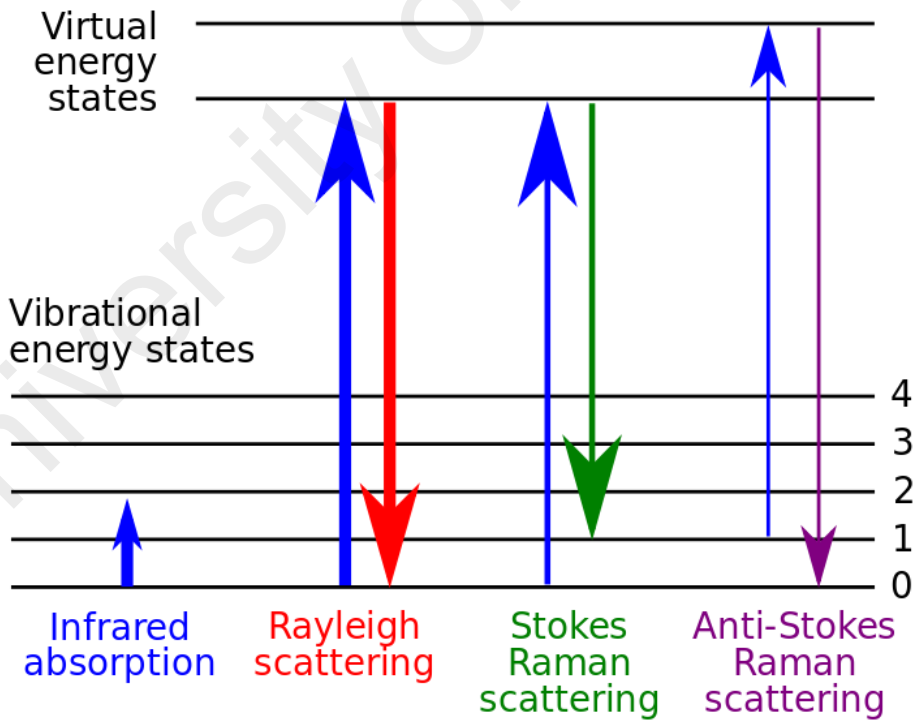

Figure 2.8: Energy level diagram of IR absorption, Rayleigh scattering and Raman scattering (http://www.huji.ac.il/unew/copyright_e.html).

2.4 Field emission

2.4.1 Introduction

The phenomenon of field emission of electron (FEE) had been introduced in mid 1700s after Winkler's earlier observation of FEE from sharp tip (Winkler, 1744) followed by first experimental observation by Wood (1897). Walter Schottky used the classical approach and hypothesized that image interaction causes the surface potential barrier reduced to zero at sufficiently high electric field (Schottky, 1923). Later Gossling (1926) of General Electric failed to confirm Schottky's theory from his investigation of FEE properties from cathode and he concluded that experimental observations would be explained by quantum mechanics. Gossling's general conclusion on quantum mechanics and Walter Schottky's hypothesis were improved by Fowler and Nordheim (1928). They solved the transmission probability of electron through triangular potential barrier, calculated the energy distribution of emitted electrons and relationship of current-voltage (I-V) characteristic was reported as $I = AF^2\exp(-B/F)$. I is the current density, A and B are constants and F is the macroscopic field. Further investigation in electrical properties was attempted by (Millikan & Lauritsen, 1929). They showed that I-V characteristics of cathode follows an equation, $I = A\exp(-B/F)$. Further milestone in the evolution of FEE was the invention of tungsten field emitter based field electron microscopy (FEM), which was later the improvement of stability and performance of tungsten field emitter in flash x-ray tubes (Grundhauser, 1966).

Contemplation of high field electron transport in semiconductor especially ZnO NSs requires a deep foray into condensed matter physics. The elucidation of electron transport is a formidable theoretical challenge. The microelectronic industries provide many practical applications for proposed theory of electron transport due to quantum size confinement effect. The one manifestation is electron emission over an energy barrier within the semiconductor devices. 1D ZnO NWs with wide band gap of 3.37 eV

have attracted much interest due to their remarkable physical and chemical properties. They were also been investigated as electron emitters as they have negative electron affinity, high mechanical strength and chemical stability (Lee et al., 2002). Besides that ZnO can be grown in various NSs reducing its size and structures using various techniques

2.4.2 Theory of field emission of electron in ZnO semiconductor

The electron emission from ZnO into a dielectric medium via tunnelling is the basis for a large variety of important practical semiconductor devices. The electron tunnelling refers solely under the influence of an electric field which opposed to thermionic emission and photoelectric emission that requires thermal energy. The behaviour of electrons delivers a fact, saying that forces normally constrain the electron to remain inside the material. According to the quantum free electron theory electrons inside n or p-type ZnO can be considered not bound to any particular atom as determine by the Fermi-Dirac Distribution Function as given by equation (1) which specifies the fraction of all status of energy, E occupied under condition of thermal equilibrium.

$$\boldsymbol{f(E) = \frac{1}{e^{\frac{E-\mu_f}{k_B T}}+1}} \ldots\ldots\ldots\ldots\ldots\ldots\ldots\ldots\ldots\ldots\ldots\ldots\ldots\ldots\ldots\ldots\ldots\ldots\ldots\ldots\ldots\ldots\ldots\ldots\ldots\ldots\ldots .. (\mathbf{2.1})$$

where, k_B is Boltzmann's constant in eV/K, μ_f is a parameter known as the chemical potential or Fermi level in eV, E is $h^2/ 8mL^2(n_x^2 + n_y^2 + n_z^2)$ and T is temperature in K. At absolute zero temperature there is no electron with energy in excess of Fermi level which is a consequence of Pauli's exclusion principle that there is no two electrons in an atom which can have exactly the same set of four quantum numbers. The field emission current density can be derived based on four assumptions. First, a simple one-band electron distribution using Fermi-Dirac statistics; second is a smooth, plane surface

where irregularities of atomic dimensions are neglected; third, a classical image force and forth, an uniform distribution of work function, results in

$$J = \frac{AF^2}{\phi} \exp\left(-\frac{B\,\phi^{\frac{3}{2}}}{F}\right) \quad (2.2)$$

where J is the current density and A and B are constants with values of 1.54×10^{-6} AV^{-2} eV and 6.83×10^{3} V $eV^{-3/2}$ μm^{-1} respectively. $F = \beta E$ where, β is the geometry dependent field enhancement factor and E is the electric field across the electrodes. β depends on the emitter geometry, aspect ratio, crystal structure, inner electrode distance and spatial distribution of emitting centers. ϕ is the work function of the emitting sample.

$$J = \frac{1.54 \times 10^{-6}\,(\beta E)^2}{\phi} \exp\left(-\frac{6.83 \times 10^{3}\phi^{\frac{3}{2}}}{\beta E}\right) \quad (2.3)$$

The well-known simplified Fowler-Nordheim (FN) equation can be written as,

$$\ln\left(\frac{J}{E^2}\right) = \ln\left(\frac{1.54 \times 10^{-6}\,\beta^2}{\phi}\right) - \left(\frac{6.83 \times 10^{3}\phi^{\frac{3}{2}}}{\beta E}\right) \quad (2.4)$$

This equation tells that, the plots of ln $[J/(E)^2]$ versus 1/E gives a straight line known as FN plot where the β corresponds to the slope of the straight line. Electrons tunnels from ZnO surface barrier in the region $0<x<L$ through vacuum barrier to anode. Electrons transmitted out with same wavelength, λ_0 equals to $2\pi/\sqrt{(2mE)}/\hbar$ as the schematic diagram in Figure 2.9. Lower electric field transport electrons through semiconductor

compared to metal-semiconductor interface (Geis et al., 1995) that could affect the degree of tunnelling. Several external agents like doped impurities can impart sufficient energy to electrons and enable it to escape from the surface. A doped ZnO does not limit emission of electrons into vacuum. But, efficiency of energy transfer from the external agent to electron is another factor to be considered in the emission of electron. The electrons tunnel through the thinning vacuum barrier (dielectric medium) in the vicinity of ZnO, via geometric deformation of the applied field by atomic scale surface undulation, result in increased probability of electron tunnelling.

Earlier investigation detailed a turn on voltage of ZnO in the range up to 6 V/μm (Lee et al., 2002). Extensive researches have embarked improved results that can be obtained from enhanced experimental technique. Zhang et al. (2004) used vapor phase transport technique and showed lower turn on field compared to Lee et al. ZnO NSs with sharp tip diameter and large surface areas can easily emit electrons and show effective photo-catalytic activity (Shinde et al., 2011; Warule et al., 2011). Pawar et al. (2013) have reported that an improvised NSs resulted in superior field emission. They fabricated cacti-like dense branching ZnO NSs with small tip diameters of ~3 nm and larger surface areas that resulted a turn on field of 2.13 Vcm^{-1} which is promising for display and photo-catalysis devices. An improved ZnO NS is believed to show better turn on field. Thus, department of chemistry from Purdue University worked out a spark discharge technique whereby carbon nanotube (CNT) had been grown on aerosol deposited ZnO nanoparticles. They found a lower turn on field ~1.7 Vcm^{-1} (Byeon & Kim, 2013) compared to 2.13 Vcm^{-1} reported by Pawar et al. (2013). Sun (2006) has reported that nanopin structured ZnO showed lower turn on field from compared to ZnO NWs. This shows, presents of sharp edges in ZnO has improved the field emission as well as the β value from 189 to 659 respectively for ZnO NWs and nanopins (Sun, 2006).

Wu et al. (2013) from Fuzhou University in China also showed improvisation in the turn on field. They have reported that at higher speed of spin coating a lower turn on field can be obtained. A spin coating technique was utilised to fabricate ZnO-adhering graphene film which exhibits a lower turn on field of 2.7 V/μm compared to ZnO film. Good electron emission stability was measured by (Wu et al., 2013) at initial current density 3.0 $mAcm^{-2}$ for a period over 3 hour and it slowly decreased to about 2.7 mA cm^{-2}. Earlier Wu *et al*. carried out another research work using the chemical vapor deposition technique. He has showed that graphene deposited on ZnO film sample has produced higher turn on field and threshold field about 2.9 and 5.2 V/μm respectively. However these values found to be lower than the pristine graphene sheet.

Earlier, Huang et al. (2013) used thermal oxidation technique to fabricate ZnO on tungsten oxide layer deposited glass substrate. The deposited zinc tungstate composite nanorods have exhibited lower turn on field 2.4 V/μm compared to ZnO nanorods (3.1 V/μm). Efficient field emission with low turn-on field (0.8 V/μm), low threshold field (2.3 V/μm), and excellent emission current uniformity has been observed in ZnO NWs grown on vertically aligned CNT mesh array (Ding et al., 2012). The stability test at $5x10^{-4}$ Pa had indicated a current fluctuation of less than 0.5 % in 80 hours compared to 5 % for bare aligned CNT. Moreover, they have reported that no current degradation has been identified in ZnO NWs grown on vertically aligned CNT mesh array. Fang et al. (2012) have worked out the effect of reaction period on turn on field of long ZnO NWs arrays. As the reaction time is increased from 22 to 60 minutes the turn on field and emission current density have decreased. They also found that leaf like ZnO NSs gave better turn on field compared to needle-like and long NWs array.

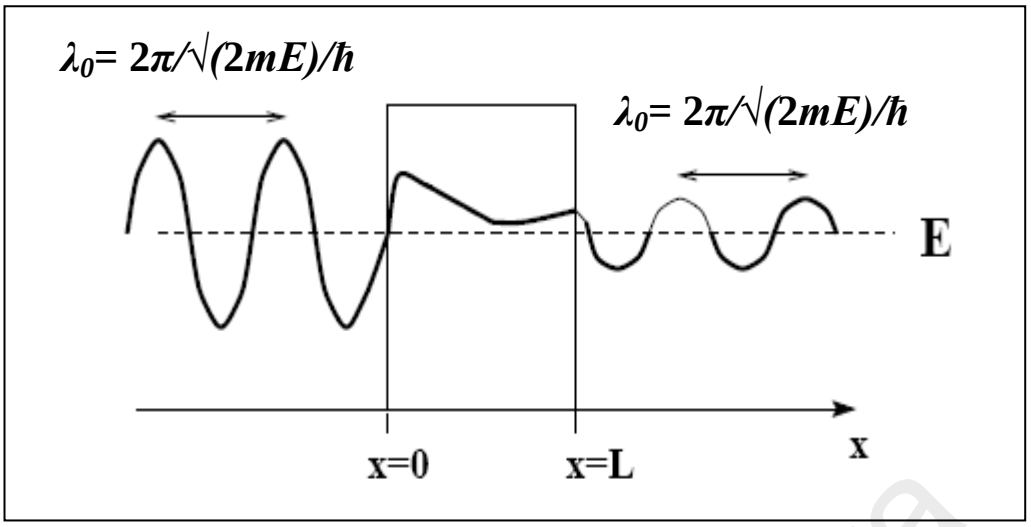

Figure 2.9: Wave oscillatory of electron through a barrier.

2.5 Growth technique of ZnO

Many techniques, physical evaporation (Ouyang & Zhu, 2008), chemical vapor deposition (CVD) (Feng et al., 2010; Wang et al., 2010b), solvothermal (Taunk et al., 2015; Tonto et al., 2008), carbothermal method (Lim et al., 2006) and flame synthesis (Hrkac et al., 2013; Reimer et al., 2014) have been reported elsewhere. These techniques involve many methods which have been employed in recent years to grow ZnO knowing its high potential in applications such as gas sensing and optical devices. The methods includes hydrothermal method, magnetron sputtering, pulse laser deposition, metal-organic chemical vapor deposition (MOCVD), vapor phase transport (VPT), carbothermal, molecular-beam epitaxy (Ashkenov et al., 2003) and etc can be segregated into three main techniques as per Table 2.2. However, the growth methods are ranged from low cost low temperature wet chemical growth technique to MOCVD technique (Jia et al., 2008) at temperatures above 1000 °C. The MOCVD technique has led to high quality growth of columnar structured film with higher growth rate but not straight forward to fabricate smooth ZnO thin film on flat surfaces. Indeed, growing ZnO film homoepitaxially on ZnO substrate using vapor phase transport (VPT) method

(Wagner et al., 2012) was favoured earlier but seem to be far from low cost and high volume production. Nevertheless VPT is still a suitable technique to grow bulky nanoscale ZnO wires, rods and thin film at reasonable cost since this method allows NWs to be grown directly from substrate and does not require any catalyst or seed layers to promote the growth of ZnO NWs (Yu et al., 2010).

Table 2.2: Growth technique and methodologies for ZnO deposition.

Growth technique	**Growth method**
Chemical Vapor Deposition (CVD)	Thermal CVD Low pressure CVD (LPCVD) Plasma enhanced CVD (PECVD) Metal-organic CVD (MOCVD) Molecular beam epitaxy Atomic layer deposition
Physical Vapor Deposition (PVD)	Thermal evaporation Electron-beam RF induction Resistive Sputtering Focused ion beam Radio frequency Magnetron Pulsed Laser Deposition
Solution-based Chemistry (SBC)	Precipitation Co-precipitation Hydrothermal Sol-gel

In late 90's methanol was used in fabrication of ZnO and most of the studies have been reported at low temperatures on selected transistion metal surfaces. Rufael et al. (1997) have reported that methanol undergoes thermal dissociation on iron, Fe (110) surface to form adsorbed methoxy (CH_3O) species and hydrogen at 100 K. Earlier Levis et al. (1989) also have reported about thermal decomposition of methanol but on palladium, Pd (110) surface, methanol decomposed into CH_3O(a) species with an additional of CH_3(a) and H_2O(a) at 125 K. Both Rufael and Levis have described that the CH_3O(a) species undergoes dehydrogenation to form CO and H_2 which later leads to formation of ZnO NSs.

2.5.1 Vapor phase transport

VPT enables the control of morphology and size of the NSs as parameters such as reaction time and temperature are adjustable. Yu et al. (2010) has reported that reaction time less than 2 hours has produced high quality ZnO NWs via VPT compared to organic solution based chemistry which takes about 2 to 12 h. Earlier, Zhu et al. (2005) used VPT method and detailed a comparative study on growth of ZnO NW using different metal catalyst and different substrate material which has imparted one dimensional ZnO NSs with different range of diameters, areal density and aspect ratios. VPT is feasible in fabricating semiconducting materials. A rich variety of NSs has been grown using VPT. This common growth technique is known for bulk ZnO, ZnO nanorods and thin films fabrication. The source semiconductor of ZnO, the Zn atoms are evaporated and get transported to the reaction chamber by an inert gas (e.g., argon or nitrogen). Later, oxygen gas or oxygen source is added to oxidise Zn vapor to ZnO. Often, the chemical process is enhanced by the additives such as carbon in ZnO mixtures for better evaporation, including possible catalytic effects, for example, the reduction of ZnO. Details on VPT are to be found elsewhere. VPT can be done in a

reactor consists of an open quartz tube, which is placed in an oven or furnace as shown in Figure 2.10. The temperature gradient in the furnace tube is controlled to initiate the growth of ZnO on suitable substrates. Liao et al. (2005) has detailed that 1D-nanostructural ZnO growth depends on the substrate and growth temperatures. Technically, VPT is also a suitable technique to deposit organic materials onto a substrate as shown in Figure 2.11.

Many had reported that the growth temperature varies based on the growth atmosphere and parameter condition. Zheng (2012) has grown ZnO at higher temperature of 1090 °C compared to the growth temperature of 500 – 950 °C used by Takahashi et al. (2000). They have demonstrated that vapor phase growth of ZnO films on sapphire (0001) substrates using atmospheric pressure by the reaction of zinc chloride and oxygen whereby nitrogen is used as carrier gas. Whereas Zheng (2012) had studied the effect of water and copper on the fabrication of resistor-shaped ZnO NWs using mixture of ZnO and graphite powder. The formation of resistor-shaped ZnO NWs in paired crystalline structure and series in line said to be potentially useful for building blocks in the fabrication of functionalized interfaces. Chen et al. (2006) had worked even at lower temperature at about 500 °C. They fabricated nanobelts with regular-triangle and needle-like heads of ZnO on Si (111) by flowing Ar at 145 sccm via selenium and Zn boat and with small amount of oxygen addition. In order to enhance the growth of ZnO NSs in vertical alignment gold nanoparticles were deposited as a catalyst. In 2004, B. J. Chen and co-workers had fabricated NWs, nanobelts and nanofibers on gold coated Si (100) via simple thermal chemical reactions vapor transport deposition method in air with a mixture of ZnO and carbon powder at 1100 °C. Zhang et al. (2004) also used gold coated Si substrate whereby ZnO NWs of 15 nm average diameters have been fabricated at 950 °C for field emission in the flat panel displays. ZnO micro-discs have been fabricated by (Yang et al., 2005) via VPT

technique at 700–850 °C mainly along the six directions of the <1010> plane whereby mixture of ZnO and graphite boat is used. Another one has reported that replacing carbon or graphite powder with activated carbon has lowered the growth temperature about 150 °C from 950 to 800 °C (Biswas et al., 2009).

Realizing various growth techniques in VPT which involves wide range of temperature from 400 to 1100 °C and different type of Zn and oxygen source, many researchers have proposed many series of growth mechanisms. The growth mechanism involves formation of various NSs including nanobelts, NWs, nanotubes and nanorods. Indeed, (Yang et al., 2005) had proposed layer by layer growth mechanism of ZnO micro-disks and quantitatively explained the suppressed growth along [0001] direction. Earlier in 2004, a group of researchers from Nanyang Technological University had proposed a growth mechanism based on thermal chemical reaction and VPT on seeded and non-seeded Si substrate (Chen et al., 2004). They found that growth of ZnO NS strongly depend on the growth temperature. Feng et al. (2010) have proposed a growth mechanism for tetrapod-like ZnO which involves pre deposition of ZnO on sapphire (001) using pulse laser deposition and thermal evaporation of metallic Zn powder at 900 °C in air. Donut shaped ZnO have been deposited via VPT utilizing mixture of ZnO, graphite and erbium oxide powder at 1000 °C (Chao & Yang, 2007). Wang et al. (2010b) also had proposed vapor solid growth mechanism as shown in Figure 2.12 for chestnut-like ZnO and Zn-ZnO hollow NSs that involves reactants Zn powder and oxygen gas. The first stage was formation of Zn polyhedron on Si(111) followed by surface oxidation and formation of hollow structure and growth of the ZnO nanoneedles and NWs on ZnO layers. The growth of ZnO nanoneedles and NWs was due to high deposition ratio of oxygen atoms in lower temperature regions of 408 °C.

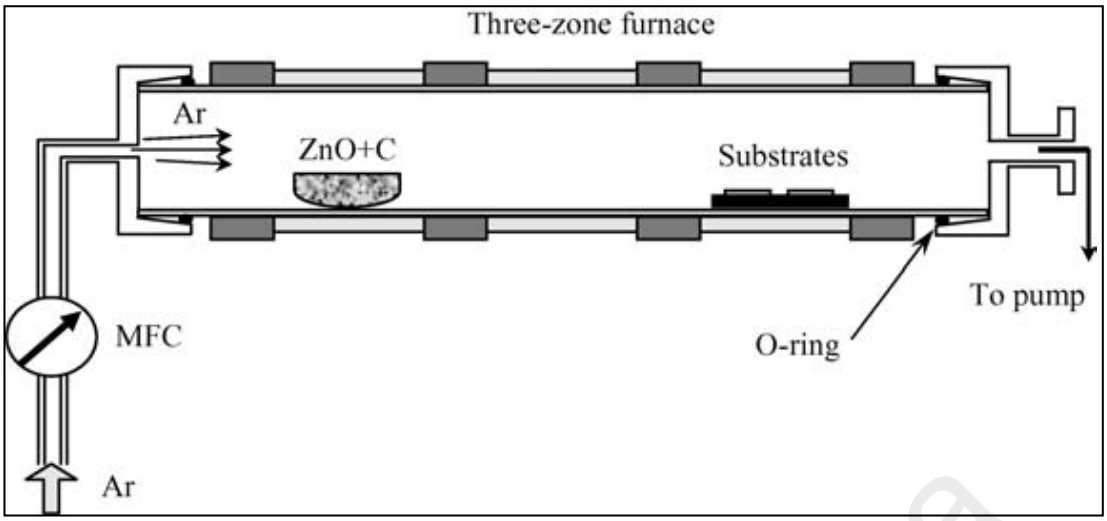

Figure 2.10: Common set-up of vapor phase transport method consist of quartz tube in furnace.

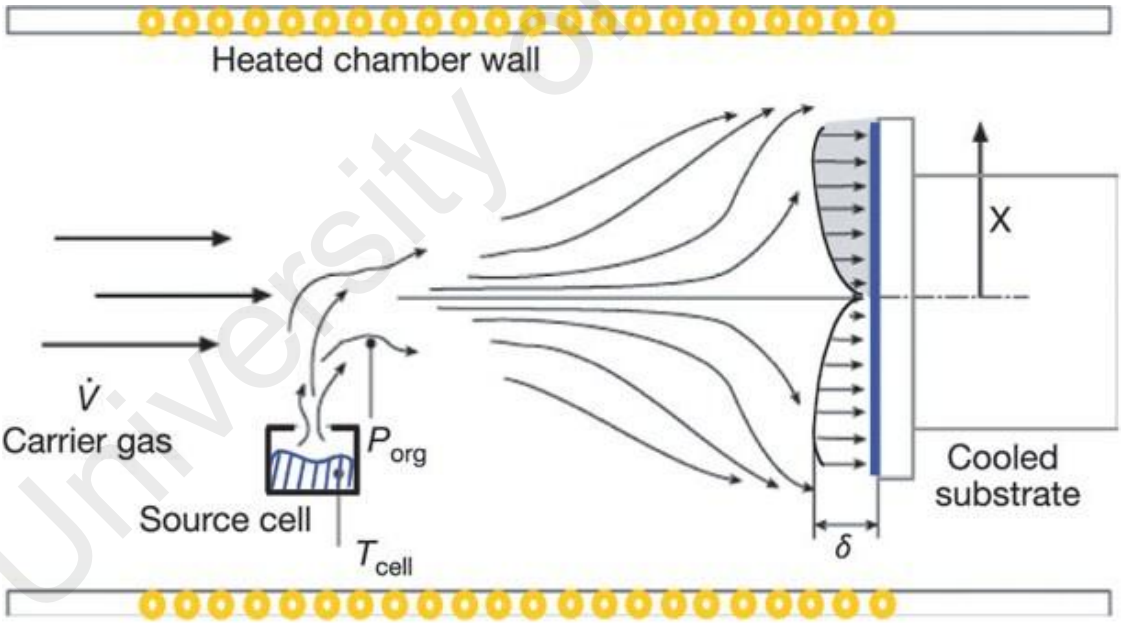

Figure 2.11: Organic vapor phase deposition using carrier gas (Forrest, 2004).

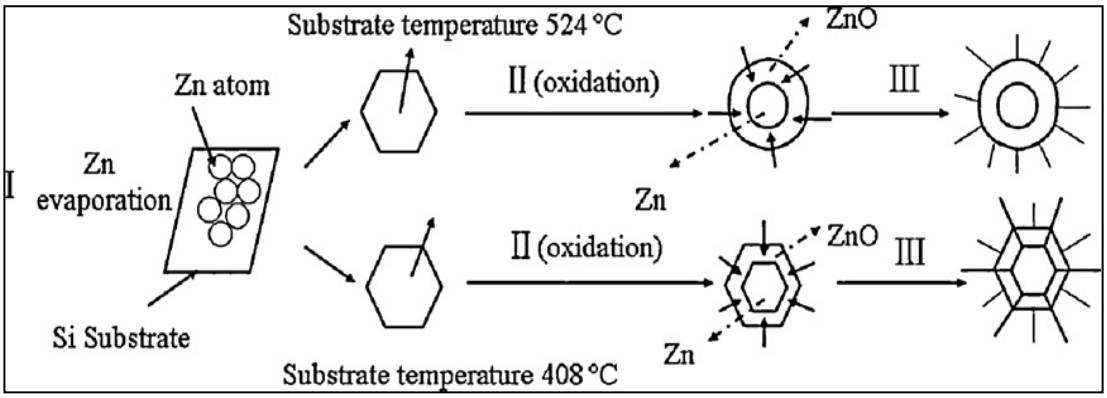

Figure 2.12: Proposed growth mechanism diagram of the as-prepared products (Wang et al., 2010b).

2.5.2 Thermal evaporation

In thermally induced evaporation, heat is supplied into the source material (often called the charge) to create a plume of vapor which travels in straight-line paths to the substrate as shown in Figure 2.13. The substrate is placed several centimetres away above the source. Upon arrival of plume of vapors at the substrate, the atoms, molecules, and clusters of molecules condense from the vapor phase to form a solid film. Here the heat of condensation is absorbed by the substrate. On a microscopic scale the localized heating from this process can be enormous. It is common, in the development of metal coating techniques for thin cross-section plastic parts, to melt substrates during the initial deposition runs. With experience, one can select source-to-substrate distances and deposition rates which will allow coating of temperature sensitive substrates without melting. Although this method is useful for deposition of many layers of different materials without chemical interaction between the layers, problems arises with film thickness uniformity and uniform doping over large area deposition (Forrest, 2004). Layer by layer deposition of zinc-tin-oxide film was achieved by Acharya et al. (2012) using thermal co-evaporation of ZnO and stanum oxide (SnO_2) where the temperature varied in between 150-550 °C for 20 minutes.

Thermal evaporation also found to be a useful technique to deposit a ultrathin contact points on a multilayers of electrode (Winkler et al., 2012). It also a good method to prepare ZnO of good optical and electrical properties which can be used in the field of photovoltaic cells (Zaier et al., 2015).

Hu et al. (2001) have used thermal evaporation of a mixture of ZnS and $Fe(NO_3)_3$ as source of Zn and O where Ar mixed with 5 % of H_2 as carrier gas. The deposition of ZnO whiskers were obtained in an alumina tube heated to 1300 °C for 12 h that has been evacuated by a mechanical rotary pump to a pressure of 4×10^{-2} Torr. Yuan et al. (2003) also used ZnS in fabrication of ZnO NWs but without any source of O. They believed that vacuum chamber that has been vacuumed to $\sim 10^{-2}$ Torr in Ar environment of 200 sccm has allowed some leakage of oxide gas into the chamber and promoted growth of ZnO NWs. In order to get high purity ZnO NWs, Lee et al. (2003) carried out thermal evaporation of ZnO powder at 1380 °C in high purity Ar environment at flow rate of 500 sccm. He concluded that vapor liquid solid (VLS) mechanism is not suitable for the growth of ZnO NWs, since ZnO NWs have been directly grown by a thermal evaporation using oxide powders without the presence of catalyst. The composition of the NWs is identical to that of the zinc oxide powder. Thus, they proposed vapor solid model based on the nucleation and growth theory. The effect of temperature as well as pressure in the fabrication of quasi one dimensional ZnO NSs via thermal evaporation has been investigated by (Liu et al., 2006a). They applied thermal heat that varied from 1090 to 1190 °C to a mixture of highly pure ZnO and C at mole ratio of 1:1 in Ar environment at flowrate of 220 sccm. The following year a group of researchers from Peking University accelerated their findings into the application of ZnO NWs. They have fabricated ZnO NWs from mixture of 99 % pure ZnO powder and graphite at molar ratio of 1:2 by thermal evaporation. The substrate

temperature was kept constant at 500 °C in a downstream region of furnace where Ar was introduced at flow of 40 cm^3 / min (Wang et al., 2007).

The demand and high prospect application of ZnO NWs has been realized in early 2005 and numerous researches have been progressed in order to obtain high purity ZnO. Realizing this, Li et al. (2008) fabricated ZnO micro and NSs by direct thermal evaporation at 1000 °C using high purity (99 %) Zn powders which has particle sizes, 80-100 meshes in air atmosphere without using any catalyst and carrier gas. Another local work from University Sains Malaysia has highlighted the growth of ZnO NSs from high purity (99.9 %) of Zn powder without catalyst. The furnace was heated slowly from 400 to 850 °C under continuous flow of highly pure Ar and O at 250 sccm Abdulgafour et al. (2010). Indeed, many extensive research works were being utilised in China. In line to that, fabrication of three types of novel ZnO hexagonal microprisms on MgO coated Si (111) via mixture of ZnO and carbon powder of weight ratio of 1:2 using the thermal evaporation has been published by Zhuang et al. (2011). Ar was flowed at 800 sccm into a furnace that was maintained at 1050 °C. The same group has published similar work in Superlattices and Microstructures in 2011 which discusses about the growth mechanism of two ZnO columns based on time-dependent (30, 35 and 40 minutes) experiment (Li et al., 2011).

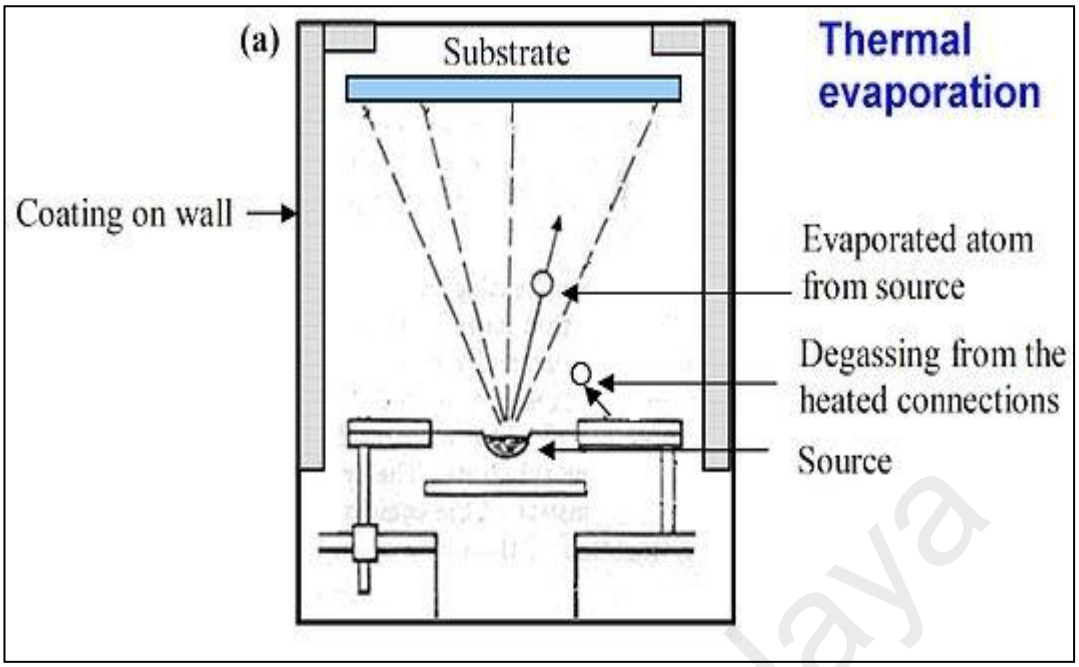

Figure 2.13: Vacuum thermal evaporation (http://science.cabot.ac.uk)

2.6 Scherer method

The breadth of the Bragg peak is a combination of both instrument and sample-dependent effects. To decouple these contributions, it is necessary to collect a diffraction pattern from the line broadening of a standard material (e.g., silicon) to determine the instrumental broadening (Chrissanthopoulos et al., 2011; Yogamalar et al., 2009). Thus, the instrumental corrected broadening (Biju et al., 2008; Rogers & Daniels, 2002) (B_{hkl}) corresponding to the diffraction peak of ZnO was estimated using the relation

$$\boldsymbol{B_{hkl} = \left[(B_{hkl})^2_{measured} - (B_{hkl})^2_{instrumental}\right]^{\frac{1}{2}}} \quad \text{.....(2.5)}$$

that is related to,

$$\boldsymbol{B_{hkl} = k\lambda/Dcos\theta} \quad \text{.....(2.6)}$$

Crystallite size of ZnO NSs was determined using the Scherer equation (2.6) where *D* is crystallite size in nanometer, *k* is shape factor (0.94) for cubic structure and λ (1.5406 Å) is the wavelength of CuK_α radiation, B_{hkl} is FWHM in radians and θ is the peak position for corresponding *hkl* (Dinesha et al., 2013).

2.7 Williamson-Hall method

The crystalinity imperfection and strain distribution in the sample can be determined using the Williamson-Hall (W-H) method. W-H (Williamson & Hall, 1953) method relies on the principle that the approximate formula for size broadening (B_{DS}) and strain broadening (B_ε), vary quite differently with respect to Bragg angle, θ (Williamson & Hall, 1953). Size broadening can be related to Debye-Scherer (B_{DS}) formula as in equation (2.6). The strain induced broadening arising from crystal imperfection and distortion can be related as in equation (2.7).

$$\boldsymbol{B_\varepsilon = C\varepsilon\, tan\theta} \quad \textbf{.....(2.7)}$$

where, ε is either maximum tensile strain alone or maximum compressive strain alone which can be calculated from the observed broadening and C is the constant equals to 4 that depends on the assumptions made concerning the nature of the inhomogeneous strain. One contribution (refer B_{DS}) varies as $1/cos\theta$ and the other as $tan\theta$ (refer B_e). If both crystallite size and strain contributions present independently to each other, then their combined effects can be determined by convolution. The simplification of W-H is to assume the convolution is sum of B_{DS} and B_ε. Using the former of

$$\boldsymbol{B_{hkl} = B_{DS} + B_\varepsilon} \quad \textbf{.....(2.8)}$$

it can be written as,

$$\boldsymbol{B_{hkl} = \frac{k\lambda}{Dcos\theta} + 4\varepsilon\, tan\theta} \text{.....(2.9)}$$

By rearranging the above equation, we get

$$\boldsymbol{B_{hkl}cos\theta = \frac{k\lambda}{D} + 4\varepsilon\, sin\theta} \text{.....(2.10)}$$

Equation (2.10) represents the uniform deformation model (UDM), where the strain is assumed to be uniform in all crystallographic directions. In order to evaluate stress in the NSs of ZnO a modified W-H model to uniform deformation stress model (UDSM) is applied. UDS and uniform deformation energy density (UDED) models were taken into account where the anisotropic nature of Young's modulus, E of the ZnO is more realistic (Khorsand Zak et al., 2011). The generalized Hooke's law referred to the strain, keeping only the linear proportionality between the stress and strain, is given by $\sigma = \varepsilon E_{hkl}$, where σ is the stress in the surface and E_{hkl} is the Young's modulus in the direction perpendicular to the set of crystal lattice planes (hkl). The W-H equation (2.10) is then modified by substituting the value of ε and we get

$$\boldsymbol{B_{hkl}\cos\theta = \left(\frac{k\lambda}{D}\right) + \frac{4\sigma \sin\theta}{E_{hkl}}} \text{.....(2.11)}$$

Since ZnO is a known hexagonal crystal phase, E_{hkl} is related to their elastic compliances S_{ij} as, (Zhang et al., 2006).

$$\boldsymbol{E_{hkl} = \frac{[h^2+\frac{(h+2k)^2}{3}+\left(\frac{al}{c}\right)^2]^2}{S_{11}(h^2+\frac{(h+2k)^2}{3})^2+S_{33}(\frac{al}{c})^4+(2S_{13}+S_{44})(h^2+\frac{(h+2k)^2}{3})(\frac{al}{c})^2}} \quad \text{.....(2.12)}$$

where S_{11}, S_{13}, S_{33} and S_{44} are the elastic compliances of ZnO and their values are 7.858×10^{-12}, -2.206×10^{-12}, 6.940×10^{-12} and 23.57×10^{-12} m^2N^{-1} respectively.

Equation (2.10) is modified to the form where energy density, *u* (energy per unit volume) is considered. According to generalised Hooke's law, the *u* as a function of strain is $u = \varepsilon^2 E_{hkl}/2$. In the strain-stress relation, all the constants of proportionality become no longer independent when the strain energy density is considered. Thus equation (2.10) can be written as

$$\boldsymbol{B_{hkl}cos\theta = \left(\frac{k\lambda}{D}\right) + \left(4sin\theta\left(\frac{2u}{E_{hkl}}\right)^{1/2}\right)} \quad \textbf{.....(2.13)}$$

2.8 Size-strain plot method

In the cases of isotropic line broadening, the size and strain parameters can be obtained from the size-strain plot (SSP) for ZnO NSs. This has a benefit that less importance is given to data from high angles of reflection where the precision is usually lower. In this estimation, it is assumed that the profile of strain and crystallite size respectively illustrated by a Gaussian and Lorenztian function as shown as equation (2.14) (Tagliente & Massaro, 2008).

$$\boldsymbol{(d_{hkl}B_{hkl}cos\theta)^2 = \frac{k}{D_v}\left(d_{hkl}^2 B_{hkl}cos\theta\right) + \left(\frac{\sigma}{2}\right)^2} \quad \textbf{.....(2.14)}$$

where k is a constant shape of particle for spherical particles it is given as 4/3 and σ is a measure of the apparent strain which is related to the root mean square (rms) strain $\varepsilon_{rms} = \sigma/(8\pi)^{1/2}$.

CHAPTER 3: METHODOLOGY

3.1 Introduction

In this chapter, a novel technique for synthesizing the ZnO NSs based on solid brass as the Zn source and alcohol vapor (methanol or ethanol) as the oxygen source is presented. The developed technique was motivated by the work of a group of scientist from Jawaharlal Nehru Centre for Advanced Scientific Research (Panchakarla et al., 2007). Our method differs significantly from reports where synthesized ZnO NSs directly on Zn (Cai et al., 2014) and brass (CuZn) alloy (An et al., 2009; Huo et al., 2007; Wang et al., 2014). We showed that ZnO NSs can be deposited on substrates based on the transport of Zn atoms from solid CuZn based on evaporation process where Zn atoms segregate to the surface at elevated temperatures and the appropriate amount of oxygen for nanostructured ZnO growth is provided by alcohol molecules.

3.2 Overview of experimental setup

The experimental setup for the fabrication of pure and doped ZnO NSs required systematic preparations of sample fabrication system and an initial optimization work. As part of that, the preparation and installation of sample fabrication system was initiated. The overall view of the sample fabrication system is shown in Figure 3.1. The developed sample fabrication system consists of a vacuum chamber, a vacuum pump, a.c power supply connected to electrical feed-throughs, gas flow system consisting of gas cylinders, mass flow controllers and vapor phase solution system connected with gas tubes, gas pressure gauge, gas pressure detector, temperature controller and air vent valve.

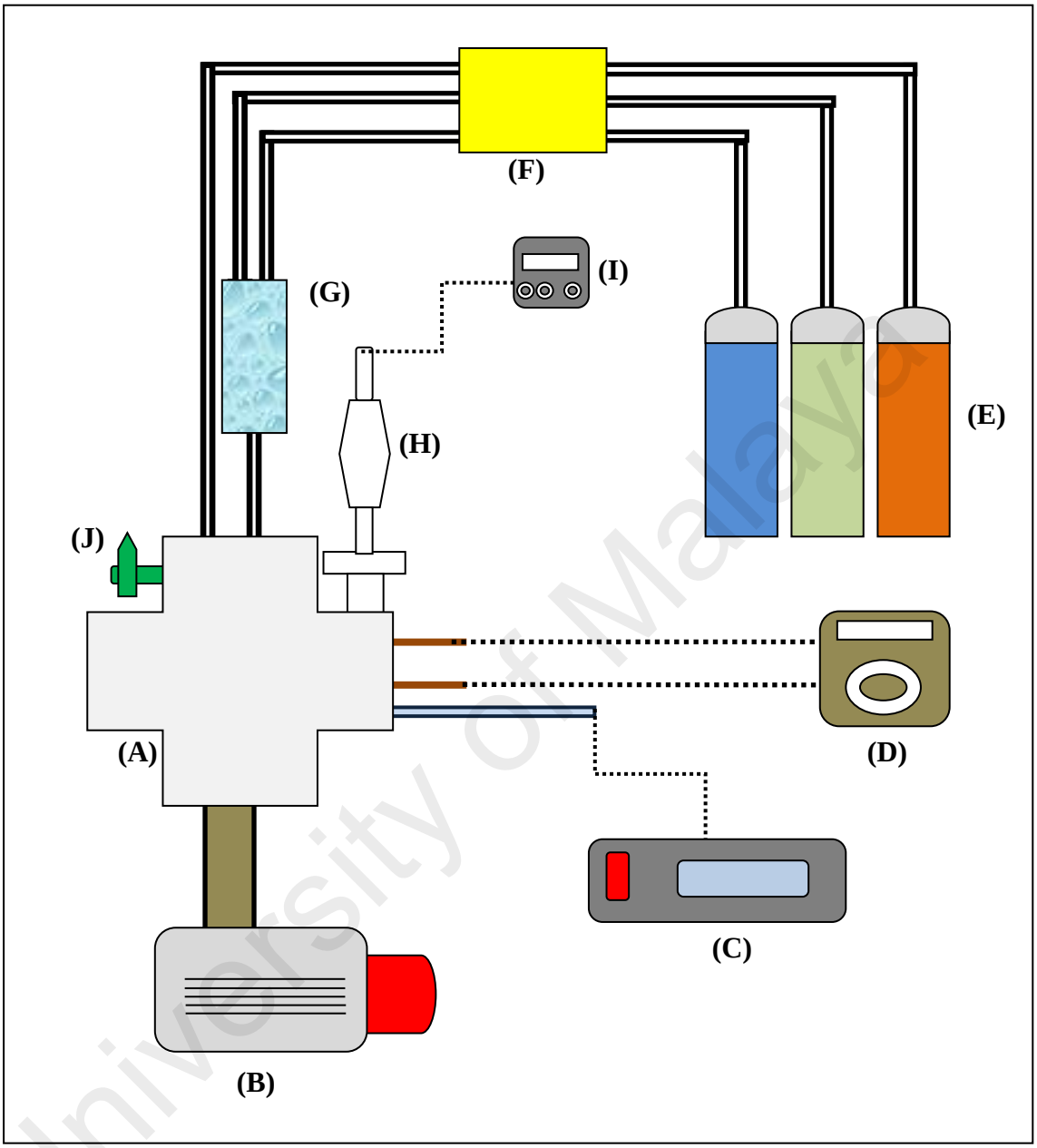

Figure 3.1: Schematic diagram of experimental setup consist of (A) vacuum chamber, (B) vacuum pump, (C) temperature detector, (D) a.c power supply connected to electrical feed-throughs, (E) gas cylinders, (F) mass flow controllers, (G) vapor phase solution, (H) gas pressure gauge, (I) gas pressure controller and (J) air vent valve.

3.3 Vacuum chamber

A stainless steel "Unequal TEE" vacuum tube as shown in Figure 3.2 was used as vacuum chamber in order to achieve a very low base pressure about 10^{-4} - 10^{-5} mbar in a short period of pumping of 30 minutes. The vacuum chamber is 13 cm in length with an inner diameter of 4.0 cm. It has three vacuum outlets; one NW25 and two NW40 vacuum outlets. One of the NW40 outlets was clamped to a stainless steel flexible bellow that mounted to a Pfeiffer Vacuum turbomolecular drag pump TMH 071P which has rotation speed, 90000 min^{-1} in order to achieve an ultimate pressures about 10^{-4} – 10^{-5} mbar. It was backed by a diaphragm pump MVP 015 – 2. Another NW40 was clamped to a stainless steel compressible bellow where the copper electrical feed-through is mounted through.

The NW25 vacuum outlet of the vacuum chamber was connected to NW25 4-way crosses. The vertically-up aligned NW25 port of the 4-way crosses was mounted with a view port to observe and determine the position of sample and to detect the deposition temperature onto Si substrate in the vacuum chamber using pyrometer. One of the horizontally aligned NW25 port was clamped to a NW25 tee port, to which was mounted a pressure controller (digital Pirani 945 series vacuum sensor), "Pirani" gauge (Kert J. Lesker 345 series) and to an air vent valve. The air vent valve allows the chamber to be brought up to atmospheric pressure before the chamber is opened. Another horizontally aligned NW25 port was used as a gas inlet.

3.4 Heating system

The heating system consist of electrical feeds-through and temperature controller. A homemade pair of copper electrical feeds-through was used. It was designed and prepared in 15 cm long and 0.5 cm diameter. At 10 cm from one end of the feeds-through a screw thread was grooved in order to be tightened to a stainless steel flange as

in Figure 3.3. The copper electrical feed-throughs were inserted into an insulator "0.25 EMI sleeve absorbers" and vacuum sealing was achieved using fast setting epoxy adhesive. The electrical feed-throughs facing inside of the vacuum chamber used to clamp filament whereas the electrical feeds-through facing out of the vacuum chamber were connected to a temperature controller as shown in the Figure 3.4. The temperature controller unit was connected to the type-K thermocouple and power supply (variable transformer). The tip of the thermocouple was placed on the surface of substrate. The operating temperature on the substrate was detected and controlled by setting a cut off temperature. The temperature of the substrate will be maintained at the selected temperature until the deposition period ends. After the deposition period the power will be manually reduced slowly to zero.

3.5 Gas flow system

Gas flow system plays an important role in any techniques that involve chemical vapor deposition and vapor phase transport. The high impact on the material functionalization to scale up to nanometer range has brought more stringent requirement on process gas purity. It is necessary to decrease gaseous impurities down to low parts per billion (ppb) levels (Chang & Sze, 1996). Due to this, high purity of gas was advised as feed gas in the fabrication of ZnO NSs. High purity gases such as purified argon (99.999%), hydrogen gas (99.999%) and purified nitrogen (99.999%) were used. These gases were connected to the vacuum chamber via desired mass flow controller using ultrahigh-purity PFA gas tubings. As a safety precaution the tubes were filled with drying agent desiccant silica gel in order to absorb any moisture content from the gas. This will allow moisture free gases enter into the vacuum chamber.

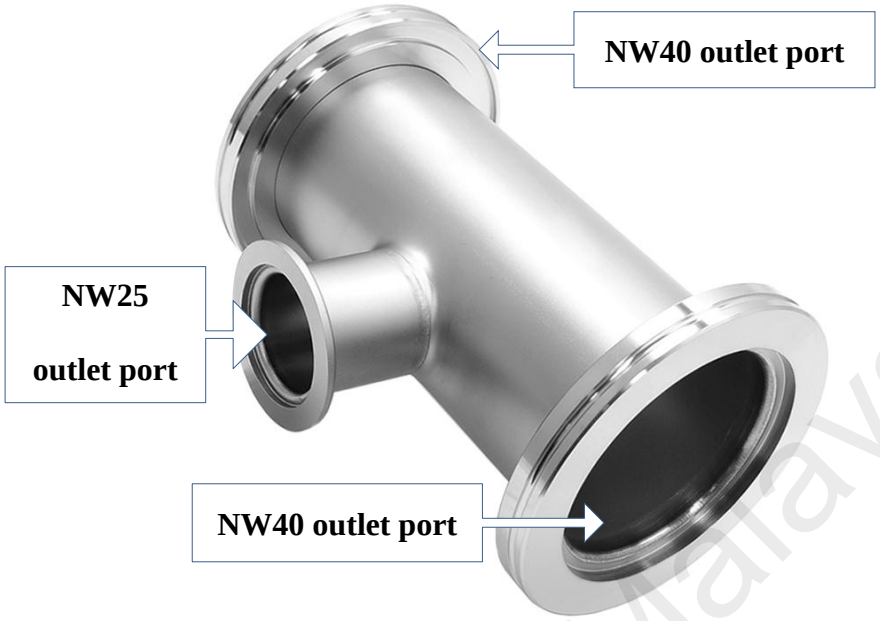

Figure 3.2: Stainless steel maiden “Unequal TEE” with two NW40 and one NW25 outlet ports used as vacuum chamber.

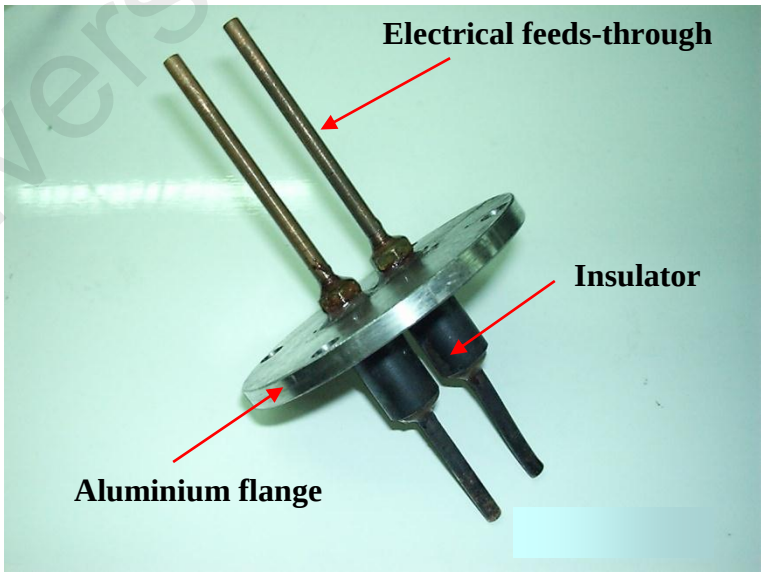

Figure 3.3: Copper electrical feed-throughs tighten to the aluminium flange and vacuum sealed with insulator sleeve absorbers.

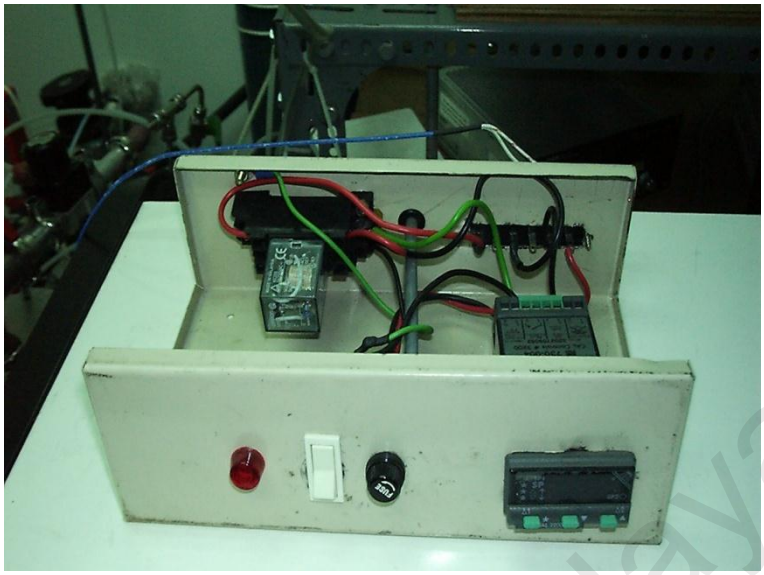

Figure 3.4: Temperature controller.

3.6 Initial optimization procedure

A technique of fabrication of ZnO NSs was developed which consists of a combination of the VPT of oxygen source chemical solution and thermal evaporation of Zn source material. Indeed, optimization of pure ZnO NSs was studied in three stages. The pure ZnO NSs were grown on Si (001) substrate. A brass (CuZn) metal rod which has composition of Cu about (> 65 %) and Zn about (< 35 %) was used as Zn source whereas methanol solution was used as source of oxygen. A smoothly finished Si (001) wafer was used as a substrate for the growth of ZnO NSs. Si was cut into chips about 1.5 by 1.5 cm and cleaned ultrasonically about 30 minutes in acetone solution to remove the presence of oxide layer and any impurities on the surface. Then the cleaned Si chips were rinsed in deionised (DI) water to remove the existing acetone solution on the Si substrate and allowed to dry in room temperature 24 °C. The dried Si chip was placed on a quartz slide before getting transferred into the vacuum chamber. A CuZn alloy plate thickness of 0.5 mm with dimension of 2.3 by 2.3 cm was prepared. A 0.5 cm hole

was drilled in the centre of the CuZn plate. This plate was then cleaned with DI water before placed on the prepared Si substrate. A CuZn alloy rod of 1.87 cm outer diameter and 2.44 cm in height with a hollow portion measured 1.94 cm depth and 1.0 cm diameter as shown in Figure 3.5 was also prepared. This one-sided hollow CuZn alloy rod as in Figure 3.5 was placed on the Si chip as it covers the whole surface of Si substrate as per illustrated in Figure 3.6. The purpose was to create CuZn environment to the surface of Si substrate.

Since the CuZn is thermally heated to only evaporate the Zn element, the selection of filament was considered as an important factor to avoid possible contamination from filament. Moreover ZnO was realized as a suitable candidate in microelectronic industries in producing n-type and p-type semiconductor. Contamination of third party element from filament was taken as one of the most fundamental understandings either to reduce or terminate the contamination. Somehow this contamination can apparently yield improvements in film quality. It could be important in applications where metal incorporation can be tolerated. Thus, the properties and characteristics of few common filaments such as tungsten (W), rhenium (Re), and tantalum (Ta) were well studied and selected.

Mechanical properties of these filaments have been studied (Lübbe et al., 1998). Rhenium filament do not carburize thus do not suffer from distortion. But tungsten filament which easily get carburize have a longer life time at 1950 ˚C. Tungsten filament is being used widely in hot filament method because of its thermal properties, which are; melting point of 3410 ˚C and boiling point of 5530 ˚C. Besides this, tungsten has the lowest vapor pressure of all metal, and at temperature over 1650 ˚C, it has the highest tensile strength. Furthermore it is an excellent corrosion resistance and is attacked only slightly by most of the mineral acids. The total emissivity of tungsten is 0.23 and 0.28 at temperatures of 1500 ˚C and 2000 ˚C respectively.

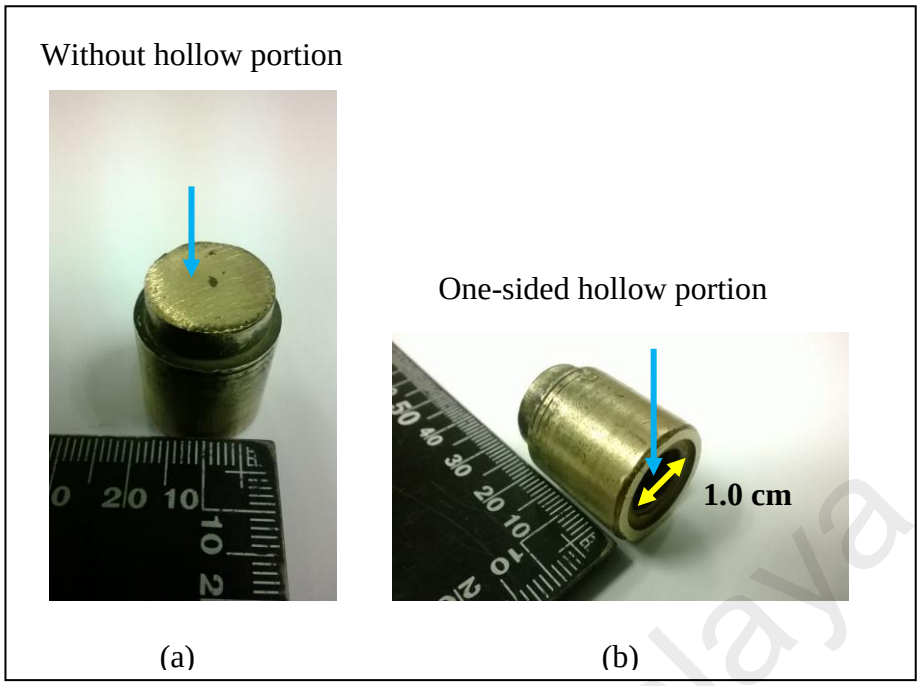

Figure 3.5: CuZn alloy rod (a) top view without hollow portion and (b) side view with one-sided hollow portion diameter of 1.0 cm.

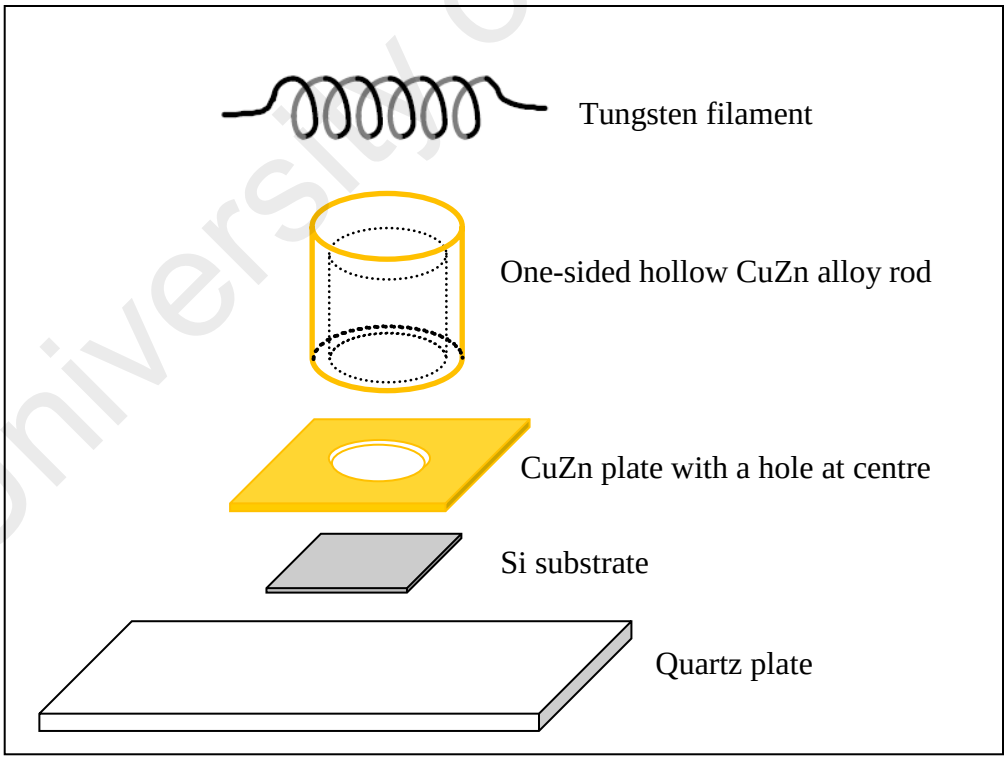

Figure 3.6: Configuration of materials used is illustrated in order from bottom; quartz plate, Si substrate, CuZn plate, one-sided hollow CuZn alloy rod and tungsten filament.

Thus, tungsten filament in 1 mm thickness was selected as heating element in the system. The filament wound about 3 turns to make a 5 mm diameter coil filament as shown in Figure 3.7. The two ends of the filament were coupled to a copper electrical feeds-through which were connected to a step-down a.c power supply. The distance between CuZn and tungsten filament was adjusted in the range of 5 – 10 mm in order to heat up the brass. Finally the stainless steel chamber that consists of filament, Si substrate, CuZn and quartz slide was evacuated to desired pressure of about 10^{-3} – 10^{-4} mbar. Thermocouples were mounted on CuZn and Si surface. The temperature of CuZn was controlled at around 800 °C while the Si temperature was detected to be around 750 °C. The procedures to obtain ZnO NSs were divided into three stages.

3.6.1 First stage: Fabrication of Zn layer

The above described procedure in section 3.6 was followed. Argon (Ar) was flowed at fixed flowrate of 100 sccm through a desiccant silica. This was to absorb moisture content in Ar that could contaminate the development of this technique. The filament switched on for 30 minutes to heat up the one sided hollow CuZn to 800 °C. Without Ar flow into the hollow portion of CuZn whereby vacuum condition was created inside the one-sided hollow CuZn metal rod. After the 30 minutes of deposition, a.c power supply was switched off but Ar was still allowed to flow at 100 sccm until the temperature of Si falls to room temperature at 24 °C.

3.6.2 Second stage: Fabrication of polycrystalline Zn layer

The above described procedure in section 3.6.1 was follwed with a minor change to the CuZn. The one sided hollow CuZn metal rod was replaced by two sided hollow CuZn metal rod. This was intentionally done to allow dried Ar flow into the hollow portion of CuZn. A Swagelok CuZn nut as shown in Figure 3.8 which has two sided hollow

portions was used. The purpose of using two sided hollow CuZn rod was to allow Ar flow into CuZn and to study the effect and role of Ar in producing Zn and ZnO NSs.

3.6.3 Third stage: Obtaining pure ZnO nanostructures in methanol with Ar flow

Procedure as in 3.6.2 was followed with an additional modification. Ar was flowed at 100 sccm through a mixture of methanol (50g) and acetone (4g) solution as shown in Figure 3.9. The purpose of methanol was determined as Ar was allowed to flow through the solution at flowrate of 100 sccm. According to Tzeng (2003), use of methanol alone as feedstock would lead to oxidation of the hotwire which could results in gradual reduction of diameter and contamination of the hotwire on Si substrate and he suggested that addition of acetone to methanol solution would prevent the deterioration of tungsten wire that being heated for 30 minutes at 1800 °C. The schematic diagram of the arrangement of materials and apparatus are shown as Figure 3.10.

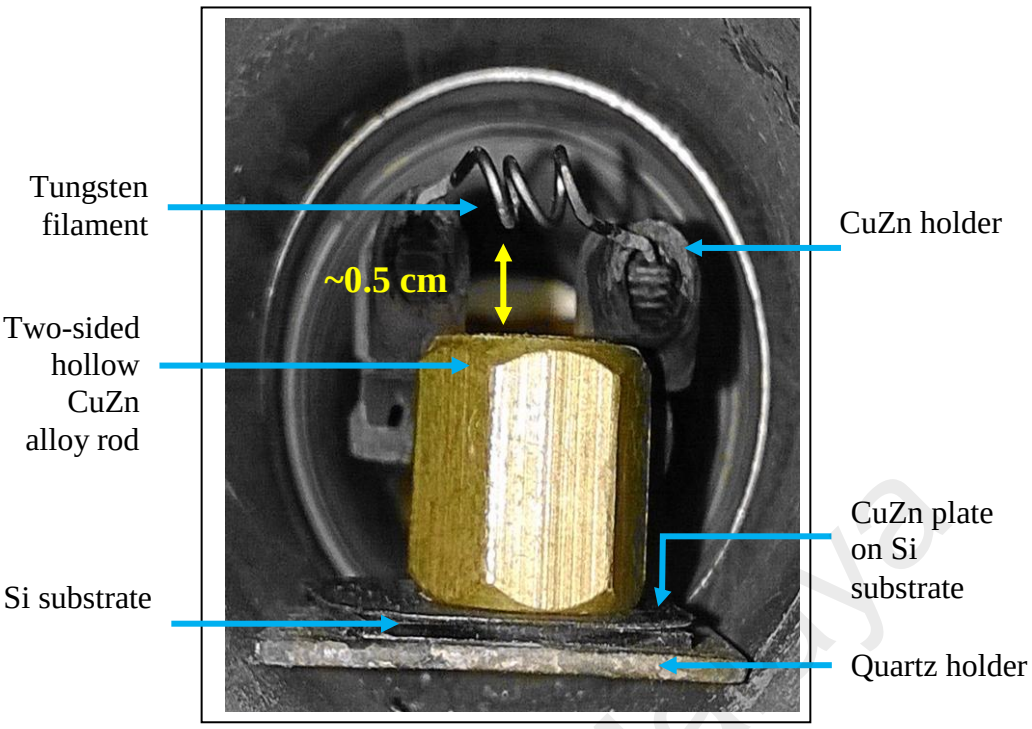

Figure 3.7: Configuration of thermal evaporation system consists of filament and CuZn alloy rod at separation distance about 0.5 cm in stainless steel vacuum chamber.

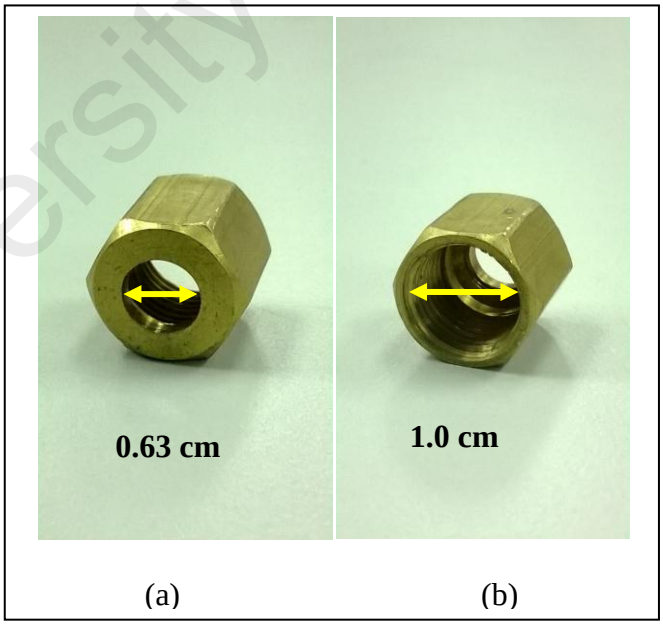

Figure 3.8: Swagelok CuZn nut which two-sided hollow is used in the experimental stage of 3.6.2 and 3.6.3 (a) top view and (b) bottom view.

3.7 Doping of ZnO nanostructures

In order to obtain doped ZnO NSs, procedure as per in section 3.6.3 was followed. Selected elements were dissolved in the chemical glassware that contains mixture of methanol and acetone solution as shown in Figure 3.9. Manganese oxide (MnO_2) and aluminium nitrate ($Al(NO_3)_3$) were used as source of manganese (Mn) and aluminium (Al) dopant. They were dissolved in the mixture of methanol and acetone solution in glassware. Ar was flowed at 100 sccm through the mixture in the glassware as the heating system turned on at 1800 °C for deposition time of 30 minutes. The growth conditions for the initial optimization study as per discussed in section 3.6.1, 3.6.2 and 3.6.3 to produce pure and doped ZnO NSs are summarized in Table 3.1.

Table 3.1: Growth condition for initial optimization study.

DESCRIPTION	**PARAMETERS**
Deposition Pressure	10 mbar
Argon flow rate	100 sccm
Filament temperature	1800 ºC
Substrate temperature	800 ºC
Methanol or ethanol solution	Source of oxygen
Filament to CuZn alloy distance	0.5 cm
Deposition Time	30 minutes
Substrates	Silicon
Filament wire	1 mm thickness; 3 turns tungsten wire

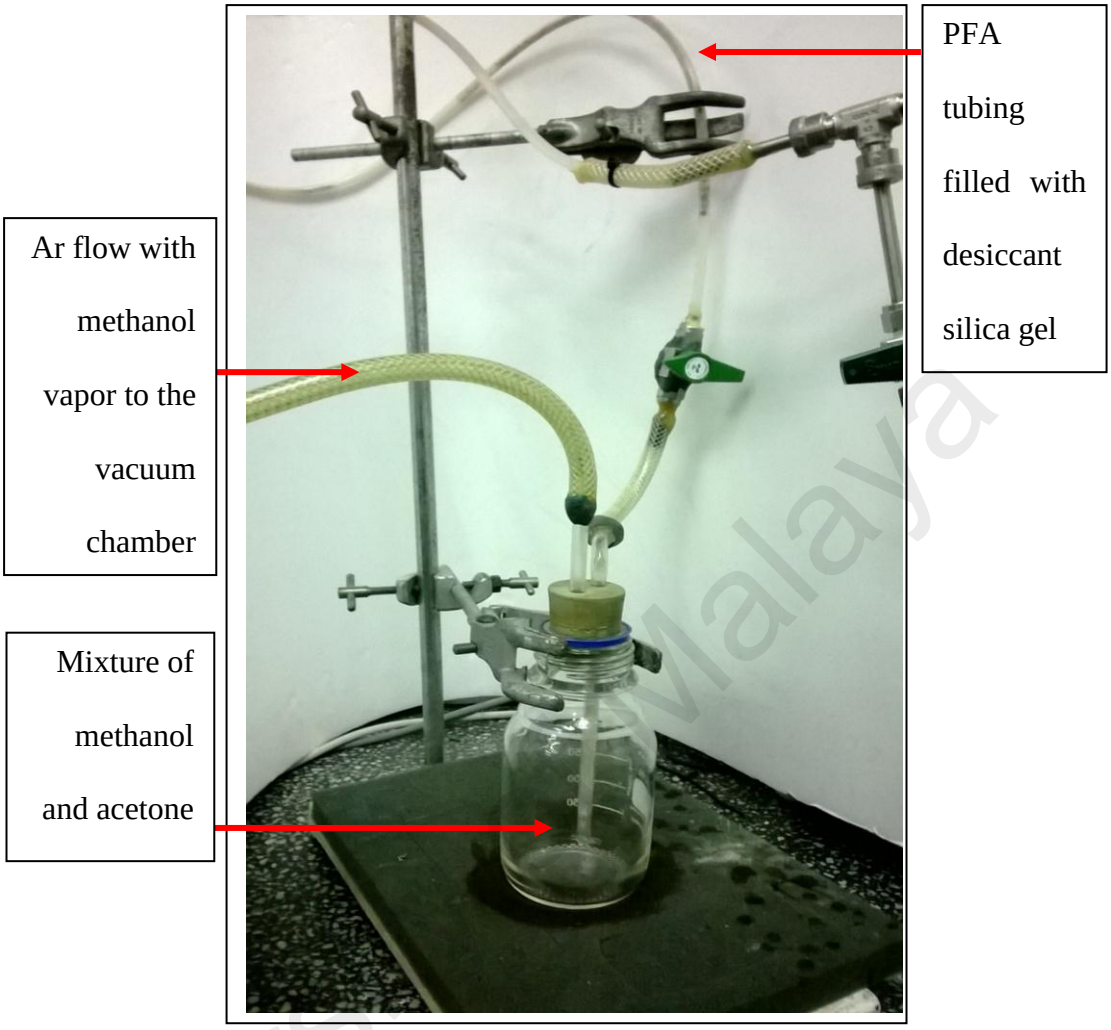

Figure 3.9: Additional setup of mixture of methanol and acetone in a chemical glassware.

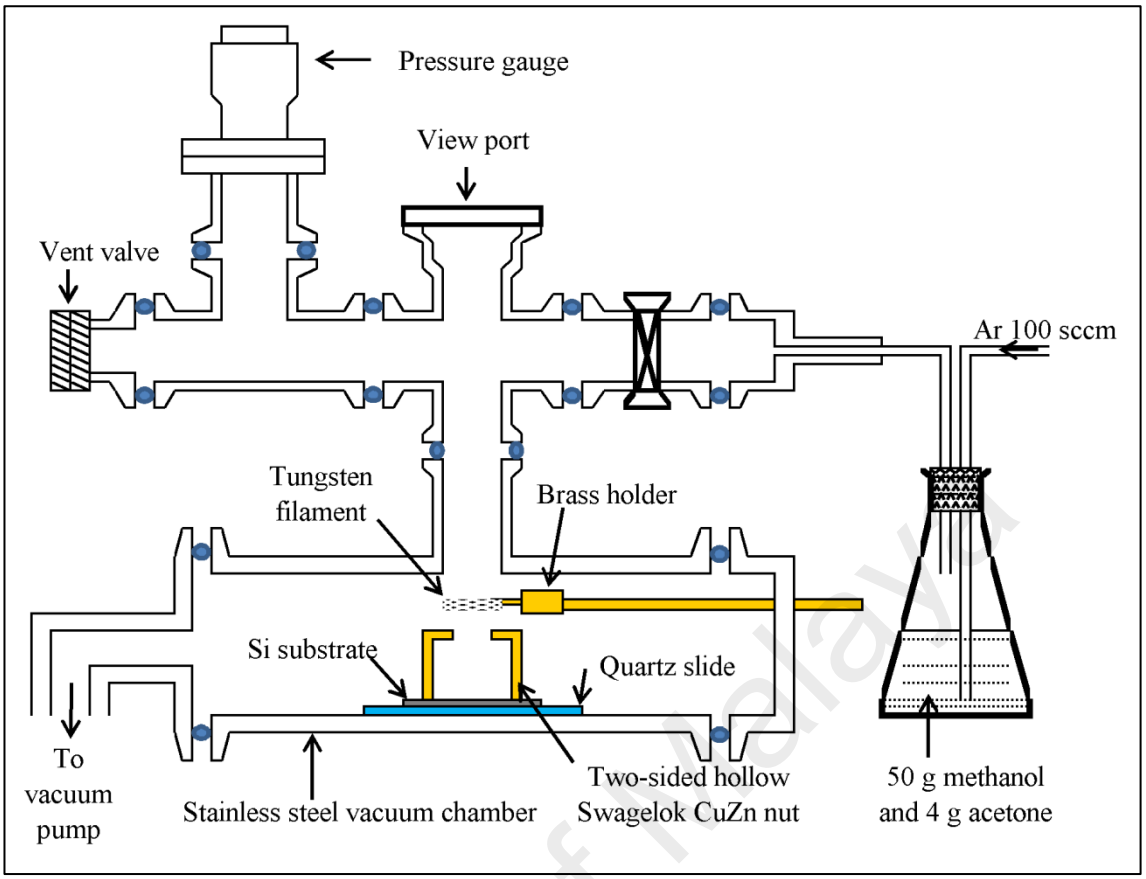

Figure 3.10: Schematic diagram of combination of vapor phase transport and thermal evaporation assisted with heated hotwire for doping of ZnO.

CHAPTER 4: ANALYTICAL TECHNIQUE

4.1 Introduction

The quality of the samples prepared in order to obtain both pure and doped ZnO NWs were characterized using a number of analytical techniques available in the Department of Physics of University of Malaya. In section 4.2 and 4.3, characterization techniques such as field emission scanning electron microscopy (FESEM) fitted with energy dispersive analytical x-ray (EDAX) and x-ray diffraction (XRD) were described.

ZnO NSs have been reported presents in various structures like NWs, nanopillars, nanocomb, spiral, nanobelt etc. Thus FESEM was utilised to observe and determine the fine surface morphology of the ZnO nanostructure. The XRD was a useful technique to determine the crystal structure and orientation of the ZnO NSs. Besides that the raw data of XRD was used to determine the properties of the ZnO. Besides that, other techniques were used to evaluate the optical properties of fabricated ZnO NSs on Si substrate. Indeed, the usefulness of micro Raman spectroscopy and photoluminescence (PL) characterization were discussed respectively in section 4.4 and 4.5.

4.2 FESEM

FESEM is an important tool to investigate the surface and morphology of NSs. It allows direct observation of 2-D localised scan images. Diameters, length, thickness, density, shape and orientation of the NSs can be estimated precisely with high resolution magnification. Figure 4.1 shows the schematic diagram of the FESEM JEOL JSM-7600F which is available in the Department of Physics of University of Malaya used in this study. The sample's surface morphology and structural information were collected at working distance of 3.7 mm from the objective lens.

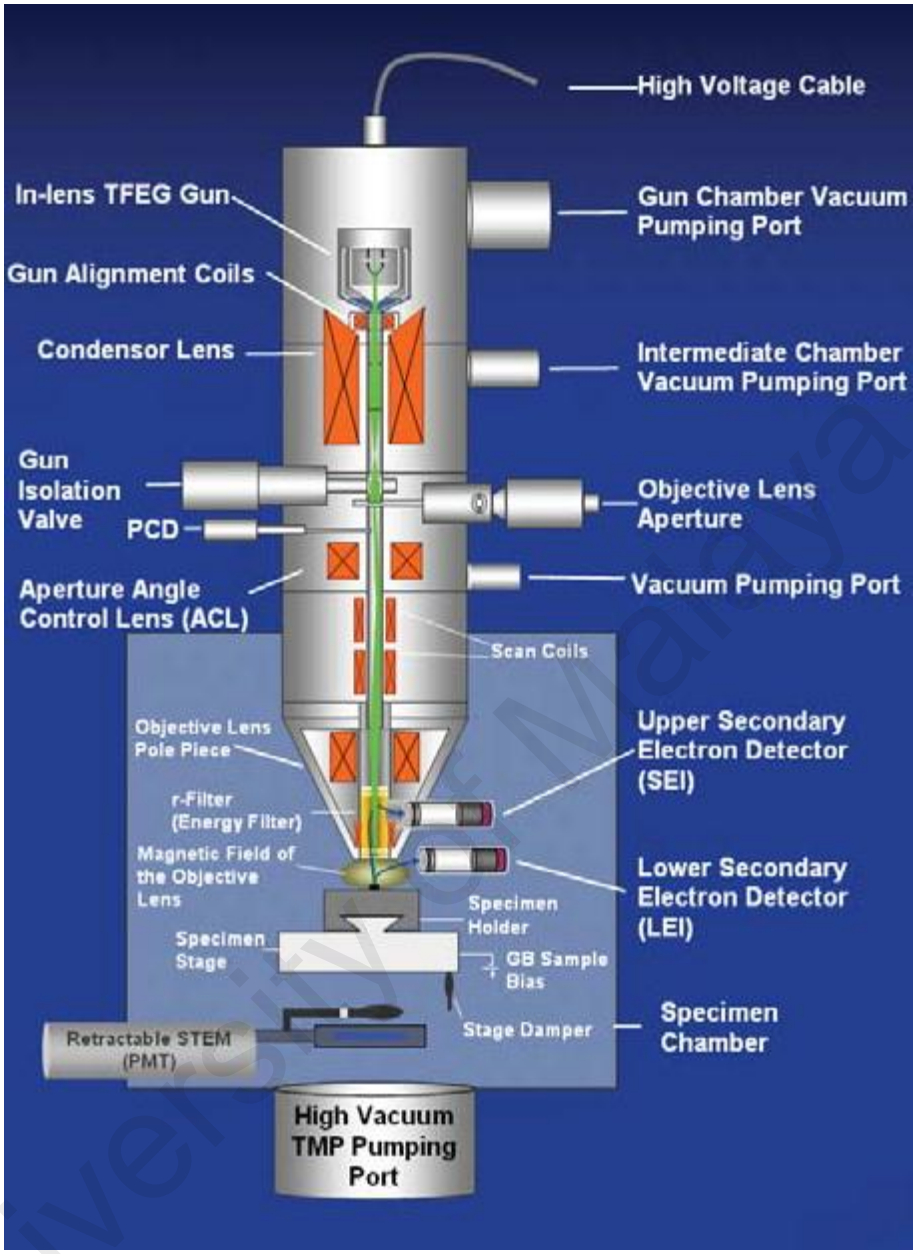

Figure 4.1: Schematic diagram of FESEM JEOL JSM-7600F
(Copyright © 2008 JEOL USA, Inc. 11/08 0.25M).

The in-lens thermal field emission gun is used to emit electrons by supplying strong electric field. A crystal of lantanumhexaboride (LaB6) mounted on extremely thin and sharp tungsten needle tip with a diameter about 10 - 100 nm works as a cold cathode. The projected electrons eject secondary and back scattered electrons after

hitting the sample. These ejected secondary and back scattered electrons from the sample are detected by detectors and these detectors transfer these detected electrons into electronic signal which is sent to a computer to display the image. During the measurements the vacuum pressure in the chamber was about 9.6×10^{-5} Pa and the electron gun voltage was 0.5 – 30 kV. The maximum resolution of the SEM was up to 10 nm. Figure 4.2 shows a typical FESEM image of ZnO NSs grown on Si substrate. The grown NWs looks like button mushroom at the tip, needle like NWs and nanorods were covered the whole substrate randomly and uniformly. The ZnO NSs are randomly orientated with estimated mean diameters in the range of 20 – 100 nm and approximately 1 – 2 μm in length.

Energy dispersive analysis of x-ray (EDAX) is the most common technique that provides rapid qualitative, or with an adequate standards, quantitative analysis of elemental compositions with a sampling depth of 1-2 microns. An example of typical EDAX spectrum of ZnO is shown as Figure 4.3. Interaction of primary beam electrons with atoms in a sample causes shell transitions which result in the emission of an x-ray that has an energy characteristic of the parent elements. It exhibits chemical information about the sample. Presence of only oxygen and Zn elements are detectable in Figure 4.3. The configuration of elements will be presented in percentage for weight and atomic. An inner shell electron can be displaced by the collision with a primary electron. An outer shell electron may fall into the inner shell to restore charge balance to emit x-ray photon. The x-ray spectrum gives information about which elements are present in the sample. Mapping is also possible, which indicates the location of elements. It should be noted that the generation of X-rays from the sample also requires high energy primary electrons and as a consequence the resolution is considerably lower (Zhou & Wang, 2007). A modern trend in electron microscopy is to fit X-ray analysis equipment as a bolt-on accessory.

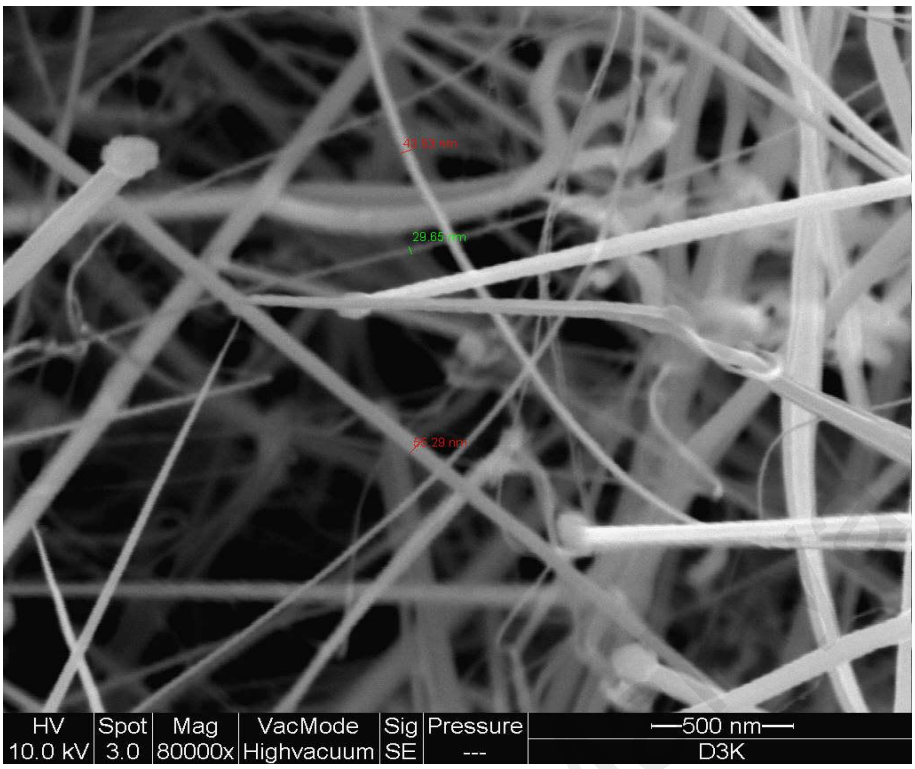

Figure 4.2: 80k X magnified typical image of ZnO nanowires in the range from 20 – 100 nm.

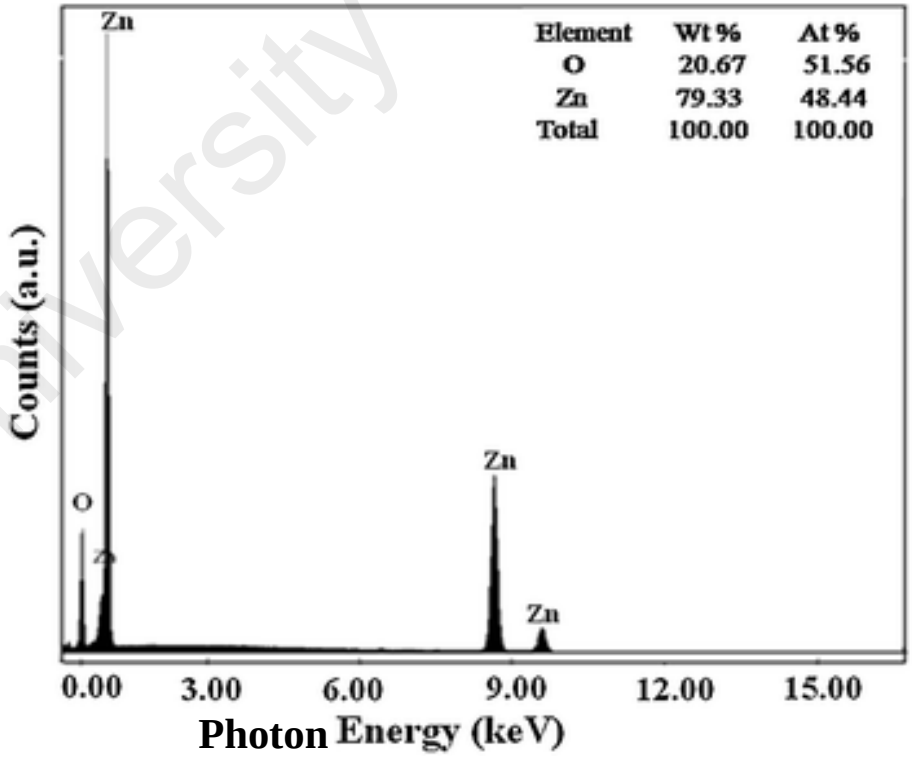

Figure 4.3: EDAX analysis of ZnO nanoparticles (Chandrappa et al., 2010).

Bombarding a specimen with electrons causes X-rays of characteristic wavelengths and energies to be emitted from the spot where the beam strikes the specimen. Computer analysis of the wavelength or energy spectra makes it possible to measure accurately the nature and quantity of different elements in the material. The technique is of little use to biologists because light elements such as carbon produce too weak X-ray signal (Madou, 2011). But it is of great value in material science, particularly because an area as small as one square micrometer can be analyzed with precision (Hearle et al., 1972).

4.3 XRD

XRD is the most common characterization and a non-destructive technique used to determine the structure and orientation of crystal. Besides that, composition, quality, lattice parameters, defects strain and stress in semiconductor materials like ZnO can be estimated. Average spacing between layers of atoms also can be calculated from the XRD profile. The SIEMENS D5000 with Cu-K_α probe beam at a wavelength of λ = 1.5406 Å was used for all measurements.

The phenomenon of x-ray diffraction by crystalline materials results from a scattering process in which x-rays are scattered by the electrons of atoms without any changes in wavelength. A diffracted beam is produced by coherent or Bragg scattering only when certain geometrical conditions are satisfied. Bragg concluded that the path difference between the two x-rays diffracted from two consecutive lattice planes as in Figure 4.4 is $2d\sin\theta$ and it leads to Bragg's law, which states that the condition for diffraction of x-rays for a crystalline material is $n\lambda = 2d\sin\theta$. The θ is the angle of incidence and λ is the wavelength of the x-rays, n is an integer and it is the order of reflection, and d is the distance between the lattice planes. The interatomic distance in solids is several Armstrong and the energy corresponds to this distance can be

calculated as E= hc/λ for λ equals to 1 Å. Therefore, E approximately equals to 12×10^3 eV. If the structure of the solid is to be probed by electromagnetic waves then these waves should have energy at least equal to the interatomic distance energies. X-rays have approximately same energy (keV) as the interatomic distance energies of solids.

Figure 4.5 shows typical XRD spectrum for ZnO NWs obtained on Si substrate. The spectrum exhibits all possible peaks that correspond to the polycrystalline nature of standard JCP2.2CA: 00-036-1451 wurtzite hexagonal ZnO peaks. A strong and sharp (101) peak with narrow spectral width indicates dominant orientation of NWs along a- or b-axis. The measuring parameters used in this measurement are listed in Table 4.1.

Table 4.1: Specification of X-Ray Diffractometer model SIEMENS D5000.

Source	Copper K_α, λ = 1.5406 Å
Power Supply	Current : 40 mA; Voltage : 40 kV
Step mode	Continuous scan
Range size	5 to 120˚
Step size	0.04˚
Step time	2s
Glancing angle	2˚
Scanning Mode	Detector scan

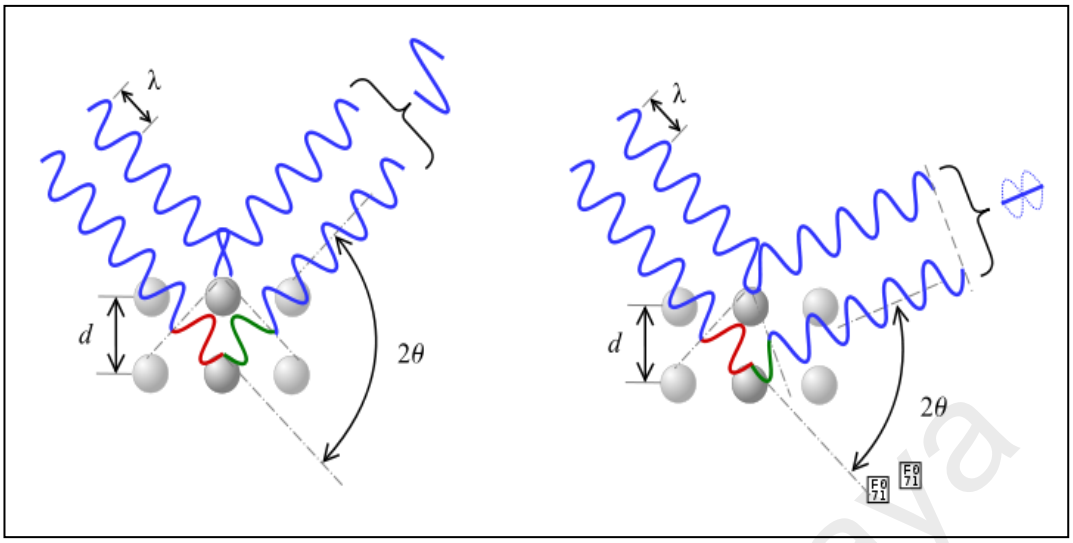

Figure 4.4: Shows a schematic diagram of Bragg reflection from crystalline lattice planes having interplanar distance "d" between two lattice planes (http://commons.wikimedia.org/wiki/File:Loi_de_bragg.png).

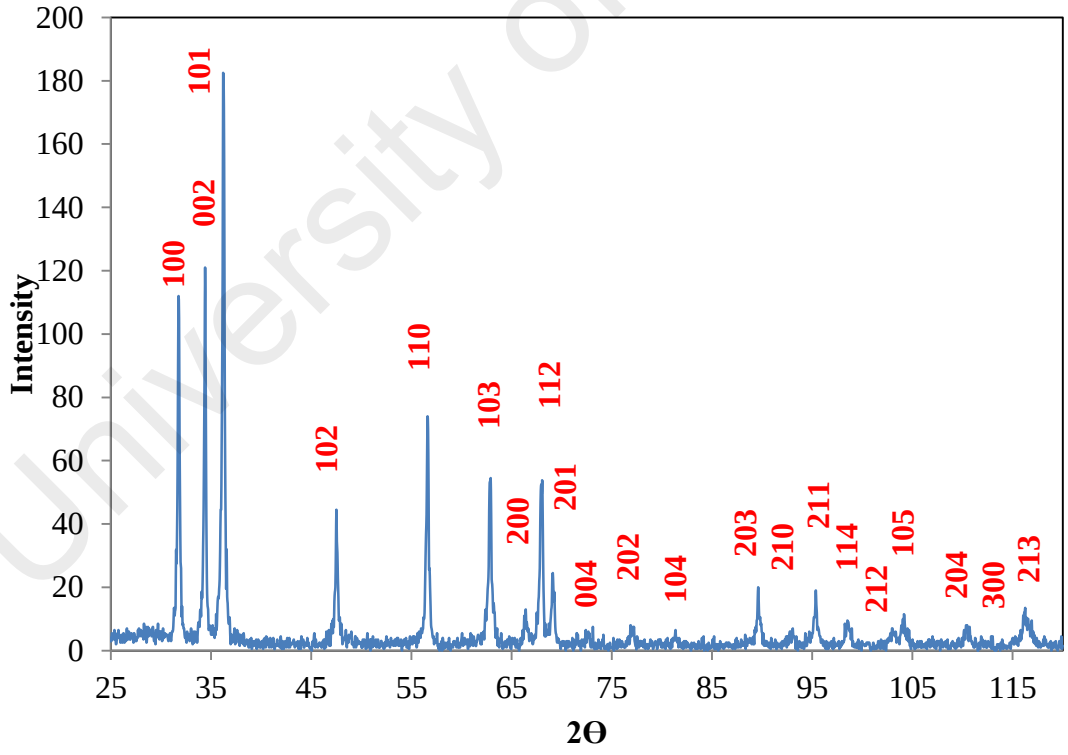

Figure 4.5: Typical XRD spectrum of polycrystalline ZnO nanowires obtained on Si substrate which corresponds to JCP2.2CA: 00-036-1451 of ZnO powder.

4.4 Micro Raman spectroscopy

Raman effect was first discovered by Sir C. V. Raman in 1928, while working on molecular light scattering (Szymanski, 1967). It is the most widespread technique for the ZnO phonon analysis. Raman spectroscopy is also versatile for characterising semiconductor materials and devices. It known as one of the non-destructive methods which enable assessment of material crystalline quality, local stress and strain, dopant and impurity level and even temperature in operating devices on a sub-micron scale. Besides that details like chemical bonding of sample, phonon frequencies, energy of electron states and electron-phonon interaction, carrier concentration can be gathered from micro-Raman spectroscopy (Szymanski, 1967; Wang & Kang, 1998; Weber & Merlin, 2000).

The spectrometer used in this study was Renishaw inVia Raman microscope as shown in Figure 4.6. An excitation wavelength of 532 nm with a grating of 1800 mm^{-1} (visible) was used to collect the Raman spectrum. The micro-spectroscopy measurements were conducted using the ×100 objective lens and detected by Renishaw charged-coupled devices (CCD) camera resolution of 578 x 400. The spectrometer is supported by the latest version 3 of its Windows®–based Raman environment software WIRE™ 3.0 Raman software. The system was calibrated to the spectral line of crystalline silicon at 520.7 cm^{-1}. Spectra were measured in the range 50 – 3200 cm^{-1} with a continuous scan option. The step size was calculated from the raw data spectrum approximately 1.65 cm^{-1}. The exposure time was set to 10 s which will improve the signal to noise ratio. The accumulation was selected to improve signal to noise ratio for the removal of cosmic ray. The laser power at 10 % was found to be appropriate for the prepared ZnO sample due to the following factors, (a) eliminate strong background due to fluorescence, (b) avoid saturated signal and (c) avoid laser ablation on the sample.

When a transparent medium (solid, liquid, or gas) is irradiated by monochromatic light from laser source (diode pumped green crystal laser 532 nm) as in Figure 4.7 with a frequency ω_L that does not correspond to any absorption line of the sample, the light will pass through the sample unaffected. However, a very small part of it will be scattered either elastically or inelastically in different direction from that of the incident beam. The incident light inelastically scattered from a sample and shifted in frequency by the energy of its characteristic molecular vibration. The vibrational properties of ZnO NSs can be easily determined from the Raman scattering (Ryu et al., 2006). Typical Raman spectrum of bulk ZnO presents 6 first-order peaks as in Figure 4.8. They are two non-polar modes (E_2^{low} and E_2^{high}) and four polar modes (A_1-TO, A_1-LO, E_1-TO and E_1-LO). The corresponding Raman frequency is shown in Table 4.2 (Cuscó et al., 2007; Damen et al., 1966; Jang et al., 2009; Özgür et al., 2005; Serrano et al., 2004).

Table 4.2: Raman modes of wurtzite ZnO crystal.

Raman peak modes	Frequency (cm^{-1})
E_2^{low}	99 – 101
E_2^{high}	437 – 438
A_1 - TO	378 – 380
A_1 - LO	574 – 579
E_1 - TO	409 – 413
E_1 - LO	583 – 591

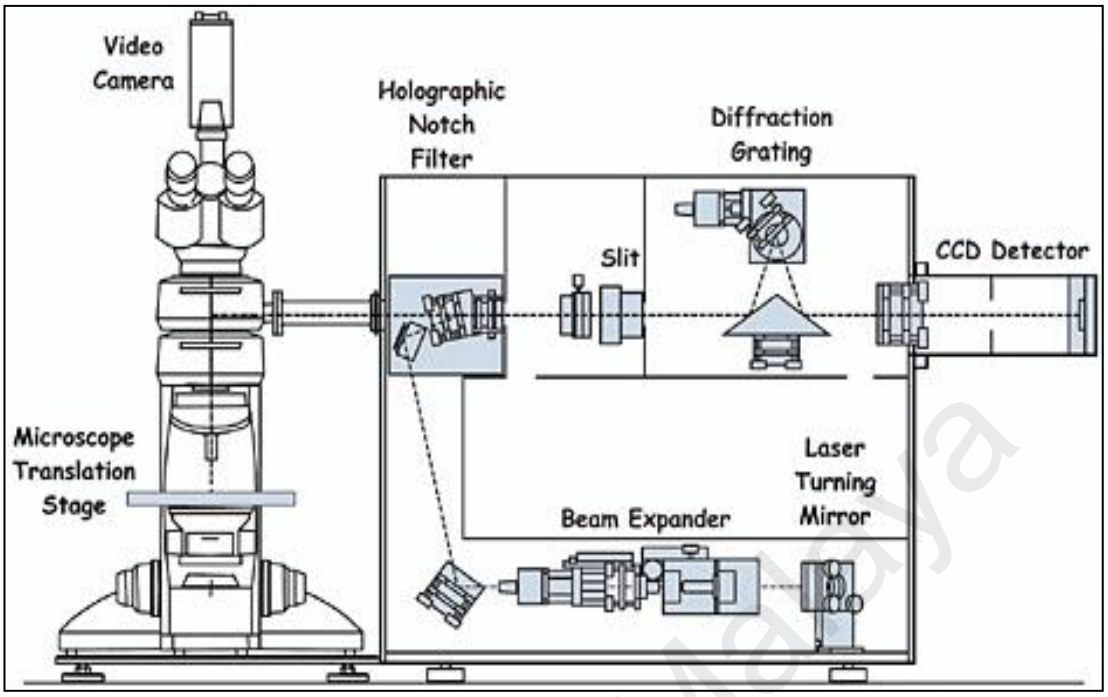

Figure 4.6: Schematic diagram of Renishaw inVia Raman/PL microscope (Smith & Clark, 2004).

Figure 4.7: Diode pump laser source of Green 532 nm laser.

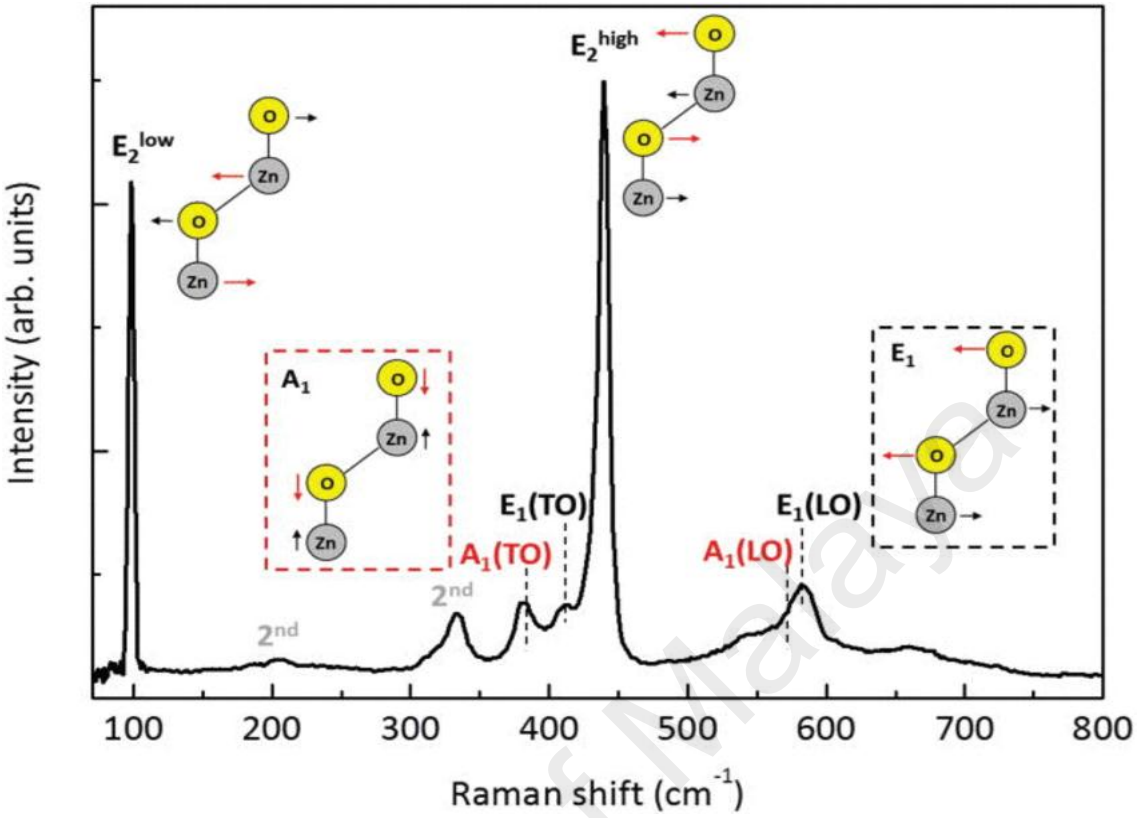

Figure 4.8: Raman spectrum of bulk ZnO excited by 532 nm green laser. Raman active modes with the corresponding vibrations of the ions are indicated (Russo et al., 2014).

4.5 Photoluminescence

Photoluminescence (PL) is one of the non-destructive techniques used for the investigation of extrinsic and intrinsic properties of semiconductors like ZnO. In this technique the ZnO nanowire is excited optically to obtain a PL spectrum of spontaneous emission. The ZnO nanowire is irradiated with a laser light that has energy greater than the band gap. Electrons in ZnO are excited and more pairs of electron and electron hole are formed. The energy of excited electrons are emitted as light when the pairs of electron and hole recombine (refer Figure 4.9). PL technique is very useful in determining the bandgap, impurity levels, defects detection and recombination process in the semiconductor materials (Gilliland, 1997). In this research work, the Renishaw

In-Via Raman/PL micro-spectrometer which is available in the Department of Physics of University of Malaya, was used for characterization. The PL measurements were performed at room temperature and pressure by using laser lines with a wavelength of 325 nm from a helium-cadmium (He-Cd) laser class IIb source as shown in Figure 4.10 which was produced by Kimmon Koha Co., Ltd. The laser was powered by a Kimmon He-Cd laser power supply as shown in Figure 4.11. Schematic diagram of the PL setup used in this research is shown in Figure 4.6. The PL measurement has three main steps,

- In the first step, the semiconductor is optically excited to create electron-hole pairs. Different kinds of lasers such as He-Cd laser with wavelength of 325 nm is commonly used for the excitations in ZnO. The laser beam pass through three visible lenses then projected on the semiconductor sample with the help of a setup as shown in the schematic diagram in Figure 4.6.
- In the second step, the excited electron-hole pairs recombine radiatively and emit light.
- In the final step, the emitted light is detected and dispersed by a diffraction grating 1200 1/mm monochromator and photomultiplier detectors. The final spectrum is collected and analysed in a computer.

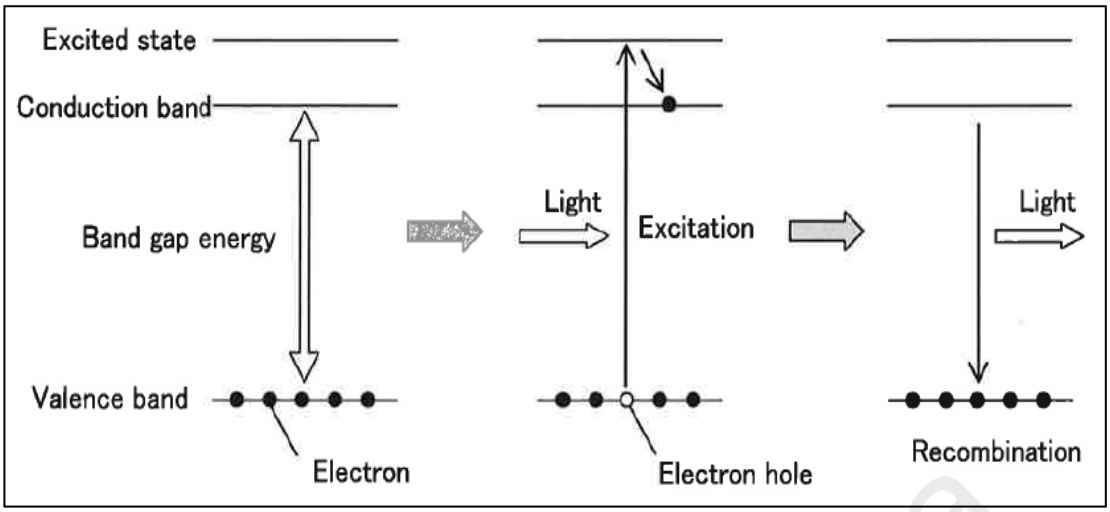

Figure 4.9: Photoluminescence process in ZnO band gap.

Figure 4.10: Kimmon He-Cd 325 nm laser system used for PL measurement.

Figure 4.11: Kimmon He-Cd laser power suppy.

CHAPTER 5: RESULTS AND DISCUSSION

5.1 Introduction

ZnO NSs have been successfully prepared on Si substrate using the combination of VPT and thermal evaporation assisted with hot wire technique. The results of initial optimization study have been presented in section 5.2. It includes a series of work which involved influence of Ar in obtaining polycrystalline Zn film on Si and fabrication of pure ZnO NSs using methanol as a source of oxygen. The results were discussed and presented in three stages based on the procedure developed in section 3.6.1, 3.6.2 and 3.6.3. First was the fabrication of polycrystalline Zn film on Si placed under one-sided hollow CuZn alloy rod. Second stage was the fabrication of standard polycrystalline Zn film on Si placed under two-sided hollow CuZn alloy rod whereas the third stage was developing ZnO NWs on Si placed under two-sided hollow CuZn alloy rod with Ar flow through methanol solution where the methanol was utilised as source of oxygen (O).

Since ZnO NWs is a promising candidate in the field of electron emission and gas sensing devices, the crystallite size and distribution of lattice strain considered as important parameters to be evaluated. Thus, fabrication of ZnO NSs using another aliphatic alcohol such as ethanol was also studied and compared with methanol to give light of view effect on the crystallite size and lattice strain distribution in ZnO NWs. The experimental procedure as per in section 3.6.3 (Chapter 3) was utilised but the methanol solution was replaced with ethanol. The samples of ZnO NWs prepared using the methanol and ethanol solutions were identified as ZnO/methanol and ZnO/ethanol respectively to ease in the discussion of results in section 5.3. Section 5.4 outlines results of effect of growth times 5, 10, 15, 20, 25 and 30 minutes for both

ZnO/methanol and ZnO/ethanol. EDAX, XRD, FESEM, PL and Raman analysis results have been utilised here.

5.2 Initial optimization study

The prepared samples via one and two-sided hollow CuZn alloy rod were characterised using EDAX to identify the constitution of elements. The images of structure and morphology were collected using the available FESEM JEOL JSM-7600F. XRD measurements were utilized using Cu $K\alpha$, 1.54 Å radiations to determine the polycrystallinity nature of the prepared samples. Based on the results, we have proposed a growth mechanism for ZnO NSs.

5.2.1 EDAX

The formation of Zn film and ZnO NSs were confirmed with EDAX analytical technique. The spectra shown as Figure 5.1(a) and 5.1(b) are the corresponding spectrum obtained for thermally evaporated one and two-sided hollow CuZn alloy rod for Ar flowrate of 100 sccm through the desiccant silica gel without flow through mixture of methanol and acetone solution. The spectra 5.1(a) and 5.1(b) show composition of 100 % of Zn nanoparticles on the Si substrate. Figure 5.1(c) represents spectrum of sample prepared for Ar flow through the mixture of methanol and acetone solution towards the thermally evaporated two-sided hollow CuZn alloy rod which was placed on Si substrate. It shows presence of 31.76 % O and 35.47 % C atom together with 28.27 % of Zn atom. This may indicate either the formation of ZnO NSs or hybrid carbon-ZnO NSs on the Si substrate. 4.51 % Si atomic was detected due to the Si substrate.

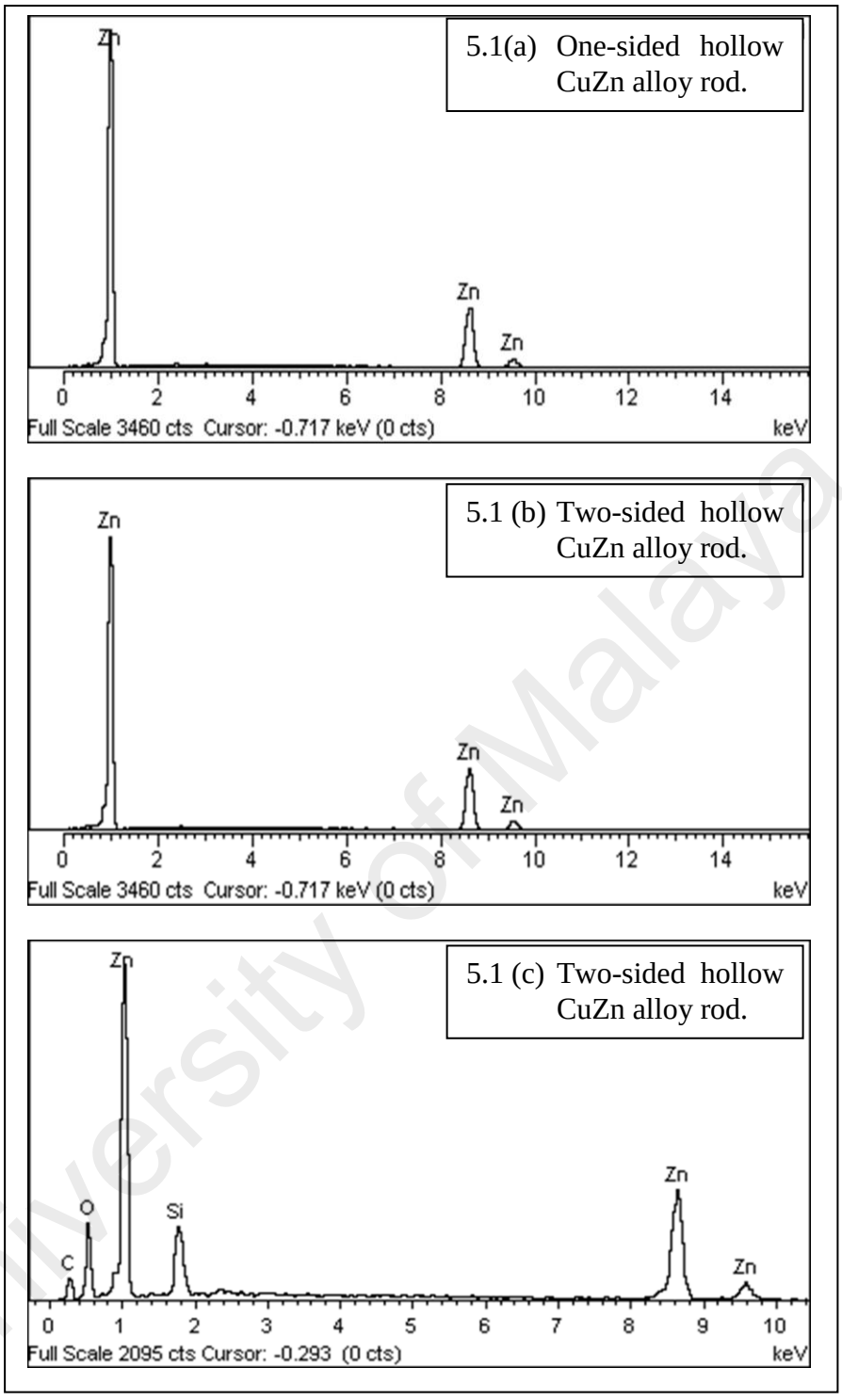

Figure 5.1: EDAX spectrum of samples prepared for conditions (a) vacuum in one-sided hollow CuZn (b) Ar flow through two-sided hollow CuZn and (c) Ar flow via mixture of methanol and acetone solution through two-sided hollow CuZn.

The possibility of chemical reaction between O, C and Zn nanoparticles could have occurred on the Si substrate. Furthermore, the role of methanol was identified by comparing the spectrum of Figure 5.1(a), 5.1(b) and 5.1(c). Without the presence of methanol vapor (refer to 3.6.1 and 3.6.2), only Zn particles from CuZn alloy rod were thermally evaporated and condensed on Si substrate to form a layer of Zn film. Meanwhile, the methanol vapor has incorporated its elements, O and C with Zn on the Si substrate. This attributes that methanol can be a source of O and C. O has incorporated to Zn in producing ZnO meanwhile C has carburized the W filament to avoid deterioration and contamination of W onto ZnO NSs. This is evident from the observation whereby the heated W filament in presence of methanol with Ar has swollen compared to the unheated W filament as shown in Figure 5.2.

Figure 5.2: (a) Heated tungsten filament in swollen stage compared to (b) non heated tungsten filament.

5.2.2 XRD

Figure 5.3 shows the XRD spectra of films fabricated on Si substrates placed under one-sided hollow CuZn alloy rod in vacuum, two-sided hollow CuZn alloy rod in Ar flow and two-sided hollow CuZn alloy rod in methanol with Ar flow which are designated as sample (a), (b) and (c). The Si peaks were not detected due to thickness of Zn film formed on Si during the deposition period of 30 minutes.

The XRD patterns 5.3(a) and 5.3(b) indicate distribution of nanosize Zn particles that correspond to the standard JCP2.2CA:00-004-0834 of Zn. But polycrystalline hexagonal structure of Zn with all its reflection planes are detectable in 5.3(b) which was prepared under two-sided hollow CuZn alloy rod in the Ar flow. It shows all the possible reflection planes at (002), (100), (101), (102), (103), (110), (004), (112), (200), (201), (104) and (202) of Zn. But suppressed growth in <002> orientation is noticeably corresponding to low intensity and enhanced <101> preferred orientation showed an average crystallite size of 43 nm. Meanwhile, spectrum 5.3(a) shows strong <002> preferred orientation in c-axis with calculated average crystallite size of 147 nm. The growth orientation in <100>, <110>, <004> and <202> are not detectable in the spectrum 5.3(a) compared to 5.3(b). Growth in <004> and <202> directions are only observable in sample 5.3(b) compared to sample 5.3(a). This indicates that in the Ar allowed environment, the crystallite size for Zn was reduced about 70 % and growth of polycrystalline Zn film has been promoted. From this we believed that the presence of Ar has changed the chemistry behind the formation of polycrystalline Zn film.

However, the Ar flow of 100 sccm through the added mixture of methanol and acetone solution to the Si substrate that was placed under two-sided hollow CuZn alloy significantly has changed the XRD profile from Zn film to ZnO NSs as in Figure 5.3(c). The film can be indexed with the JCP2.2CA: 00-036-1451 hexagonal wurtzite crystal structure of ZnO. This explains that methanol vapor has promoted oxidation of Zn into

ZnO that correspond with Figure 5.1(c) of EDAX. But the crucial part of chemistry that involved in a formation of ZnO is still not explainable unless with proper analytical management. The XRD spectrum 5.3(c) most likely exhibits growth of ZnO NWs or nanorods due to its growth in <002> along the c-axis direction.

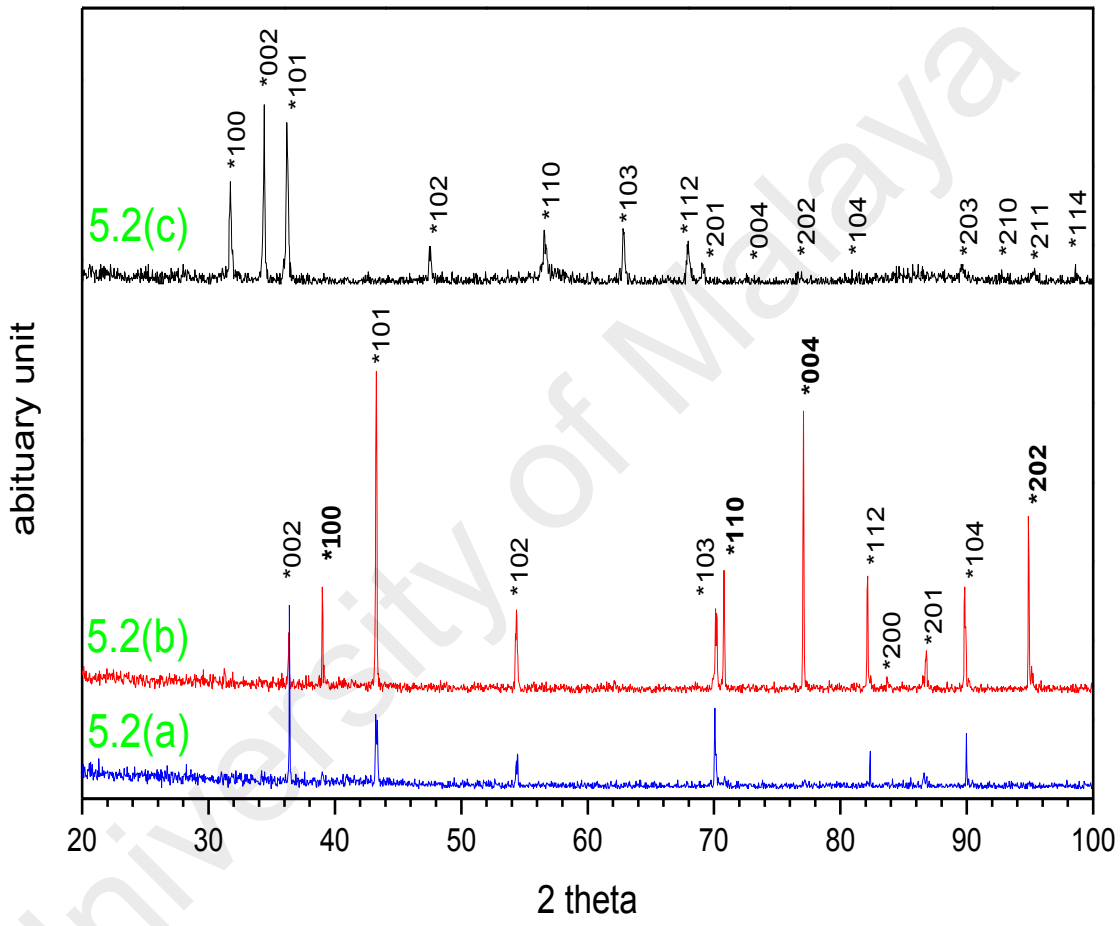

Figure 5.3: XRD spectra of as deposited Zn film on Si substrate under 5.3(a): one-sided hollow CuZn alloy rod in vacuum, 5.3(b): two-sided hollow CuZn alloy in Ar flow and 5.3(c): ZnO nanowire as function of Ar flowrate 100 sccm through mixture of methanol and acetone via two-sided hollow CuZn alloy rod.

5.2.3 FESEM

The surface morphology of grown layers, which were obtained under one and two-sided hollow CuZn alloy rod as function of Ar flow 100 sccm without flow through mixture of methanol and acetone solution exhibits formation of Zn film only on the Si substrate as shown as Figure 5.4(a) and 5.4(b). Growth like NWs as in Figure 5.4(c) were obtained in the Ar allowed environment via mixture of methanol and acetone solution towards Si substrate which was placed under two-sided hollow CuZn alloy rod.

Zn film has been fabricated in Ar disallowed and allowed environment without the presence of methanol vapor which was thermally evaporated from its CuZn alloy. Comparative study between Figure 5.4(a) and 5.4(b) depicts that Ar has played an important role in the formation of smaller grain Zn film. Figure 5.4(a) taken at magnification of 100000X is observed to be Zn film with larger grain in size shows formation of layer by layer during the growth compared to Figure 5.4(b) which was taken at 100000X. Figure 5.4(b) reveals the distribution of nanosized Zn grains on Si substrate. The difference in the morphology and structure comfortably corresponds to the crystallite size 147 and 43 nm that was calculated from the XRD profile in section 5.2.2.

However, Figure 5.4(c) reveals growth like wires on the Si substrate placed under two-sided hollow CuZn alloy where Ar was flowed through methanol solution. The image also corresponds well with the EDAX and XRD profile of ZnO that has been discussed in section 5.2.1 and 5.2.2 which shows presence of O and C elements in the EDAX profile and formation of hexagonal wurtzite polycrystalline structure of ZnO peaks that can be related to JCP2.2CA: 00-036-1451. The C could have decorated the surface of ZnO. The addition of methanol vapor significantly has changed the image profile from polycrystalline Zn film to polycrystalline ZnO NWs. O elements in the methanol vapor may have been cleaved from C and subsequently bonded with Zn

elements. Figure 5.4(d) is the lower magnification 10000X of Figure 5.4(c). It reveals three points "S" where growth of ZnO NWs also has been initiated as Zn particles made bonding with O atoms as seen in Figure 5.4(c).

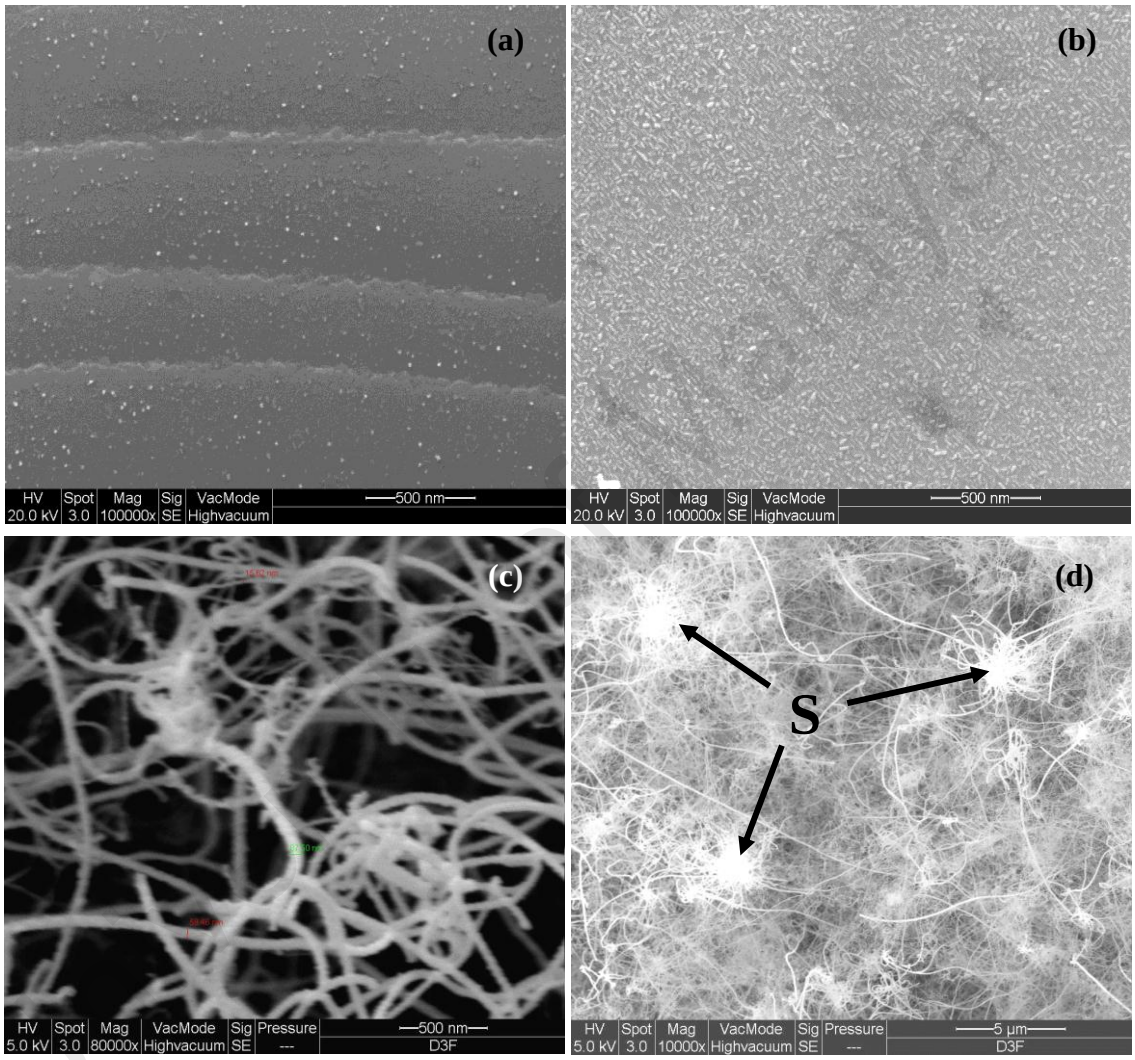

Figure 5.4: FESEM images (a) Zn film, (b) Zn film and (c) ZnO NWs obtained on Si substrate respectively for vacuum in one-sided hollow CuZn alloy,Ar flow and methanol with Ar flow through two-sided hollow CuZn alloy. Image (d) is lower magnification 10000X of image image (c).

The Zn particles that have been randomly evaporated from CuZn alloy subsequently deposited on Si substrate and promoted the growth of ZnO NWs as in Figure 5.4(c). The NWs length up to 15 μm and diameters in the range 20-100 nm are observable in Figure 5.4(c). This shows that growth technique and mechanisms of ZnO NWs is established using methanol and CuZn alloys. The combination of VPT of methanol and thermal evaporation of CuZn alloy also can be utilized in fabricating ZnO NWs.

5.2.4 Photoluminescence

Photoluminescence (PL) measurement was performed on samples prepared as per discussed in section 3.6.2 and 3.6.3 which were confirmed to be Zn film and ZnO NWs by EDAX, XRD and FESEM analysis. Room temperature PL characteristics of Zn film at 325 nm excitation is shown as Figure 5.5. Luminescence in the range of 450 to 750 nm corresponds to below bandgap emission which reveals the presence of deep level traps within the forbidden band of ZnO. The energy distribution of the trap states in the forbidden band cause a broad emission centred around 600 nm (2.07 eV). The PL emission of metallic solid Zn is mainly dependent on the electron transistion between the Fermi level (E_f) and the 3d band (Lin et al., 2014).

Two possible assisted trap routes would explain the emission of a photon with 2.07 eV (600 nm). First is the capture of a free electron from the conduction band (CB) by a trap state (unoccupied trap) and second is the recombination of an electron in a trap state (occupied trap) with a hole in the valence band (VB). Later it was predicted that trap energy states are located in the forbidden band of Zn that closer to the CB. In such a scenario, incident photons with energy higher than 2.07 eV (but less than 3.37 eV of ZnO) excite electrons from the VB directly to the trap states. This is followed by light emission at 600 nm when the excited electrons recombined with hole in the VB.

Whereas, the ZnO NWs prepared on Si via two-sided hollow CuZn alloy rod by flowing Ar through mixture of methanol and acetone solution shows significant changes in the PL band. Dominant broaden peak around 542 nm (2.30 eV) reflects yellowish green emission band. Yellow luminescence at ~560 nm (2.20 eV) is attributed to recombination of donors with acceptors from methanol solution believed to be H acceptors. Very low intensity of near band edge (NBE) emission at 378 nm (3.28 eV) was due to the changes in the crystallinity of the sample due the influence of methanol. Besides that the NBE also can be attributed to the effect of impurities and structural defects such as oxygen vacancy (V_o) and dislocations (Bagnall et al., 1998).

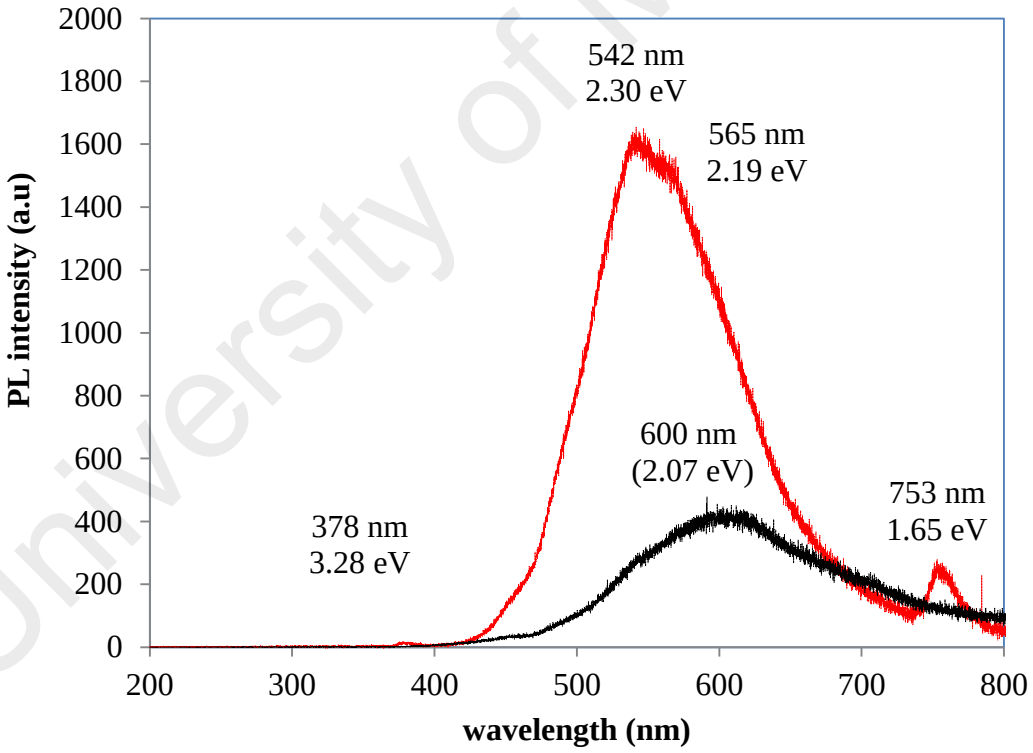

Figure 5.5: Photoluminescence of Zn film (black line) ZnO NWs (red line) prepared via two-sided hollow CuZn alloy rod in Ar flow for growth time of 30 minutes.

5.2.5 Proposed growth mechanism for ZnO nanowires

A series of chemical mechanism were proposed based on various outcomes that have been established elsewhere (Panchakarla et al., 2007). The thermally heated CuZn alloy has allowed only Zn atoms to escape as Zn vapors at temperatures greater than 395 °C which then condensed as Zn solid on Si substrate. This corresponds to the FESEM photomicrographs, 5.4(a) and 5.4(b) that exhibit merely morphology of Zn film.

$$\mathrm{ZnCu\ (solid\ brass)} \xrightarrow{>395\ ^{\circ}\mathrm{C}} \mathrm{Zn\ (vapor)} \longrightarrow \mathrm{Zn\ film}$$

Here, the presence of Ar environment (Lv et al., 2010) has played an important role in changing the morphology of Zn film from large boundary to nanosized grain. The presence of Ar at 100 sccm in the isolated system thermodynamically has rearranged and reduced the crystallite size of Zn. The calculated crystallite size, 43 nm of Zn in the Ar allowed environment through two-sided hollow CuZn (as in Figure 5.4(b)) showed a reduction about 70% from the crystallite size of Zn, 147 nm (as in Figure 5.4(a)) which was obtained in the Ar disallowed environment via one-sided hollow CuZn alloy. Nevertheless, more preferred growth of Zn particles in <002> direction in the Ar disallowed environment, has been changed to <101> growth direction after the Ar flow was allowed through two-sided hollow CuZn alloy. Thus, the presence of Ar has promoted the growth of polycrystalline Zn film (as in Figure 5.4(b)) that corresponds to the standard JCP2.2CA:00-004-0834 of hexagonal Zn.

The growth of ZnO NWs as in Figure 5.4(c) were obtained by allowing methanol vapor as Ar flowed at 100 sccm passing through the mixture of methanol and acetone solution through two-sided hollow CuZn. The C, H and O atoms in methanol have undergone a dehydrogenation in the presence of Cu (in CuZn alloy) at 300 °C.

$$CH_3OH\,(a) \xrightarrow{Cu,\ 300°C} CH_3O^- + H^+$$

$$CH_3O^- \xrightarrow{Cu,\ 300°C} HCHO(a) + H^+$$

Based on that, Cu in CuZn has acted as an catalyst and has oxidized the methanol vapor (Chen & Masel, 1995) into an intermediate absorbable methoxy species (CH_3O^-) and hydrogen atom (H^+). The CH_3O^- is thermodynamically unstable and were readily converted to formaldehyde (HCHO) by releasing a H^+. The higher bond energy of C=O in HCHO is thermodynamically unfavourable and the polarity of carbonyl group and its high basicity lowered the transition state energy of activation and therefore results in faster rate of reaction with readily presence species (Bruice, 2006). So the chemically unstable HCHO vapor easily reacts with Zn vapor or Zn atoms that have been thermally evaporated at temperatures above 395 °C to form ZnO NWs. Besides that, further oxidation of HCHO to HCOOH is not predicted due to absence of O_2 environment.

Apart of this, C-O bond in $CH_3O_{(a)}$ was readily cleaved by Zn vapors (Harikumar & Rao, 1999). Co-adsorption of $O_{(a)}$ and $Zn_{(a)}$ appeared to give rise to a reactive oxygen ions (O^{2-}) and Zn ions (Zn^{2+}) on the Si substrate. Thus Zn^{2+} ionically bond with O^{2-} to form ZnO NSs.

$$CH_3O^- \longrightarrow O^{2-} + CH_3^+$$

$$Zn(a) \longrightarrow Zn^{2+} + 2e^-$$

$$Zn^{2+} + O^{2-} \longrightarrow ZnO(NWs)$$

5.2.6 Conclusion

The combination of VPT and thermal evaporation of CuZn alloy assisted by hotwire is a feasible technique that can be utilized in synthesizing ZnO NWs in the laboratory with close operating conditions. The reduction of Zn crystallite size from 147 to 43 nm has proved that presence of Ar has reduced about 70 % of its crystallite size. Ar has changed the chemical constitution and energy of the Zn particles which later condensed on the Si. The comparison of XRD profile 5.3(a) and 5.3(b) further confirmed that Ar has played an important part and enhanced the growth of Zn particles in planes (100), (110), (004) and (202) that corresponds to the standard JCP2.2CA:00-004-0834 of Zn. The presence of methanol has promoted the formation of ZnO NWs. Methanol has been converted to absorbable species HCHO and CH_3O^- at temperatures 300 °C with the presence of Cu as catalyst. The respective C=O and C-O bond in $HCHO_{(a)}$ and CH_3O^- is cleaved by Zn vapor to form ZnO NWs. Thus, aliphatic alcohol like methanol can be used as source of O to replace commercially available purified oxygen gas. Swagelok CuZn can be used as source of Zn to form ZnO NWs.

5.3 Comparative studies between the effect of methanol and ethanol

Based on the initial optimization study, growth of ZnO NWs by replacing methanol with higher order aliphatic alcohol was suggested. So, the methanol was replaced with ethanol. Comparative studies on the effect on the crystalline size and lattice strain distribution in ZnO were carried out. The samples of ZnO NWs prepared using the methanol and ethanol solutions were identified as ZnO/methanol and ZnO/ethanol respectively in the discussions.

5.3.1 FESEM of ZnO/methanol and ZnO/ethanol

The grown ZnO/methanol shows distinct and interesting structural and morphological features at two different positions as highlighted in Figure 5.6 and 5.7. Figure 5.6 attributes growth of ZnO NWs, nanorods and ZnO flakes on the Si substrate. The ZnO nanoflakes were distributed over the surface of the NWs and nanorods as identical in the photomicrograph. Some ZnO nanoflakes observed to be rolled around other ZnO nanorods and NWs. Point "X" as in Figure 5.6 reveals growth of ZnO needle like NWs.

Figure 5.7 shows presence of ZnO nanoneedles without ZnO nanoflakes. The nanoneedles are distributed randomly in all directions in the range of 10 – 100 nm diameters. The magnified version of Figure 5.7 is shown as Figure 5.8. A closer look at the photomicrograph reveals that, diameter of single NW changes from 100 nm at the bottom to 10 nm to the tip which looks like needle like growth. Growth of needle like ZnO NSs would enhance the electron emission properties. On the other hand tetrapod like growth also had been identified in ZnO/methanol indicated as "Y" in Figure 5.7. Most of the tetrapod ZnO/methanol could have been trapped under the ZnO nanoflakes in Figure 5.6 (Wang, 2004a; Wang, 2004b).

ZnO/ethanol as in Figure 5.9 exhibits various diameters of NWs ranges from 10 - 100 nm randomly orientated on Si substrate. The area highlighted in bigger circle indicates growth of single ZnO/ethanol NW on polar surface (0001) along [1010] direction. This attributes growth of "comb-like" nanobranches in the range of 5 – 15 nm on the side of (0001) polar surface of single ZnO NW (Wang, 2004a). Tripod like growth of ZnO/ethanol is identified at point "Z" as in Figure 5.9. The magnified version of point "Z" as in Figure 5.10 attributes ZnO NW in a diameter of 20 nm.

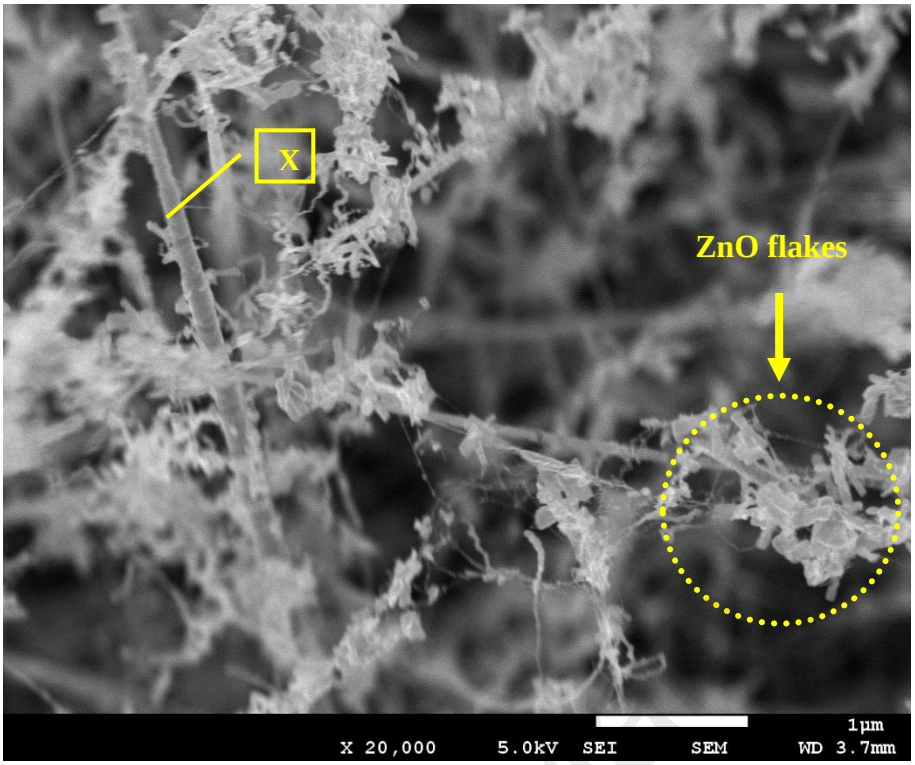

Figure 5.6: 20k X magnified ZnO/methanol shows presence of ZnO flakes, NWs and point "X" is nanorods in needle shape.

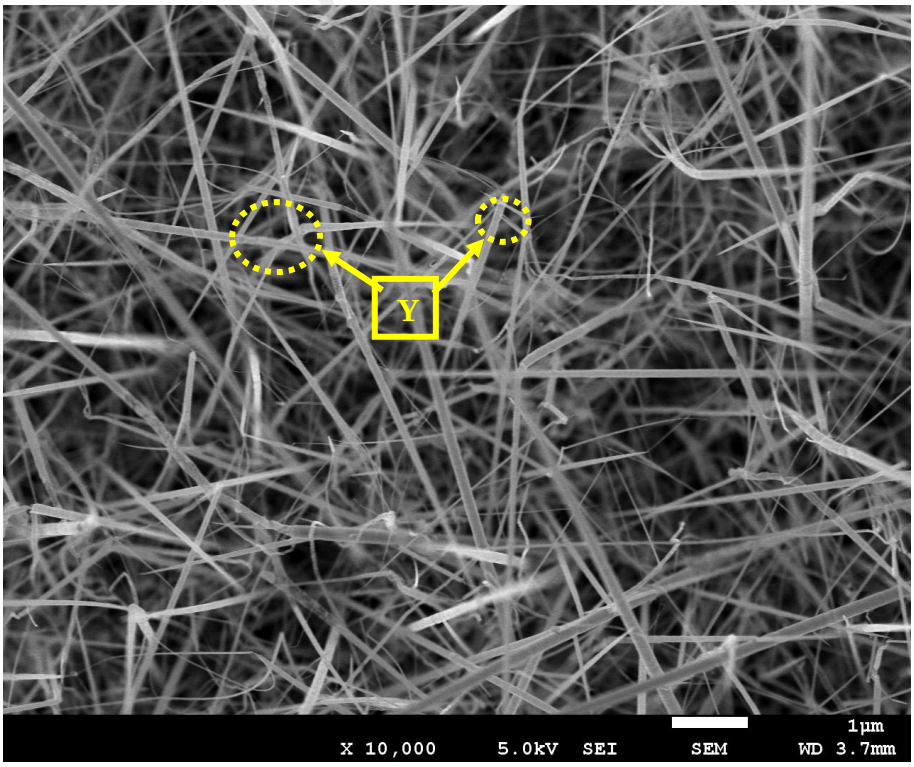

Figure 5.7: 10k X magnification of needle like growth of ZnO/methanol NWs.

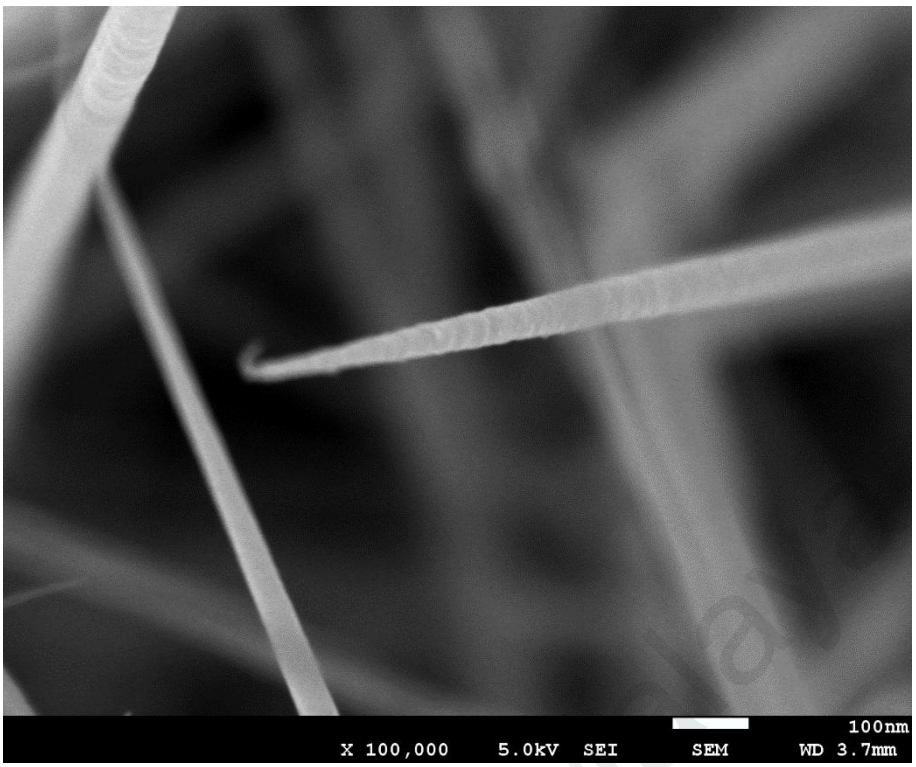

Figure 5.8: 100k X magnification of needle like ZnO/methanol.

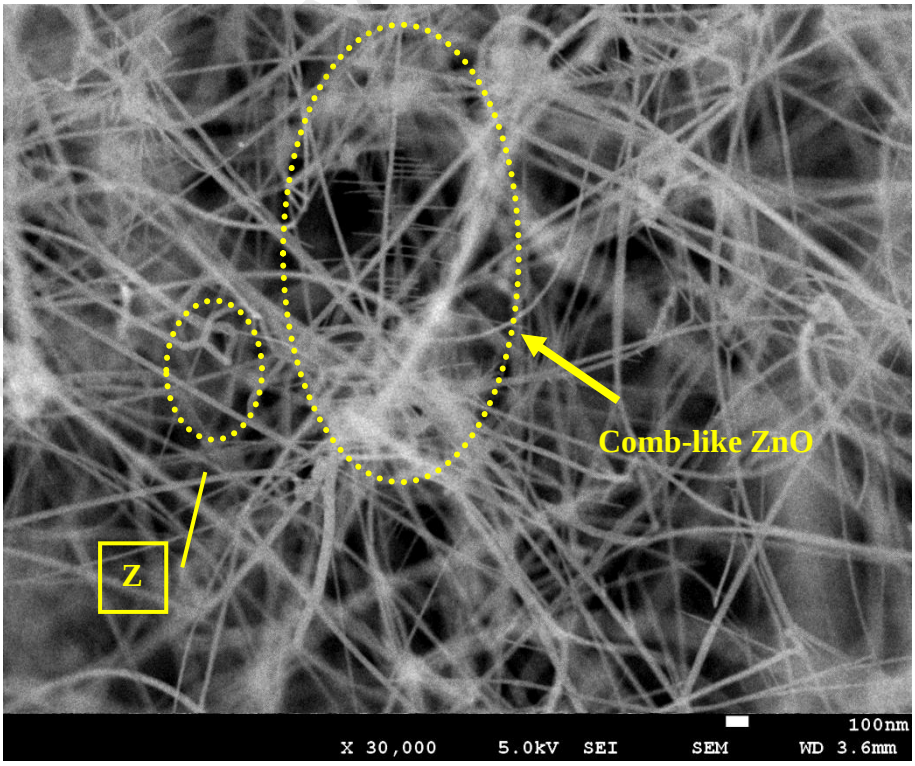

Figure 5.9: 30k X ZnO/ethanol shows growth of comb like on polar surface and tripod growth pointed as “Z” with randomly orientated NWs.

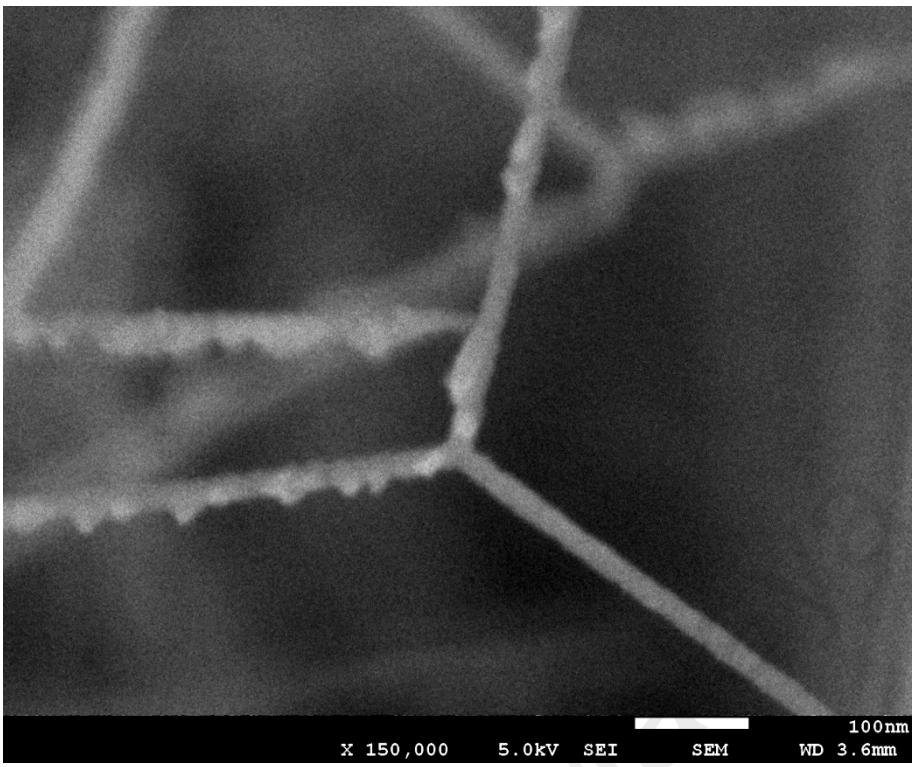

Figure 5.10: 150k X ZnO/ethanol shows growth of tripod NWs with a diameter of 20 nm.

5.3.2 XRD of ZnO/methanol and ZnO/ethanol

The ZnO NWs prepared using methanol and ethanol which were discussed in the previous section further studied using the XRD technique. The x-ray detector parameters as per detailed in section 4.3 (Chapter 4) was used. The XRD profile of as prepared ZnO NWs using the methanol and ethanol solution are shown as Figure 5.11 and 5.12 for 2Θ range of 20 – 80 °. All the detectable peaks can be indexed as hexagonal wurtzite ZnO that found as in the standard reference data JCP2.2CA: 00-036-1451. ZnO/ethanol NWs peaks as in Figure 5.12 observed to be broader than the Figure 5.11. This reflects the distribution of inhomogeneously strained crystallite in the ZnO/ethanol NWs is greater compared to the ZnO/methanol NWs. The growth of NWs in Figure 5.12 also found to be preferred in direction <101> while Figure 5.11 exhibits preferred growth in direction <002>.

Gaussian deconvoluted peaks of (100), (002), (101), (102), (110) and (103) were obtained for the ZnO/methanol and ZnO/ethanol and compared with the standard peak of JCP2.2CA: 00-036-1451 ZnO. The quantitative comparisons are detailed in Table 5.1. All the peaks positions for ZnO/methanol NWs as in Figure 5.11 found to be shifted to the right. This may reflect distribution of tensile stress in the ZnO/methanol NWs prepared on Si substrate. Whereas, ZnO/ethanol NWs exhibits peak positions shifted to both right and left with broadening in the peak width. This shows that the deposited ZnO NWs were inhomogeneously strained on the Si substrate which could be both tensile stress and compressive stress. This also reflects anisotropic nature of ZnO/ethanol NWs has been deposited on Si substrate.

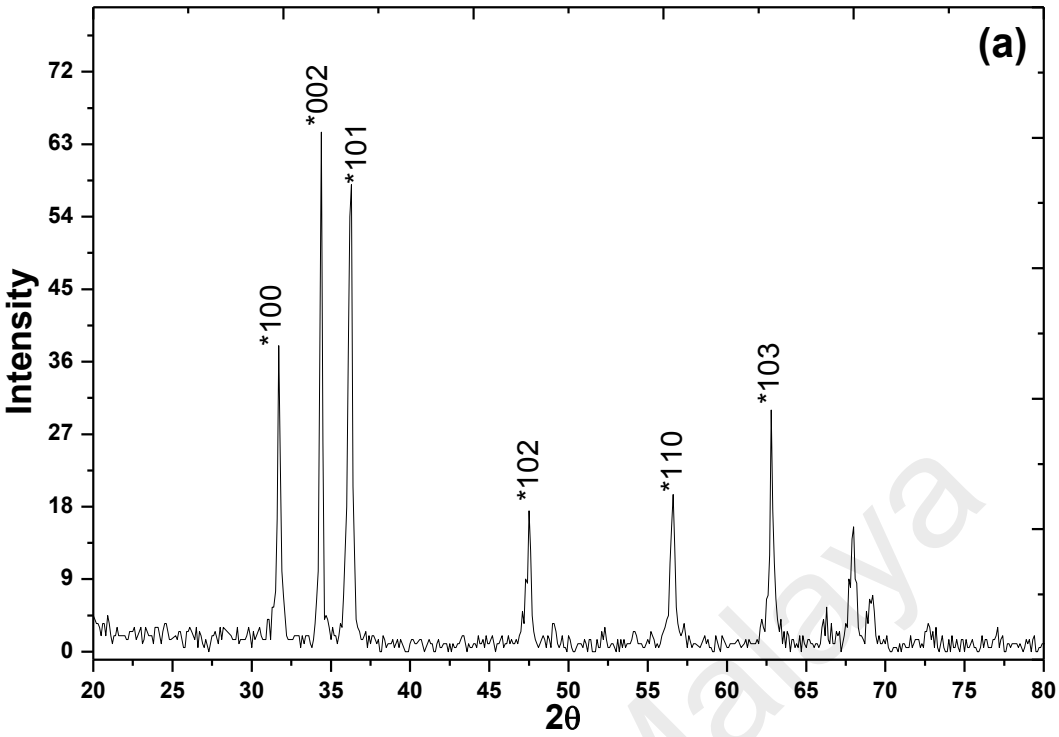

Figure 5.11: XRD spectrum of ZnO/methanol NWs fabricated on Si substrate for deposition period of 30 minutes.

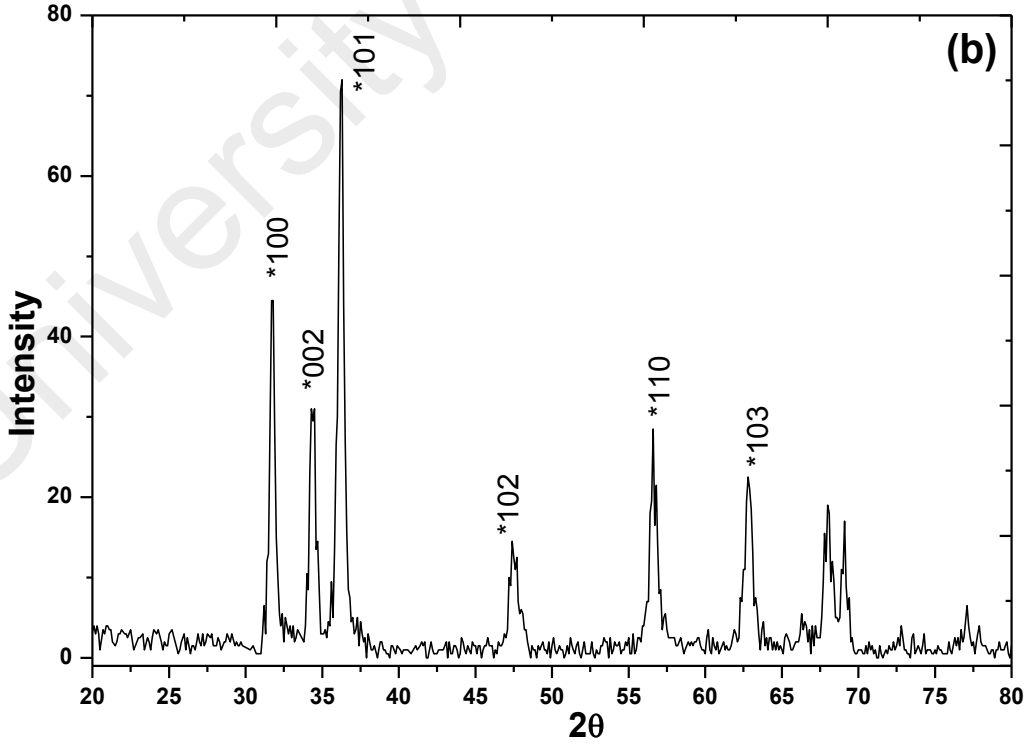

Figure 5.12: XRD spectrum of ZnO/ethanol NWs fabricated on Si substrate for deposition period of 30 minutes.

Table 5.1: Details of ZnO NWs peaks prepared using methanol and ethanol compared with the standard ZnO peak.

Plane	**Standard peak**	**ZnO/methanol**			**ZnO/ethanol**		
	JCP2.2CA: 00-036-1451 (X_0 ± 0.001°)	Peak center (X_m ± 0.001°)	X_0-X_m ± 0.001°	FWHM ± 0.001°	Peak center (X_e ± 0.001°)	X_0-X_e ± 0.001°	FWHM ± 0.001°
100	31.770°	31.716°	+0.054°	0.2074°	31.750°	+0.020°	0.3586°
002	34.442°	34.387°	+0.055°	0.1896°	34.386°	+0.056°	0.4580°
101	36.253°	36.227°	+0.026°	0.3160°	36.234°	+0.019°	0.4154°
102	47.539°	47.498°	+0.041°	0.3166°	47.520°	+0.019°	0.6529°
110	56.603°	56.570°	+0.033°	0.3264°	56.635°	-0.032°	0.5729°
103	62.864°	62.819°	+0.045°	0.2155°	62.838°	+0.026°	0.5916°
112	67.963°	67.954°	+0.009°	0.4681°	68.029°	-0.066°	0.6212°

5.3.2.1 Scherer method

Crystallite size of the ZnO/methanol and ZnO/ethanol was determined using the Scherer equation (refer section 2.6). The average crystalline size of ZnO/methanol and ZnO/ethanol was calculated at about 44 and 20 nm respectively. However, a plot was drawn with $1/B_{hkl}$ along the *x*-axis and cosθ along the *y*-axis for both ZnO/methanol and ZnO/ethanol NWs as in Figure 5.13 and 5.14 respectively by setting a fixed intercept at 0. Thus the crystallite size was estimated to be 35 and 18 nm relatively for ZnO/methanol and ZnO/ethanol NWs. Neglecting the fixed intercept at 0, the plot of $1/B_{hkl}$ against cosθ shows linear proportion that intersects the y-axis as in Figure 5.13 and 5.14. This indicates that crystal imperfection and distortion may have occurred in the NWs of ZnO/methanol and ZnO/ethanol. Furthermore, the apparent shift in diffraction peaks from their corresponding crystal data indicates a uniform stress has arose in the film due to the thermal evaporation in the Ar flow (Kumar et al., 2010).

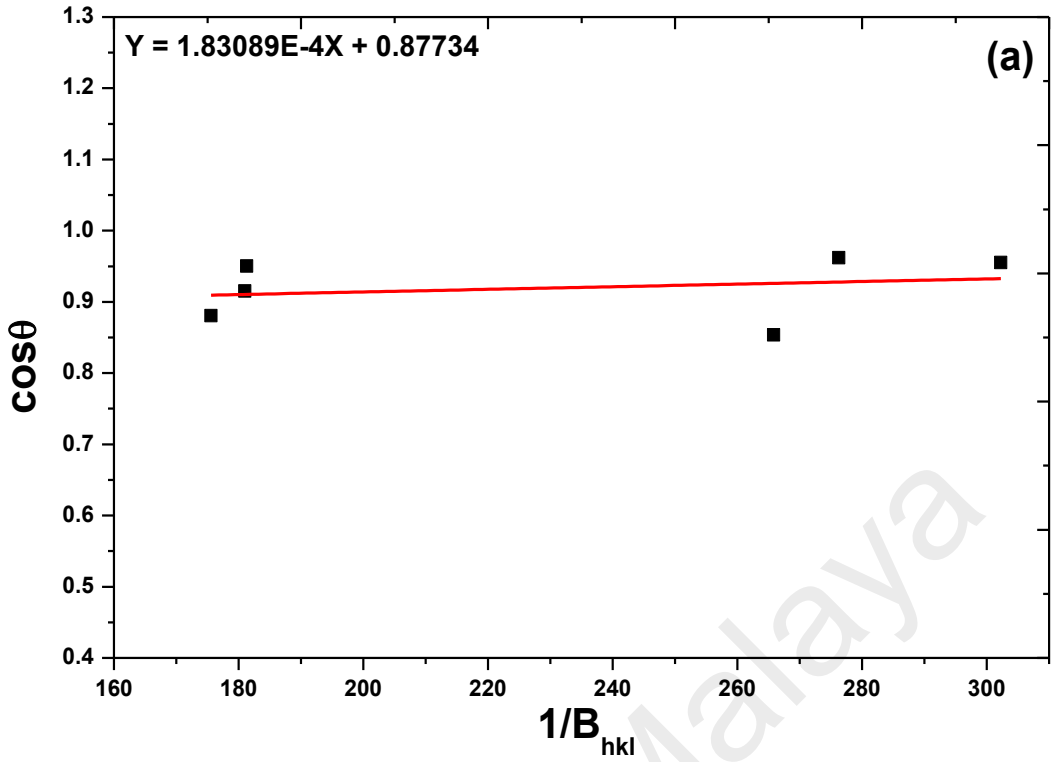

Figure 5.13: Scherer plot ZnO/methanol NWs fabricated on Si substrate for deposition period of 30 minutes.

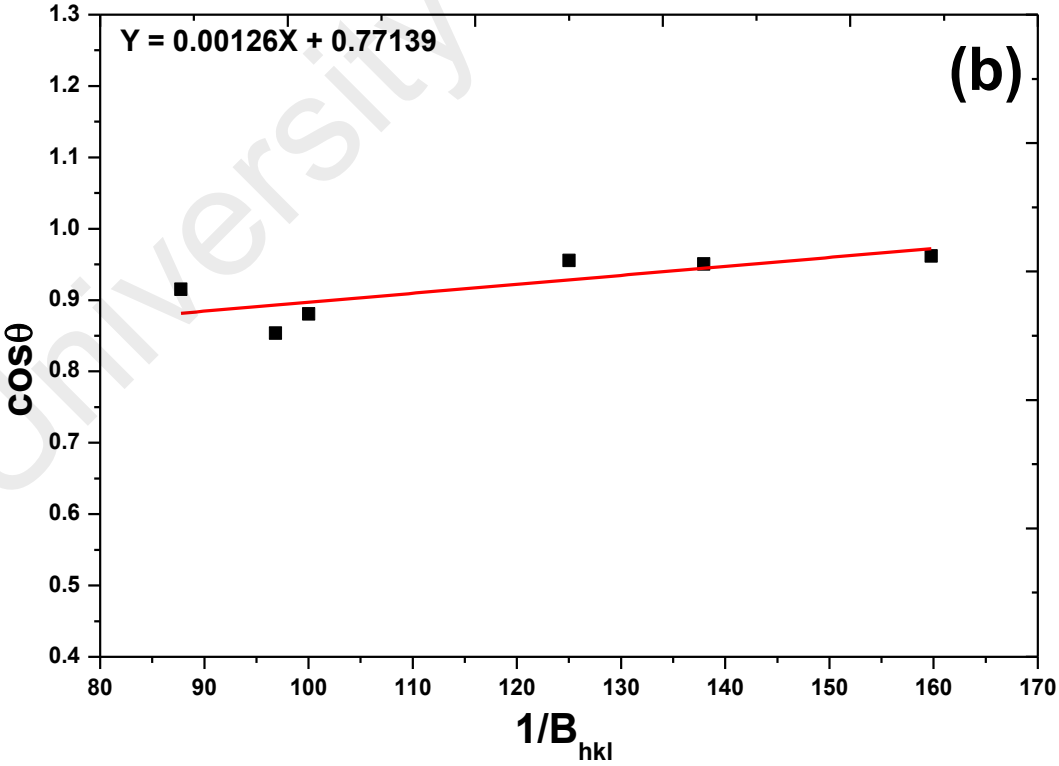

Figure 5.14: Scherer plot ZnO/ethanol NWs fabricated on Si substrate for deposition period of 30 minutes.

5.3.2.2 Williamson-Hall method

The crystalinity imperfection and strain distribution in the sample is determined using the W-H method. Thus considering the isotropic nature of the crystal, where all material properties are independent along the direction which they are measured, the UDM for as-prepared ZnO/methanol and ZnO/ethanol are shown as Figure 5.15 and 5.16. The plot $B_{hkl}cos\theta$ againts $sin\theta$ would give crystallite size that corresponds to the y-intercept and strain due to lattice deformation in the sample that can be calculated from the slope of the graph. Indeed, preferred orientation (100), (002), (101), (102), (110) and (103) of NWs of ZnO/methanol and ZnO/ethanol are selected to geometrically determine the crystallite size and strain in that sample.

The plotted graph clearly indicates that ZnO/methanol and ZnO/ethanol NWs exhibits positive gradient which represents the positive strain in the sample. The microstrain was estimated about $2.31x10^{-4}$ units for ZnO/methanol is smaller than of ZnO/ethanol which is $26.8x10^{-4}$ units. The crystallite size calculated for ZnO/methanol and ZnO/ethanol are quite similar which 36 and 34 nm respectively is. In order to evaluate stress in the NSs of ZnO/methanol and ZnO/ethanol a modified W-H model to uniform deformation stress model (UDSM) is applied.UDS and uniform deformation energy density (UDED) models were taken into account where the anisotropic nature of Young's modulus, E of the ZnO/methanol and ethanol is more realistic (Khorsand Zak et al., 2011).

The uniform stress in the ZnO/methanol and ZnO/ethanol NWs is calculated from the slope of plotted graph between $B_{hkl}\cos\theta$ and $\sin\theta/E_{hkl}$ as shown in Figure 5.17 and 5.18 respectively. The crystallite size *D* can be determined from the intercept at y-axis. The UDSM brought forth positive stress and strain in NWs of ZnO/methanol and ZnO/ethanol which can be related to the presence of tensile stress. This corresponds with the UDM value saying that expand of lattice occurred in the sample ZnO/ethanol is

greater than of ZnO/methanol. The greater crystallite size of ZnO/methanol (40 nm) than of ZnO/ethanol (33 nm) with microstrain and microstress distributed ZnO NSs preferred to be a good candidate in the field of electronics. The micro tensile stress in both samples can be associated with the formation of grain boundaries due to the coalescence of ZnO NSs.

A plot of $B_{hkl}\cos\Theta$ versus $\sin\Theta(2/E_{hkl})^{1/2}$ as shown in Figure 5.19 and 5.20 gives the UDED value that corresponds to the slope of the graph. The y-intercept fits the D value which is 38.2 and 33.6 nm for ZnO/methanol and ZnO/ethanol respectively. The strain, stress and uniform energy density in ZnO/ethanol found to be in greater extend compared to ZnO/methanol. It is noted that the UDM, UDSM and UDEDM has attributed higher D value of ZnO/methanol than of ZnO/ethanol.

The D value of ZnO/ethanol (33.6 nm) is in good agreement with the other D values obtained from UDM (34 nm) and UDSM (33 nm) compared to Scherer method which has exhibited 20 nm. However, ZnO/methanol has exhibited D value 38.2 nm from UDEDM, which is in good agreement with UDM (36 nm), UDSM (40 nm) and also Scherer method (44 nm). This study shed the necessity of models in determining crystallite size of ZnO NWs prepared using methanol and ethanol. The calculated strain and stress values are differing to greater extend due to the inclusion of anisotropic nature of the prepared samples. The calculated strain distribution in ZnO/methanol from UDM, UDSM and UDEDM are very much smaller compared to the ZnO/ethanol as shown in Table 5.2.

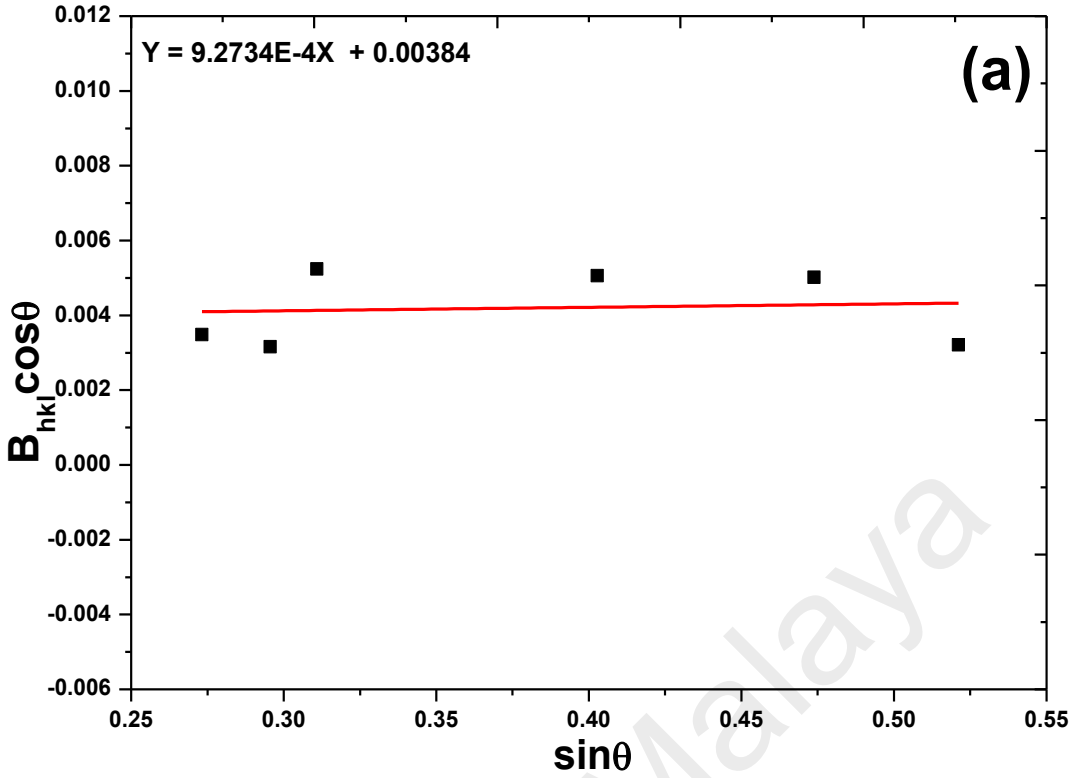

Figure 5.15: Plot of B_{hkl} cosΘ against sinΘ of ZnO/methanol NWs.

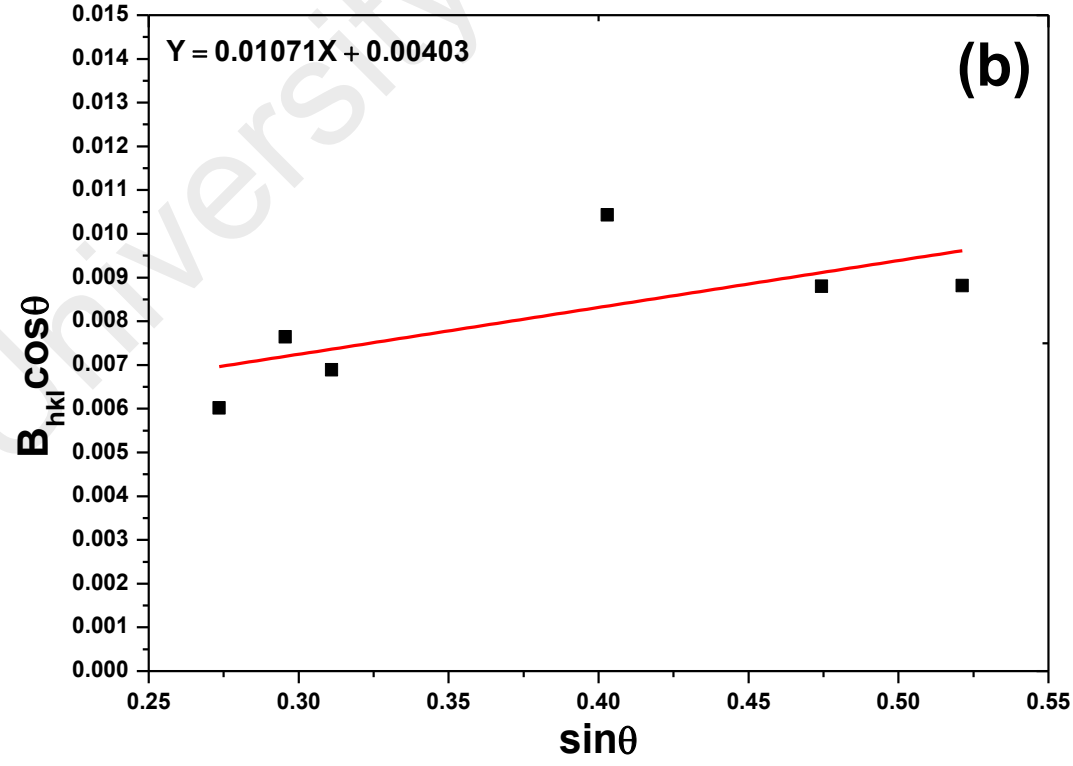

Figure 5.16: Plot of B_{hkl} cosΘ against sinΘ of ZnO/ethanol NWs.

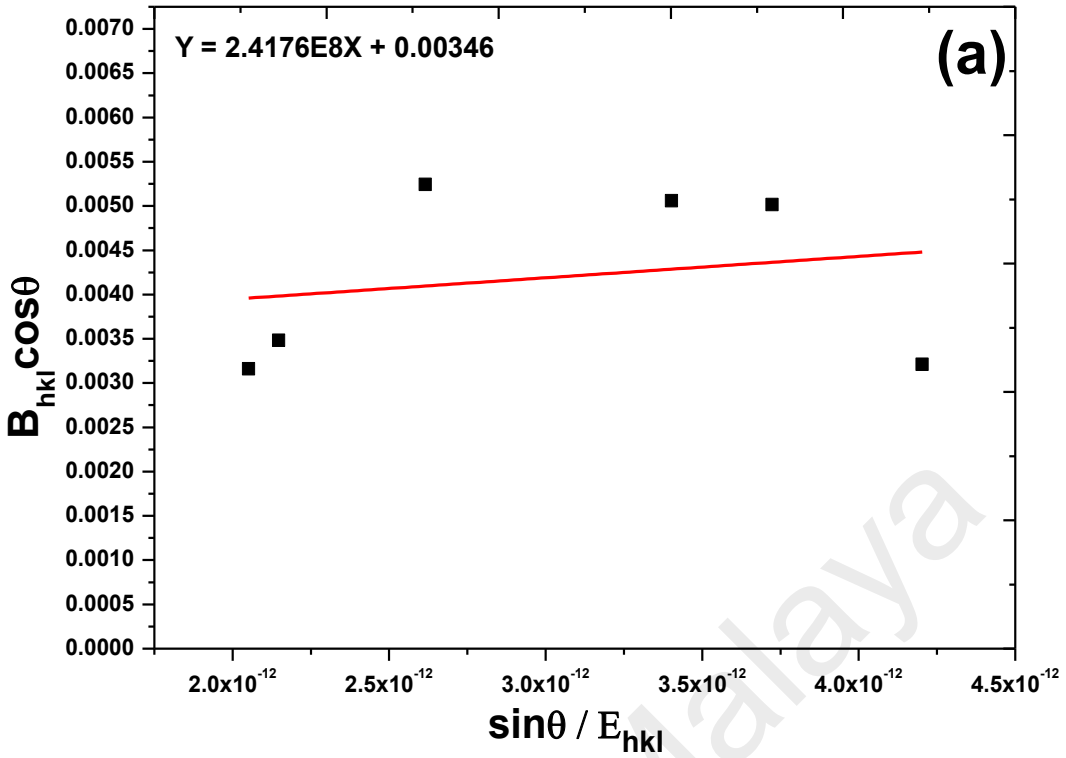

Figure 5.17: Plot of B_{hkl} cosΘ against sinΘ/E_{hkl} of ZnO/methanol NWs.

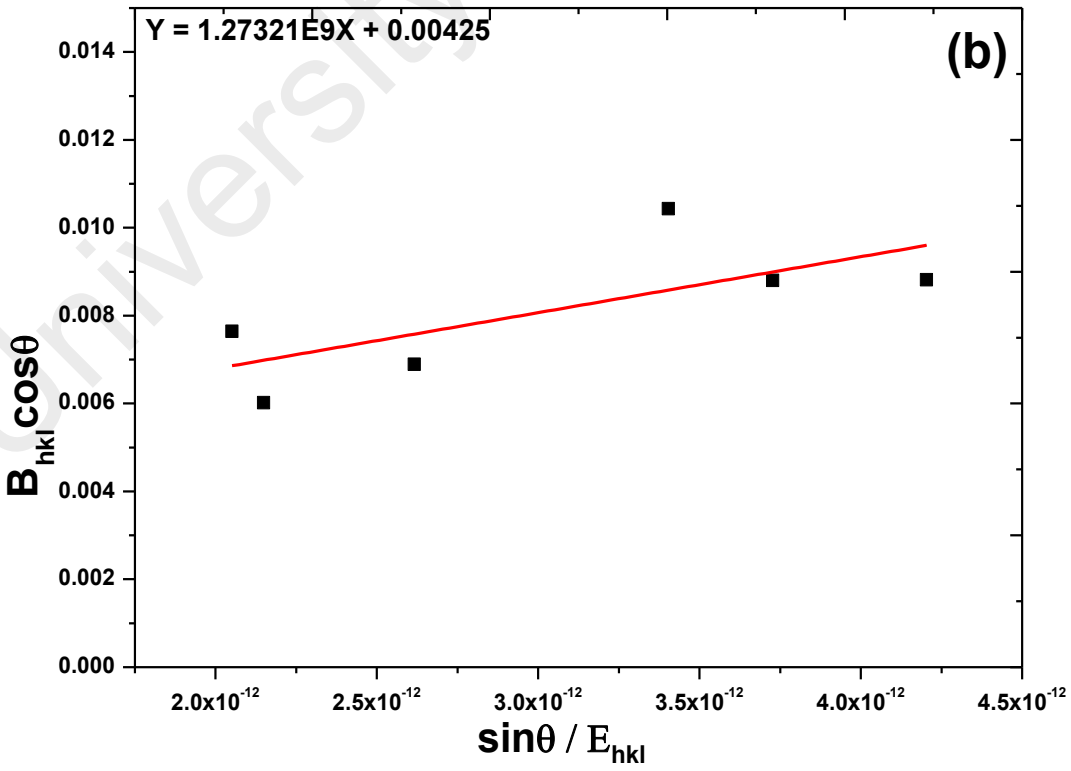

Figure 5.18: Plot of B_{hkl} cosΘ against sinΘ/E_{hkl} of ZnO/ethanol NWs.

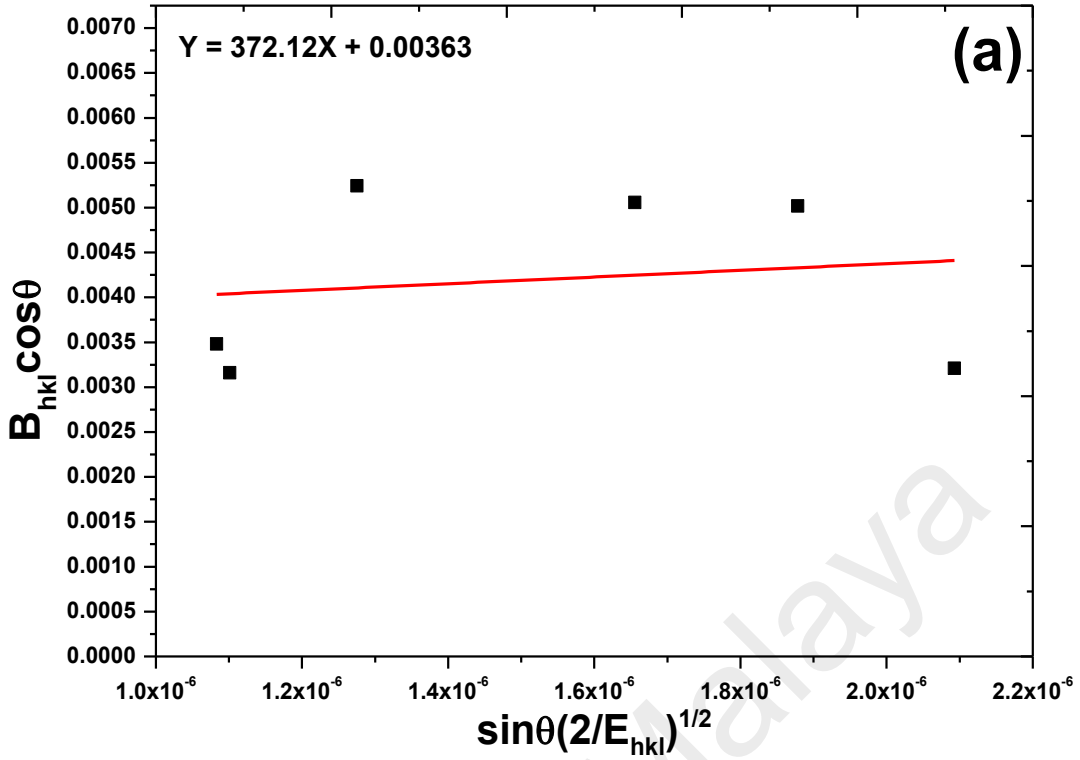

Figure 5.19: Plot of $B_{hkl}\cos\Theta$ against $\sin\Theta(2/E_{hkl})^{1/2}$ of ZnO/methanol NWs.

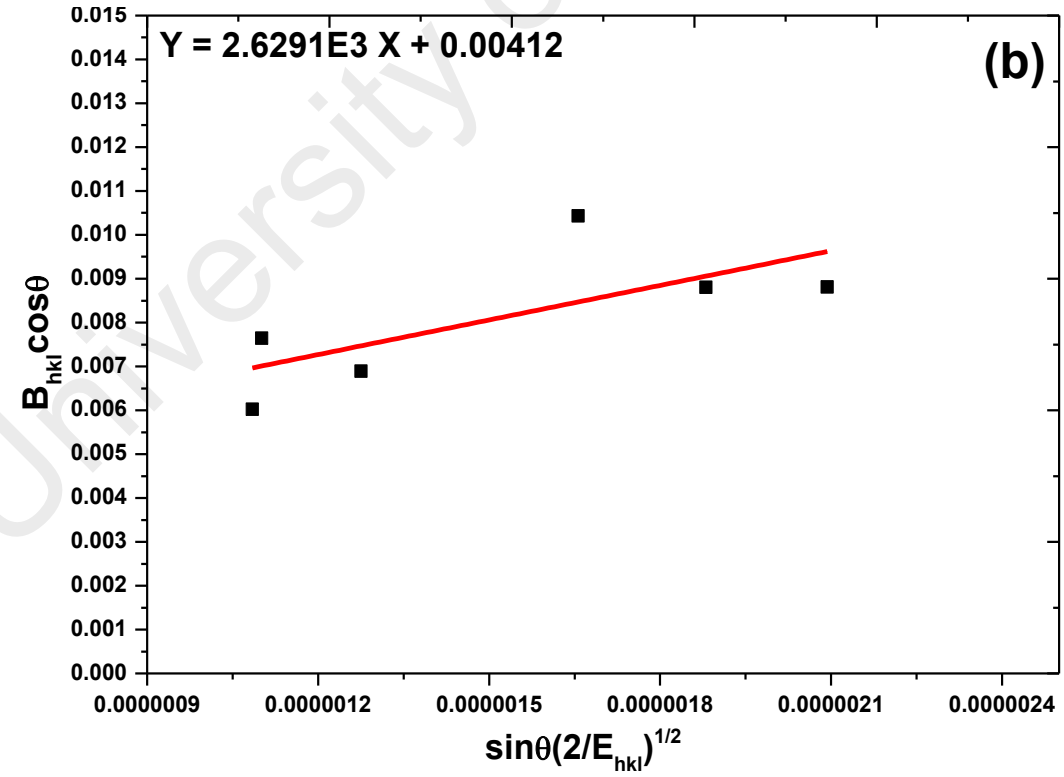

Figure 5.20: Plot of $B_{hkl}\cos\Theta$ against $\sin\Theta(2/E_{hkl})^{1/2}$ of ZnO/ethanol NWs.

5.3.2.3 Size-strain plot method

The size-strain plot (SSP) for ZnO/methanol and ZnO/ethanol NWs are shown as Figure 5.21 and 5.22 respectively. The $d^2B_{hkl}\cos\theta$ and $(d_{hkl}B_{hkl}\cos\theta)^2$ were taken on x- axis and y-axis respectively for all peaks of ZnO/methanol and ZnO/ethanol with the wurtzite hexagonal phase for Bragg angles from 30 to 80°. Volume averaged crystallite size, D_v is calculated from the slope of linearly fitted data and the root of the y-intercept gives the ε_{rms}. The calculated microstructural parameters of the investigated samples ZnO/methanol and ZnO/ethanol are summarized in Table 5.2. ZnO/methanol exhibits slightly higher value of D_v compared to ZnO/ethanol. The ε_{rms} of ZnO/methanol calculated to be $1.205\text{x}10^{-4}$ units is very low as ZnO/ethanol exhibits $3.525\text{x}10^{-4}$ units. As far as we concerned, a detailed study using these models on the ZnO NSs synthesized using methanol and ethanol has not been reported yet.

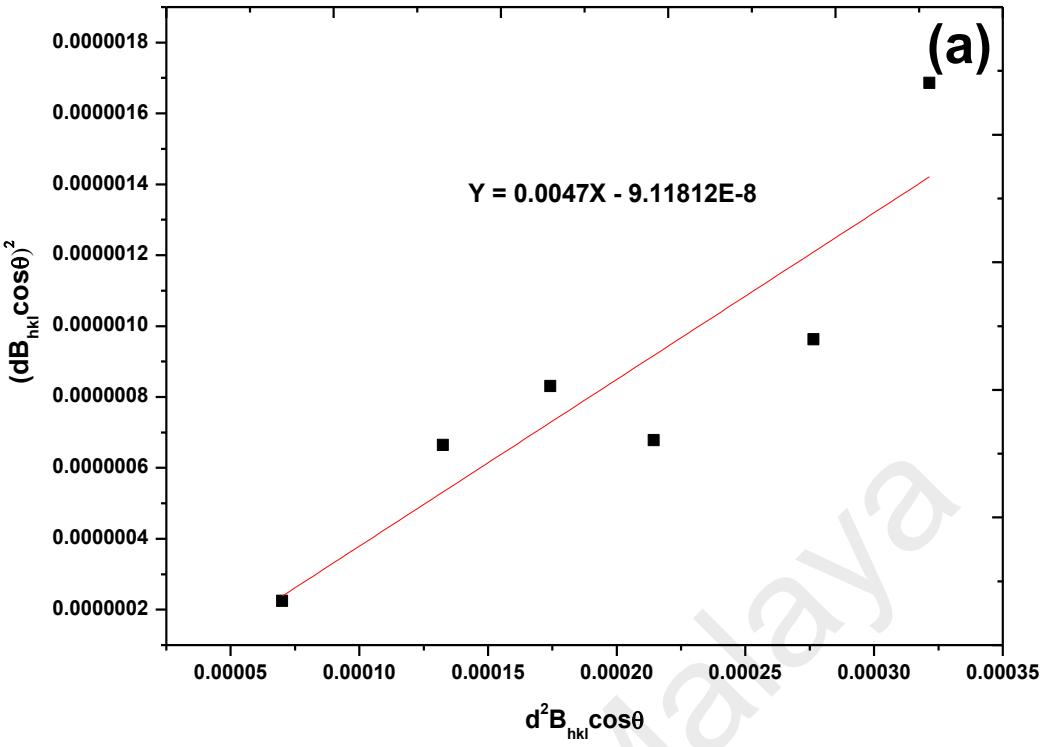

Figure 5.21: Size-strain plot for ZnO/methanol NWs.

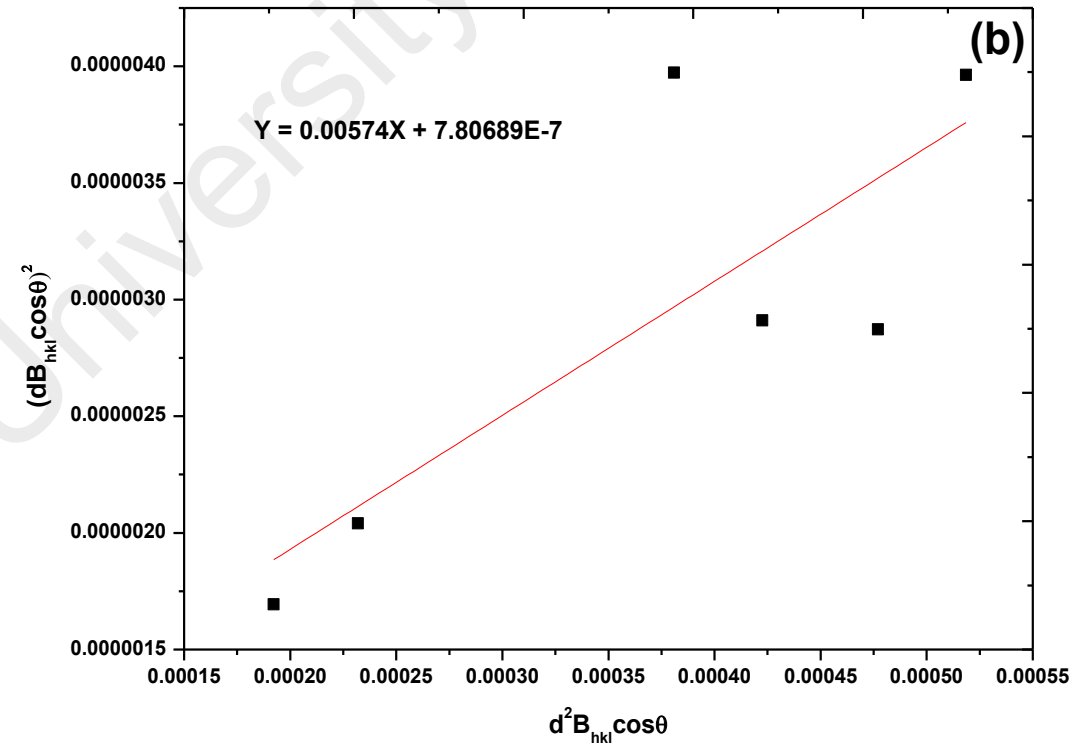

Figure 5.22: Size-strain plot for ZnO/ethanol NWs.

Table 5.2: Geometric parameter of ZnO NWs deposited using methanol and ethanol.

Sample type	**Scherer method**	**Williamson-Hall method**									**Size-strain plot**	
		UDM		UDSM			UDEDM					
	Crystallite size D (plane) (nm)	Crystallite size D (nm)	Strain ε (10^{-4})	Crystallite size D (nm)	Strain ε (10^{-4})	Stress σ (10^{6}) (Pa)	Crystallite size D (nm)	Strain ε (10^{-4})	Stress σ (10^{6}) (Pa)	Energy density U (10^{3}) (Jm^{-3})	Crystallite size D_v (nm)	Strain ε_{rms} (10^{-4})
ZnO/ methanol	44 (002)	36	2.31	40	4.79	60	38.2	3.17	28	8.65	28(3)	1.205
ZnO/ ethanol	20 (101)	34	26.8	33	25.20	318	33.6	20.50	184	432	23(3)	3.525

5.3.3 Conclusion

The FESEM images showed that significant changes had occured to the ZnO NWs due to the vapor phase transport of methanol replaced with ethanol. ZnO NWs were synthesized by the combination of VPT of aliphatic alcohol (methanol and ethanol) and thermal evaporation of CuZn alloys assisted with hotwire. The metastable wurtzite hexagonal structure of ZnO was confirmed by powder XRD. The line broadening of as-prepared ZnO/methanol and ZnO/ethanol NWs due to small crystallite size and lattice strain were confirmed by DS formula, modified W-H analysis and SSP method. The modified W-H models can be accepted to determine the D value and strain due to lattice deformation. SSP method indicated the D value for ZnO/ethanol nanowire is in good agreement with Scherer method compared to ZnO/methanol nanowire as shown in Figure 5.23. With the assumption of hexagonal anisotropic crystalline nature in ZnO/ethanol NWs the ε_{rms} differs from the strain calculated from UDM, UDSM and UDEDM. The ε_{rms} of ZnO/methanol shows good agreement with strain calculated from UDM, UDSM and UDEDM which may indicates formation of hexagonal isotropic crystalline nature in ZnO/methanol NWs. Other physical parameters stress and energy density found to be very low in ZnO/methanol NWs compared to ZnO/ethanol NWs. The W-H deformation models (UDM, UDSM and UDEDM) and SSP method were very helpful in determining the strain, stress and energy density with a certain approximation, and hence these models are highly preferable to define the crystal perfection. We suggest fabrications of ZnO NWs using methanol for the future application in the field of electron emission and optical devices are to be considered due to lower strain, stress and energy density compared to ethanol.

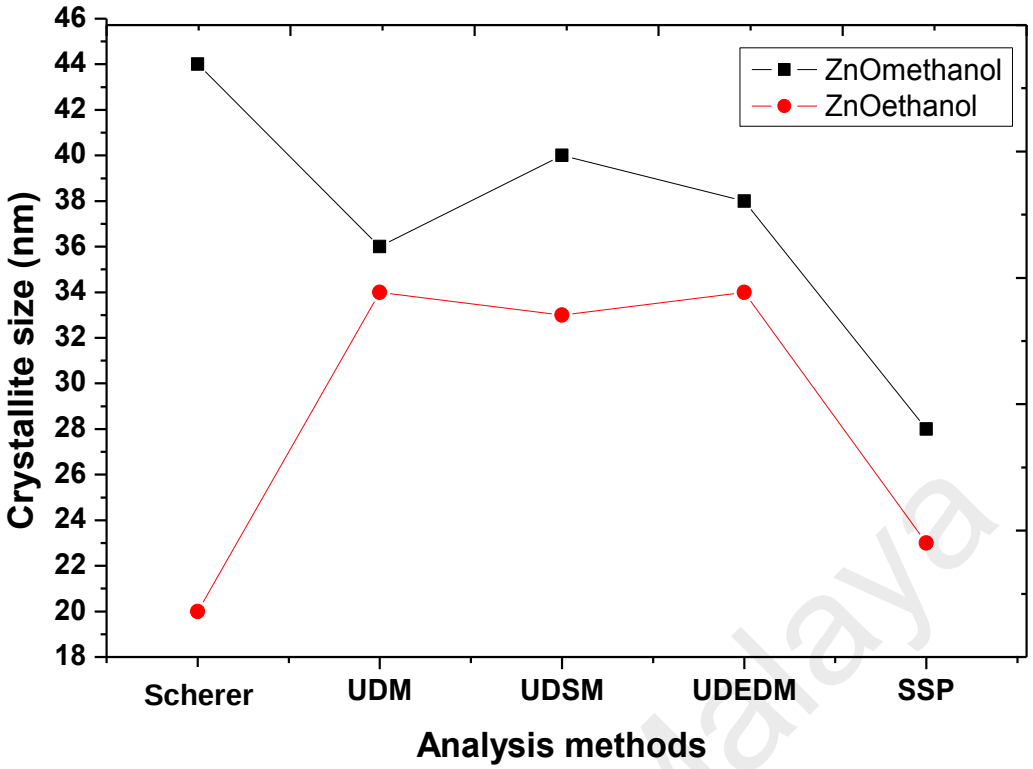

Figure 5.23: Comparison of crystallite size of ZnO/methanol and ZnO/ethanol NWs measured using Scherer, W-H and SSP method.

5.4 Effect of growth time-dependent

In this section ZnO nanowire samples that have been prepared using the methanol solution at various growth times of 5, 10, 15, 20, 25 and 30 minutes were characterized. The structural characterizations gave useful information on the effect of growth time on morphological and structural changes. The spectroscopic studies involving the PL characterization was conducted to investigate the extrinsic and intrinsic properties of ZnO NWs as a semiconductor. The studies were focused on the effect of methanol as source of oxygen on deep level emissions of ZnO NWs. The growth time-dependent of 5, 10, 15, 20, 25 and 30 minutes believed would affect structural and morphology of ZnO. Indeed, defects like lattice strain and stress are other imperfections in the ZnO NWs to be investigated since the growth time is varied. Besides that, the W-H analysing model has been discussed briefly to investigate the crystallite size and distribution of lattice strain and stress in the NWs of ZnO/methanol and ZnO/ethanol.

5.4.1 FESEM: ZnO/methanol

Figure 5.24, 5.25, 5.26, 5.27, 5.28 and 5.29 shows photomicrographs obtained for ZnO/methanol NWs prepared at various growth times of 5, 10, 15, 20, 25 and 30 minutes. The experimental setup as per section 3.6.3 was used to obtain pure ZnO/methanol NWs. Significant changes in the morphology and structure of ZnO/methanol are identical as the growth time was varied. Growth like hexagonal nanorods and NWs are observable in the displayed photomicrographs. They can be attributed to hexagonal wurtzite ZnO structure.

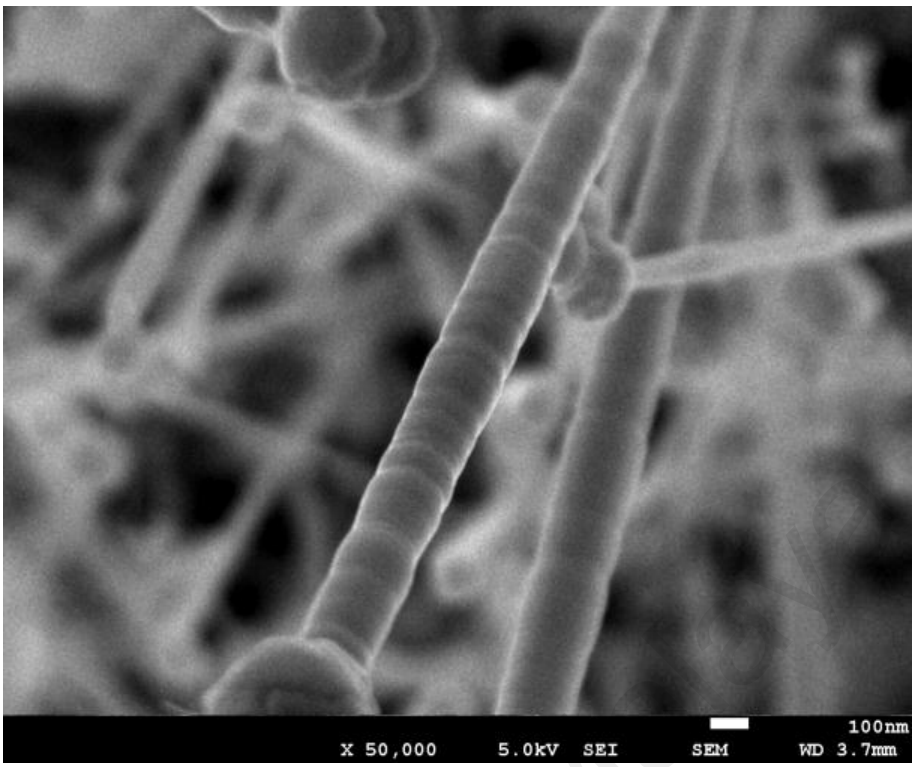

Figure 5.24: Image of ZnO/methanol NWs prepared at deposition time 5 minutes in Ar flow.

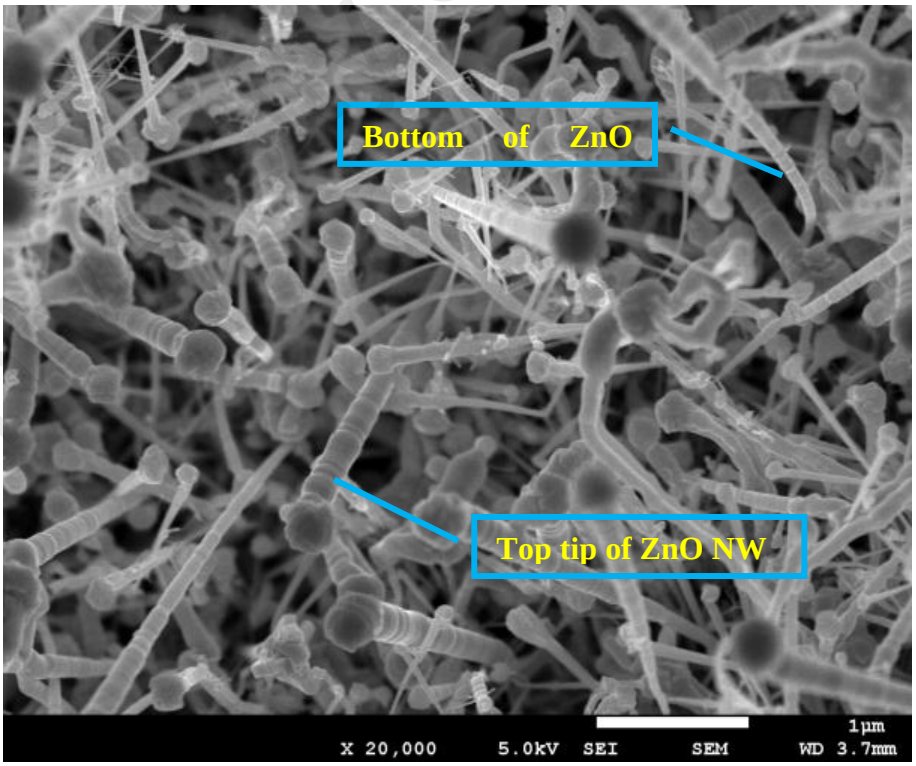

Figure 5.25: Image of ZnO/methanol NWs prepared at deposition time 10 minutes in Ar flow.

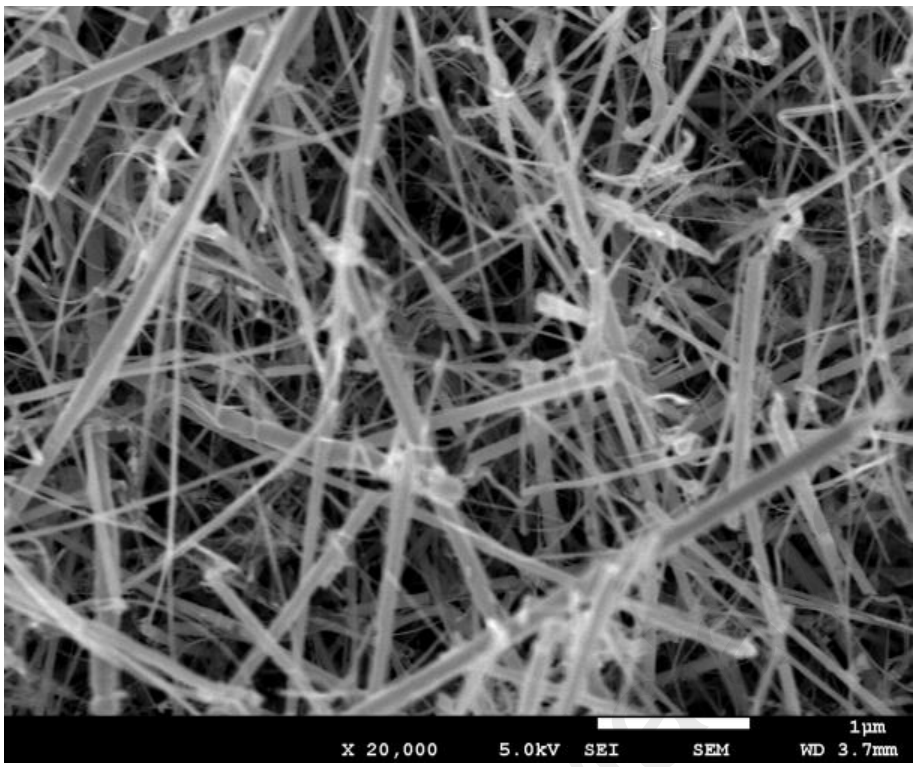

Figure 5.26: Image of ZnO/methanol NWs prepared at deposition time 15 minutes in Ar flow.

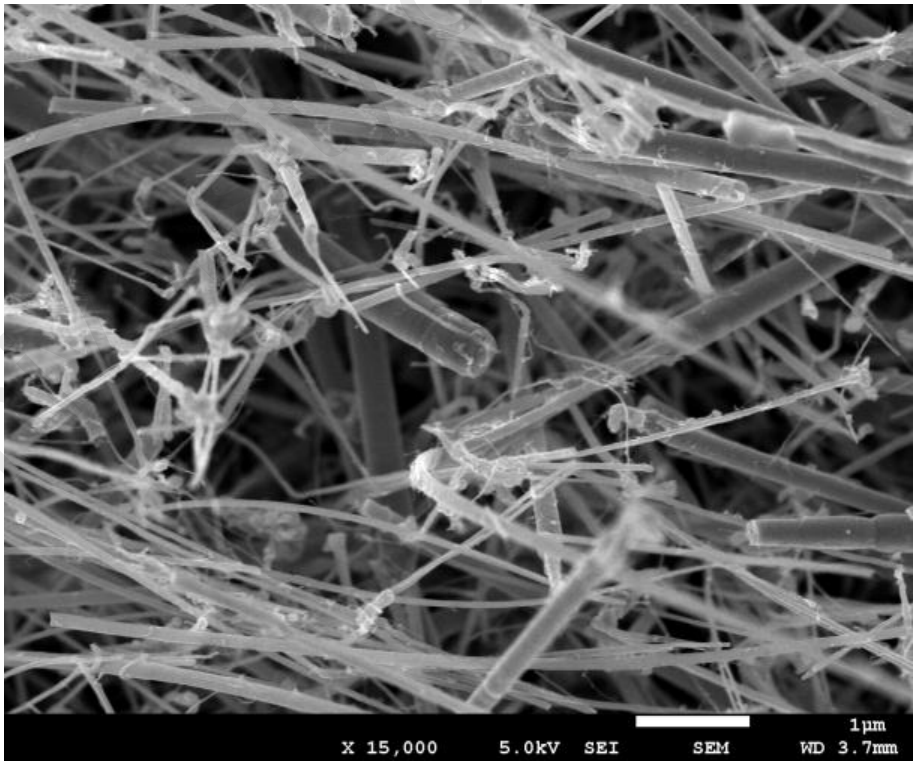

Figure 5.27: Image of ZnO/methanol NWs prepared at deposition time 20 minutes in Ar flow.

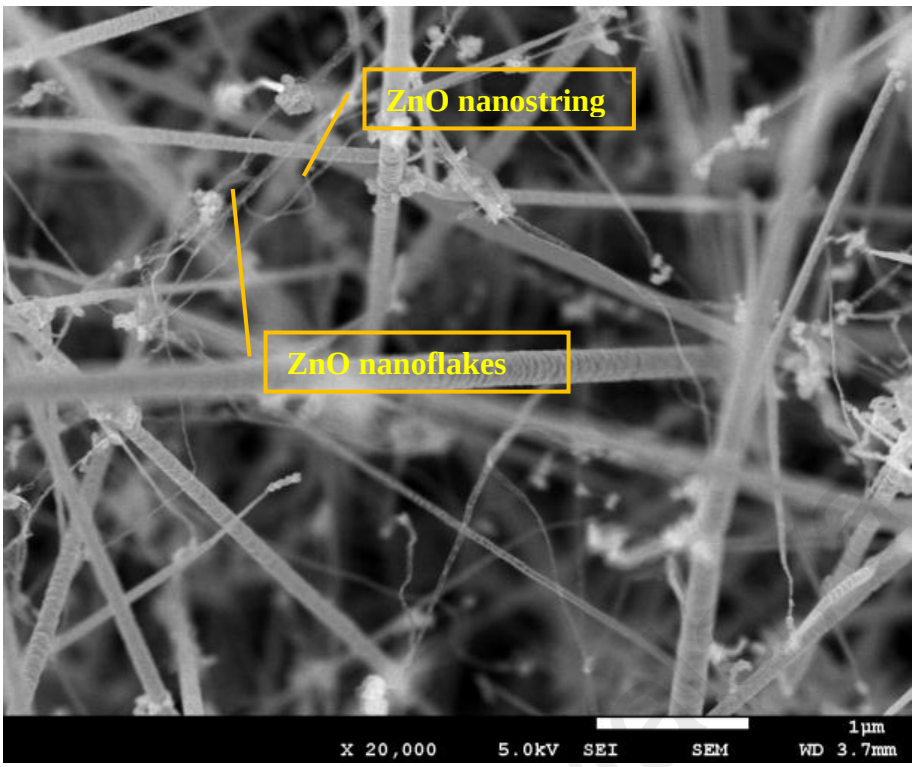

Figure 5.28: Image of ZnO/methanol NWs prepared at deposition time 25 minutes in Ar flow.

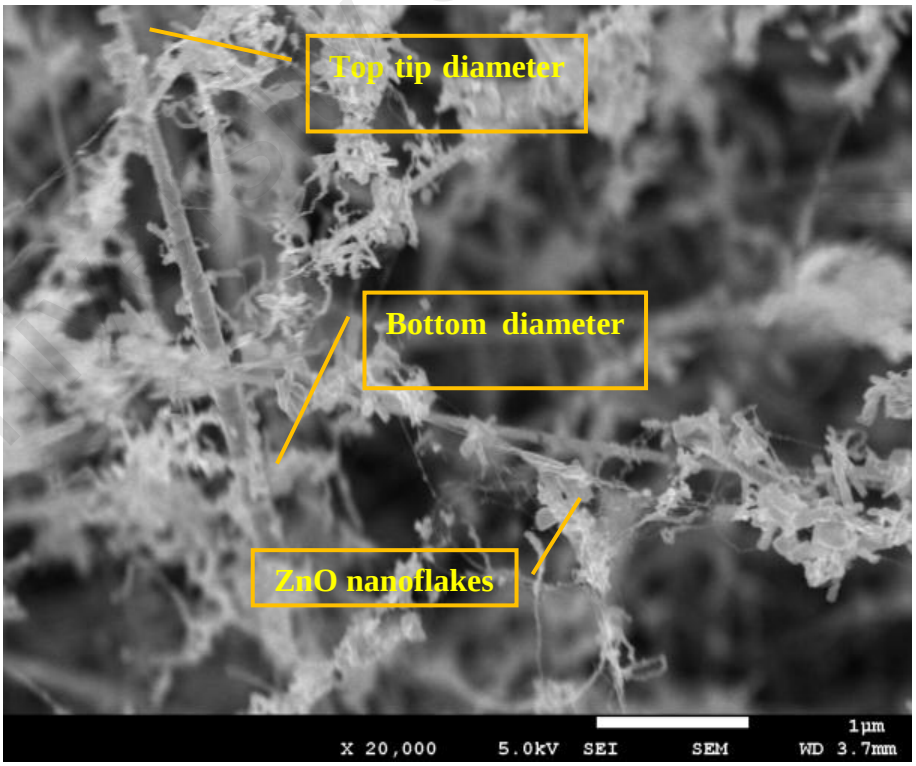

Figure 5.29: Image of ZnO/methanol NWs prepared at deposition time 30 minutes in Ar flow.

At growth times of 5 and 10 minutes, growth like button mushrooms are observable as shown in Figure 5.24 and 5.25. The diameters of the NWs are ranged from 10 nm at the bottom to few hundred nm to the top tip. They seem to be stacks of ZnO plates in a single NW. The stacked ZnO NWs in hexagonal shape are randomly orientated in long and straight dimension in whole direction on the Si substrate as seen in the Figure 5.24 and 5.25.

The Figure 5.26 and 5.27 are images of ZnO/methanol NWs produced for growth time of 15 and 20 minutes. They also randomly orientated in long and straight NWs on Si substrate. The lengths are observed to be up to few microns greater than ZnO/methanol prepared at growth time of 5 and 10 minutes. Their diameters ranged from 10 to 100 nm. Besides that, formations of ZnO flakes are observable in the photomicrograph of ZnO/methanol prepared at growth time of 20 minutes which could be an initial stage of formation of ZnO nanoflakes. More ZnO nanoflakes observed to be around the NWs of ZnO/methanol prepared at growth time of 25 and 30 minutes. Tiny nanostrings also are grown connecting the ZnO nanoflakes as seen in Figure 5.29. However, the diameters are ranged from 100 nm at the bottom to 10 nm to the top tip which looks like nanoneedles. This growth of ZnO/methanol nanoneedles believed to be in opposite direction of ZnO/methanol of 5 and 10 minutes growth time.

Based on the results and images of ZnO/methanol prepared in growth time variation of 5 minutes depicts a controversial growth mechanism that have not been reported elsewhere. Figure 5.30 shows an illustration of proposed growth mechanism. Structural transformation during the growth of ZnO/methanol has taken place. The shape has changed from button mushroom to NWs/nanorods and to nanoneedles as the growth time was increased from 5 minutes to 30 minutes. Figure 5.31 shows magnified version of Figure 5.28 of ZnO NWs grown in 25 minutes. The image indicates initial growth of nanoneedles from a base of ~150 nm diameter of ZnO. A ZnO nanostring

seems to be connected between the nanoneedle and ZnO flakes. As the growth time was increased to 30 minutes formation of nanoneedles observed to be in a cone shape as in Figure 5.32.

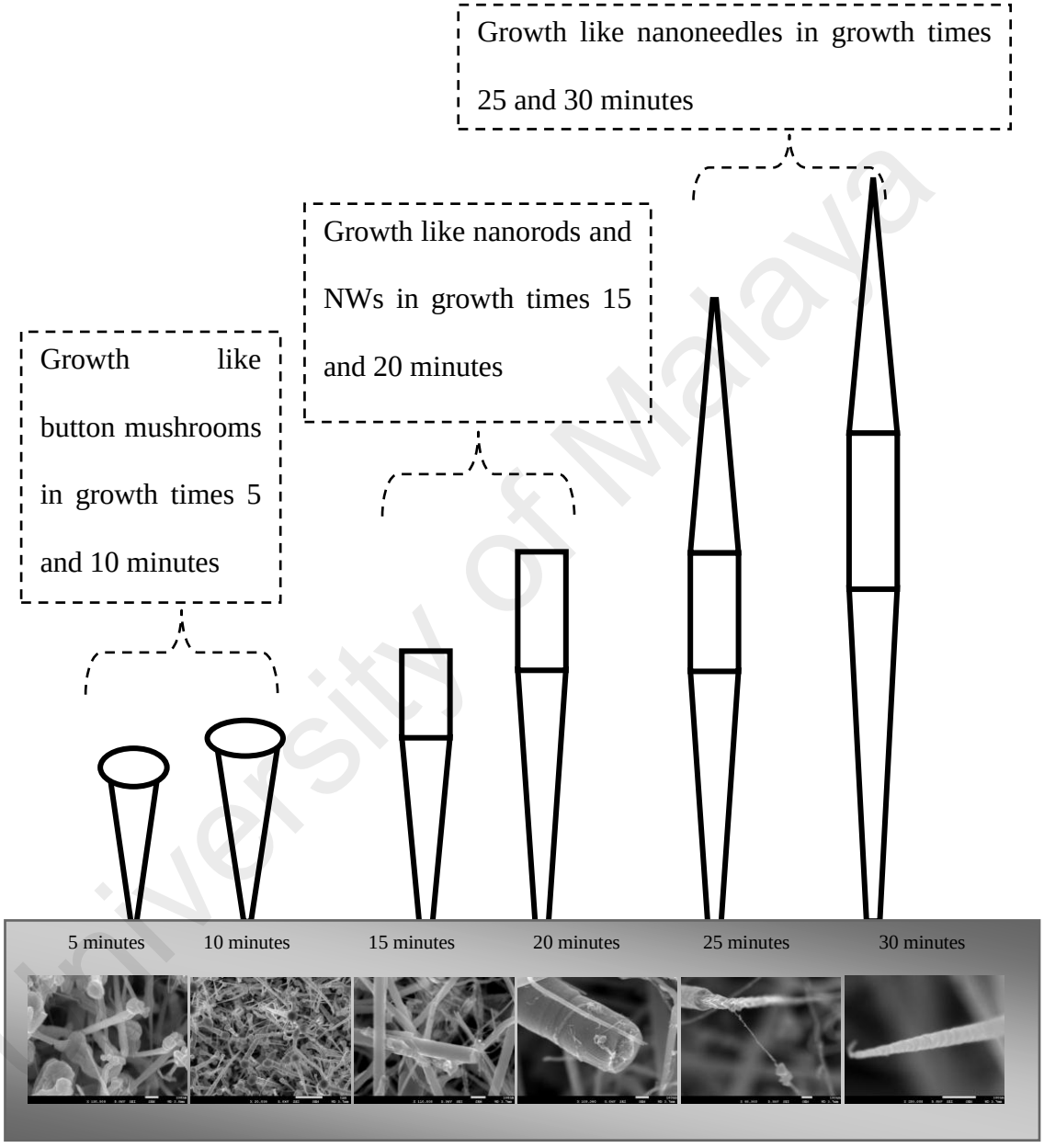

Figure 5.30: Predicted growth mechanism for ZnO/methanol NWs produced as growth time varies from 5 to 30 minutes. The respective FESEM images are inserted to show the illustration of the growth.

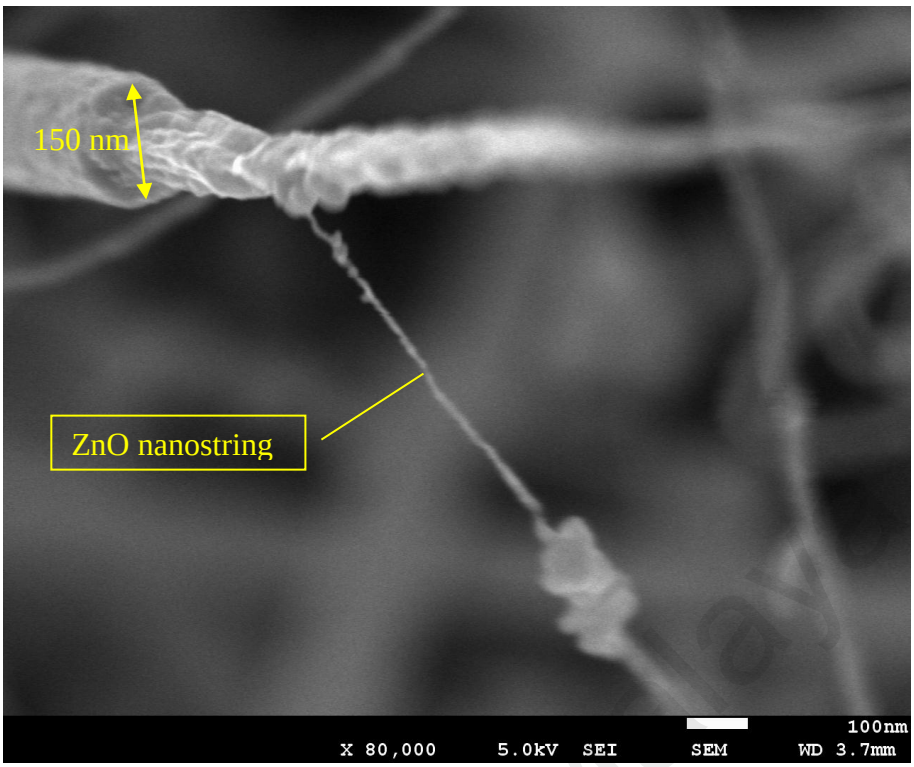

Figure 5.31: Magnification of X 80000 of ZnO/methanol grown for 25 minutes shows initial growth of nanoneedle.

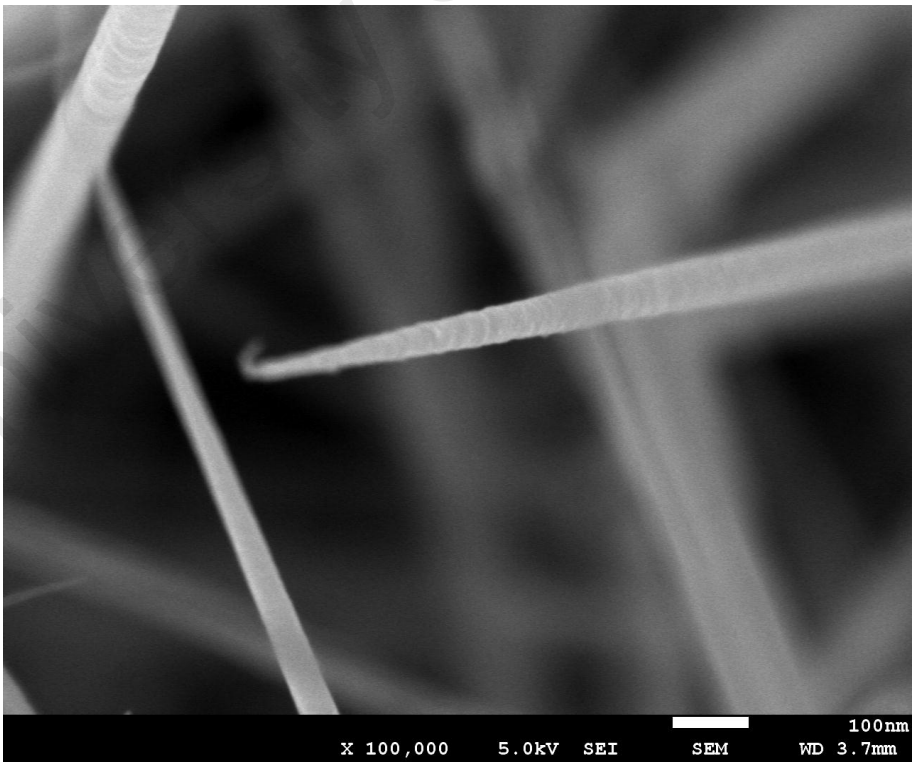

Figure 5.32: Magnification X 100000 of ZnO/methanol grown for 30 minutes shows growth of nanoneedle in cone shape.

5.4.2 XRD: ZnO/methanol

Figure 5.33 shows the XRD spectra of ZnO NSs deposited on Si substrate for growth times of 5, 10, 15, 20, 25 and 30 minutes. The diffracted peaks attribute the polycrystalline nature of ZnO which can be indexed to the hexagonal wurtzite type ZnO (JCP2.2CA: 00-036-1451). The prevalence of the peak that corresponds to (100) and (101) directions points to a preferential deposition time of 5, 10 and 15 minutes, whereas preferred growth in (002) plane direction is observable for growth times of 20, 25 and 30 minutes. This may be due to the fact that there are no enough energized particles in the beginning of 5 to15 minutes to move to low-energy sites that induced strain in the film.

Significant contribution in the (100), (002) and (101) directions are noticeable when the deposition time is increased from 20 to 30 minutes but very slight preferred orientation is noticed in <002> direction. This renders that more energized particles occupied the low-energy sites in c-axis direction. Based on the preferred growth direction (002) with the increased deposition time, crystallite size (*D*) of ZnO is calculated using Scherer formula (Chen et al., 2006). The peak center of (002) from Gaussian deconvoluted shows slight shift to the left compared to the standard peak center 2Θ of 34.422 of bulk ZnO (5.20661 Å). This indicates uniform tensile stress is distributed with higher calculated d spacing value of 2.604 Å.

Table 5.3 shows crystallite size has increased as the growth time increased. Figure 5.34 shows distribution of crystallite size at growth times ranged 5 to 30 minutes. The crystallite size found to be increased at low rate during the growth time of 5, 10 and 15 minutes which could be due to formation of low energy site of lattice ZnO. During 20, 25 and 30 minutes of growth time, the crystallite size dramatically increased to 49.8, 67.5 and 44.0 nm respectively. This could be due to condensation of energized particles such as O species onto the low energy site of ZnO.

At higher growth time, the density of growth of ZnO might have increased which could be due to condensation of more energized particles into NWs. The percentage of increment of crystallite size of ZnO NWs is worked out for an increased deposition time of 5 minutes as shown below,

$$\begin{aligned} &\textit{increment of crystallite size}: \quad 17\% \qquad 5\% \qquad 40\% \qquad 35\% \qquad -34\% \\ &\textit{Deposition time}: 5 - - \rightarrow 10 - - \rightarrow 15 - - \rightarrow 20 - - \rightarrow 25 - - \rightarrow 30. \end{aligned}$$

The high percentage of increment 17%, 40%, 35% and 34% are identified for the increment of 5 minutes of deposition time from 5 to 10 minutes, 15 to 20 minutes, 20 to 25 minutes and 25 to 30 minutes. This is due to more energized particles has occupied the low energy sites of the lattice of ZnO NWs. Whereas low percentage, 5% only for the increment of 5 minutes of deposition time from 10 to 15 minutes indicates that no enough energized particles occupying the lattice of ZnO NWs. The discernible change of growth percentage of ZnO NWs explicates a sinusoidal growth trend whereby creation and occupancy of low energy sites simultaneously has taken place for the each increment of 5 minutes deposition time. However, optimization in the growth time is noticed after 25 minutes of deposition.

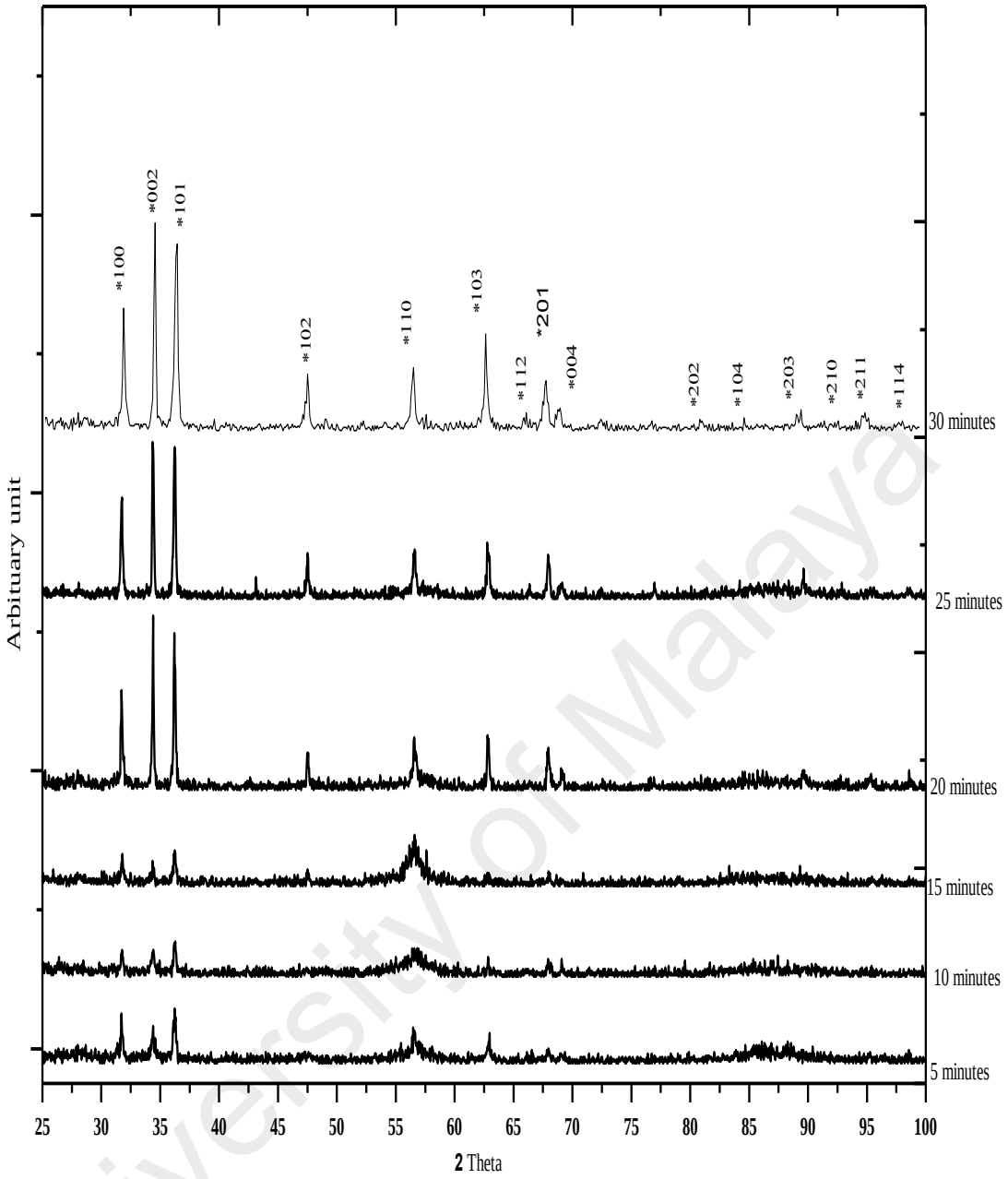

Figure 5.33: XRD spectra of ZnO/methanol NWs prepared at growth times of 5, 10, 15, 20, 25 and 30 minutes are stacked up.

Table 5.3: Details of XRD for ZnO/methanol NWs deposited at growth time of 5, 10, 15, 20, 25 and 30 minutes.

Deposition time (minutes)	Peak center (2θ) (002)	Crystallite size, D (nm)	D spacing (Å)		Lattice parameter (Å)		Ratio c/a	Volume (nm^3)
			(002)	(101)	a	c		
5	34.388	23.6	2.60482	2.47700	3.25102	5.20960	1.6025	47.68
10	34.380	28.3	2.60528	2.47562	3.24865	5.21082	1.6040	47.63
15	34.390	29.8	2.60432	2.47619	3.24990	5.20933	1.6029	47.65
20	34.393	49.8	2.60449	2.47642	3.25039	5.20893	1.6026	47.64
25	34.396	67.5	2.60400	2.47684	3.25111	5.20846	1.6021	47.68
30	34.387	44.0	2.60486	2.47667	3.25063	5.20972	1.6027	47.67

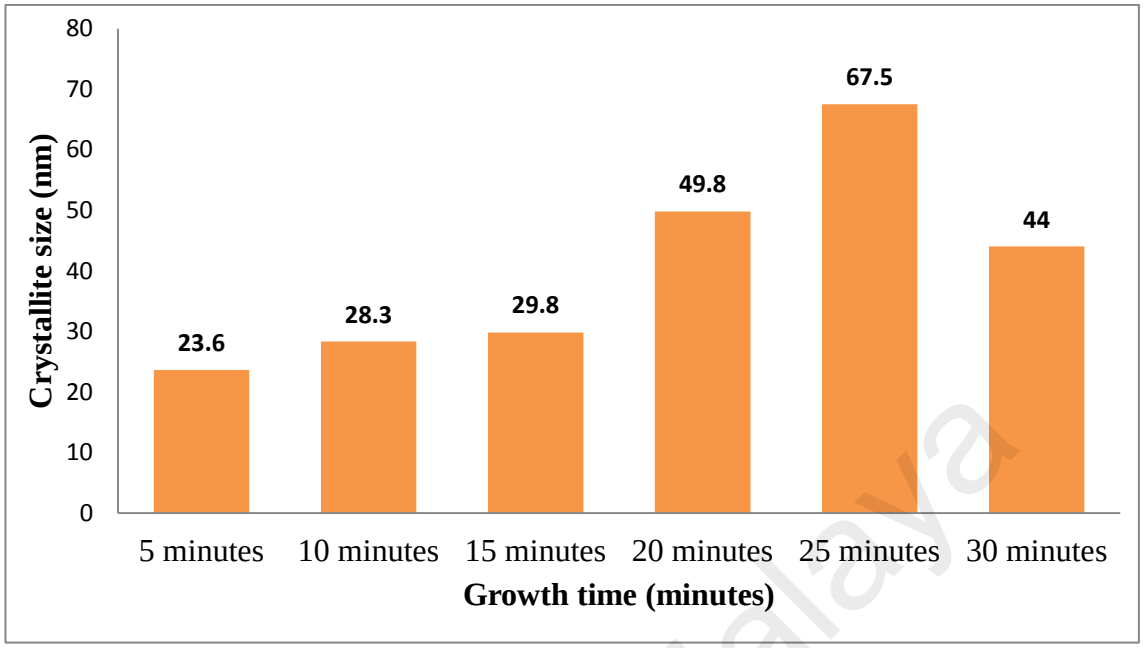

Figure 5.34: Crystallite size of ZnO/methanol NWs obtained at growth times of 5, 10, 15, 20, 25 and 30 minutes.

Table 5.4 shows details of data collected using W-H analysis method as per discussed in section 4.3.3.2. A plot $B_{hkl}\cos\theta$ versus $\sin\theta$ would give crystallite size that corresponds to the y-intercept and strain due to lattice deformation in the sample that can be calculated from the slope of graph. Preferred orientations (100), (002), (101), (110), (103) and (112) of ZnO sample deposited for deposition time of 5, 10 and 15 minutes are selected to geometrically determine the crystallite size and strain in that sample. Whereas for deposition time of 20, 25 and 30 minutes, the preferred orientations of (100), (002), (101), (102), (110), (103) and (112) are used to determine the crystallite size and strain. The strain is assumed to be uniform in all crystallographic directions, thus considering the isotropic nature of the crystal, where all material properties are independent of the direction along which they are measured.

Table 5.4: Details of crystallite size, strain, stress energy density of ZnO/methanol NWs deposited at growth time of 5, 10, 15, 20, 25 and 30 minutes.

Deposition time (minutes)	Scherer (nm) D(002)	Williamson Hall (W-H) method								
		Uniform Deformation Model (UDM)		Uniform Deformation Stress Model (UDSM)			Uniform Deformation Energy Density Model (UDEDM)			
	Crystallite size	Crystallite size (nm)	Strain $\varepsilon \times 10^{-4}$	Crystallite size (nm)	Strain $\varepsilon \times 10^{-4}$	Stress $\sigma \times 10^{6}$ (Pa)	Crystallite size (nm)	Strain $\varepsilon \times 10^{-4}$	Stress $\sigma \times 10^{6}$ (Pa)	Energy density $u \times 10^{3}$ (Jm^{-3})
5 minutes	23.6	31.6	7.03	23.9	-18.1	-1.26	29.4	15.987	67.877	4.7107
10 minutes	28.3	20.5	-22.10	23.5	-181.2	-12.58	21.0	278.945	283.527	19.6768
15 minutes	29.8	48.0	9.88	39.0	59.6	4.14	44.0	41.326	109.131	7.5737
20 minutes	49.8	61.9	7.90	50.2	507.4	3.52	59.4	33.452	98.185	6.8141
25 minutes	67.5	71.4	7.03	68.6	691.2	4.80	73.7	33.964	98.934	6.8661
30 minutes	44.0	36.0	2.31	40.0	4.79	60	38.2	3.17	28.000	8.6500

The plotted graph clearly indicates an increasing trend in crystallite size as the deposition time is increased. The W-H crystallite sizes are calculated to be higher than Scherer crystallite sizes except for the deposition time of 10 and 30 minutes. This could be a non-uniformity distribution of crystallite sizes due to surface strain and stress distribution during the deposition. Positive strain is found in ZnO NWs prepared at 5, 15, 20, 25 and 30 minutes. This corresponds well with the higher value of a (3.25102, 3.24990, 3.25039, 3.25111 and 3.25063) compared to the standard a_0 = 3.24982 Å. ZnO/methanol NWs of 10 minutes exhibits negative strain which could be due to the lattice shrinkage that corresponds to the calculated lower value of lattice parameters as shown in Table 5.3 compared with a_0. Lattice parameters along the c-axis for samples prepared from 5 to 30 minutes of deposition time shows higher calculated value compared to the standard c_0 (5.20661 Å). This explicates that stretched lattice happened along the c-axis of ZnO NWs that have the tendency of growth towards vertical direction. Thus, we can say that strain distribution in the prepared ZnO NWs samples corresponds well with <101> growth direction and lattice a.

The UDS and UDED models were taken into account where the anisotropic nature of Young's modulus, E of the ZnO NWs prepared at various deposition time is more realistic (Yogamalar et al., 2009). The uniform stress can be calculated from the slope of plotted graph between $B_{hkl}\cos\theta$ and $4\sin\theta/E_{hkl}$ and the crystallite size D, from the intercept at y-axis. The USDM brought forth negative stress and strain value in ZnO/methanol NWs deposited at 5 and 10 minutes. This only corresponds with the UDM value saying that shrinkage of lattice has occurred in the sample deposited at 10 minutes. But the ZnO/methanol NWs prepared at 5 minutes may indicates that the shrinkage of lattice is not in <101> direction. Positive strain presents in ZnO NWs deposited at 15, 20, 25 and 30 minutes corresponds with the UDM. A compressive stress in ZnO/methanol NWs prepared at 5 and 10 minutes were evaluated whereas

tensile stress was measured in samples prepared at 15, 20, 25 and 30 minutes. Compressive stress in the early stage of growth at 5 and 10 minutes is depicted before the coalescence of film. This can be attributed to the surface capillary forces on the isolated clusters to form grain boundaries. At 15, 20, 25 and 30 minutes tensile stress were calculated and can be associated with the formation of grain boundaries due to the coalescence of ZnO NWs. This is the effect of nonequilibrium state of ZnO NWs during deposition, most probably due to a raising chemical potential of the surface is higher than it would be if the surface were in equilibrium (Cammarata et al., 2000; Freund & Chason, 2001). The raising chemical potential provides a driving force that causes the flow of Zn and O vapors into the grain boundaries. With the formation of grain boundaries, the compressive stress slowly develops into tensile stress again that it corresponds to the sample prepared at 25 and 30 minutes.

A plot of $B_{hkl}\cos\Theta$ versus $\sin\Theta(2/Ehkl)^{1/2}$ gives the UDED value that corresponds to the slope of the graph. The y-intercept fits the D value. The D values are in good agreement with the values obtained from UDM, USDM and Scherrer's formula as in Table 5.4. This study shed the necessity of models in determining crystallite size of ZnO NWs. It is noted that the D value increases as the deposition time increased from 5 to 25 minutes. At growth time 30 minutes the D value reduces. This could be due to formation of Zno/methanol nanoneedles as shown in Figure 5.7. As far as we concerned, a detailed study using these models on the ZnO NWs synthesized samples at 5, 10, 15, 20, 25 and 30 minutes is not reported yet. The calculated strain and stress values are differing to greater extend due to the inclusion of anisotropic nature of the prepared samples.

5.4.3 Photoluminescence: ZnO/methanol

PL study was carried out using Renishaw invia Raman microscope at room temperature in the wavelength range from 350 to 800 nm using a 325 nm helium-cadmium (He-Cd) laser light which passes through three visible lens sets and a diffraction grating of 1200 lines/mm. The respective PL profile for ZnO/methanol prepared at various growth times of 5, 10, 15, 20, 25 and 30 minutes is shown as Figure 5.35. It is generally accepted that the surface states plays a crucial role in PL spectra of ZnO nanomaterials (Vanheusden et al., 1996a). Energy transition within the ZnO/methanol NWs and relationship between material colour and defect structure were determined. The normalised PL showed a low near band-edge (NBE) emissions at ~382 nm, deep level (DL) emissions at ~540 nm and near infrared emissions at ~765 nm for all the samples.

Figure 5.36 shows an enlarged version of PL spectra ranged from 370 to 410 nm. The NBE is often assigned to radiative annihilation of excitons due to exciton-exciton collisions in the ZnO. The intensity of the emissions found to be has decreased as the growth time was increased. This indicates reduction in the exciton recombinations as the time dependence growth increased from 5 to 30 minutes. This can be related to the reduction in the formation of excitons due to low coulomb attraction (Vasil'ev & Smetanin, 2006). Furthermore, reduced peak broadening effect at NBE with increased time dependence growth agrees the reduction of exciton recombination in ZnO (Zhu et al., 2014). The increased integral intensity of NBE emission indicates significant changes in the crystallinity of ZnO/methanol NWs as well as the diameter of NWs (Huang et al., 2001). High crystallinity of ZnO/methanol is related to decrease of impurities and structural defects such as oxygen vacancy (V_o) and dislocations (Bagnall et al., 1998). The decreased NBE also indicates rapid recombination of charge carriers in the defect energy states, which gives rise to intense DL emission as observed in Figure 5.35.

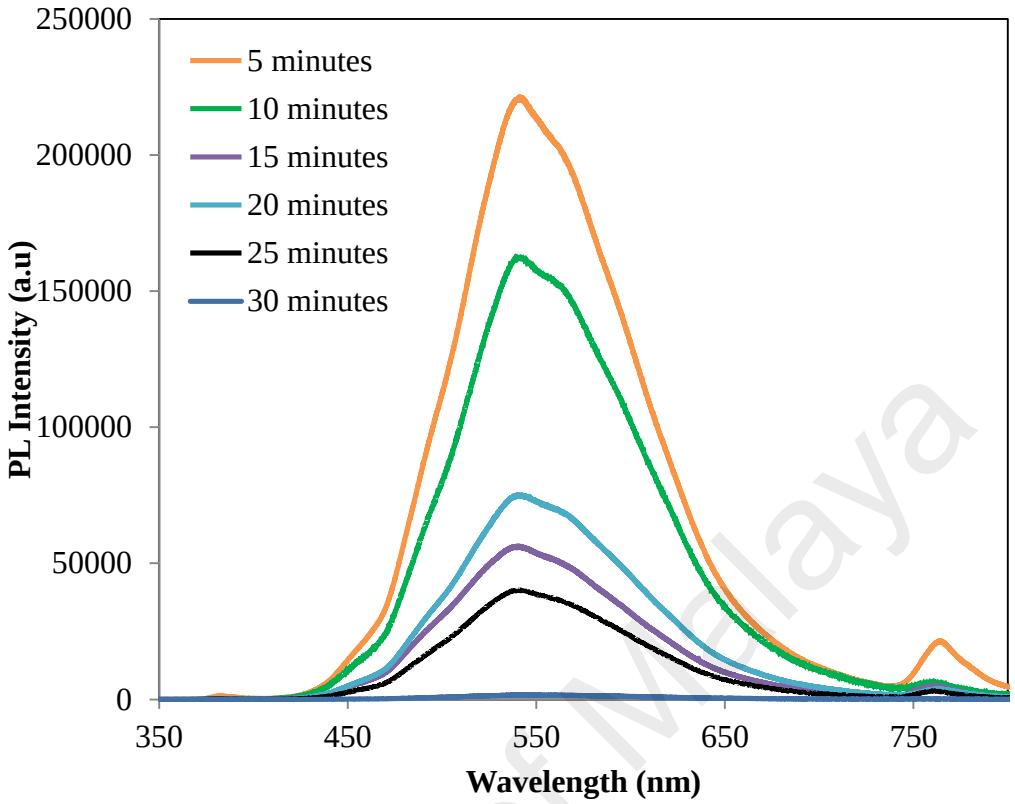

Figure 5.35: Photoluminescence spectra of ZnO/methanol NWs deposited at various growth time of 5, 10, 15, 20, 25 and 30 minutes.

Table 5.5: Details of photoluminescence peaks of ZnO/methanol NWs near band edge, deep level and near infrared emissions obtained from Gaussian fits.

Deposition time (minutes)	NBE		DL		NIR	
	Peak position	Energy (eV)	Peak position	Energy (eV)	Peak position	Energy (eV)
5 minutes	382 nm	3.24	541 nm	2.29	764 nm	1.62
10 minutes	381 nm	3.25	541 nm	2.28	761 nm	1.62
15 minutes	381 nm	3.25	540 nm	2.29	761 nm	1.63
20 minutes	382 nm	3.24	540 nm	2.29	762 nm	1.62
25 minutes	381 nm	3.25	540 nm	2.28	762 nm	1.63
30 minutes	378 nm	3.28	541 nm	2.28	755 nm	1.64

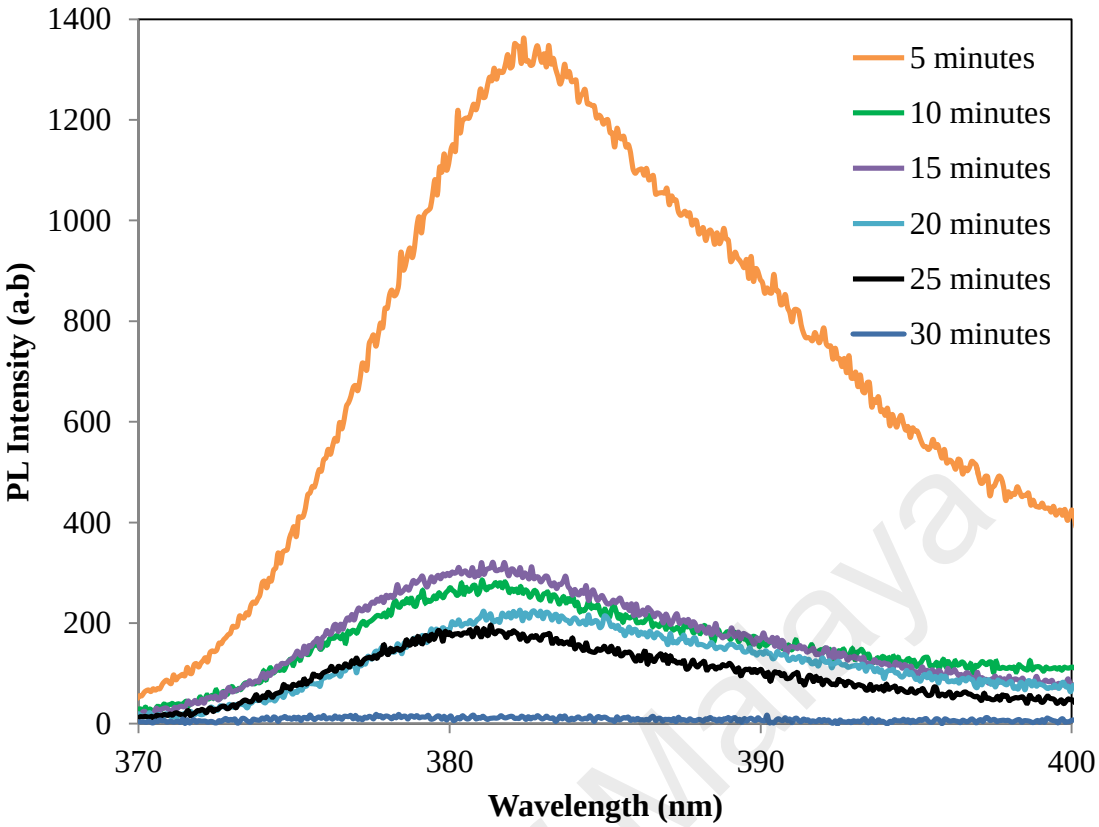

Figure 5.36: Photoluminescence spectra of ZnO/methanol NWs enlarged at range 370 – 410 nm.

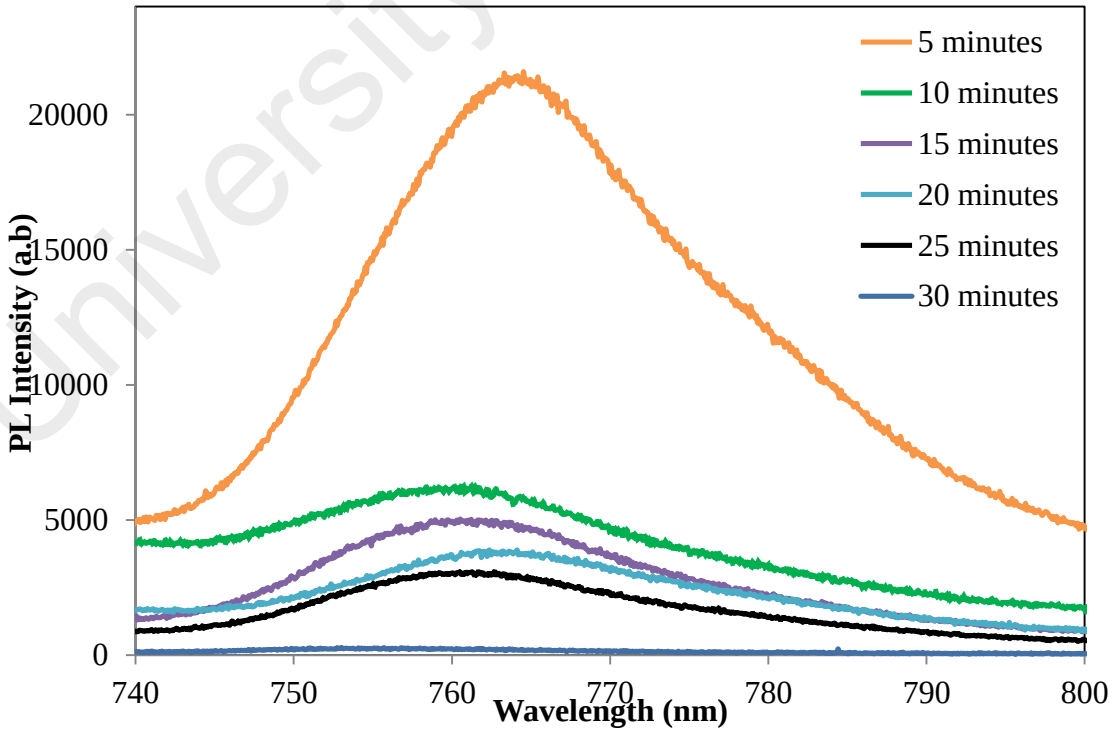

Figure 5.37: Photoluminescence spectra of ZnO/methanol NWs enlarged at range 740 – 800 nm.

The dependence of this DL emission on the growth times was analysed to investigate the defect structure in ZnO/methanol. In order to compare the relative contributions to the emissions Gaussian deconvoluted peaks were obtained for NBE, DL and NIR and detailed in Table 5.5. Blue region around 460 nm (2.70 eV) can be linked to the presence of complexes of zinc interstitials (Zn_i) (Look et al., 2005). The broad DLE green emissions at ~540 nm (2.29 eV) can be related to oxygen vacancies (V_o) (Vanheusden et al., 1996a; Wu et al., 2001; Yamauchi et al., 2004). Halliburton et al. (2005) have shown that DLE green emission is due to shallow donors or conduction band electrons. Zhang et al. (2001) and Patterson (2006) have proven that V_o is an unlikely contributor to green emission compared to zinc vacancies (V_{zn}^{2-}) based on the electron transition state. V_{zn}^{2-} has the lowest formation energy in O-rich conditions as the growth time was increased. The methanol environment provided excess of oxygen for reactions. Thus, V_{zn}^{2-} are the most energetically favourable and stable defects to form in the ZnO nanorods. small broad shoulder ~560 nm (2.21 eV) which indicates emissions of yellowish-green band from all ZnO/methanol samples prepared at growth times of 5, 10, 15, 20, 25 and 30 minutes. This can be related to H^+ defects that present from the methanol solution, also can be considered to be shallow donor in ZnO nanorods. ZnO/methanol NWs are believed to be a good candidate to study doping levels in ZnO NSs. The observed yellow luminescence at ~560 nm (2.20 eV) is attributed to recombination of donors with acceptors from methanol solution believed to be H acceptors.

Near infrared (Rekha et al.) luminescence ~762 nm observed in all ZnO/methanol samples except for sample prepared at growth time of 30 minutes which shows NIR at 755 nm (Cross et al., 2005; Wang et al., 2012; Zhu et al., 2014). The enlarged version ranged from 740 to 800 nm is shown as Figure 5.37. The intensity of the peak noticed to be shifted to left from 764 to 755 nm which is to higher energy level

in the NIR region. Nevertheless, the intensity of NIR luminescence is observed to be far higher than the intensity of NBE luminescence. This is contradictory to some researchers' findings that NIR band originates due to second order diffraction of NBE luminescence (Zhu et al., 2014). The ratio of intensity of NIR to intensity of NBE (I_{NIR}/I_{NBE}) for all the samples is greater than 1 unit. This reveals that increase of V_o concentration in the sample as the time dependence growth is increased from 5 to 30 minutes (Tseng et al., 2003).

5.4.4 Raman scattering: ZnO/methanol

In the following, ZnO/methanol NWs grown using VPT assisted by thermal evaporation was characterized by Raman spectroscopy. These samples were taken as host crystals for the doping of manganese (Mn) and aluminium (Al).

As will be shown in the course of this thesis, the pure ZnO may contain residual impurities far below the EDX detection limit (as per our discussion in section 5.2.1) and Raman detection limits which does not influence the Raman studies were presented in this section. Hence, the pure ZnO NWs can be considered as a model system for well-ordered, pure ZnO. Usually, Raman spectra of ZnO shows two large band, one in the lower wavenumber which is below 300 cm^{-1} resulting from vibrations of the Zn sublattices and the other at higher wavenumber (300-700 cm^{-1}), ascribed to O-related modes.

Figure 5.38, 5.39 and 5.40 shows Raman spectrum of such ZnO NWs which were prepared at various growth times of 10, 20 and 30 minutes. Dominant peak at 143 cm^{-1} is noticeable in ZnO/methanol NWs deposited at growth time of 10 minutes whereas dominant peak at 145 cm^{-1} is observable in ZnO/methanol NWs of growth time of 20 and 30 minutes. The intensity at 143 cm^{-1} found to be enhanced as the growth time of ZnO/methanol NWs was increased by 10 minutes at constant substrate

temperature of 800 °C. This observable peaks at 143 cm^{-1} in the room temperatures Raman scattering are contradiction to Cuscó et al. (2007). They also has observed the same peak and has reported that intensity enhancement and sharpening of the peak at 142 cm^{-1} as Raman scattering was done at lower temperatures at 80 K due to local mode origin of the peak.

Two peaks at lower wavenumber around 72 and 82 cm^{-1} were noticed in ZnO/methanol NWs of all samples. It is found to be that peaks 72 and 82 cm^{-1} splitting from a single peak for the lower growth times of 10 minutes. As the growth time was increased to 20 and 30 minutes peak at 72 cm^{-1} diminished and the peak at 82 cm^{-1} found to be sharper. A research team from Germany have reported that this Raman peak at 82 cm^{-1} is related to bare ZnO nanoparticles obtained by decomposing Zn oximate in dimethyl formamide (DMF) (Khanderi et al., 2009). The same group also has reported that Raman peak at 105 cm^{-1} can be assigned to ZnO/MWCNT which is similar to peaks 107 and 109 cm^{-1} which were obtained in the sample of ZnO/methanol NWs prepared for growth times of 10, 20 and 30 minutes. The similarity in observation attributes incorporation of carbon particles from methanol to bond with ZnO NWs. The observed peaks at ~82, ~109, ~143 and ~282 cm^{-1} which are below 300 cm^{-1} can be related to vibrations of Zn sublattice. Coincidently, peak ~282 cm^{-1} that has A_1 symmetry can be assigned to B_1^{high}-B_1^{low} mode. This peak was shifted to 287 and 288 cm^{-1} for longer growth times of 20 and 30 minutes respectively.

At the intermediate low frequency region the E_2^{high} mode at 437, 438, and 439 cm^{-1} are noticeable respectively in samples prepared at growth times of 10, 20 and 30 minutes. These peaks found to be sharper as the growth time was increased. This is an indication of O stoichiometry completion for longer growth time whereby Zn particles were bonded to O to form ZnO NWs. Peaks 343, 338 and 340 cm^{-1} which has A_1 symmetry is observable respectively in ZnO/methanol NWs prepared at growth time 10,

20 and 30 minutes. These modes are in good agreement with the difference between E_2^{high} and E_2^{low} frequencies. However, 343 cm^{-1} in ZnO/methanol NWs of 10 minutes observed to be broaden due to split up into 82 and 107 cm^{-1} frequency.

Peak at 382 cm^{-1} is observable only in ZnO/methanol NWs which was prepared in 20 minutes. This peak reflects A_1(TO) mode measured in the room temperature Raman scattering is contradict to Cuscó et al. (2007) of spectrum recorded at 80 K. A broad band in region 500 - 600 cm^{-1} found to be diminished as the growth time was increased. It is broadening with centred at 541 cm^{-1} for ZnO/methanol NWs prepared at growth time of 10 minutes. This can be assigned to A_1 symmetry and attributed to $2B_1^{low}$ and LA overtones along L, M and H lines. As the broadening is diminishes relatively to the increased growth time, extra peaks at 564 and 578 cm^{-1} were noticed. As in Figure 5.39 only one extra peak at 564 cm^{-1} is noticeable for ZnO/methanol NWs of 20 minutes while two peaks at 564 and 578 cm^{-1} are detectable for ZnO/methanol NWs prepared at growth time of 30 minutes. Peak 564 cm^{-1} can be revealed to non-resonance Raman scattering whereas 578 cm^{-1} which is close to A_1(LO) mode has been reported by Ye et al. (2009) in resonance Raman spectra of ZnO quantum dots. This peak in the proximity of A_1(LO) were assigned to surface optical modes predicted theoretically and O vacancies, Zn interstials or combination of the two (Baskoutas et al., 2007).

High frequency region from 820 – 1120 cm^{-1} has been reported formed by optical overtones and combinations (Serrano et al., 2004). A weak peak at 1048 cm^{-1} which is observable in ZnO/methanol NWs of 10 minutes can be assigned to TO+LO combination modes at the A and H points. As the growth time was increased to 20 and 30 minutes the peak has been shifted to right to 1051 cm^{-1}. In sample ZnO/methanol of 30 minutes, the peak found to be sharper with high intensity. Additionally, a peak at 1075 and 1090 cm^{-1} only on ZnO/methanol of 20 and 30 minutes are respectively

noticeable. These peaks can be assigned to be TO+LO combination modes at M and L points. ZnO/methanol NWs of 20 and 30 minutes of growth time show first order Raman absorption for the disordered band D and G. A weak shoulder band D at 1358 and 1337 cm^{-1} found in sample prepared at growth time of 20 and 30 minutes respectively. The G band appeared to be broader compared to the D band. The G bands around 1589 and 1575 cm^{-1} is observable in ZnO/methanol NWs of 20 and 30 minutes. As the growth time was increased from 20 to 30 minutes both the D and G band were shifted to left. The presence of D and G band clearly states incorporation of C particles in the lattices of ZnO/methanol NWs prepared using methanol vapor.

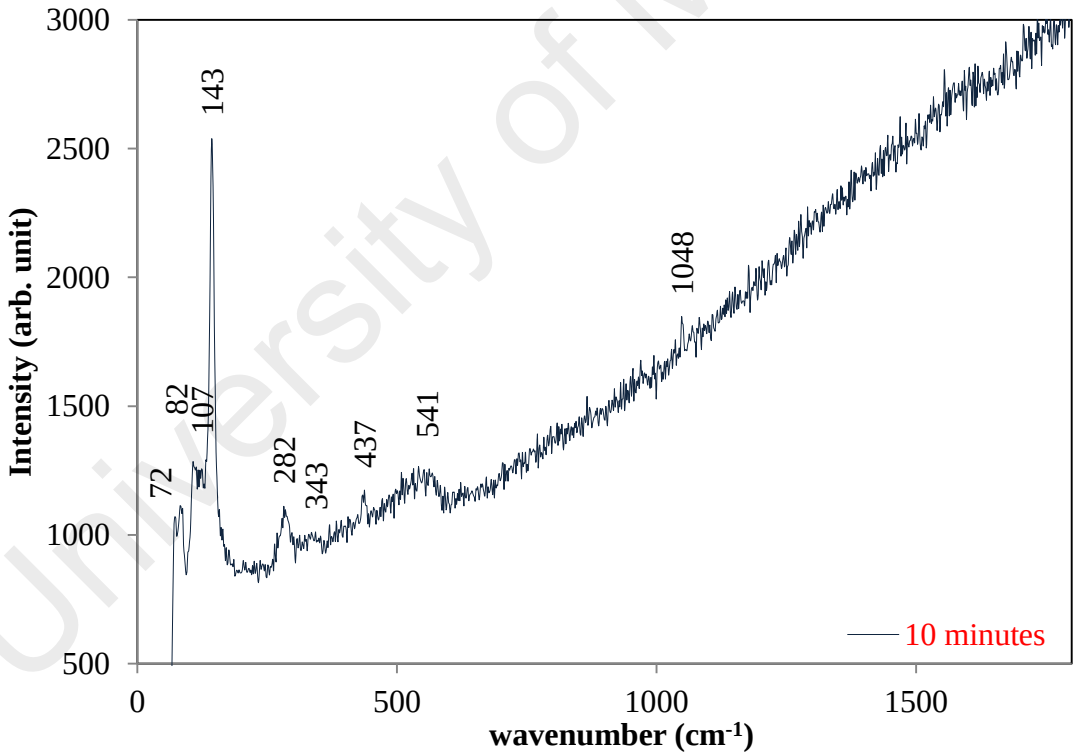

Figure 5.38: Raman scattering of ZnO/methanol NWs prepared at growth time of 10 minutes.

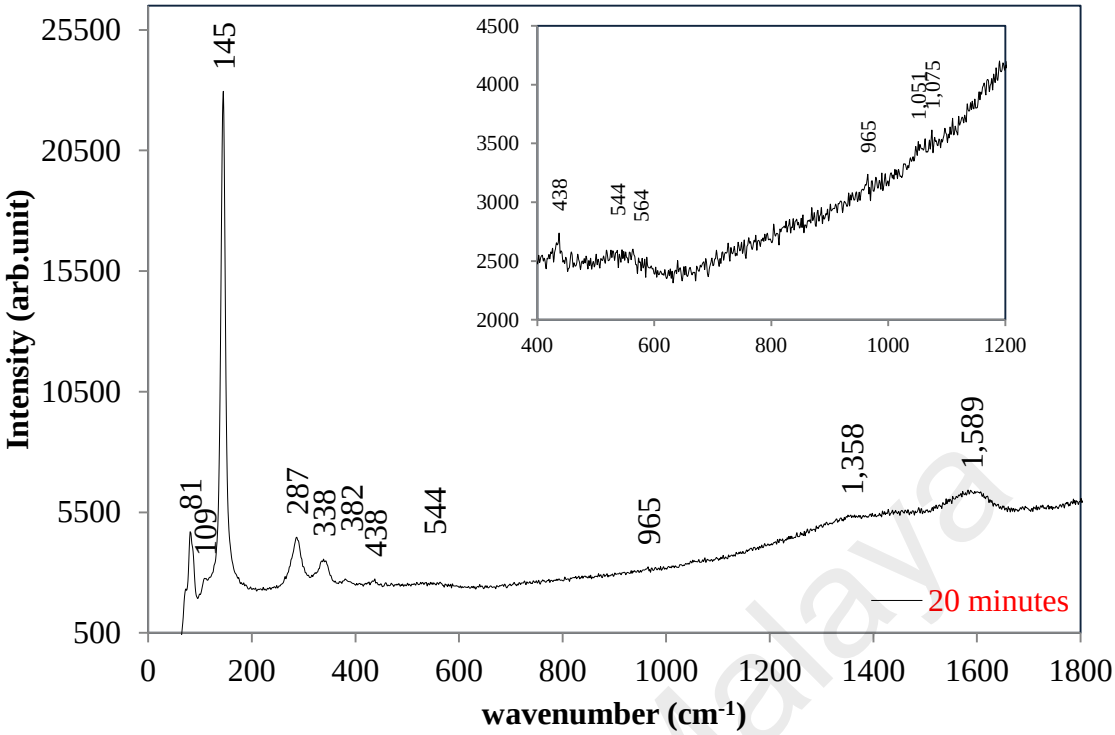

Figure 5.39: Raman scattering of ZnO/methanol NWs prepared at growth time of 20 minutes.

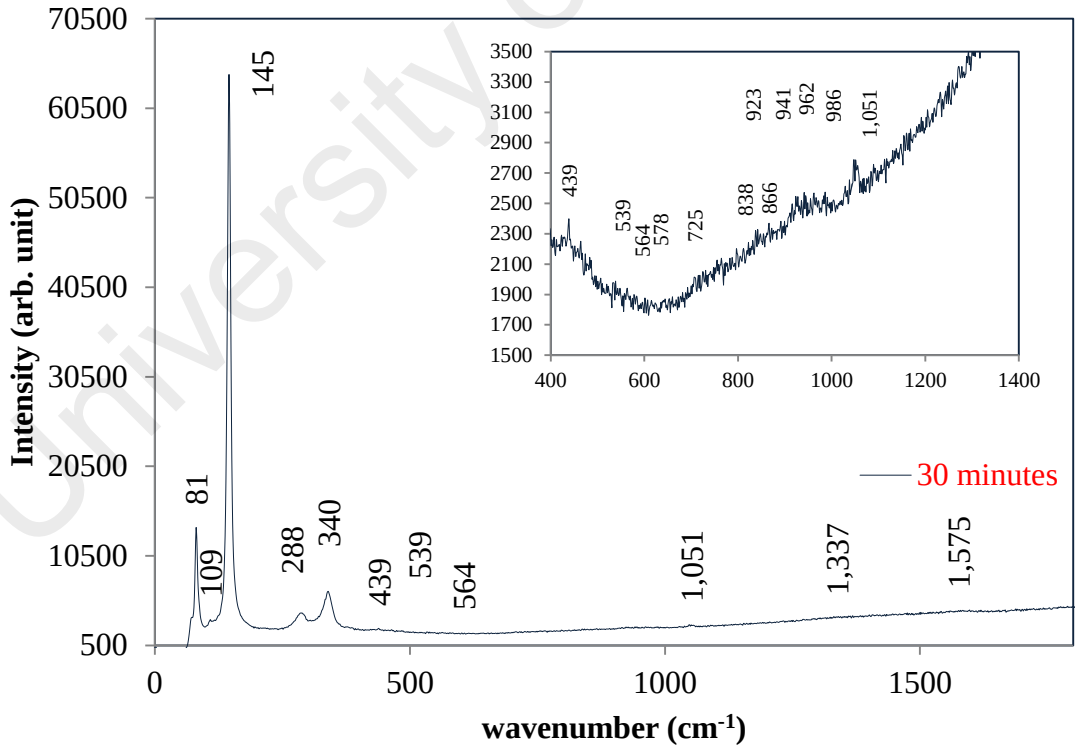

Figure 5.40: Raman scattering of ZnO/methanol NWs prepared at growth time of 30 minutes.

5.4.5 Conclusion

A series of photomicrograph of ZnO/methanol and ZnO/ethanol for growth times 5, 10, 15, 20, 25 and 30 minutes gave significant changes in the morphology and structure. All the photomicrographs showed that ZnO NWs were randomly orientated on Si substrate. However ZnO/methanol has shown structural changes from button mushroom to NWs/rods and to nanoneedles as the growth time is increased to 30 minutes whereas ZnO/ethanol (refer Figure 5.9) only shown growth of ZnO pillars to comb like shape. Comparatively, fabrication of ZnO NWs using methanol is preferred due to growth of nanoneedles.

5.5 Influence of Ethanol in preparing ZnO nanowires

The experimental setup as per in section 3.6.3 was used in preparing ZnO/ethanol NWs in ethanol with Ar flow through two-sided hollow CuZn alloy rod. Methanol solution was replaced with ethanol solution. Ethanol has higher percentage of carbon per molecule about 52.2 % compared to methanol which has only about 37.5 %, was believed would affect the structural and morphology of ZnO NWs as well as the optical properties of ZnO.

5.5.1 FESEM: ZnO/ethanol

ZnO/ethanol was prepared at growth times 5, 10, 15, 20, 25 and 30 minutes and the respective photomicrograph images are identified as Figure 5.41, 5.42, 5.43, 5.44, 5.45 and 5.46 . The overall observation depicts that diameter of NWs of ZnO/ethanol are smaller for growth times of 5, 10 and 30 minutes compared to 15, 20 and 25 minutes. ZnO/ethanol NWs for growth times 5 and 10 minutes measured to be in the range of 10 to 30 nm.

ZnO/ethanol NWs grown for 15 minutes exhibited larger diameter than ZnO/ethanol of 5 and 10 minutes. They ranged from 10 to 50 nm and almost vertically aligned as seen in the Figure 5.43. Growth time of 20 minutes enabled formation of ZnO NWs with average diameters up to 200 nm. Figure 5.44 shows growth like branch in a single NW. They were grown like pillars with hexagonal pyramid at the top tip. Few researchers have described this as tetrapod growth which branch out from a single NW. A comparison observation between Figure 5.43 and 5.44 attributes that density of NWs has reduced as the growth time was increased from 15 to 20 minutes. Both photomicrograph of ZnO/ethanol for 15 and 20 minutes exhibits NWs with hexagonal shape whereas tiny NWs or nanostrings are observable in the photomicrograph of growth times 5 and 10 minutes.

As the growth time is increased to 25 minutes, the growth density seems to be greater with a reduced diameter as in the Figure 5.45. In addition, ZnO/ethanol nanopillars were grown in hexagonal shape and orientated randomly over Si substrate. Furthermore more tetrapod ZnO/ethanol nanopillars with an average diameter of 100 nm found to be protruding from a larger ZnO/ethanol plate in about 200 nm. The ZnO/ethanol plate became a base for the growth of other ZnO tetrapods which is in about 100 nm diameter. Figure 5.46 of ZnO/ethanol at growth time of 30 minutes exhibits various diameters of NWs ranges from 10 – 100 nm. The area highlighted indicates growth of single NW on polar surface (0001) along [1010] direction. This attributes growth of “comb-like” nanobranches in the range of 5 – 15 nm on the side of (0001) polar single ZnO/ethanol NW.

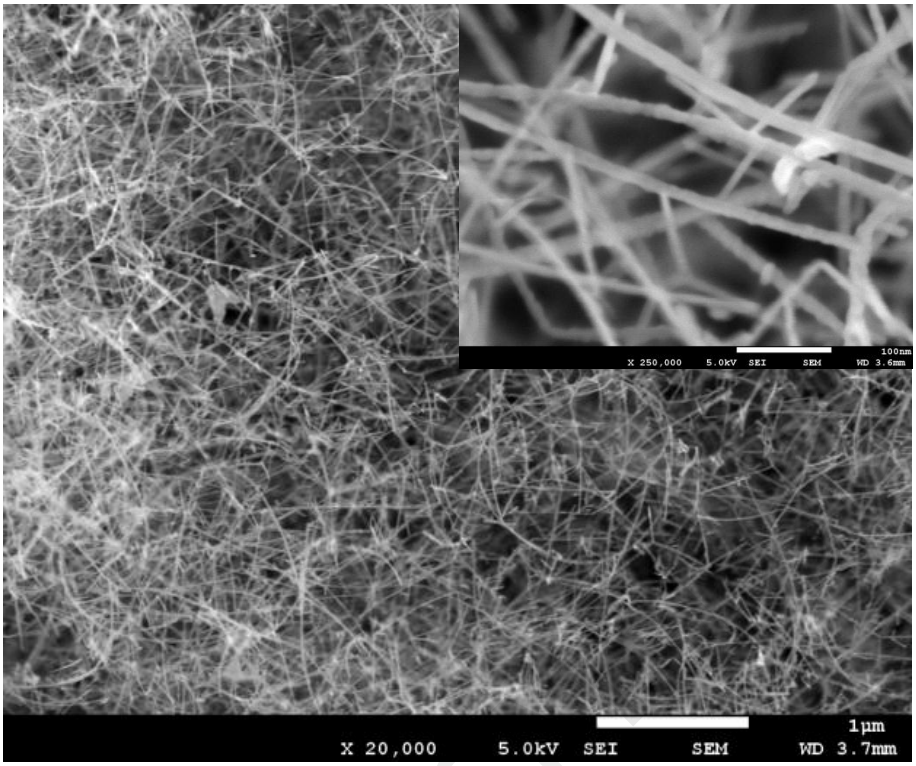

Figure 5.41: Images of ZnO/ethanol NWs prepared at deposition time 5 minutes in Ar flow. The magnified version X 250000 is shown at top right corner.

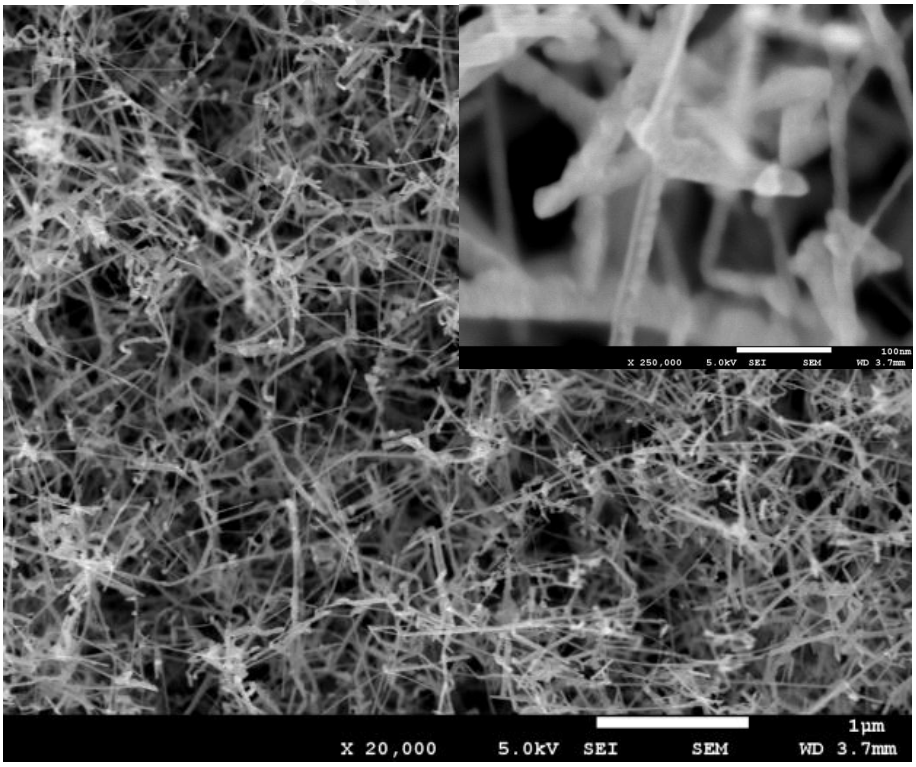

Figure 5.42: Images of ZnO/ethanol NWs prepared at deposition time 10 minutes in Ar flow. The magnified version X 250000 is shown at top right corner.

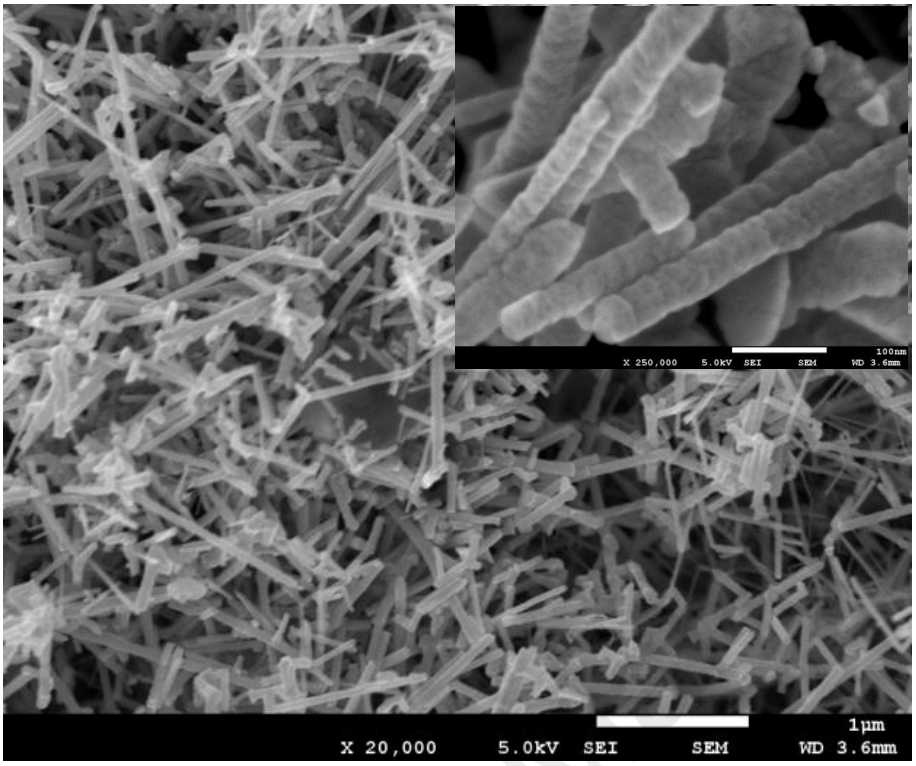

Figure 5.43: Images of ZnO/ethanol NWs prepared at deposition time 15 minutes in Ar flow. The magnified version X 250000 is shown at top right corner.

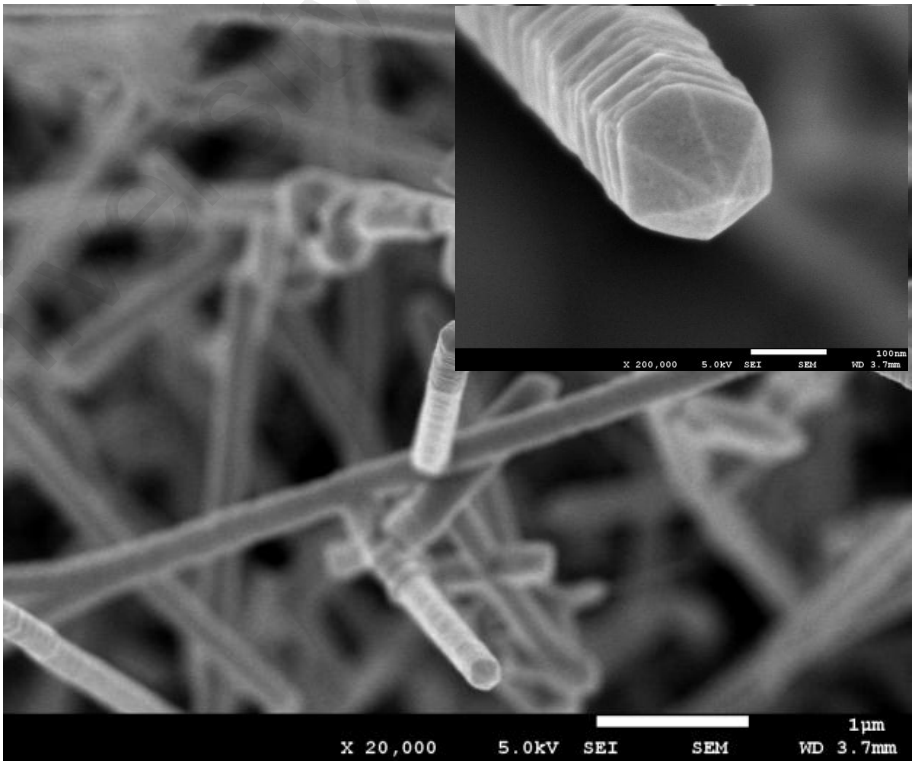

Figure 5.44: Images of ZnO/ethanol NWs prepared at deposition time 20 minutes in Ar flow. The magnified version X 200000 is shown at top right corner.

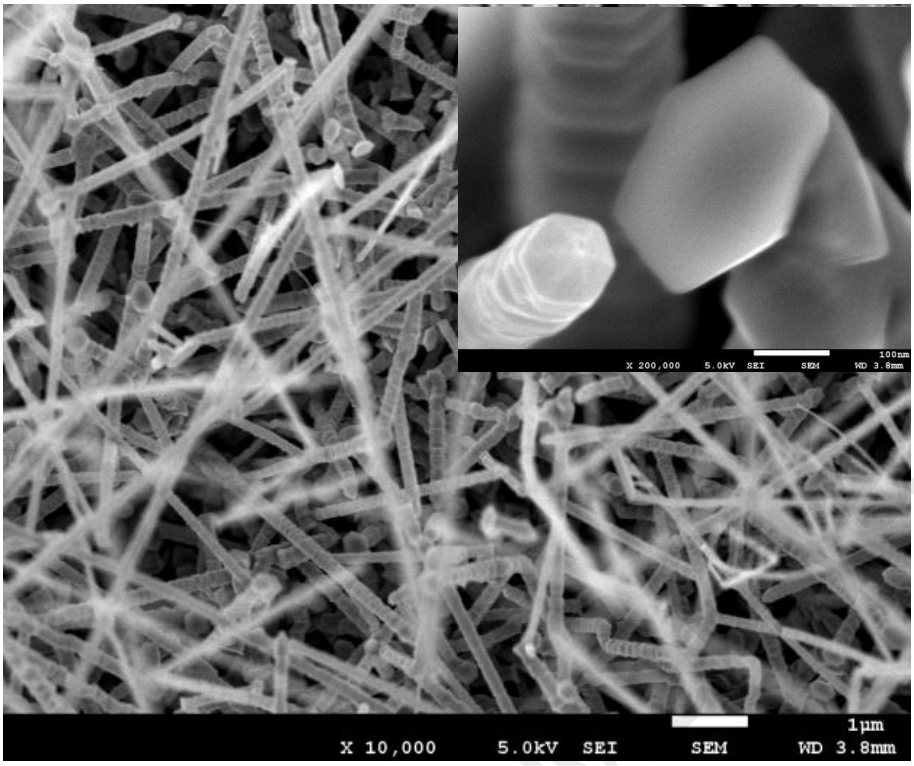

Figure 5.45: Images of ZnO/ethanol NWs prepared at deposition time 25 minutes in Ar flow. The magnified version X 200000 is shown at top right corner.

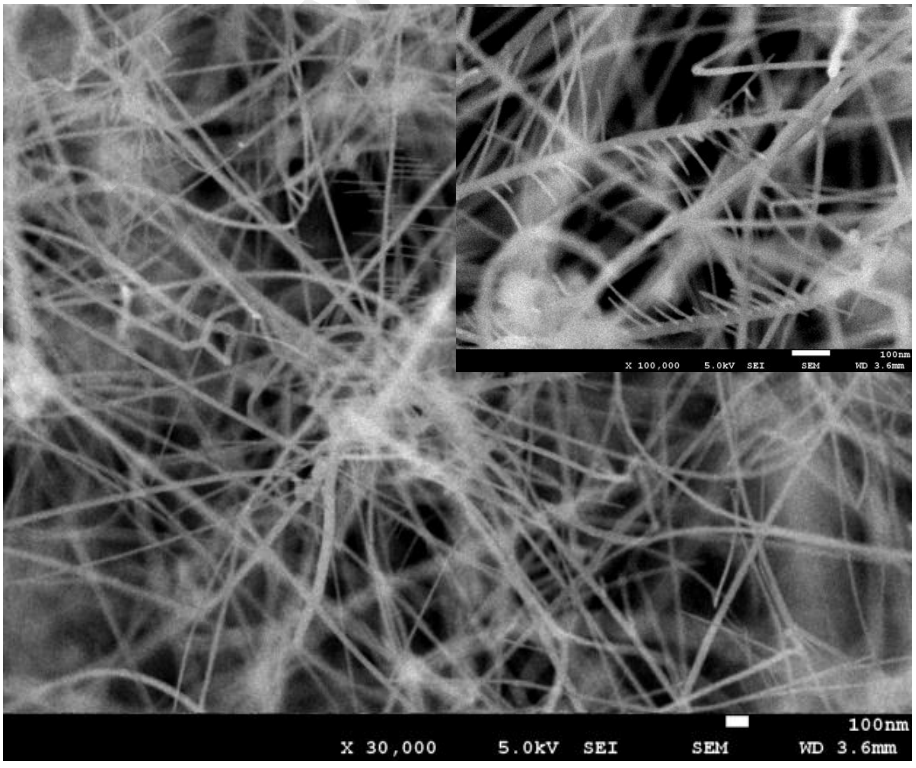

Figure 5.46: Images of ZnO/ethanol NWs prepared at deposition time 30 minutes in Ar flow. The magnified version X 100000 is shown at top right corner.

The overall observation from the photomicrographs shows random orientation of ZnO/ethanol NWs on Si substrate. Figure 5.47 shows the relation between the distributions of various diameters of ZnO/ethanol NWs with the increased growth time. The average diameter is depicted based on the sizes of few nanopillars. ZnO/ethanol NWs prepared in growth times of 5, 10, 15 and 20 minutes shows increasing trend in the diameter compared to ZnO/ethanol NWs prepared in 25 and 30 minutes. An extreme increase in the diameter from 50 to 200 nm is noticed when the deposition time was increased from 15 to 20 minutes. This show supersaturation of vapors taken place on the Si substrate. Transformation of ZnO/ethanol NSs from NW → NW → thicker NW (circular shape) → thicker nanopillars (hexagonal shape) is an evident that supersaturation of vapors strongly affected the formation of variety of ZnO/ethanol NSs. As the deposition time was increased supersaturation level of vapors has increased which is also evident from the increased diameter of ZnO/ethanol NWs. However a sudden decrease in the diameter from 200 to 50 nm shows decrease of supersaturation of vapors although the deposition time was increased from 20 to 30 minutes. An optimization in the diameter of ZnO/ethanol NWs about 200 nm depicts that deposition time ranged from 15 to 25 minutes is a crucial parameter in preparing ZnO NWs with greater diameter using the established deposition system. The kinetics of reactions during VPT of ethanol vapor assisted with thermal evaporation of Zn under hotwire which leads to formation of ZnO/ethanol NWs is complex and may involves other interdependent variables like temperature and deposition pressure.

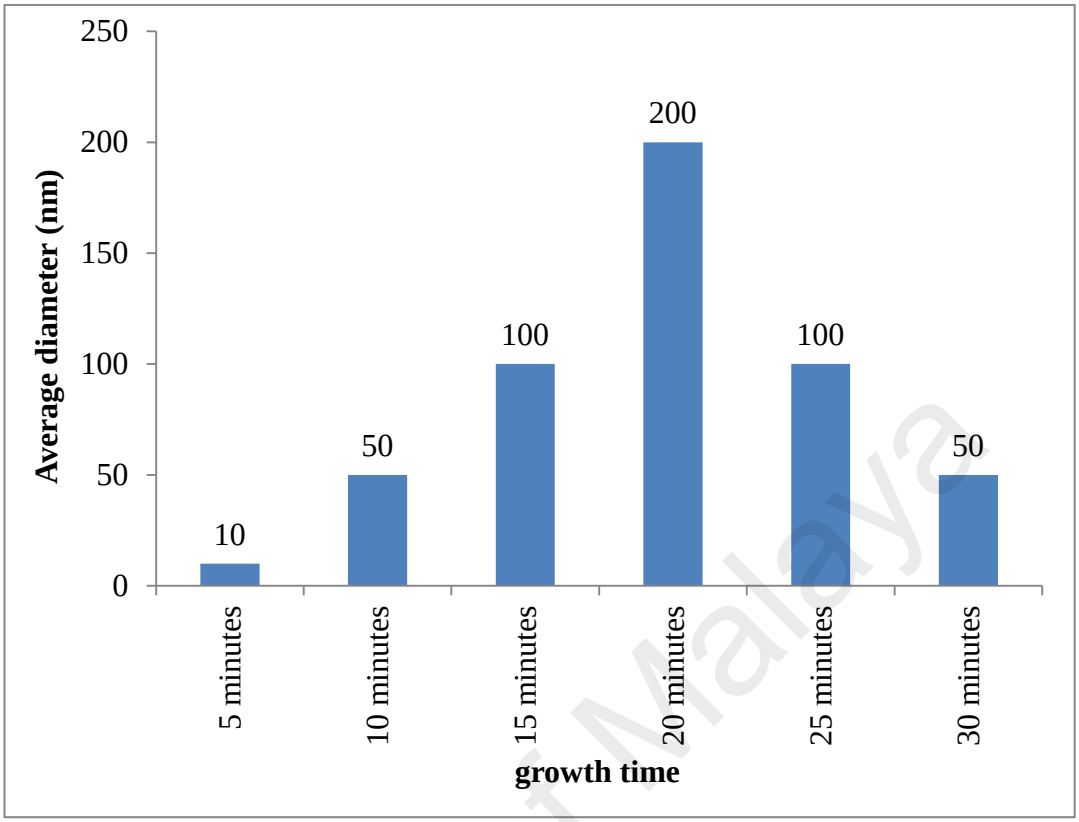

Figure 5.47: Distributions of average diameter of ZnO NWs relative to the growth time.

5.5.2 XRD: ZnO/ethanol

Significant changes have been observed in the XRD profile ZnO/ethanol NWs as in Figure 5.48. The diffracted peaks attribute the polycrystalline nature of ZnO which can be indexed to the hexagonal wurtzite type ZnO (JCP2.2CA: 00-036-1451). The prevalence of the peak corresponds to (100) and (101) directions points to a preferential deposition time of 5, 10, 15, 20, 25 and 30 minutes compared to (002) direction. This may be due to the fact that there are no enough energized particles from ethanol to promote growth of ZnO/ethanol NWs in the direction of (002).

Introduction of ethanol as source of oxygen has imparted growth direction in <101>. Increase in the intensity is also noticeable as the growth time was increased from 5 to 30 minutes. ZnO/ethanol NSs grown on Si were oriented in the <100> and <101> direction because both the planes of ZnO have the higher surface energy due to

surface termination with Zn. The orientation can also be determined by surface diffusion which promotes both c-axis and a-axis orientation. It is widely recognised that during the lower deposition time interaction between the Si substrate and particles arriving on Si play an important role in nucleation. Formation of initial Zn layer covering the Si and continuous condensation of oxygen source particles from ethanol determines the specific direction of ZnO NWs. Earlier we have explained that use of methanol slowly imparts growth direction into <002> direction as the deposition time was increased from 5 to 30 minutes. But presence of ethanol as source of oxygen has promoted growth in <101> direction. This shows that presence of higher percentage of C per molecule has formed hexagonal shaped ZnO in <101> direction.

Based on the preferred growth direction (101) with the increased deposition time, crystallite size (*D*) of ZnO is calculated using Scherer formula (Chen et al., 2006). The peak center of (101) from Gaussian deconvoluted shows slight shift to the left compare to the standard peak center 2Θ of 36.253 of bulk ZnO as in Table 5.6. This indicates distribution of tensile stress in ZnO/ethanol NWs due to higher d spacing compared to the bulk ZnO. The calculated average crystalline size using the Debye-Scherer formula found to be higher at deposition time ranged from 20 to 30 minutes. This agrees with the increased diameter of ZnO/ethanol NWs at the same range. Optimum deposition time range of 20 – 25 minutes is found to be a suitable parameter in this self-established deposition chamber. As a result, the ZnO/ethanol NWs growth direction is mostly along [0001], in accordance with the crystallographic habits of ZnO. The growth kinetics of ethanol source can be dramatically different from methanol source. The mobility of particles is high enough to smooth up the high energy side faces and diffuse to lower-energy front faces. As the ZnO (0001) faces are the highest energy low index planes, a fast growth in [0001] is thermodynamically favoured over in <1120> and <0110>.

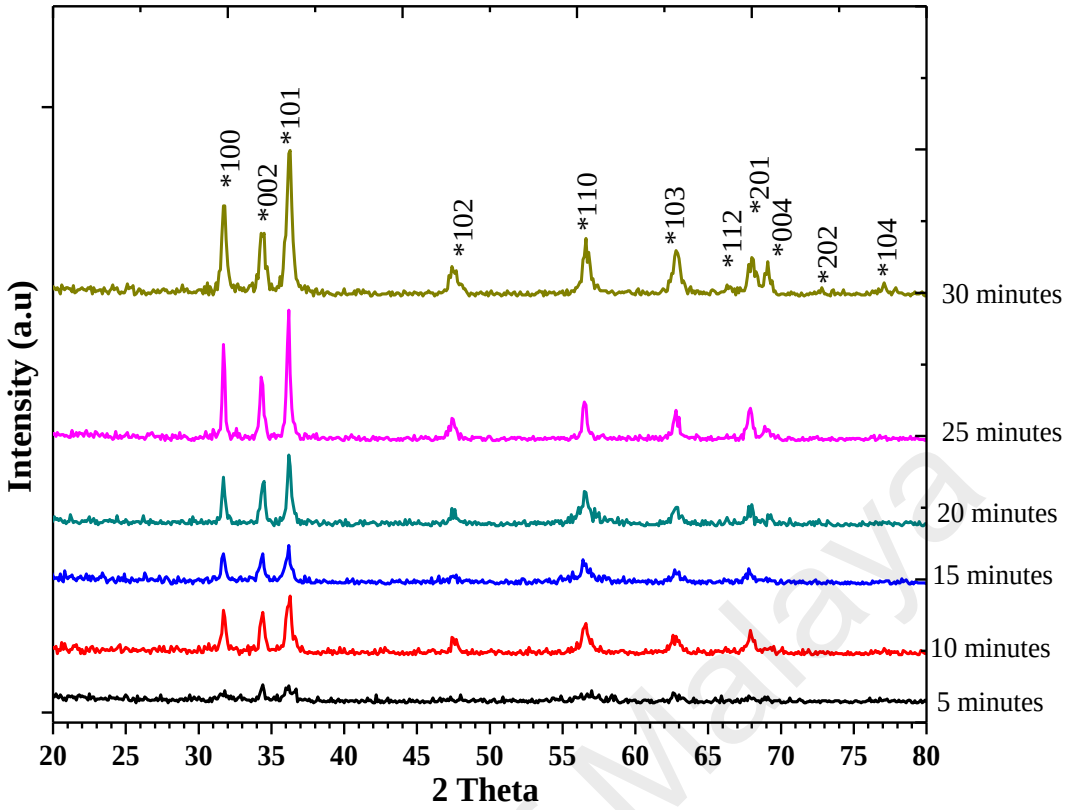

Figure 5.48: XRD spectra of growth time-dependent for ZnO/ethanol NWs prepared in Ar flow.

Table 5.6: Details of ZnO/ethanol NWs deposited at growth time of 5, 10, 15, 20, 25 and 30 minutes.

Deposition time (minutes)	Peak center (2θ) (101)	Crystallite size, D (nm)	D spacing (Å) (101)
5	-	-	-
10	36.210	18.7	2.4779
15	36.154	16.8	2.4815
20	36.229	27.2	2.4765
25	36.178	30.6	2.4799
30	36.234	19.6	2.4762

5.5.3 Photoluminescence: ZnO/ethanol

The respective PL profiles for ZnO/ethanol NWs prepared at various deposition times of 5, 10, 15, 20, 25 and 30 minutes are shown as Figure 5.49. It is generally accepted that the surface states play a crucial role in PL spectra of ZnO nanomaterials (Vanheusden et al., 1996a). Energy transition within the ZnO/ethanol NWs and relationship between material colour and defect structure were determined. The normalised PL showed a low near band-edge (NBE) emission at ~390 nm, deep level (DL) emissions at ~560 nm and near infrared (Rekha et al.) emissions at ~775 nm for all the samples.

Figure 5.49 shows that the PL intensity of the emissions of ZnO/ethanol NWs has increased not consistently as the growth time was increased. This is in contradictory with Figure 5.35 of ZnO/methanol NWs which showed increasing intensity with decreased deposition time. Moreover the intensity of ZnO/methanol NWs is very much higher compared to the of ZnO/ethanol NWs. Significant changes in the morphology and structure of ZnO/ethanol NWs as seen in photomicrographs believed has changed property as well as the emission intensity. The decreased integral intensity of NBE emission indicates changes in the crystallinity of ZnO/ethanol NWs as well as the diameter of the NWs (Huang et al., 2001). This could be due to poor crystallinity of ZnO/ethanol NWs which is apparently in agreement with the XRD profile of ZnO/ethanol NWs. However high crystallinity of ZnO/ethanol is also related to the decrease of impurities and structural defects such as dislocations and V_o (Bagnall et al., 1998). The contribution of the emission peaks obtained from Gaussian deconvolution for NBE, DL and NIR are detailed in Table 5.7. The emission at the NBE, DL and NIR found to be inconsistent for ZnO/ethanol compared to ZnO/methanol.

The peak emissions at NBE as shown in Figure 5.50 are at lower wavelength for the deposition time of 5, 20, 25 and 30 minutes which is ~390 nm whereas for

deposition time of 10 and 15 minutes is ~417 nm. At growth time of 30 minutes, another intense shoulder is noticed at 402 nm. Ethanol which has higher percentage of C and H per molecule shows significant contribution in the PL emission at NBE. Earlier, Banerjee et al. (2004) had explained that contribution of C had reduced the NBE emission and enhanced the DL green emission in his studies. But based on our findings, we believed that contribution of C was overtaken by H atoms from ethanol. Thus, NBE emission has increased for the increased deposition time that indicates rapid recombination of charge carriers in the defect energy states. The dominant contribution of H atoms of ethanol also has reduced the V_o. This is due to lower intense NBE of ZnO/ethanol compared to ZnO/methanol. Banerjee et al. (2004) had explained that UV peak emission intensity for ZnO NWs has been detected in H_2 annealed sample. The NBE also gives rise to the intensity of DL emission. Blue region around 460 nm (2.70 eV) and violet region 446 nm (2.78 eV) found to be emitted by direct transition and recombination of carriers from the conduction band to the radiative center V_{Zn} and from radiative center Zn_i to valence band. According to Look et al. (2005) they can be linked to the presence of complexes of Zn_i where it is noticed to be increasing as the deposition time was increased to 15, 20, 25 and 30 minutes which are contradicting to ZnO/methanol NWs.

The dependence of this DL emission on the growth times was also analysed to investigate the defect structure in ZnO/ethanol NWs. Some researchers had suggested that the broad DL green emissions can be related to V_o and V_{zn}^{2-}. V_{zn}^{2-} has the lowest formation energy in O-rich conditions as the growth time was increased to 25 and 30 minutes. DL green emission is not observable for ZnO/ethanol NWs of 5, 10, 15 and 20 minutes of deposition time. We believed that the ethanol environment provided excess of oxygen for reactions as well as the methanol. Thus, V_{zn}^{2-} is the most energetically favourable and stable defects to form in the ZnO nanorods at deposition time of 25 and

30 minutes. Zhang et al. (2001) and Patterson (2006) have proved that V_o is an unlikely contributor to green emission compared to V_{zn}^{2-} based on the electron transition state. Halliburton et al. (2005) also have shown that DL green emission is due to shallow donors or conduction band electrons.

It is extensively been reported that broad deep band emission from 420 – 750 nm is a defect related emission and it is a superposition of different defect bands emitting in different wavelengths (Børseth et al., 2006; Klason et al., 2008; Özgür et al., 2005). Broad shoulder centered at 572 and 564 nm for ZnO/ethanol NWs of 5 and 20 minutes indicates emissions of yellowish-green band that can be related to H^+ defects due to the use of ethanol as a source of oxygen. The presence of extra two H atoms that covalently bonded to C atoms in ethanol has shifted the emission peak to higher wavelength. This shows H defects plays an important role in determining the PL emission peaks. For time dependence growth of 25 and 30 minutes attributed green emission band around relatively 548 and 550 nm that can also be related to H^+ defects. However, the ZnO/ethanol NWs prepared at deposition time of 10 and 15 minutes depicted yellowish-orange emission region at 602 and 597 nm. This was due to the diminished H defects and an increase of excess oxygen during the deposition.

Figure 5.51 shows red emission band ~780 nm was noticed in all samples except in ZnO/ethanol NWs prepared at deposition time of 10 minutes which exhibits higher wavelength at 816 nm. This could be due to incorporation of excess O and C with ZnO at lower deposition time of 10 minutes. ZnO/ethanol NWs of 20 and 25 minutes shows dominant Si PL peak at around 1060 nm (1.17 eV) which indicates penetration of He-Cd 325 nm laser light to the surface of Si substrate (An et al., 2004).

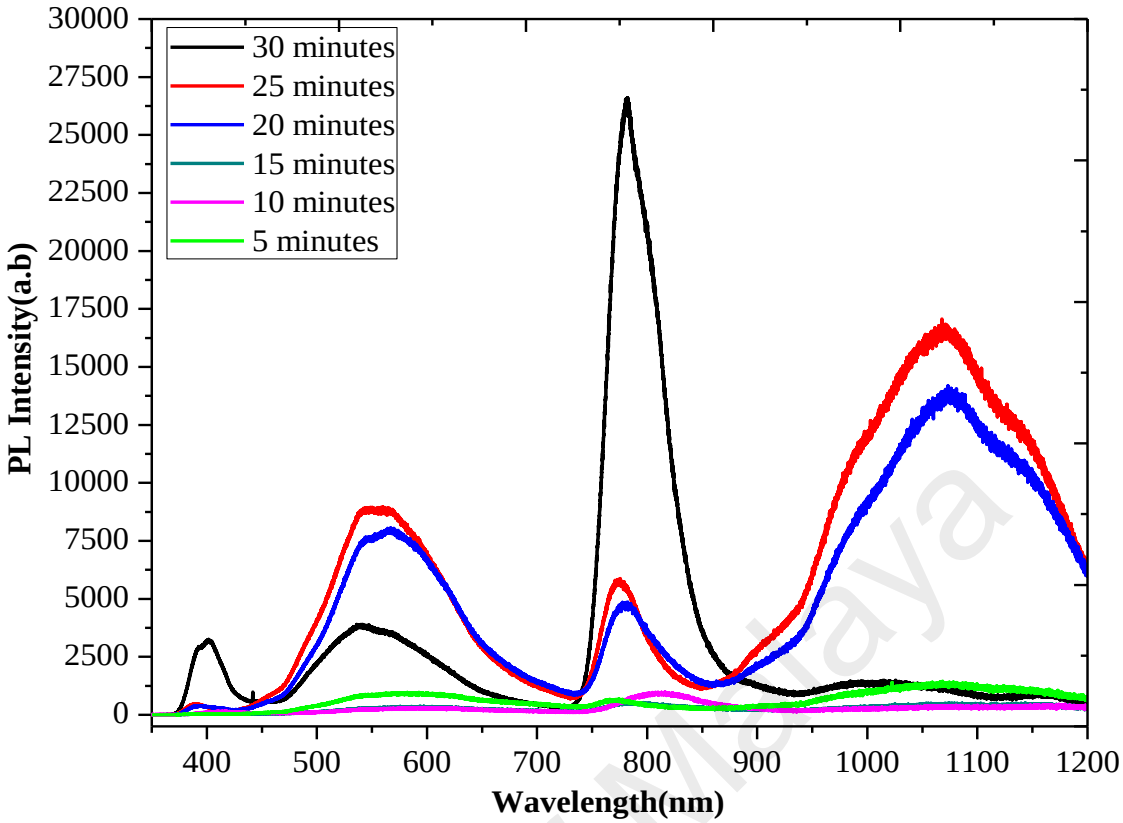

Figure 5.49: Photoluminescence spectra of ZnO/ethanol NWs prepared at various deposition time of 5, 10, 15, 20, 25 and 30 minutes.

Table 5.7: Details of photoluminescence peaks of ZnO/ethanol NWs at NBE, DL and NIR emissions obtained from Gaussian fits.

Deposition time (minutes)	NBE		DL		NIR	
	Peak position	Energy (eV)	Peak position	Energy (eV)	Peak position	Energy (eV)
5 minutes	389 nm	3.19	572 nm	2.16	774 nm	1.60
10 minutes	417 nm	2.97	602 nm	2.06	816 nm	1.51
15 minutes	416 nm	2.97	597 nm	2.07	783 nm	1.58
20 minutes	391 nm	3.17	564 nm	2.20	777 nm	1.60
25 minutes	390 nm	3.18	548 nm	2.26	775 nm	1.60
30 minutes	402 nm	3.08	550 nm	2.25	781 nm	1.59

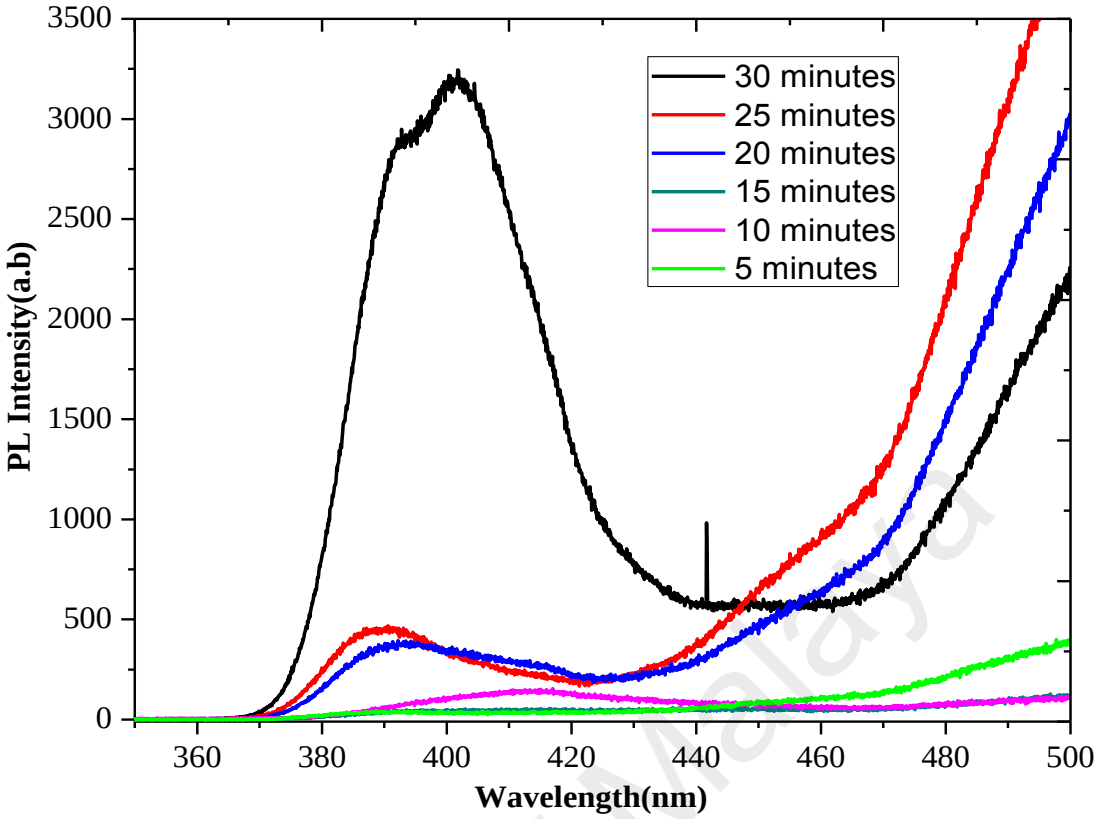

Figure 5.50: Photoluminescence spectra of ZnO/ethanol NWs enlarged at range 350 – 500 nm.

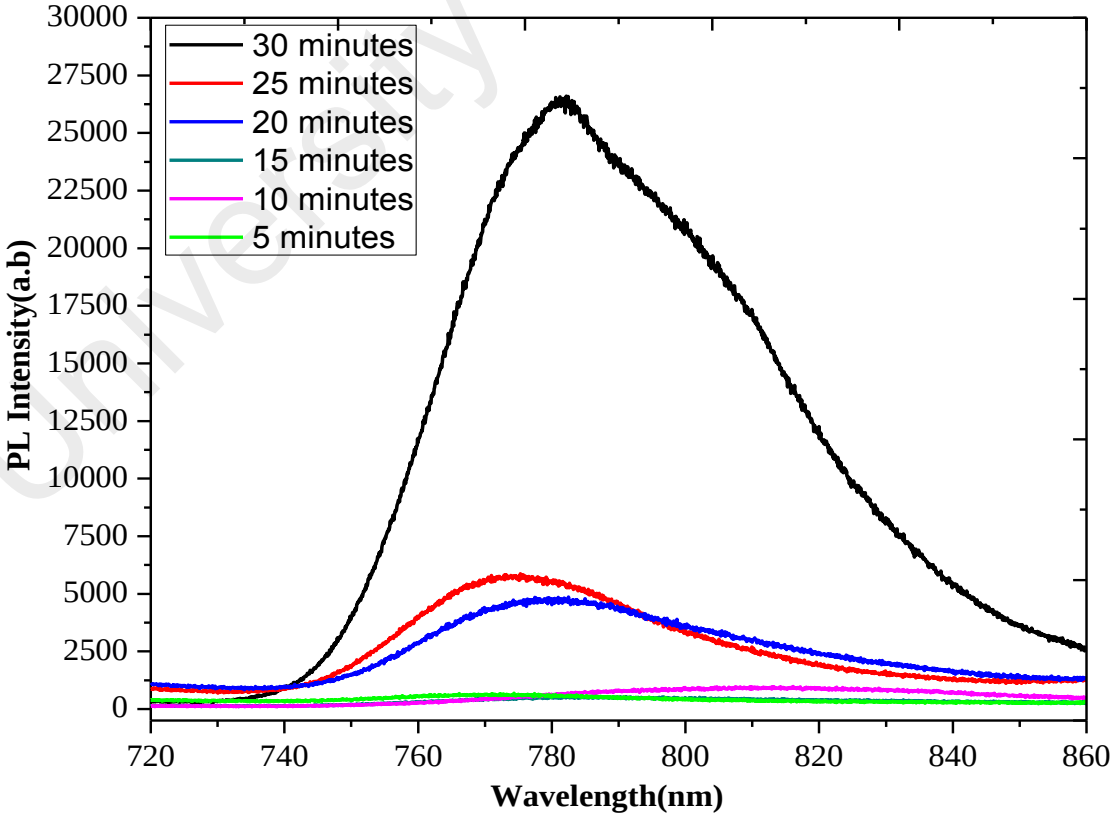

Figure 5.51: Photoluminescence spectra of ZnO/ethanol NWs enlarged at range 720 – 860 nm.

5.5.4 Raman scattering: ZnO/ethanol

The Raman scattering results of ZnO/ethanol NWs which were prepared in the ethanol with Ar flow through two-sided hollow CuZn alloy for the respective time dependence growth of 5, 10, 15, 20, 25 and 30 minutes are displayed as Figure 5.52, 5.53, 5.54, 5.55, 5.56 and 5.57. The ZnO/ethanol NWs prepared at 30 minutes did not show profound peaks as distributed in other samples (time dependence growth of 5, 10, 15, 20 and 25 minutes) as of the intensity of the peaks found to be much lower in ZnO/ethanol 30 minutes. High intensity of the TO peak at 521 cm^{-1} and the two phonon 2TO mode at around 960 cm^{-1} can be detected, as well as a peak at 303 cm^{-1}, which is the two phonon 2TA mode for Si (Quiroga-González et al., 2014) as in Figure 5.52 for growth time of 5 minutes. However these three peaks of Si are traced to be diminished to a very low intensity as the deposition time was increased. This was due to an increased in the thickness and density of the ZnO/ethanol NWs on the Si substrate as the deposition period increased.

All the ZnO/ethanol NWs of 5, 10, 15, 20 and 25 minutes of deposition time prevailed two dominant peaks at around 407 and 575 cm^{-1} except ZnO/ethanol NWs of 30 minutes. However, peak at 407 cm^{-1} which can be attributed to E_1(TO) mode was not detected in the ZnO/methanol samples of Figure 5.38 – 5.40, whereas the A_1(LO) mode of 575 cm^{-1} cannot be precluded for ZnO/methanol samples due to disorder-induced enhancement of their intensities in that sample. The peaks 407 and 575 cm^{-1} which are A_1 and E_1 phonons are known as oxygen-dominated polar modes. The Zn and O atoms in the ZnO hexagonal structure move parallel or perpendicular to the c axis respectively for the A_1 and E_1 symmetry.

Adding to that, peak at 545, 531, 534, 535 and 545 cm^{-1} is also identical in all samples of ZnO/ethanol NWs for the respective deposition time of 10, 15, 20, 25 and 30 minutes. They can be assigned to A_1 symmetry and attributed to $2B_1^{low}$ and 2LA

overtones along L, M and H. In ZnO/ethanol NWs of 5 minutes it is not detectable due to detection of high intensity of Si peak at 521 cm^{-1} which override the intensity of peak around 545 cm^{-1}. ZnO/ethanol NWs has resulted an enhanced intensity of $2B_1^{low}$ and 2LA overtones along L, M and H compared to ZnO/methanol NWs. According to Frohlich scattering, dependence of the intensity around 541 and 575 cm^{-1} in the range from 520 – 600 cm^{-1} can be assigned to ion implantation in ZnO. Thus, we may predict that higher percentage of C from ethanol has decorated ZnO/ethanol NWs compared to ZnO/methanol. Besides that E_1(LO) with low intensity at around 585 cm^{-1} is also detectable only in ZnO/ethanol deposited at growth time of 10, 15 and 30 minutes compared to ZnO/methanol NWs. This peak can be related to local vibration modes associated with intrinsic lattice defects in ZnO/ethanol NWs, similar to peak which has been observed by Hasuike et al. (2004) and Kaschner et al. (2002) in their doped ZnO sample. Bundesmann et al. (2003) said that similar peak at 585 cm^{-1} has been related to intrinsic defects that were favoured or activated by doping effects.

Another dominant peak around 407 cm^{-1} of E_1(TO) mode clearly indicates growth of polycrystalline structures of ZnO/ethanol NWs on Si substrate (Sreenivas et al., 2005). The intensity was found to increase as the deposition time was increased from 5 to 25 minutes except for ZnO/ethanol of 30 minutes. This is merely due to low density growth, which randomly distributed on the Si substrate as notice in the FESEM (Figure 5.46) compared to other photomicrographs. The absence of E_1(TO) mode in the ZnO/methanol NWs as noticed in Figure 5.38 – 5.25 depicts that growth of aligned c-axis oriented structures of ZnO/methanol compared to ZnO/ethanol NWs. In 1969 Arguello et al. (1969) have reported that ZnO nanocolumns that have been deposited on Si substrate at temperature more than 400 °C using the pulse laser deposition technique showed absence of E_1(TO) mode. In contrast it was observed in this work that the present technique has enhanced the presence of E_1(TO) mode in ZnO/ethanol for Si

temperatures up to 800 °C but both E_1(TO) and E_1(LO) modes were not noticed in ZnO/methanol NWs.

Two peaks at around 72 and 86 cm^{-1} which has been noticed in ZnO/methanol NWs samples also noticeable in the Raman scattering spectrum of ZnO/ethanol NWs. E_2^{low} mode found to be split up into 86 and 107 cm^{-1} in ZnO/ethanol NWs. Peak 86 cm^{-1} noticed to be diminished whereas 107 cm^{-1} showed an enhanced intensity with increasing deposition time compared to ZnO/methanol NWs. This similar peak has been reported by a group of scientist from Germany in ZnO NWs decorated with MWCNT (Khanderi et al., 2009). So, the peaks can be assigned to incorporation of C atoms from methanol and ethanol onto ZnO NWs (Khanderi et al., 2009). The $E_2^{high} – E_2^{low}$ mode at around 330 cm^{-1} frequency is only detectable for growth time of 25 and 30 minutes. It was an obvious broad peak in ZnO/methanol NWs compared to ZnO/ethanol Nws. However, all these peaks can be associated with Zn sublattice (Ashkenov et al., 2003; Scott, 1970). The A_1(TO) mode is only traceable in ZnO/ethanol NWs of 10 minutes at 375 cm^{-1} frequency.

Above 600 cm^{-1} acoustic and optical combination frequencies were observed. The peaks at 612, 626, 624 and 610 for ZnO/ethanol NWs of 5, 10, 25 and 30 minutes of growth time could be tentatively assigned to TA+TO at the H and M points. Rise of doublet in the range of 657 – 666 cm^{-1} were observed due to TA+LO combinations (Calleja & Cardona, 1977). The lower frequency component of the doublet which is assigned to E_1 and E_2 symmetry is only noticeable for ZnO/ethanol of 5 and 25 minutes growth time whereas the symmetry of the higher component which is A_1 is traceable in ZnO/ethanol of 5 and 10 minutes at 677 and 662 cm^{-1}. ZnO/ethanol NWs prepared in growth time dependence of 15, 20 and 30 minutes did not show any corresponding peaks of TA+TO and TA+LO in the range from 600 – 670 cm^{-1}.

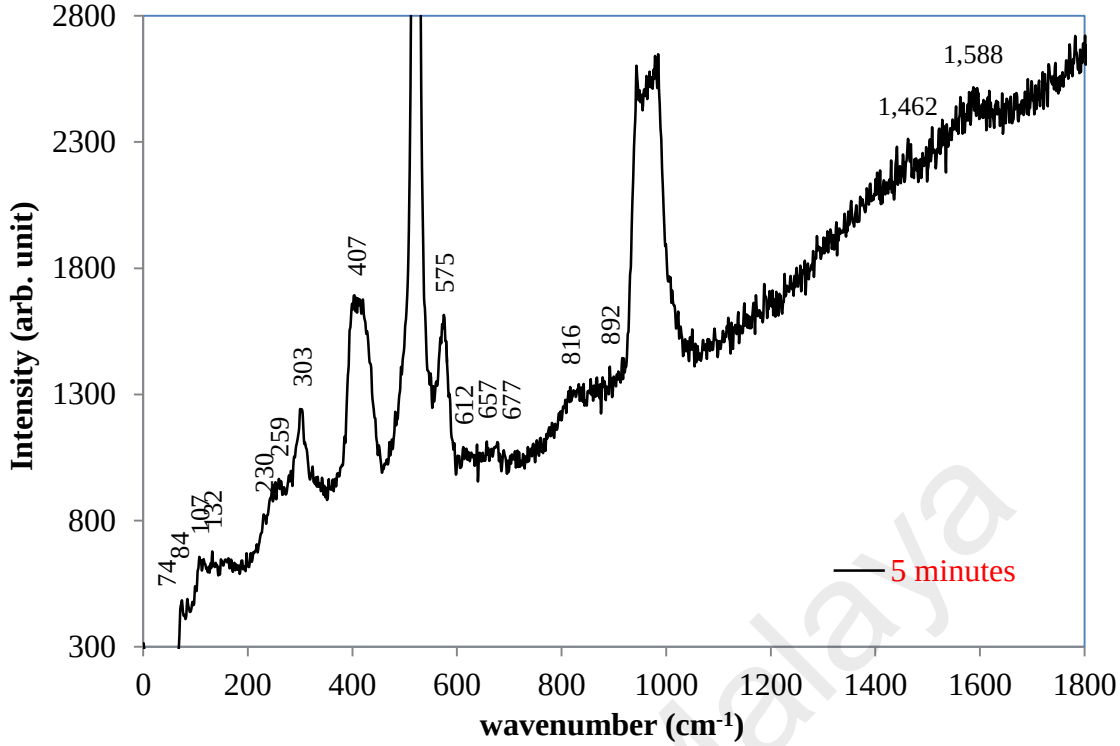

Figure 5.52: Raman scattering of ZnO/ethanol NWs prepared at growth time of 5 minutes.

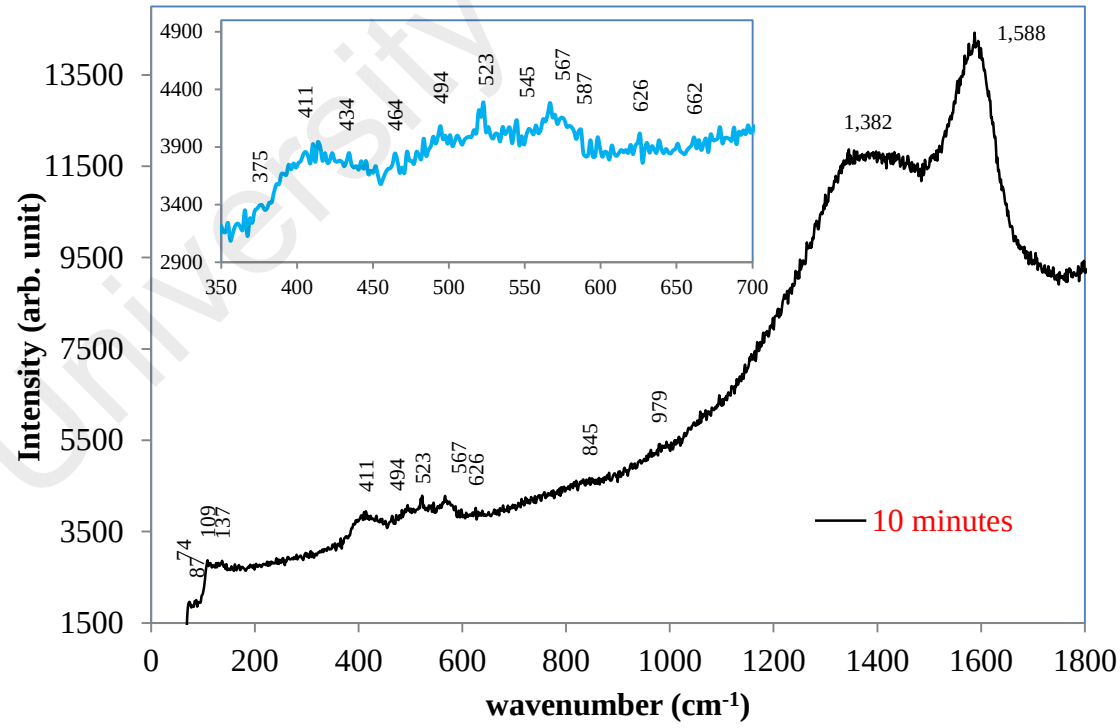

Figure 5.53: Raman scattering of ZnO/ethanol NWs prepared at growth time of 10 minutes.

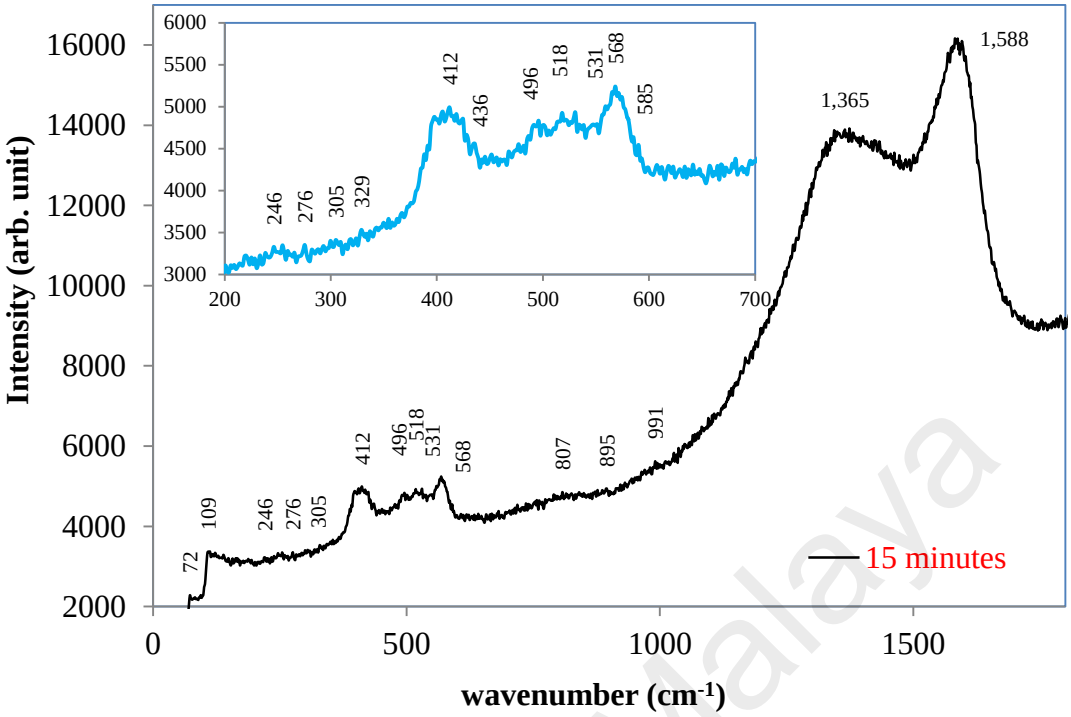

Figure 5.54: Raman scattering of ZnO/ethanol NWs prepared at growth time of 15 minutes.

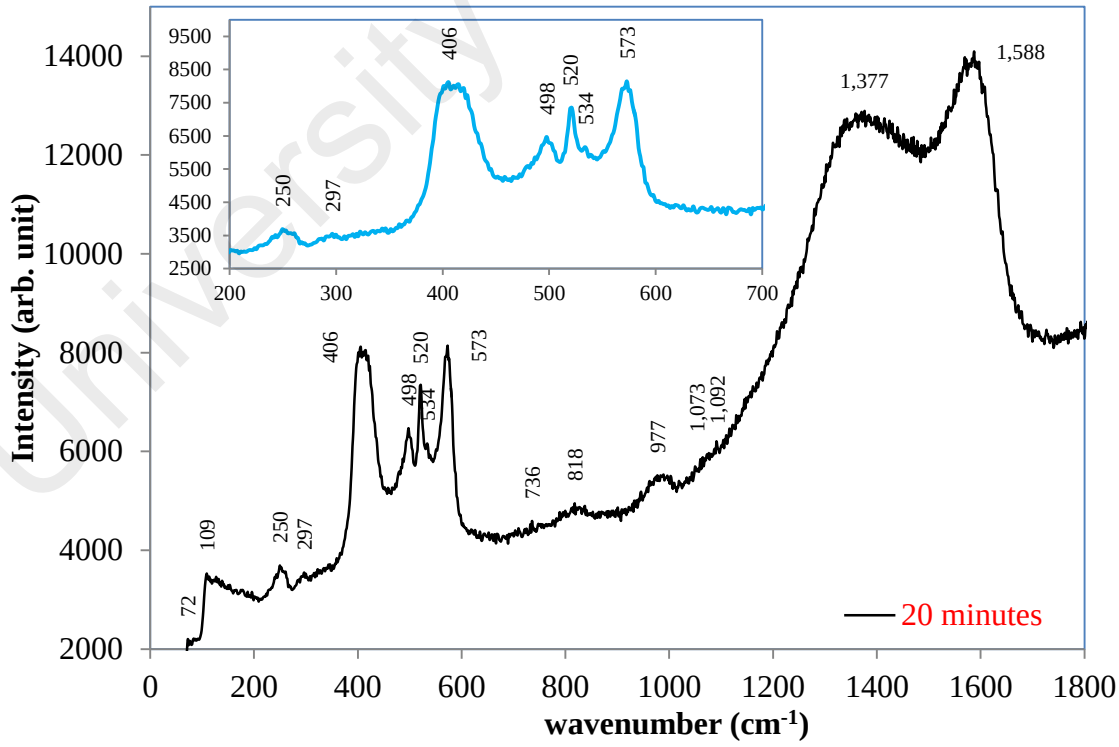

Figure 5.55: Raman scattering of ZnO/ethanol NWs prepared at growth time of 20 minutes.

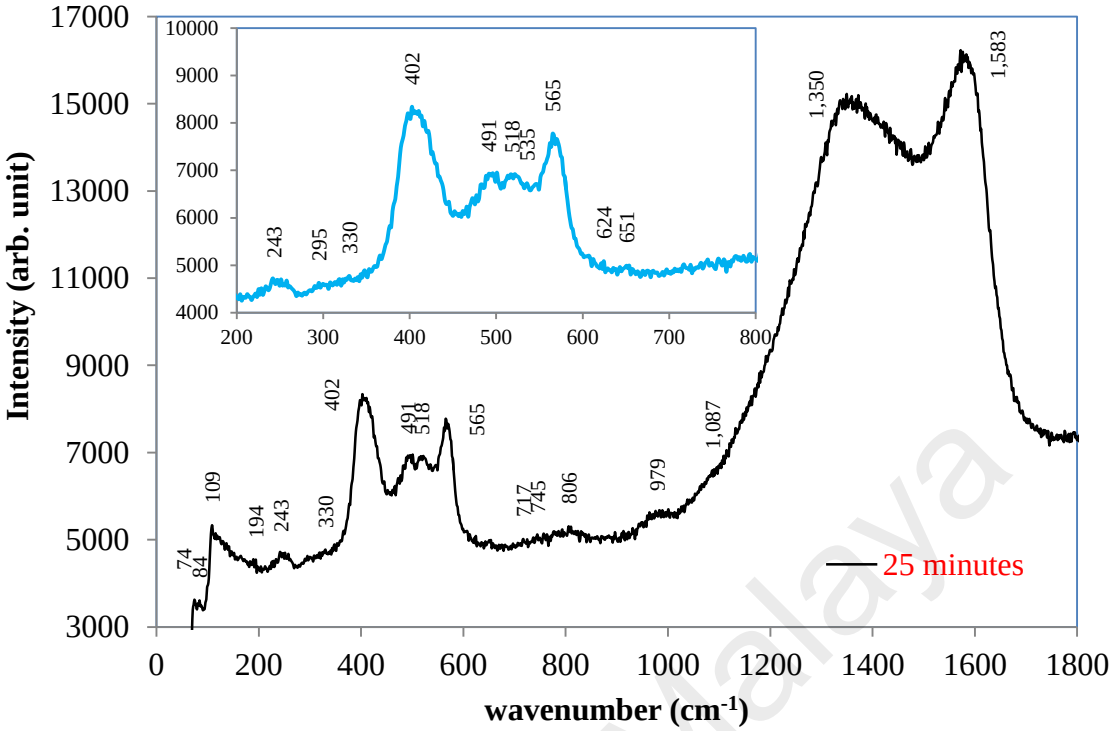

Figure 5.56: Raman scattering of ZnO/ethanol NWs prepared at growth time of 25 minutes.

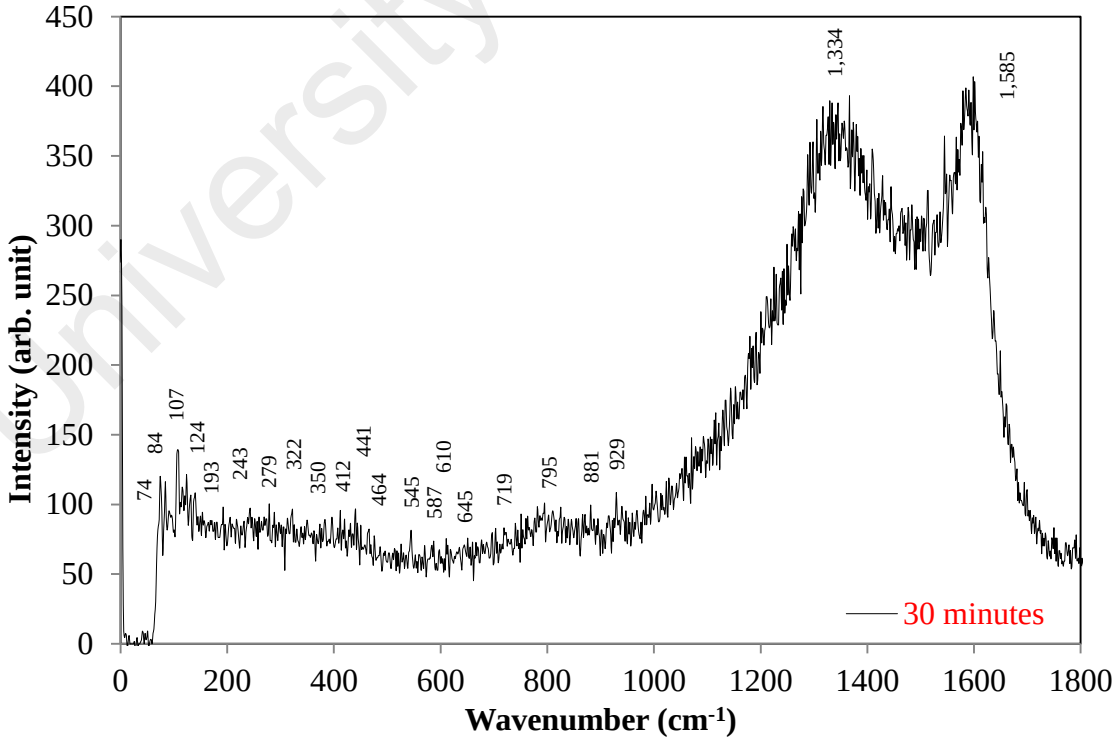

Figure 5.57: Raman scattering of ZnO/ethanol NWs prepared at growth time of 30 minutes.

Low intensity modes which were not detected in the ZnO/methanol NWs samples mainly the A_1 symmetry of LA+TO and LA+LO were detected in ZnO/ethanol NWs prepared at growth time of 20, 25 and 30 minutes. They can tentatively be assigned to acoustic and optical combinations in the range from 700 – 820 cm^{-1} (Cuscó et al., 2007). Peak at 818, 806 and 795 cm^{-1} frequency of 20, 25 and 30 minutes of growth time were at L and M points. It is noteworthy that, the second order peaks to be appeared as the deposition time is increased. A weak broad band with peak centred at 977 and 979 cm^{-1} is only observable in ZnO/ethanol NWs of 20 and 25 minutes as in ZnO/methanol NWs of 30 minutes. These peaks can be attributed to TO overtones.

A weak shoulder at 1073 cm^{-1} and very low intense peak at 1092 cm^{-1} is noticeable in ZnO/ethanol NWs deposited for 20 minutes (Figure 5.55). However the ZnO/methanol NWs as in Figure 5.38 – 5.40 has exhibited the 2LO mode for increasing growth time compared to ZnO/ethanol NWs. Mode at 1073 cm^{-1} can be attributed to TO+LO combinations at the L and M lines whereas the 1092 cm^{-1} to 2LO mode at H and K lines. The ZnO/ethanol NWs of 25 minutes only exhibited TO+LO mode at 1087 cm^{-1} which is less broad compared to that of ZnO/ethanol of 20 minutes. All the ZnO/ethanol NWs show first order Raman absorptions for disordered D and G band as in Figure 5.52 – 5.57.

ZnO/ethanol NWs of 5 minutes only exhibits low intensity of G peak at 1588 cm^{-1} meanwhile the other samples deposited at growth time of 10, 15, 20, 25 and 30 minutes shows broaden D and G band. The D band found to be broader compared to the G band. The respective D and G band is noticeable at around 1382 and 1588 cm^{-1}. The broader D band centered around 1382 cm^{-1} for ZnO/ethanol NWs of 10, 15, 20 and 25 minutes found to be shifted to 1334 cm^{-1} in ZnO/ethanol NWs of 30 minutes. Nevertheless, the increased growth time attributed increased intensity ratio of D band to G band. This attributes incorporation of C onto ZnO/ethanol NWs. Use of ethanol has

decorated the ZnO NWs due to it higher percentage of C per molecule compared to methanol that shows possible functionalization on the surface of ZnO/ethanol NWs.

5.5.5 Conclusion

ZnO/ethanol NWs were successfully synthesized in the home made system in laboratory. Use of ethanol as source of O has produced ZnO/ethanol NWs with greater diameter and hexagonal wurtzite structure whereas ZnO/methanol NWs were nanoneedles as the deposition period increased to 30 minutes. Methanol and ethanol has contributed in producing polycrystalline ZnO NWs. ZnO/methanol NWs were grown preferentially in c-axis <002> direction compared to <101> direction for ZnO/ethanol NWs. Highly crystalline ZnO with decreased impurities and structural defects such as dislocations and V_o were produced by methanol compared to ethanol. Shift of DL emission peak from 541 to 572 nm profoundly showed ethanol has created more H defects in the ZnO compared to methanol. Moreover an unlikely emission at 816 nm from ZnO/ethanol NWs is related to possible functionalization on ZnO NWs due to excess C from ethanol. Additional to that identification of Raman peaks at 407 and 565 cm^{-1} clearly indicates the E_1(TO) and A_1(LO) mode of ZnO NWs. Besides that, prevailing first order Raman absorptions for disordered D and G band in ZnO/ethanol NWs compared to ZnO/methanol NWs shows functionalization on ZnO/ethanol NWs.

5.6 Doping in ZnO

The experimental setup as per detailed in section 3.6.3 was utilized in preparing doped ZnO NWs in methanol with Ar flow through two-sided hollow CuZn alloy. In order to obtain a doped ZnO NWs, aluminium nitrate ($Al(NO_3)_3$) and manganese oxide (MnO_2) substance were used as source of Al and Mn. They were diluted separately in the prepared mixture of methanol and acetone solution. Ar was flowed at constant rate of 100 sccm into the two-sided hollow CuZn alloy rod for growth time of 30 minutes. The Al and Mn doped ZnO NWs were identified as ZnO:Al NWs and ZnO:Mn NWs respectively to ease the discussion.

5.6.1 FESEM

5.6.1.1 FESEM of Mn-doped ZnO NSs

Figure 5.58 shows the photomicrograph image of ZnO:Mn NSs prepared at Mn wt. % of 1.82 in methanol with Ar flow through two-sided hollow CuZn. The Mn-doped ZnO NSs are randomly grown as nanocapsules (NCs) and NWs on Si substrate. The NWs found to be grown from the end structure of the NCs. The sizes of NCs are in similar sizes with average length and diameter were measured to around 1000 and 100 nm respectively. The diameter of the NW was measured at 50 nm as observed in the inserted magnified Figure 5.58.

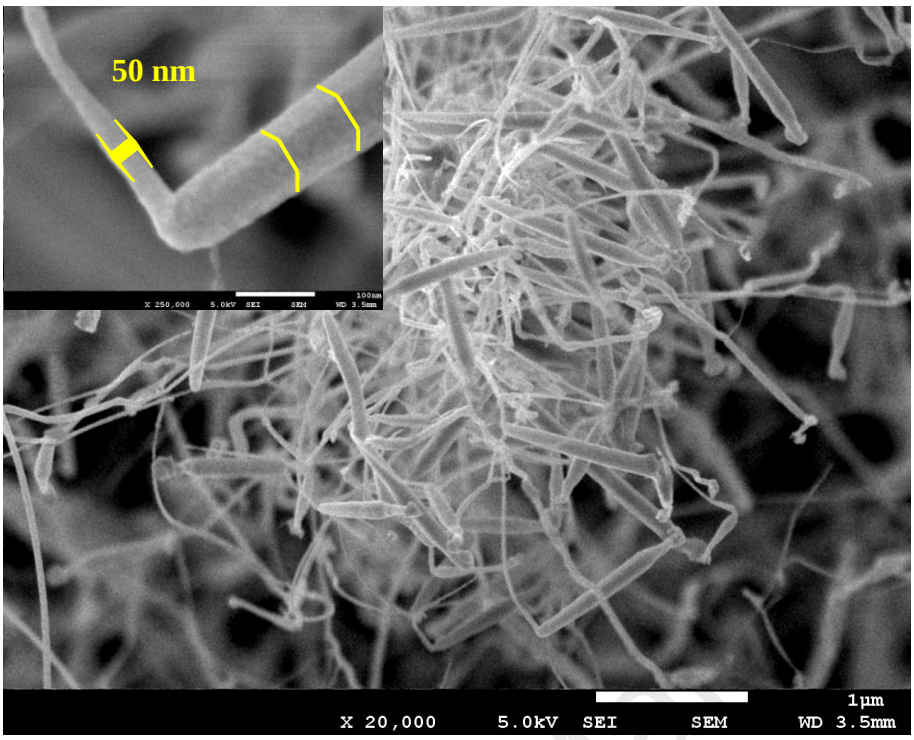

Figure 5.58: FESEM images of ZnO:Mn NSs prepared at Mn concentration 1.82 wt. % in the methanol with Ar flow.

5.6.1.2 FESEM of Al-doped ZnO NSs

Figure 5.59, 5.60 and 5.61 show the FESEM images for ZnO:Al NSs of 0.73, 1.28 and 1.82 wt. %. Significant changes were found on the surface of ZnO:Al compared to pure ZnO NSs. Growth like button-mushroom is observable in all ZnO:Al NSs whereas nanoneedle structure with ZnO nanoflakes in the pure ZnO NSs. In our earlier report, the time dependence growth of pure ZnO NSs showed growth from button-mushroom for growth time of 5 and 10 minutes to nanoneedle structures for growth time of 30 minutes. This is in contrary to all the ZnO:Al which were found to be remained as button-mushroom structure for the growth time of 30 minutes. In addition, uncommon features in the images of Al-doped samples are in comparable with the pure ZnO NSs. The effect of Al incorporation is noticeable on the wall of Al-doped ZnO sample as in the inserted magnified images of Figure 5.59, 5.60 and 5.61. The inserted photomicrographs of ZnO:Al NSs shows diameter in descending order about 450, 400 and 300 nm with increasing Al wt. %. These diameters values are almost 4 times

greater than that of pure ZnO NSs. Formation of tiny bumps is observable on the wall of ZnO:Al 0.73 wt. % whereas ZnO:Al 1.28 wt. % shows few rows of grooves and protuberance grown on the stem of the button-mushroom like ZnO:Al NSs. The effects of Al on the wall of ZnO NSs found to be obvious as the Al wt. % was increased to 1.82 as in Figure 5.61. This could be due to doping effect in ZnO NSs.

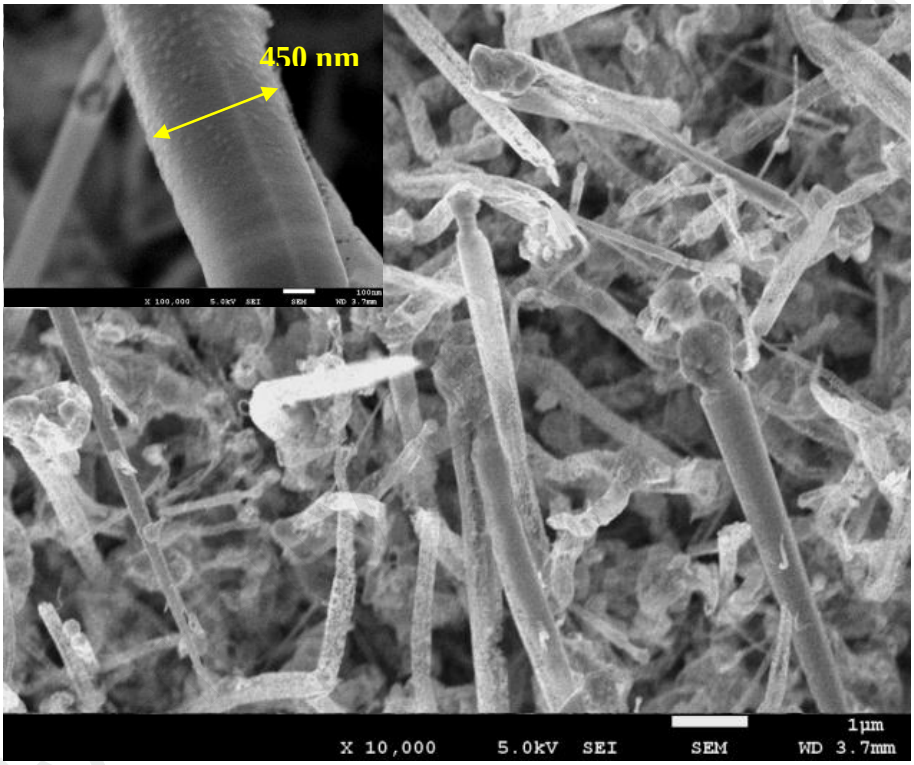

Figure 5.59: FESEM image of ZnO:Al NSs prepared at Al concentration of 0.73 wt. % in the methanol with Ar flow.

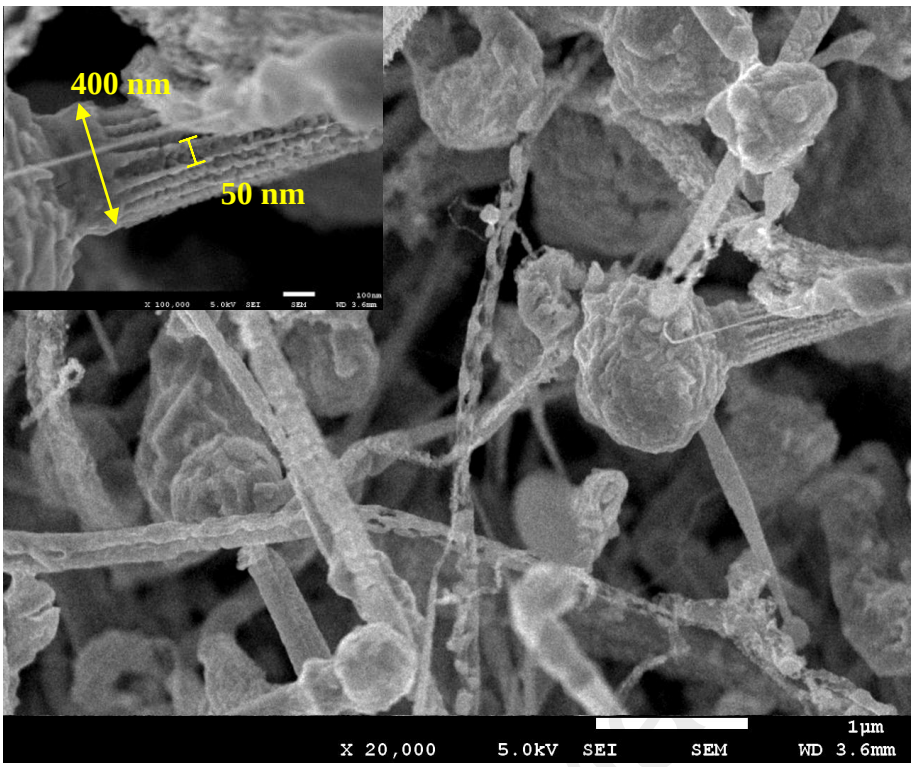

Figure 5.60: FESEM image of ZnO:Al NWs prepared at Al concentration 1.28 wt. % in the methanol with Ar flow.

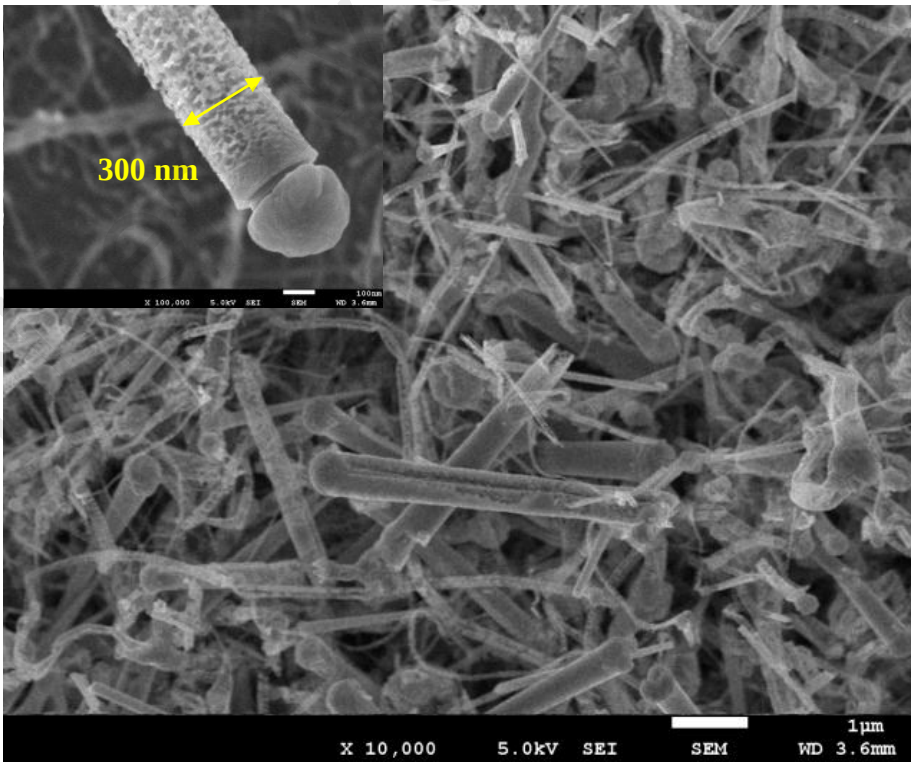

Figure 5.61: FESEM image of ZnO:Al NWs prepared at Al concentration 1.82 wt. % in the methanol with Ar flow.

5.6.2 XRD

5.6.2.1 XRD of Mn-doped ZnO NSs

Figure 5.62 show XRD spectrum of (a) pure and (b) Mn doped ZnO NSs obtained via two-sided hollow CuZn alloy rod. Spectrum (b) shows significant changes in the crystallographic structure compared to the pure ZnO. Spectrum (a) is indexed with a JCP2.2CA: 00-036-1451 that corresponds to the hexagonal wurtzite crystal structure of ZnO. On the other hand additional peaks and broaden peaks in spectrum (b) are related to the un-limitation of this technique in detecting the intrinsic defect due to Mn doping into the lattice of ZnO.

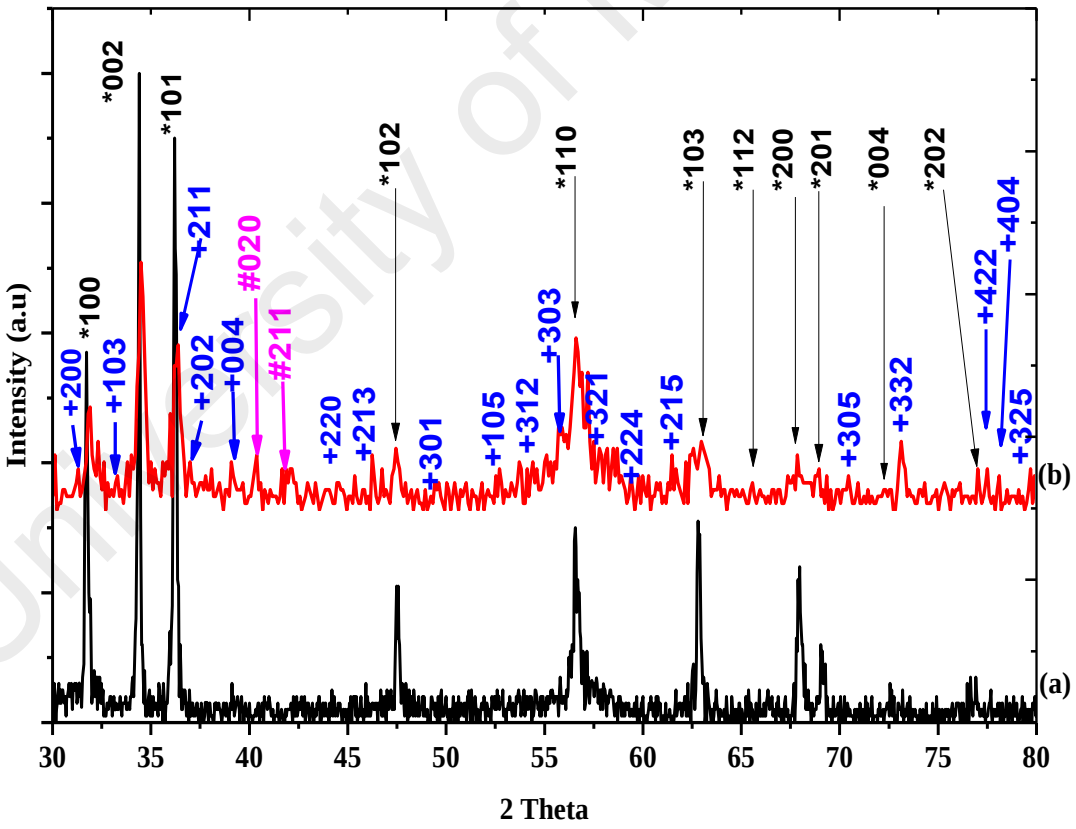

Figure 5.62: XRD spectra of (a) pure ZnO NWs and (b) Mn-doped ZnO NSs.

The observed peaks in the Mn-doped ZnO can be indexed to wurtizite ZnO and tetragonal $ZnMn_2O_4$ (JCP2.2CA:01-071-2499) diffraction peaks which were identified as (200), (103), (211), (202), (004), (220), (213), (305), (105), (312), (303), (321), (224), (215), (305), (332), (422), (404) and (325) as shown in Figure 5.62. Other two peaks (#020) and (#211) were related to orthorhombic MnO_2 (JCP2.2CA:01-072-1983). The ZnO diffraction peaks in spectrum (b) not shifted as reported by Jinxia Duan *et al.* (2006 and 2012) whereas they were broadened may be due to decrease in the crystallite size (Deka & Joy, 2007; Luo et al., 2005). The calculated average crystallite size was 20 and 67.5 nm for the Mn-doped and pure ZnO. This shows proof of incorporation of Mn ion inside the ZnO crystal lattice.

Nevertheless, the lattice parameter a of Mn-doped ZnO (2.8606 Å) is lower than the pure ZnO which is 3.2511 Å but the lattice parameter c of Mn-doped ZnO is 5.2096 Å is slightly higher than 5.2085 Å of pure ZnO (Rekha et al., 2010). The decrement in lattice parameter *a* and an increment in *c* may correspond to the broadening effect in ZnO peaks as in spectrum (b). This presumably resulted from the substitution of larger ionic radii of Zn^{2+} (88 pm) with manganese ions (Mn^{2+}) of smaller ionic radii (81 pm). Furthermore, indication of this substitution of Mn into the lattice of ZnO is accepted due to the un-limitation of XRD technique providing changes in the profile (Sharma et al., 2012).

5.6.2.2 XRD of Al-doped ZnO NSs

The XRD spectra of ZnO:Al NWs prepared at various concentrations 0.73, 1.28 and 1.82 wt. % of Al were compared with the pure ZnO NWs as displayed in Figure 5.63. All the detectable peaks can be indexed as hexagonal wurtzite ZnO that found as in the standard reference data JCP2.2CA: 00-036-1451. The XRD profile strongly shows various crystalline nature of ZnO:Al NWs compared to the pure ZnO NWs. There are

additional peaks observable in the XRD spectra of Al-doped ZnO NSs which are marked as "+" in Figure 5.63. These peaks can be attributed incorporation of Al^{3+} of ionic radius 53 pm which is smaller than the Zn^{2+} (74 pm) is successfully incorporated into ZnO NSs. However no other impurities but peak splitting is noticeable in the XRD profile. No peaks or secondary phase is observed either from Al or other impurities but peak splitting which is noticeable in the XRD profile.

Significant changes in the intensity and FWHM were noticed from the three main dominant peaks (100), (002) and (101) which could be due to the effect of Al doping into the NSs of ZnO NWs (Zhou et al., 2007). Preferential growth direction changes as the doping concentration of Al was increased. ZnO:Al 0.73 wt. % shows highest (002) diffraction peak intensity. More preferential growth direction at <101> is noticeable at higher Al concentration of 1.82 wt. % compared to the pure ZnO which shows preferential growth direction in <002>. The presence of Al changed the diffusion rate of Zn and O on the Si substrate during deposition. Thus, it alters the energetic balance between (002) and (101) orientations which further lead to weakening of (002) orientation and preferred (101) texture orientation appeared (Liu et al., 2009). The peak intensities of ZnO:Al 0.73 and 1.28 wt. % found to be lower compared to the pure ZnO NWs. This is indicating that Al atom has occupied the position of Zn in the ZnO lattice as a substitutional atom. The effect of Al doping also can be observed as a minute variation in the 2θ values of diffraction peaks of (100), (002) and (101). Table 5.8 shows the detailed Gaussian deconvoluted peaks for the Al-doped ZnO NWs which were compared with the pure ZnO. Peak center of ZnO:Al 0.73 wt.% found to be shifted to the right relative to the pure ZnO NWs. The ZnO:Al 1.28 wt.% shows right shift for (100) and (101) whereas peak (002) found to be shifted to left. Further increased of Al concentration to 1.82 wt. % attributed right shift for (100) and left shift for (002) and (101).

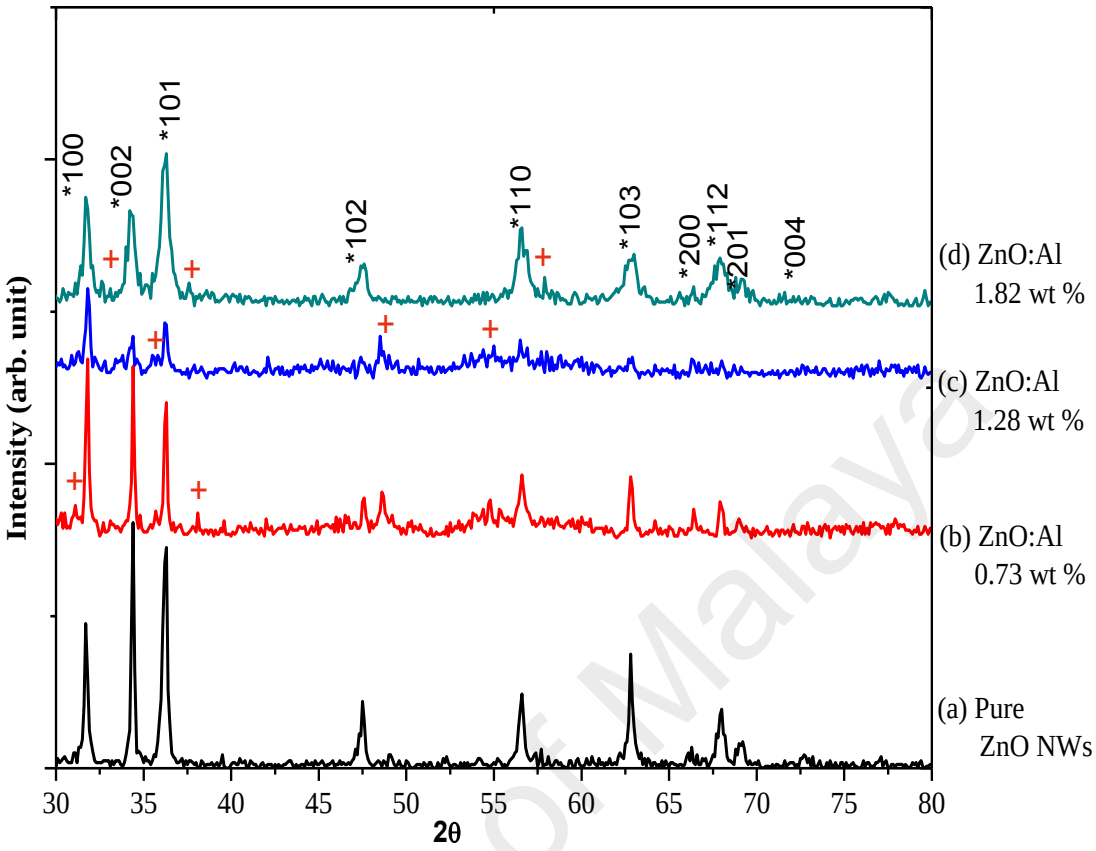

Figure 5.63: XRD spectra of (a) pure ZnO and doped ZnO NWs with Al concentration (b) 0.73, (c) 1.28 and (d) 1.82 wt. %.

The peak shift towards high angle as compared to the standard ZnO XRD pattern, indicating the replacement of larger Zn^{2+} (74 pm) by the smaller Al^{3+} (53 pm) in the lattice and the formation of the smaller Al-doped ZnO lattice (Henley et al., 2004; Jeong et al., 2008). Higher deviation of (100) diffraction peak in Al-doped ZnO 0.73 wt. % compared to 1.28 and 1.82 wt. % attributes high concentration of defects inside the Al-doped ZnO lattice (Zeng et al., 2010). Peak broadening is also noticed to be increased for the increased Al concentration. Although high intensity and narrower peak broadening often related to high crystal quality (Gedamu et al., 2014) as in Al-doped ZnO 0.73 wt. %, identification of noise and peak shift shows that deterioration of cryatal quality in all Al-doped ZnO NSs samples. Greater peak broadening is noticeable

in Al-doped ZnO NSs 1.82 wt. %. This reflects non-uniform strain due to incorporation of Al atom into lattice of ZnO. This also shows that the crystallinity of ZnO NWs has deteriorated as the Al concentration was increased (Wang et al., 2007). Therefore, the deterioration of crystallinity is the evidence for the incorporation of Al^{3+} replacing the greater radii Zn^{2+} into the ZnO NSs lattice.

Table 5.8: Details of Gaussian deconvoluted XRD peaks of pure and Al-doped ZnO. Peak shift is in red.

Sample wt. %	(100)		(002)		(101)	
	Peak center ±0.001° Δ 2θ	FWHM	Peak center ±0.001° Δ 2θ	FWHM	Peak center ±0.001° Δ 2θ	FWHM
Pure ZnO	31.716°	0.207°	34.387°	0.189°	36.227°	0.316°
ZnO:Al 0.73 %	31.780° +0.064°	0.169°	34.405° +0.018°	0.106°	36.241° +0.014°	0.134°
ZnO:Al 1.28 %	31.791° +0.075°	0.208°	34.337° (-0.050°)	0.298°	36.249° +0.022°	0.213°
ZnO:Al 1.82 %	31.728° +0.012°	0.466°	34.320° (-0.067°)	0.3733	36.188° (-0.039°)	0.518°

5.6.3 Photoluminescence

5.6.3.1 Photoluminescence of Mn-doped ZnO NSs

Figure 5.64 and 5.65 are the PL spectrum of pure and Mn-doped ZnO NSs measured at room temperature. The comparative study of the spectrum exhibits the ultraviolet (UV) emission peak, green luminescence (GL) broadband and red luminescence (RL) band peaks shifted to the right in the Mn-doped ZnO compared to the pure ZnO NSs. Spectrum of pure ZnO shows a weak UV peak at 381 nm (3.25 eV) while the Mn-doped ZnO shows a shifted UV peak to 417 nm (2.97 eV). This may be due to sp-d spin exchange interaction between the band electrons and localized d electron of Mn ions substituting in cations sites (Fukumura et al., 1999; Mote et al., 2013).

The UV emission near the band edge transition of pure ZnO is to be related to the recombination of free excitons through an exciton-exciton collision process (Kong et al., 2001; Zeng et al., 2010). The pure ZnO NSs also exhibits a broad band from 800 - 1300 nm that is more dominant than of the 420 - 750 nm. The band from 420 - 750 nm in the pure ZnO is subjected to the GL band, which is due to the radial recombination of a photo-generated hole with the electron of singly ionized charged particles in the V_o (Hsieh et al., 2003; Vanheusden et al., 1996a; Vanheusden et al., 1996b). On the other hand the broad GL band is shifted to the yellow luminescence (YL) with extremely very low intensity in the Mn-doped ZnO NSs. Suppression in the intensity as in Mn-doped ZnO NSs has been reported earlier (Ruan et al., 2011; Srinivasan & Kumar, 2008). This indicates presence of low oxygen defects due to the trapped of Mn particles into the V_o of ZnO NSs which suppresses the formation of V_o during the growth of Mn-doped ZnO NSs (Oo et al., 2009).

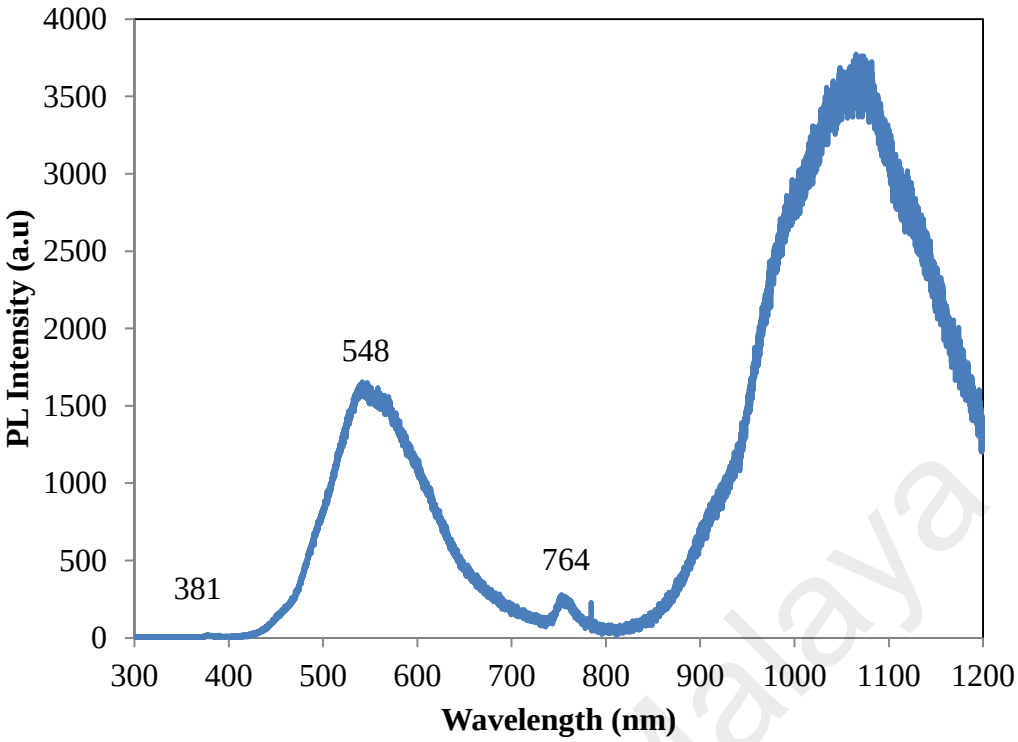

Figure 5.64: Photoluminescence spectrum of pure ZnO NWs prepared in methanol with Ar flow for deposition time 30 minutes.

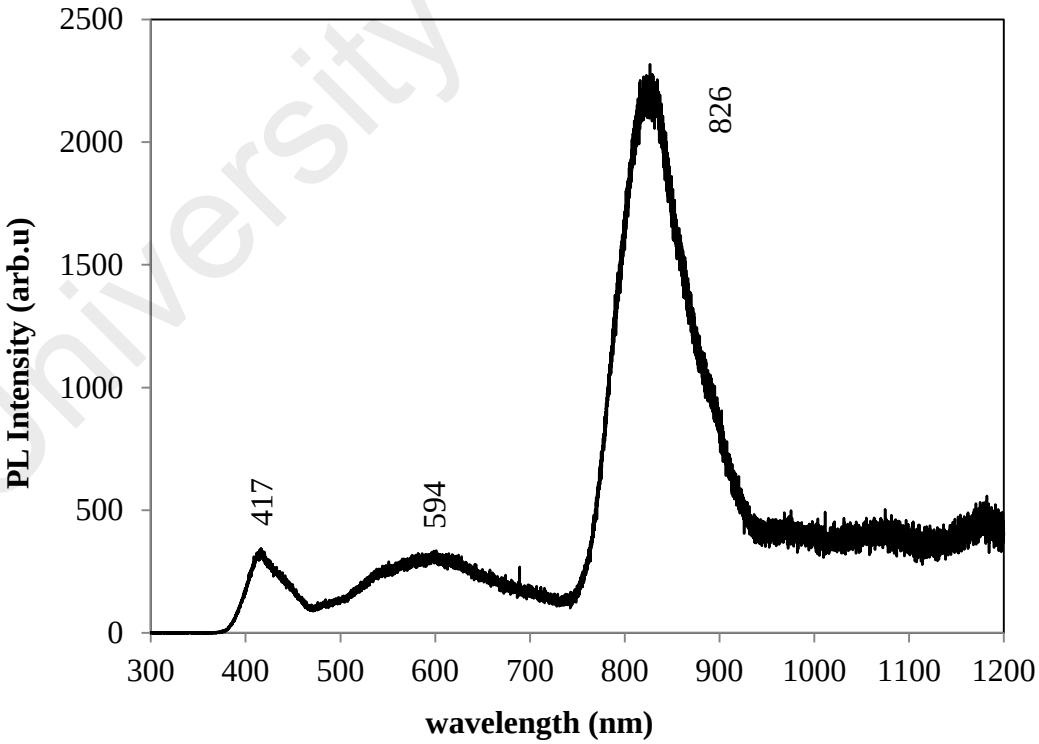

Figure 5.65: Photoluminescence spectrum of Mn-doped ZnO NWs prepared in methanol with Ar flow for deposition time 30 minutes.

Furthermore, the reduced intensity can be related to lattice and surface defects, which produces various non-radiative centers between the bandgap of Mn-doped ZnO (Xu et al., 2005). This further proposes that the potential of our method, combination of the solvothermal of MnO salt in the mixture of methanol and acetone, and thermal evaporation of Zn from CuZn have produced a low concentration of oxygen defects and high optical quality of Mn-doped ZnO NSs (Gao et al., 2005; Zu et al., 1997). In addition, a broad peak is observable from 775 - 945 nm in the Mn-doped ZnO NSs corresponds to the infrared luminescence at 826 nm whereas the pure ZnO shows near infrared at 755 nm. The dominant broad peak in the pure ZnO that relates to the far infrared region is likely not observable in the Mn-doped ZnO due to very low oxygen defects which resulted from the Mn interstitials in the lattice of ZnO.

A closer look and analysis using the Gaussian curve fit to the UV emission peak, GL broad band and red band peaks of pure and Mn-doped ZnO shown as in Figure 5.66 was noticed and summarized in Table 5.9. The pure ZnO NSs shows three peaks that attributes to UV emission band ~376 nm (3.29 eV), 381 nm (3.25 eV) and 387 nm (3.20 eV) nm with high intensity centered at 381 nm. This attributed to 1-longitudinal optical (LO) phonon replicas of neutral donors (D^oX) or ionized donors (D^+X) (Liu et al., 2010). The Mn-doped ZnO exhibits six peaks 395 nm (3.14 eV), 409 nm (3.03 eV), 417 nm (2.97 eV), 425 nm (2.92 eV), 427 nm (2.90 eV), 444 nm (2.79 eV) and 460 nm (2.69 eV) that attribute to the violet emission region. The high intensity of violet emission region of Mn-doped ZnO is noticeable at 417 nm (2.97 eV) and could be ascribed due to the transition occurring from Zn_i to the valence band (Chey et al., 2013). The pure ZnO also exhibits broad peak of visible PL emission ranged from 400-750 nm. At this broad range seven peaks were indentified at 459, 490, 518, 538, 548, 585 and 655 nm with the respective energy of 2.70, 2.53, 2.39, 2.30, 2.26, 2.12 and 1.89 eV. The high intensity centered at 548 nm (2.26 eV) that corresponds to the GL band near to the

yellow region. This visible PL emission in the pure ZnO NSs can be attributed to different intrinsic defects such as Zn_i, O_i, V_{zn}, V_{Zn}^-, V_o, V_o^+, O_{Zn} (Liu et al., 2010). Nevertheless, defects due to carbon incorporation in the pure ZnO NSs are also responsible as reported earlier by Chrissanthopoulos et al. (2011). This corresponds to the EDAX spectrum Figure 5.1c (section 5.2.1) which has exhibited C peak in pure ZnO. On the other hand the Mn-doped ZnO exhibited high intensity of peak centred at 594 nm (2.09 eV) that relates to the YL near to the orange region (Tanaka et al., 2000). Additional of six shifted peaks were identified in the Mn-doped ZnO using the Gaussian curve fit at 488, 549, 571, 620, 653, 692 nm. The shifts from the UV emission band to the violet region and from GL band to yellow luminescence clearly reveals Mn-doping in the ZnO NSs.

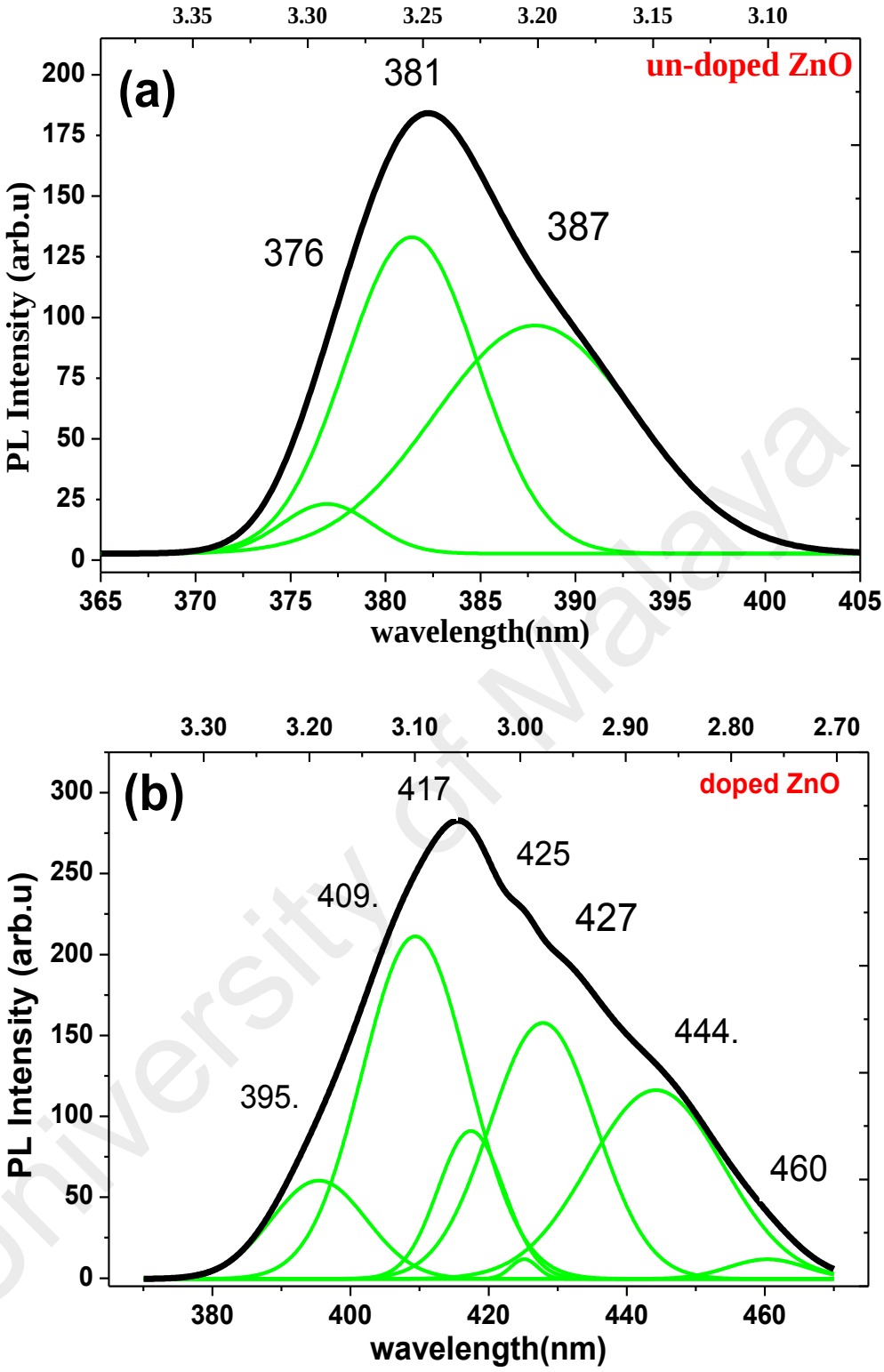

Figure 5.66: The Gaussian curve is fitted at UV emission band and GL band for (a) and (c) of pure and (b) and (d) of Mn-doped ZnO NSs (continued).

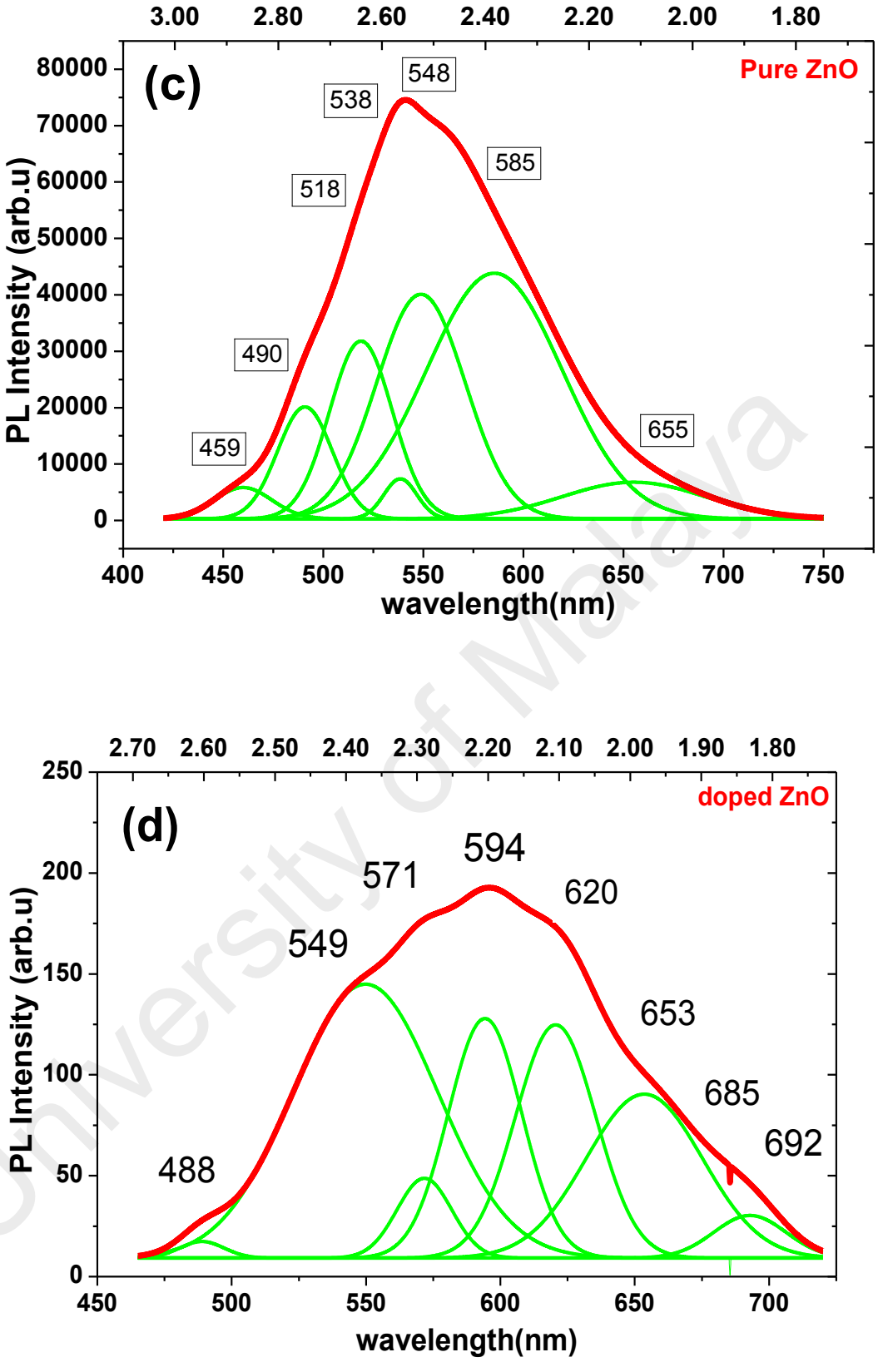

Figure 5.66: The Gaussian curve is fitted at UV emission band and GL band for (a) and (c) of pure and (b) and (d) of Mn-doped ZnO NSs.

Table 5.9: The PL peaks of pure and Mn-doped ZnO NSs at UV emission, GL and RL band.

PL band	**PL peaks in nm (eV) and proposed transition**			
	Pure ZnO	**Proposed transition**	**Mn-doped ZnO**	**Proposed transition**
UV Emission	376 (3.29)	singly ionized O vacancy	395 (3.14)	Phonon replicas
	381 (3.25)	O vacancy	409 (3.03)	Zn vacancy
	387 (3.20)	donor-acceptor pair	417 (2.97)	Mn interstitials
			425 (2.92)	O vacancy
			427 (2.90)	Mn interstitials
			444 (2.79)	O vacancy
			460 (2.69)	hole trapped at O vacancy
GL band	459 (2.70)	Zn vacancy	488 (2.54)	O vacancy
	490 (2.53)	O vacancy	549 (2.25)	Singly ionized O vacancy
	518 (2.39)	singly ionized O	571 (2.17)	O vacancy
	538 (2.30)	O vacancy	594 (2.09)	O/Mn interstitial
	548 (2.26)	Donor-acceptor	620 (2.00)	O/Mn interstitial
	585 (2.12)	O interstitial	653 (1.90)	Zn/O vacancy
	655 (1.89)	Zn/O vacancy	692 (1.79)	Mn interstitials

5.6.3.2 Photoluminescence of Al-doped ZnO NSs

The effect of Al doping into ZnO NWs was investigated from the PL profile as shown in Figure 5.67. Figure 5.65 shows PL properties of pure ZnO NWs and ZnO:Al 0.78, 1.28 and 1.82 wt. %. Significant changes were noticed at NBE, DL and NIR emission regions. It is found that all the Al-doped ZnO NWs samples shows higher intensity compared to the pure ZnO NWs. However the intensity of PL at DL emission decreased as the Al concentration was increased (Louhichi et al., 2015; Lupan et al., 2009). Similar outcome has been reported by (Wang et al., 2007) for ZnO thin film samples annealed at 850 ºC.

Significant changes at NBE range 360 - 430 nm corresponds to the recombination of free excitons through exciton-exciton collision process. The pure ZnO NSs exhibits UV emission band ~378 nm (3.28 eV) as in Figure 5.68. Broad shoulder ~395 and ~417 nm for ZnO:Al 0.73 wt. % whereas 397 and 418 nm for ZnO:Al wt. % of 1.28 attributes UV emission and violet luminescence (VL) region respectively. The UV is red shifted from 378 nm to 395 and 397 nm in Al-doped ZnO is due to Zn_i (Manouni et al., 2006). The VL band noticed to be sharper ~415nm (2.99 eV) as the Al wt. % increased to 1.82. It is clear that the NBE was violet shifted due to Al doping. The combined effect of optical transition to the excitonic state of ZnO and electronic transitions involving crystal-field split is responsible for the violet shift. The shift of UV to VL can be ascribed to Al_i beside the Zn_i. This was generated by the substitution of Zn sites with Al atoms (Lü et al., 2011). The schematic band diagram of the NBE emission is shown in Figure 5.69. Shan et al. have reported similar VL band in Al-doped ZnO that was prepared at room temperature compared to Al-doped ZnO annealed at 500 °C which attributes UV emission at 377 nm (Shan et al., 2003).

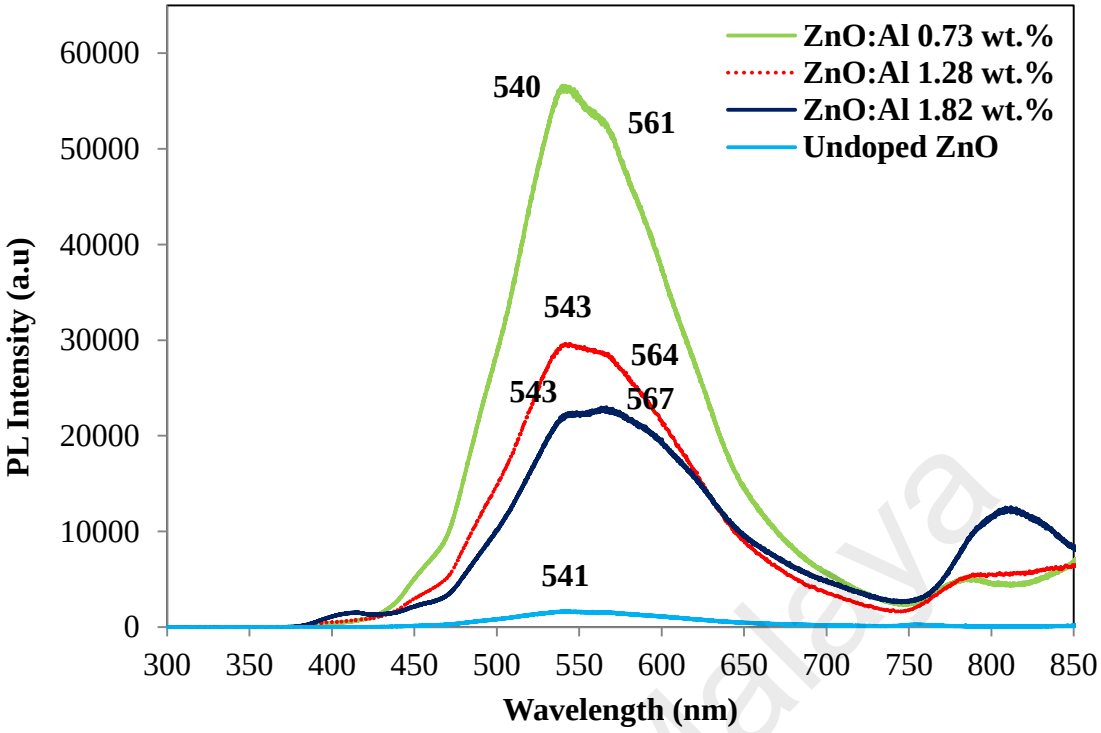

Figure 5.67: Photoluminescence spectra of ZnO:Al wt % of 0.73, 1.28 and 1.82 compare to pure ZnO.

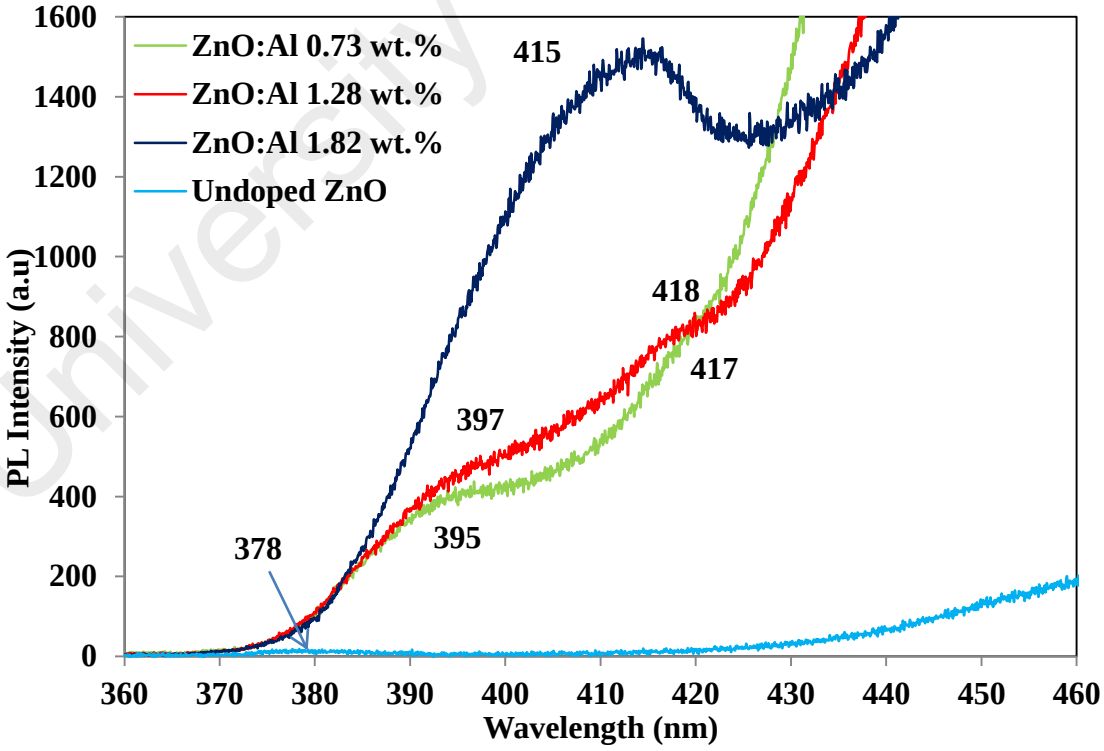

Figure 5.68: Photoluminescence spectra of ZnO:Al wt. % of 0.73, 1.28 and 1.82 compare to pure ZnO at NBE.

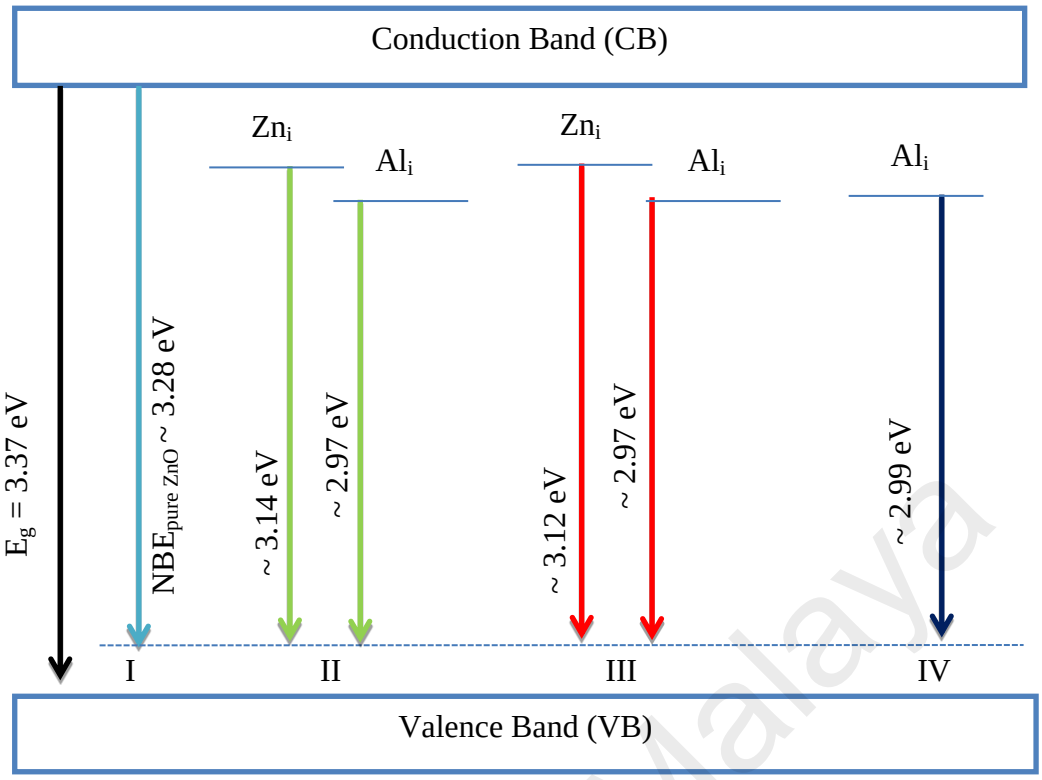

Figure 5.69: Schematic band diagram of NBE based on photoluminescence data of (I) pure ZnO and Al-doped ZnO wt. % of 0.73, (III) 1.28 and (IV) 1.82 at NBE.

Dominant broad peak from 430 to 750 nm is noticeable the PL profile. Figure 5.70 shows the Gaussian deconvoluted peaks at this region for pure and Al-doped ZnO NSs samples. DL green emission at around 540 (2.28 eV) is noticeable for ZnO:Al NWs of 0.73 and pure ZnO NWs. Both the ZnO:Al NWs wt. % of 1.28 and 1.82 exhibits DL green emission at around 534 nm (2.26 eV). However the intensity of ZnO:Al NWs has suppressed with the increased Al wt. %. This is due to O and Zn defects. Although many works been reported, Zhang et al. (2001) and Patterson (2006) have proved that V_o is an unlikely contributor to green emission compared to V_{zn}^{2-} based on the electron transition state. The V_{zn}^{2-} is the most energetically favourable and stable defects to form in the ZnO NWs. A small broad shoulder around 557 nm (2.22 eV) in the pure ZnO as shown in Figure 5.70 (a) can be attributed to yellowish-green (YG) band. This YG band also observed at 565 and 568 nm in ZnO:Al of 0.73 and 1.28

wt. %. The YG band shoulder found to be broader with the increased wt. % of Al. Whereas in Al-doped ZnO of 1.82 wt. %, the YG band found to be broader with a peak centered at 548 nm (2.26 eV). A closer look at the deconvoluted PL profile as in Figure 5.70 (d) exhibited most intense peak at 596 nm (2.09 eV) that relates to YL near to orange region. This is due to the substitution of Zn^{2+} (74 pm) with smaller radii Al^{3+} (53 pm) in the NSs of ZnO. Besides that, the intensity ratio of green to YG emission found to be increased as the wt. % of Al increased. This significantly shows the incorporation of Al^{3+} into the texture of ZnO NSs. Recombination of donors with Al acceptors in the lattice of ZnO NSs seem to be the cause of YG luminescence. At lower wavelength, the ZnO:Al of 1.82 wt. % shows blue shifted region to left to 410 nm (3.02 eV) compared to the pure ZnO which is 460 nm (2.69 eV).

Red luminescence at 755 nm (1.64 eV) in pure ZnO NWs found to be far to the left compared to the Al doped ZnO NWs which shows NIR emissions in Figure 5.71. The ZnO:Al 0.73 wt. % shows small broad shoulder ranged from 750 – 800 nm with a peak centred at 783 nm (1.58 eV). The ZnO: Al 1.28 wt. % shows broader shoulder ranged from 750 – 850 nm compared to the ZnO:Al 0.73 wt. %. Three bulged peaks were identified as 786, 812 and 834 nm in ZnO:Al 1.28 wt. %. This shows transition of free ecxitons has occurred in ZnO NWs doped with Al wt. % of 1.28. Significant change is observable in the PL profile of ZnO:Al 1.82 wt. %. Dominant NIR band from 750 – 880 nm with a peak centred at 812 nm (1.53 eV). This could be due to incorporation of smaller radii Al particle into lattices of ZnO.

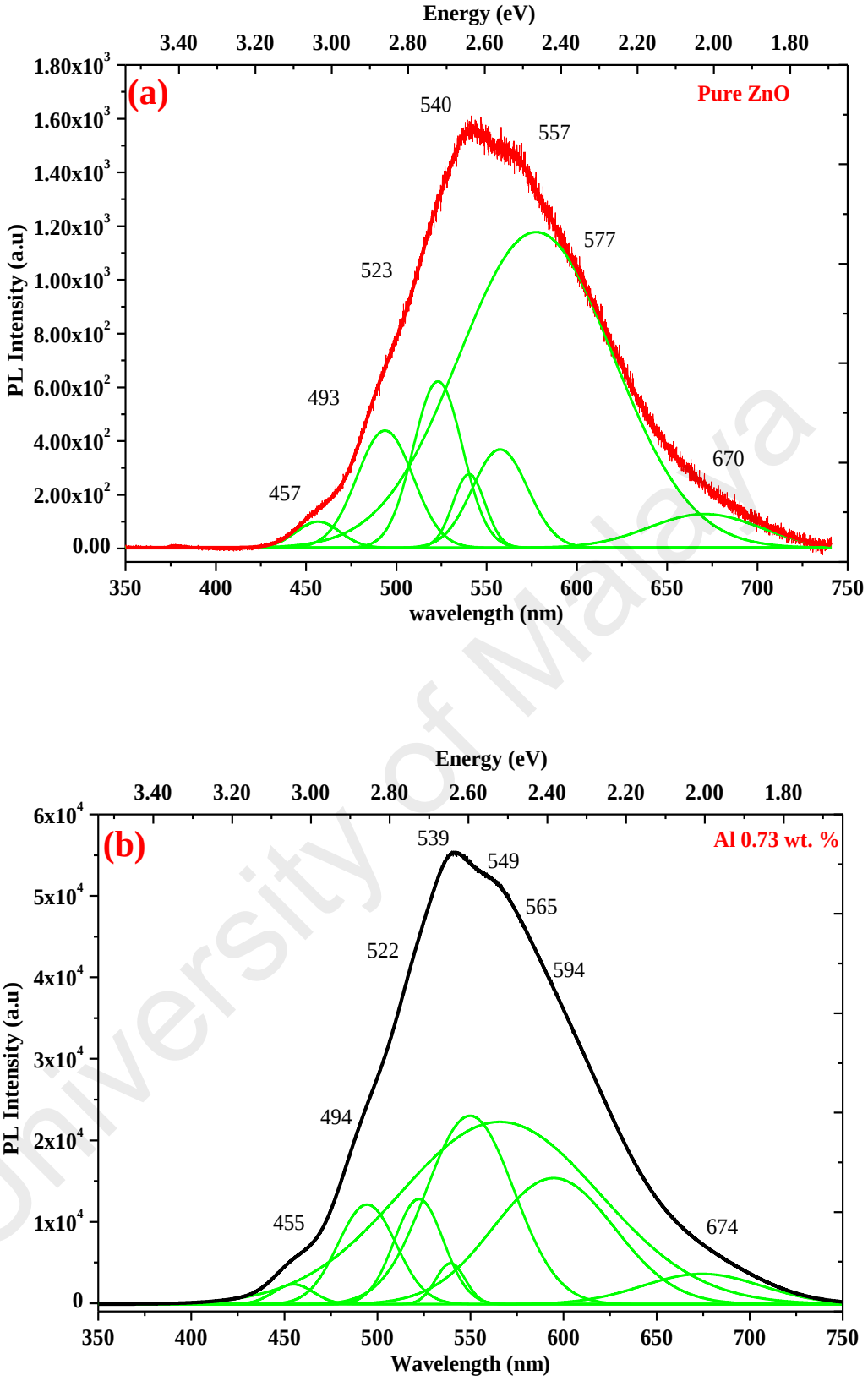

Figure 5.70: The Gaussian curve fitted green luminescence photoluminescence profile of (a) pure ZnO and Al-doped ZnO wt. % of (b) 0.73, (c) 1.28 and (d) 1.82. (continued).

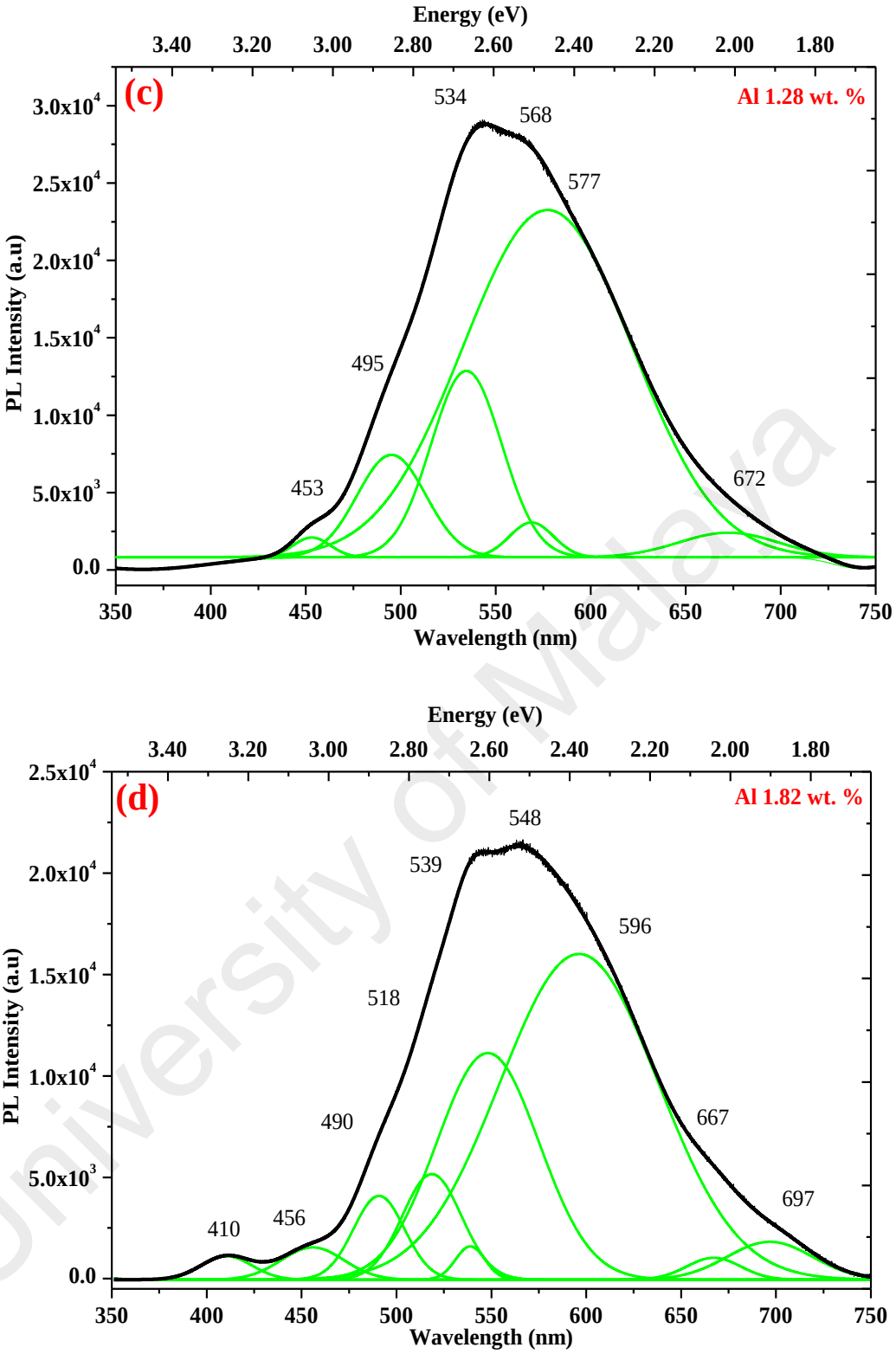

Figure 5.70: The Gaussian curve fitted green luminescence photoluminescence profile of (a) pure ZnO and Al-doped ZnO wt. % of (b) 0.73, (c) 1.28 and (d) 1.82.

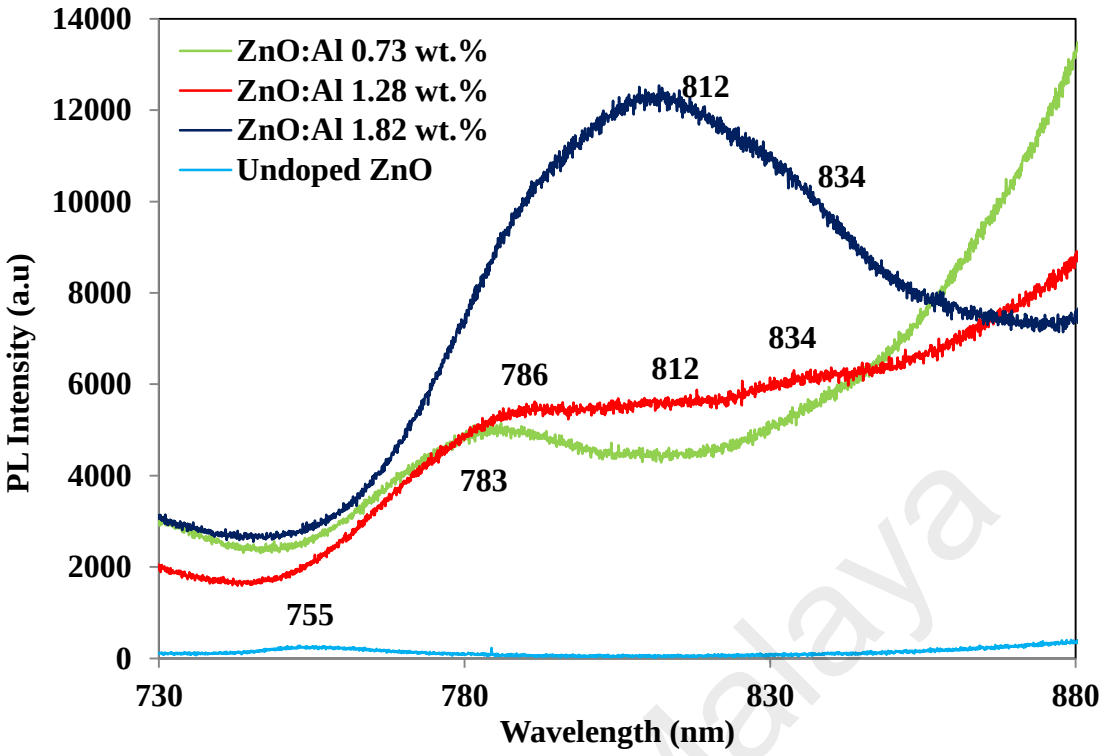

Figure 5.71: Photoluminescence spectra of ZnO:Al wt % of 0.73, 1.28 and 1.82 compare to pure ZnO at NIR.

5.6.4 Raman scattering

5.6.4.1 Raman scattering of Mn-doped ZnO NSs

Figure 5.72 shows the room temperature unpolarized Raman scattering results obtained for Mn-doped ZnO NSs. The spectrum exhibits mostly shifted peaks compared to the pure ZnO NWs. Peaks 81, 109, 145 and 288 cm^{-1} due to vibration of Zn sublattices found to be shifted respectively to 84, 114, 140 and 279 cm^{-1}. However these peaks intensity are very low compared to the pure ZnO NWs. This shows disordered arrangement of particles has occurred and significantly exhibits poor crystal quality. The magnified portion of the spectrum from 0 - 1000 cm^{-1} is shown as Figure 5.73.

Peaks 72 and 84 cm^{-1} can be related to decoration of carbon particles from methanol on the surface structure of ZnO. The 279 cm^{-1} can be attributed to A_1 symmetry due to process B_1^{high}-B_1^{low}. O-related mode at 434 and 330 can be ascribed to nonpolar optical phonon E_2^{high} and A_1(TO) modes of ZnO. Peaks at 528, 557 and 575

cm^{-1} vibrations are noticed to be shifted respectively from 539, 564 and 578 cm^{-1}. The 528 and 575 cm^{-1} can be ascribed to $2B_1^{low}$ and A_1(LO) modes.

At wavenumber more than 700 cm^{-1} due to optical overtones and combinations 722 and 816 cm^{-1} of LA+TO processing modes are identical in the Mn-doped ZnO NSs. Additional peak at 233, 507, 641 and 683 cm^{-1} which is not detectable in the pure ZnO NWs can be related to incorporation of smaller radii Mn ions replacing Zn ion in the structure of ZnO NWs. The Raman absorption for the disordered D and G band which is detectable respectively at 1362 and 1585 cm^{-1} Mn-doped ZnO NSs was due to decoration of C clusters from methanol on the wall of ZnO NWs. But intensity enhancement was noticed in Mn-doped sample compared to pure ZnO NWs. The intensity ratio of D band (I_D) to G band (I_G), (I_D/I_G) was calculated as 0.86 which shows low disordered degree in Mn-doped ZnO NSs.

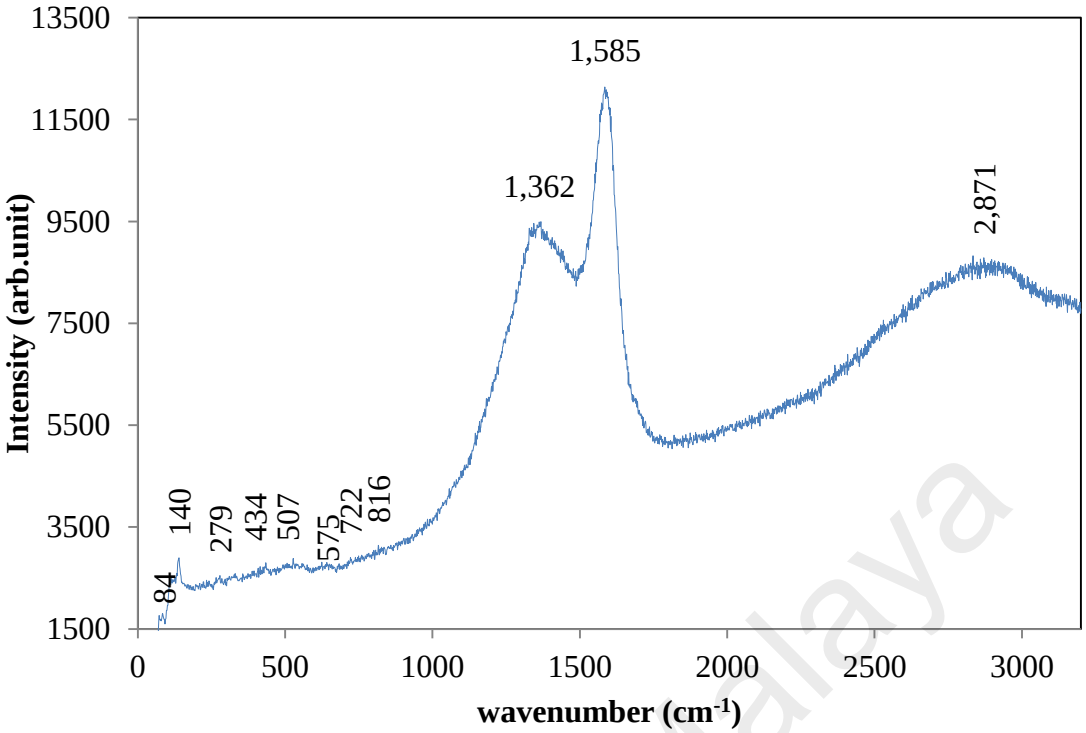

Figure 5.72: Raman scattering of Mn-doped ZnO NSs prepared in methanol with Ar flow.

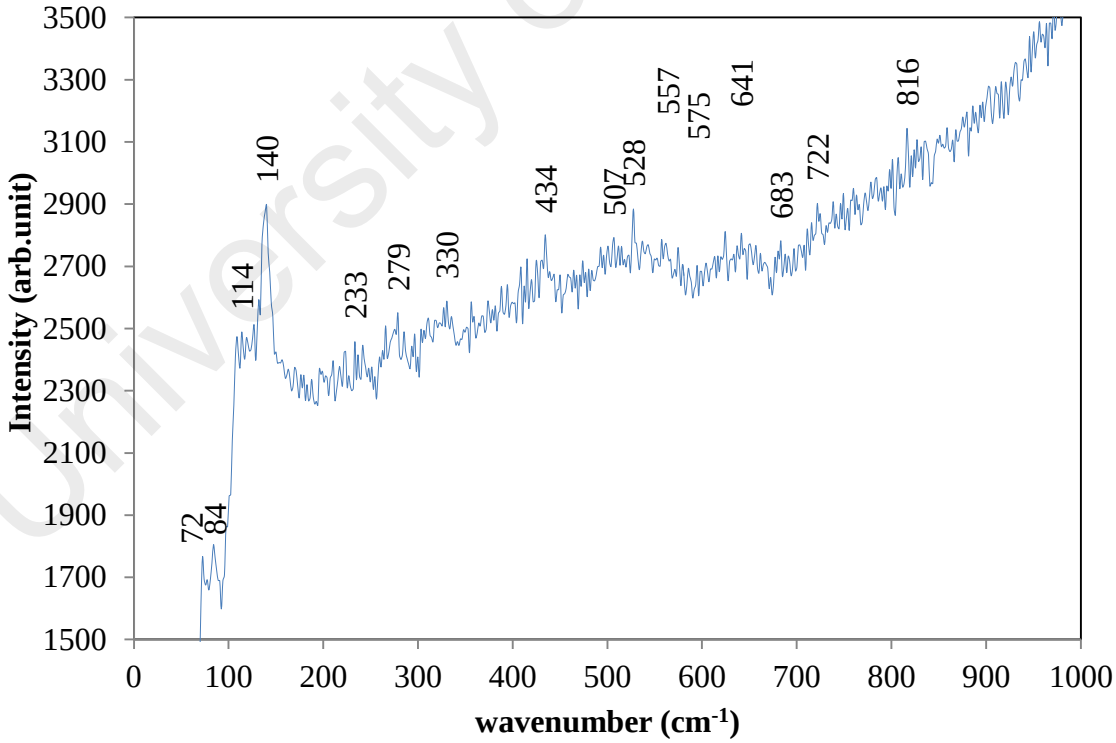

Figure 5.73: Raman scattering of Mn-doped ZnO NSs at range 0-1000 cm^{-1}.

5.6.4.2 Raman scattering of Al-doped ZnO NSs

In this section the Raman scattering of pure ZnO NWs which was discussed in section 5.4.4 is compared with Al-doped ZnO NWs. The Raman scattering of ZnO:Al of 0.73, 1.28 and 1.82 of wt. % and (d) pure ZnO NWs that were prepared in methanol with Ar flow for 30 minutes are shown in Figure 5.74, 5.75, 5.76 and 5.77. The figures exhibits significant changes in the peak positions between ZnO:Al NWs samples and the pure ZnO NWs. Generally the Raman spectral intensity of the Al-doped ZnO NWs for 0.73, 1.28 and 1.82 wt. % were significantly decreased in all the measured frequency regions compared to that of the pure ZnO NWs (Das et al., 2010; Kim et al., 2010).

Peaks that can be related due to vibration of Zn sublattices (below 300 cm^{-1}) were found at around 82, 109, 138 and 274 cm^{-1} in all ZnO:Al samples. The peaks at around 82 and 109 cm^{-1} found to be similar to the pure ZnO but peak 109 cm^{-1} found to be diminished with increasing Al dopant concentration compared to the pure ZnO. These two peaks (82 and 109 cm^{-1}) can be attributed to the incorporation of C clusters from methanol which is in compatible to a work reported by Khanderi et al. (2009). The local mode origin of peak 145 cm^{-1} (Cuscó et al., 2007) which has been detected in the pure ZnO NWs is noticed to be shifted to an anomalous mode around 138 cm^{-1} in ZnO:Al of 0.73, 1.28 and 1.82 wt. %. This anomalous mode can be attributed to the effect of Al doping in ZnO NWs. In the pure ZnO, the A_1 symmetry peak 288 cm^{-1} that can be assigned to B_1^{high}-B_1^{low} mode also found to be shifted to another anomalous mode at peak 274 cm^{-1}. These two anomalous peaks 138 and 274 cm^{-1} which were shifted to low wavenumber can be related to intrinsic host lattice defects in ZnO where the defect has become activated vibrating complexes due to the incorporation of Al dopants (Bundesmann et al., 2003). The shift can also be regarded as stress or strain induced by Al ion in the ZnO lattice.

The numbers of frequencies related to O modes in the range of 300 – 700 cm^{-1} were vanished in the Al-doped ZnO NWs compared to the pure ZnO NWs. The E_2^{high} mode for the ZnO:Al NWs of 1.28 and 1.82 wt. % was shifted to 434 and 433 cm^{-1} whereas the pure ZnO NWs shows profound peak at 439 cm^{-1}. But the E_2^{high} mode is not detectable in ZnO:Al 0.73 wt. % as in Figure 5.74. The A_1 symmetrical peak 340 cm^{-1} in the pure ZnO NWs attributes a good agreement with E_2^{high} - E_2^{low} frequencies. A great shift about 26 cm^{-1} was noticed in the ZnO:Al NWs which are to 364, 367 and 366 cm^{-1} for the respective Al concentration of 0.73, 1.28 and 1.82 wt. %.

The Al-doped ZnO NWs exhibited small broader shoulder at around 535 cm^{-1} whereas in the pure ZnO NWs it found to be diminished. They can be assigned to A_1 symmetry and attributed to $2B_1^{low}$ and LA overtones along L, M and H lines. Presence of Al has bulged out to be broad shoulder. The undetectable E_1-LO mode in the pure ZnO NWs at 590 cm^{-1} was only detected in ZnO:Al of 1.82 wt. % compared to ZnO:Al of 0.73 and 1.28 wt. %. This could be due to Al incorporation into ZnO has triggered the vibration frequency of O related sublattices in ZnO. An anomalous mode which was detected in the pure ZnO at 832 cm^{-1} turn out to be more profound in ZnO:Al NWs of 1.28 wt. % compared to ZnO:Al NWs of 0.73 and 1.82 wt. %. This mode could be due to the influence of Al and the C clusters from methanol. Other peaks that have been detected and discussed earlier in pure ZnO NWs in section 5.4.4 such as 866, 923, 941, 962 and 986 cm^{-1} noticed to be vanished in all Al-doped ZnO NWs. Peak at 1090 and 1051 that can be assigned to be TO+LO combination modes respectively at M, L and A, H points were vanished in Al-doped ZnO. However the 1051 cm^{-1} could be shifted to 1061 cm^{-1} as detectable only in the ZnO:Al NWs of 1.82 wt. %.

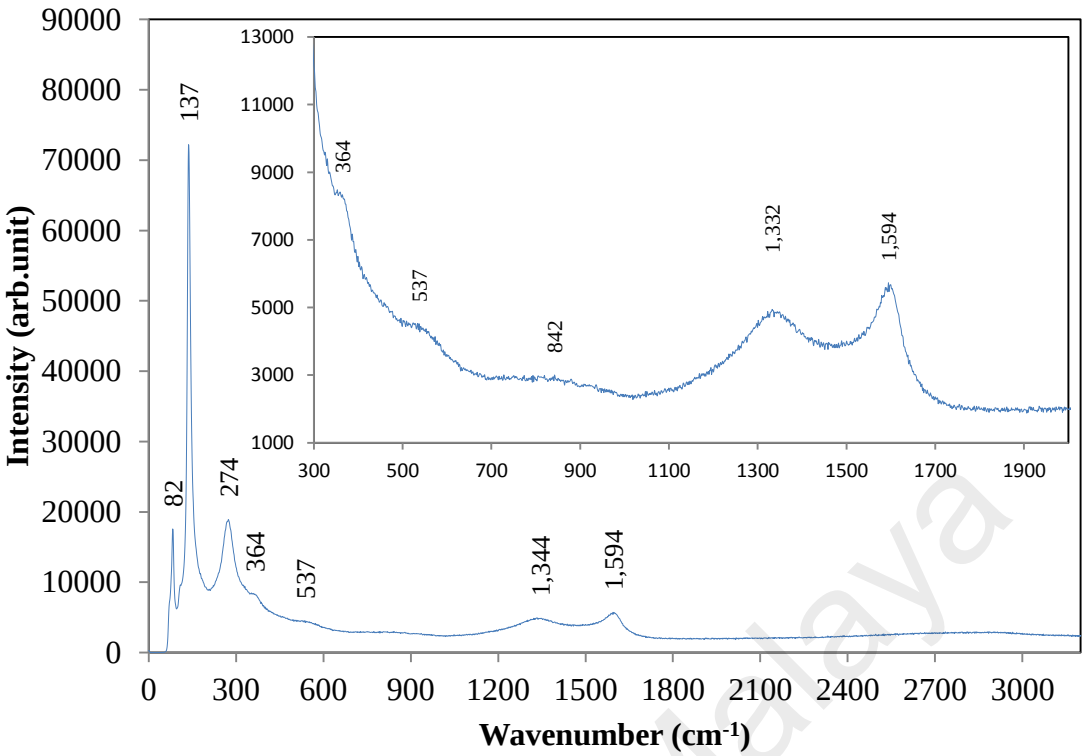

Figure 5.74: Raman scattering of doped ZnO NWs with Al concentration 0.73 wt. %.

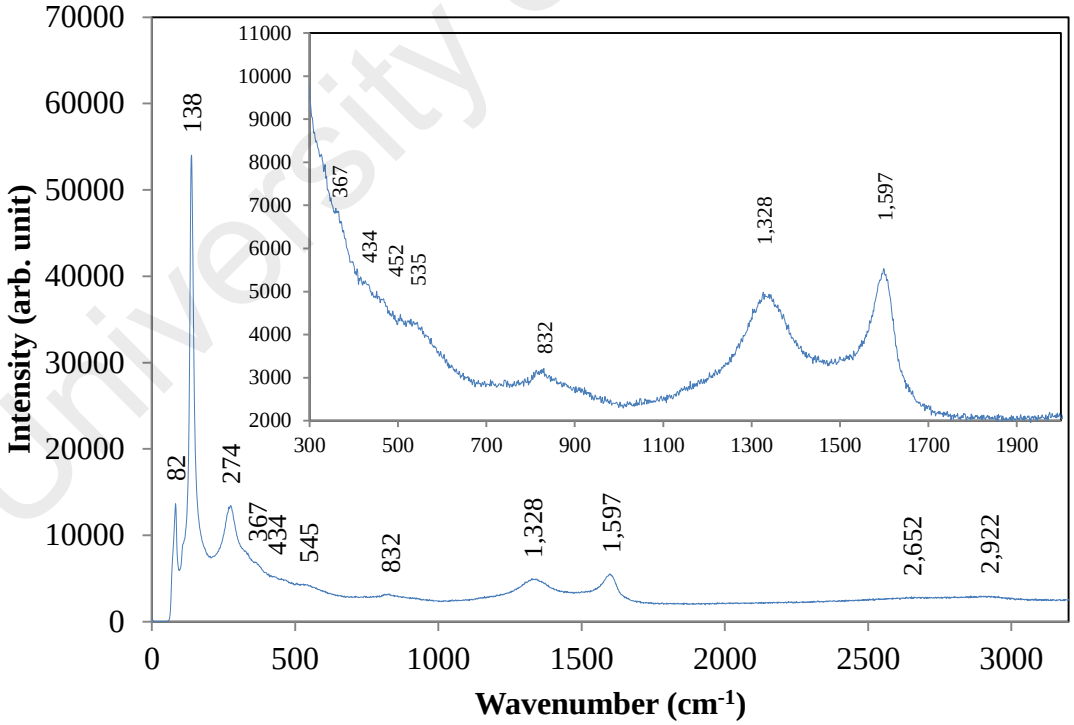

Figure 5.75: Raman scattering of doped ZnO NWs with Al concentration 1.28 wt. %.

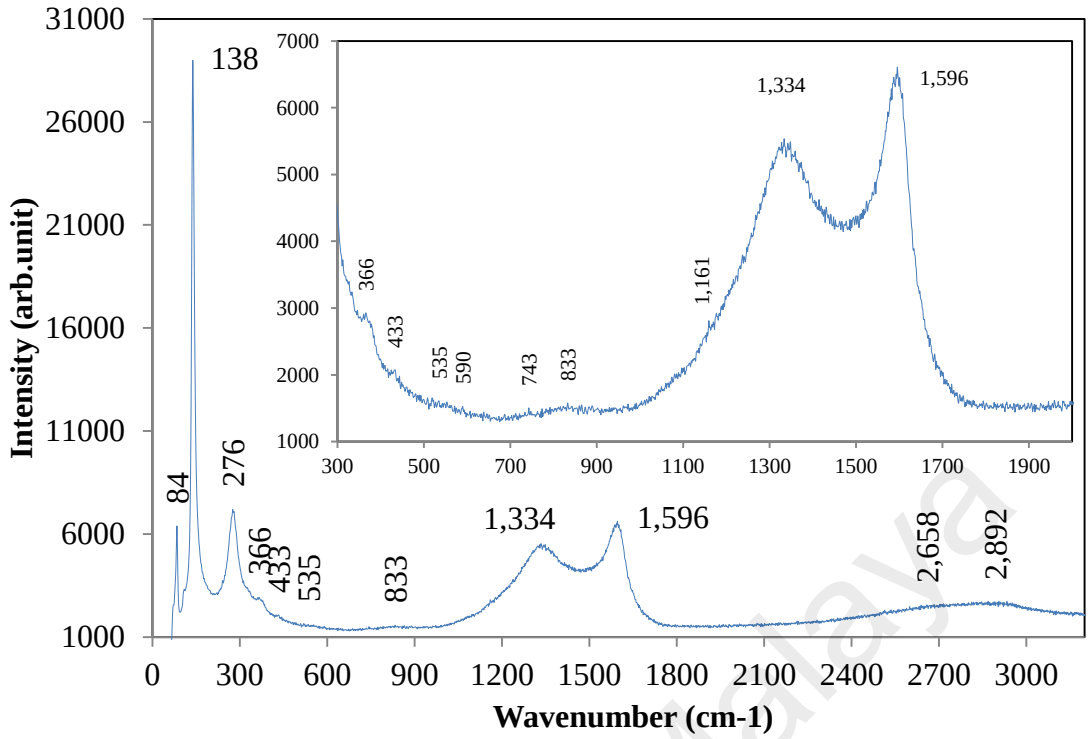

Figure 5.76: Raman scattering of doped ZnO NWs with Al concentration 1.82 wt. %.

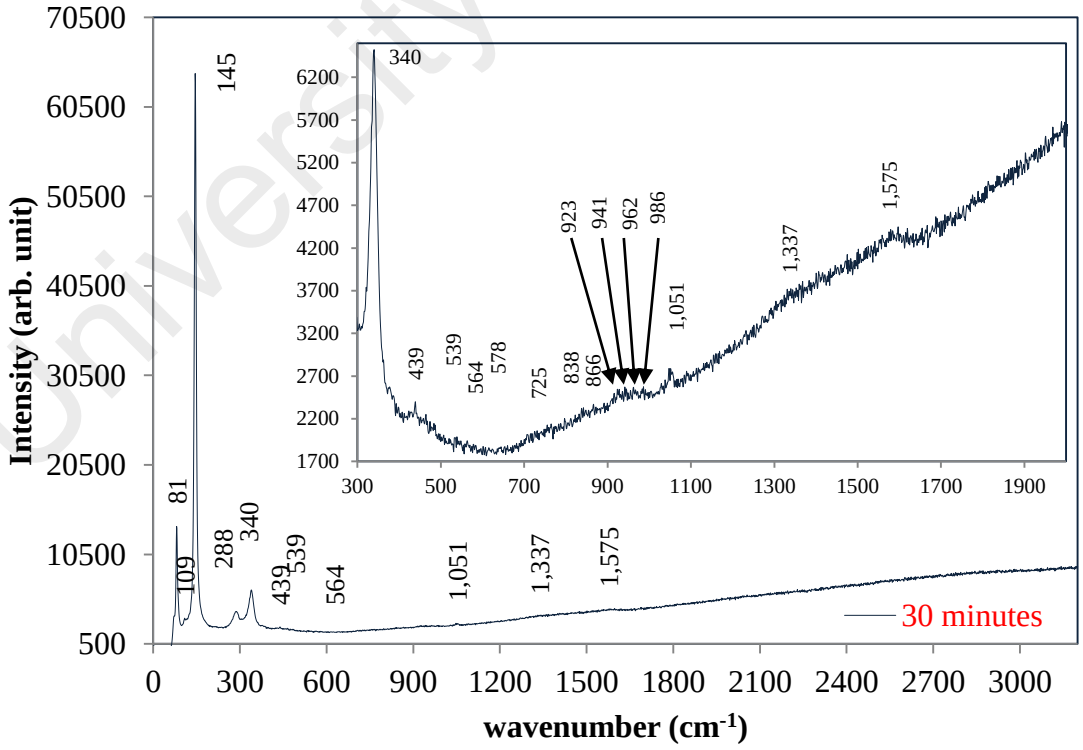

Figure 5.77: Raman scattering of pure ZnO NWs.

The Raman absorption for the disordered D and G band which is detectable respectively at 1337 and 1575 cm^{-1} in pure ZnO NWs can be related to that C clusters from methanol has decorated the wall of ZnO NWs. But intensity enhancement was noticed in all Al-doped ZnO NWs. The disordered D band was identified as 1332, 1328 and 1334 cm^{-1} whereas the disordered G band was 1594, 1597 and 1596 cm^{-1} for ZnO:Al of 0.73, 1.28 and 1.82 wt. %. The intensity ratios of D band (I_D) to G band (I_G), (I_D/I_G) were calculated to be 0.86, 0.90 and 0.89. The low value of I_D/I_G shows low disordered degree in the low concentrated ZnO:Al of 0.73 wt. %. Increasing the Al concentration in methanol highly has influenced the incorporation of C clusters in decorating the wall of ZnO NWs.

5.6.5 Proposed growth mechanism of doped ZnO NSs

MnO_2 and $Al(NO_3)_3$ in methanol, dissolves completely to form manganese methoxide ($(CH_3O)_4Mn$) and aluminium methoxide ($(CH_3O)_3Al$) which further dissolves in excess methanol. Here, the methanol also acts as oxidizer for both Mn and Al. The growth of doped ZnO NSs were obtained by allowing $(CH_3O)_4Mn$ and $(CH_3O)_3Al$ vapor as Ar was flowed at 100 sccm through the mixture of the dopant solution via the two sided hollow CuZn. We believed that C, H and O atoms in $(CH_3O)_4Mn$ and $(CH_3O)_3Al$ underwent a dehydrogenation process in the presence of Cu (in CuZn alloy) at 300 °C.

$$(CH_3O)_3Al\,(a) \xrightarrow{Cu,\ 300°C} CH_3O^-\,(a) + Al^{3+}(a)$$

$$(CH_3O)_4Mn\,(a) \xrightarrow{Cu,\ 300°C} CH_3O^-\,(a) + Mn^{2+}(a)$$

Based on that, Cu in CuZn has acted as an catalyst and oxidized the methanol vapor into an intermediate absorbable methoxy species (CH_3O^-) (Chen & Masel, 1995)

and Al species (Al^{3+}). The CH_3O^- is thermodynamically unstable and were readily converted to formaldehyde (HCHO) by releasing a $H_{(a)}$.

$$CH_3O^-(a) \xrightarrow{Cu,\ 300°C} HCHO(a) + H^+(a)$$

The higher bond energy of C=O in HCHO is thermodynamically unfavourable and the polarity of carbonyl group and its high basicity lowered the transition state energy of activation and therefore results in faster rate of reaction with readily presence species (Bruice PY). So the chemically unstable HCHO vapor easily reacts with Zn vapor or Zn atoms which have been thermally evaporated at temperatures above 395 °C to form hexagonal ZnO NSs. Besides that, further oxidation of HCHO to HCOOH is not predicted due to O_2 absence environment. The Mn(a) and Al(a) condensed as dopant into the lattices of ZnO NSs as it dropped on Si substrate. Apart of this, C-O bond in $CH_3O_{(a)}$ was readily cleaved by Zn vapors (Harikumar & Rao, 1999). Co-adsorption of $O_{(a)}$ and $Zn_{(a)}$ appeared to give rise to a reactive oxygen ions (O^{2-}) and Zn ions (Zn^{2+}) on the Si substrate. Thus Zn^{2+} ionically bond with O^{2-} to form ZnO NSs.

$$CH_3O^- \longrightarrow O^{2-} + CH_3^+$$

$$Zn(a) \longrightarrow Zn^{2+} + 2e^-$$

$$Zn^{2+} + O^{2-} \longrightarrow ZnO(NWs)$$

5.6.6 Conclusion

Mn- and Al-doped ZnO NSs were successfully prepared on Si substrate using the VPT of mixture of methanol and acetone solution via thermal evaporation of two-sided hollow CuZn alloy. All the doped ZnO NSs samples exhibited comparatively with different structure and morphology compared to the pure ZnO (nanoneedle like growth).

The profound changes as in the FESEM images further proved effect and incorporation of Mn and Al dopant into the NSs of ZnO.

Peak shifts and widening in FWHM of (100), (002) and (101) in Al-doped ZnO has induced distribution of non-uniform strain during growth which is due to the incorporation of smaller radii of Al^{3+} into the lattices ZnO NSs. The UV and GL band of pure ZnO at 378 and 548 nm respectively have been shifted to 417 and 594 nm in the Mn-doped ZnO NSs. The PL significantly attributed greater peak shift at NBE from 378 to 415 and red luminescence peak shift from 755 to 812 at NIR emissions can be related to the evidence obtained from FESEM and XRD results. The enhanced D and G band in all Al-doped ZnO NSs shows possible functionalization and doping process has occurred in ZnO NSs. The shift of dominant Raman signal from 145 (pure ZnO) to 140 and 138 cm^{-1} in Mn- and Al-doped ZnO NSs respectively confirmed possible doping in ZnO NSs. Furthermore, presence of Raman signal at 743 cm^{-1} boosted the technique and method that was established. This further confirmed possible Al^{3+} incorporation in the lattices of ZnO. Additional Raman signal at around 274 cm^{-1} compared to the pure ZnO NSs has confirmed incorporation of Al^{3+} into the lattices of ZnO.

5.7 Field emission of electron of ZnO

The effect of doping on FEE is investigated by the addition of trace amounts of impurities into the semiconductor to modify the electronic properties. Al has proven to be an effective n-type dopant for ZnO NSs (Ahn et al., 2009) while continuous difficulties with p-type doping of ZnO slowly perished due to extensive research elsewhere. Thus the FEE characteristics of pure ZnO NSs prepared using mixture of methanol and acetone was compared with Mn-doped ZnO NSs. Figure 5.78 shows the plots of field emission current density versus applied electric field for the pure and Mn-doped ZnO NSs respectively.

The threshold electric field is measured to be 3.12 and 2.06 $V\mu m^{-1}$ for pure and Mn-doped ZnO NSs at a current density 0.1 μAcm^{-2}. The current density of Mn-doped ZnO NSs reached 5.07×10^{-11} $A\mu m^{-2}$ at 7.31 $V\mu m^{-1}$ whereas the pure ZnO NSs showed current density of 2.21×10^{-11} $A\mu m^{-2}$ at 5.98 $V\mu m^{-1}$. According to the FN equation (2.3), β is estimated from the slope of ln (J/E^2) against 1/E plot as in Figure 5.79. The β value is measured to be 1754 and 4548 respectively for the pure and Mn-doped ZnO NSs. As predicted the pure ZnO NSs showed lower β value compared to Mn-doped ZnO NSs. This is due to the structure of NSs and amount of traced Mn impurities in the ZnO sample prepared at 1.82 wt. %. Although the pure ZnO NSs found to be in needle like structure has exhibited low electron emission compared to Mn-doped ZnO which is in NCs as in Figure 5.58. The presence of Mn impurities in Mn-doped ZnO NCs has enhanced the electron emission property. This is useful for employing them as 1D ZnO field emitters. Electron transport channels in the ZnO NSs are amplified with the presence of Mn impurities in the Mn-doped ZnO NSs. This also could be due to increased number of ZnO nanoparticles that contributes to local field strengthening and emission current.

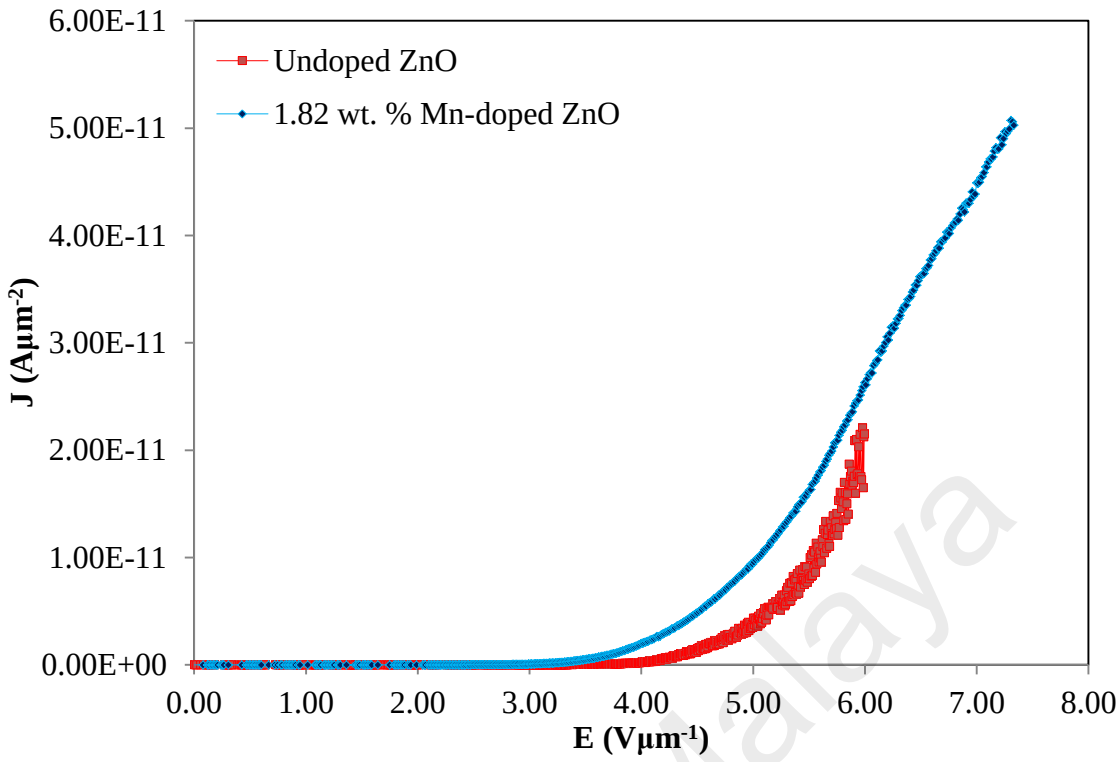

Figure 5.78: Field electron emission current density versus electric field of pure and Mn-doped ZnO NSs.

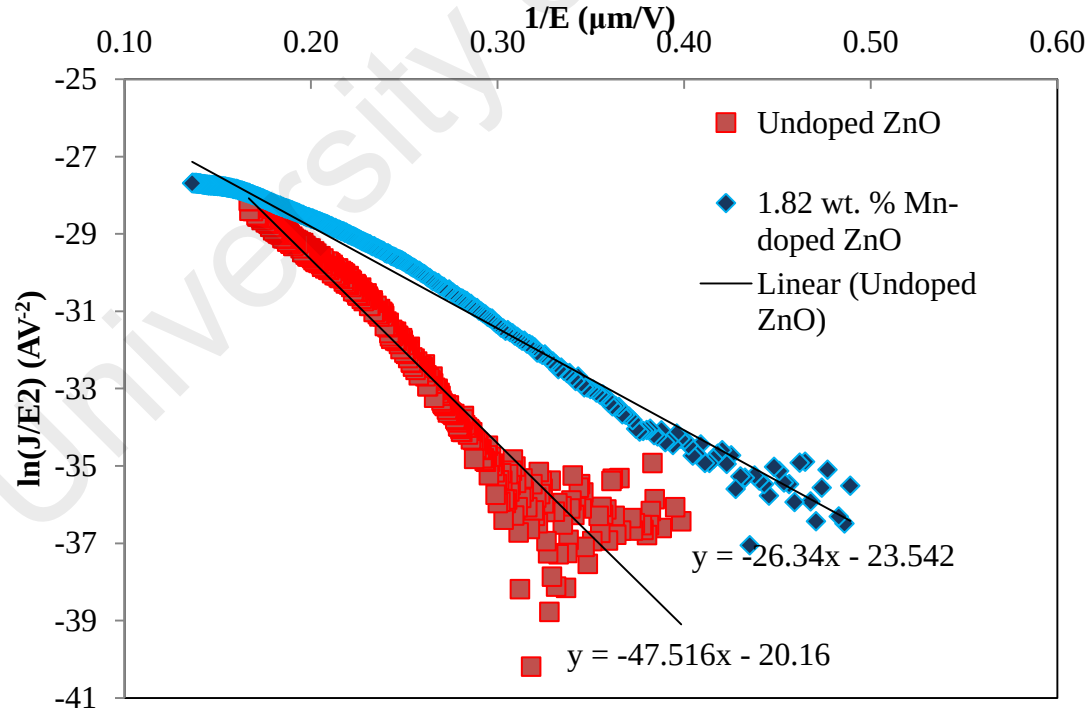

Figure 5.79: Fowler-Nordheim plot of pure and Mn-doped ZnO NSs.

CHAPTER 6: CONCLUSION

6.1 Conclusion

The new technique based on the transport of Zn atoms from CuZn alloy to synthesize pure and doped ZnO NSs has been demonstrated. The processes was clearly demonstrated when only Zn metal films were formed on the substrates when deposition was done in vacuum or under direct Ar flow, and ZnO NSs were obtained when Ar was flowed through methanol or ethanol. These tests showed that Zn atoms were transported to the Si substrates and alcohol molecules were crucial in the formation of the ZnO NSs.

Comparative study on the effect of methanol and ethanol in the growth of ZnO NWs was conducted based on the evaluation of XRD profile using the Debye-Scherer formula, the modified Williamson-Hall models and size-strain plot methods. Methanol and ethanol has contributed in producing polycrystalline ZnO NWs. Different preferential growth in c-axis <002> and <101> directions were observed for growth using methanol and ethanol, respectively. This can be due to the greater percentage of C per molecule in ethanol which changed the preferential growth direction <002> as in ZnO prepared using methanol to <101> due to higher C and H defects in ZnO growth using ethanol. Generally, it was found that ZnO NSs synthesized using methanol showed lower strain and stress values due to its lower effect of C and H defects that led to formation of nanoneedle liked growth. In addition lowest strain distribution and U value in samples using methanol deposited for 30 minutes.

Significant changes in the structure and morphology of ZnO NSs synthesized using methanol, from button mushroom liked (growth times 5 and 10 minutes) to nanorods (growth times 15 and 20 minutes) and then to nanoneedles (growth time 25 and 30 minutes) demonstrated the profound effect of growth time. Furthermore, at longer growth times of 25 and 30 minutes ZnO nanostrings were also formed. The

estimated crystallite size was generally independent of the growth time with slight decrease for ZnO growth using methanol deposited after 25 minutes.

Growth using methanol has also gave ZnO NSs with less defects based on PL measurement. Shift of DL emission peak from 541 nm of ZnO NWs growth using methanol to 572 nm in ZnO NWs growth using ethanol indicated more H defects were formed during. Thus, V_{Zn}^{2-} is likely a contributor in the DL green emission region. The yellow emission region related recombination of donors to H^{+} defects sides. Blue region around 460 nm (2.70 eV) confirmed the presence of complexes of Zn_i. Moreover an unlikely emission at 816 nm from ZnO growth using ethanol was related to possible C functionalization on ZnO NWs due to excess C from ethanol.

Raman peaks at 407 and 565 cm^{-1} clearly indicated E_1(TO) and A_1(LO) mode of ZnO NWs. Raman peaks at around 1332 and 1594 cm^{-1} also confirmed decoration of the wall of ZnO NWs with C particles from methanol and ethanol. Prevailing first order Raman absorptions for disordered D and G band in ZnO growth using ethanol compared to ZnO growth using methanol NWs showed possible functionalization on the ZnO NWs produced using ethanol. As a result ZnO samples prepared using methanol and ethanol showed anomalous 138 and 274 cm^{-1} vibration which are contradictory to other works that have been reported earlier.

Based on FESEM imaging, XRD, PL and Raman analysis it was confirmed that the technique which involved combination of VPT and thermal evaporation was capable of producing Mn and Al-doped ZnO nanostructures. Incorporation of Mn^{2+} and Al^{3+} into the lattices of ZnO and positions of peak shift compared to the pure ZnO NWs as in the XRD profile further proved that dopant elements, Greater peak shift at NBE from 378 nm of pure ZnO NWs to 417 and 415 nm respectively for Mn-doped and Al-doped ZnO NSs enhanced the luminescence property in ZnO NWs.

6.2 Suggested future work

The proposed growth technique using VPT of methanol vapor and thermal evaporation of CuZn alloy is a breakthrough in this era to promote aliphatic alcohols and Zn base alloys in the fabrication of ZnO based materials. This technique can be further modified and implemented to produce doped and functionalized ZnO materials. Other carbon source material which has greater percentage of C per molecule can be implemented in producing hybrid or functionalized ZnO materials. This method also can be applied to grow ZnO NWs on graphene coated layer. Any Zn source material rather than CuZn can be utilized in fabrication of ZnO NSs. In order to grow vertically aligned ZnO NWs the Si substrate can be further coated with gold nanoparticles.

REFERENCES

Abaira, R., Buffagni, E., Matoussi, A., Khmakhem, H., & Ferrari, C. (2015). Synthesis and structural properties of vanadium doped zinc oxide. *Superlattices and Microstructures, 86*, 438-445.

Abdulgafour, H. I., Hassan, Z., Al-Hardan, N., & Yam, F. K. (2010). Growth of zinc oxide nanoflowers by thermal evaporation method. *Physica B-Condensed Matter, 405*(11), 2570-2572.

Acharya, R., Zhang, Y., & Cao, X. (2012). Characterization of zinc-tin-oxide films deposited by thermal co-evaporation. *Thin Solid Films, 520*(19), 6130-6133.

Ahn, C. H., Kim, Y. Y., Kim, D. C., Mohanta, S. K., & Cho, H. K. (2009). A comparative analysis of deep level emission in ZnO layers deposited by various methods. *Journal of Applied Physics, 105*(1), 13502-13505.

Alvi, N., Usman Ali, S., Hussain, S., Nur, O., & Willander, M. (2011). Fabrication and comparative optical characterization of n-ZnO nanostructures (nanowalls, nanorods, nanoflowers and nanotubes)/p-GaN white-light-emitting diodes. *Scripta Materialia, 64*(8), 697-700.

An, Q., Xin, Y., Huo, K., Cai, X., & Chu, P. K. (2009). Corrosion behavior of ZnO nanosheets on brass substrate in NaCl solutions. *Materials Chemistry and Physics, 115*(1), 439-443.

An, Z., Fu, R. K., Li, W., Chen, P., Chu, P. K., Li, K., . . . Lin, C. (2004). Low-temperature photoluminescence of hydrogen Ion and plasma implanted silicon and porous silicon. *Journal of Applied Physics, 96*(1), 248-251.

Arguello, C., Rousseau, D., & Porto, S. P. d. S. (1969). First-order Raman effect in wurtzite-type crystals. *Physical Review, 181*(3), 1351-1363.

Ashkenov, N., Mbenkum, B., Bundesmann, C., Riede, V., Lorenz, M., Spemann, D., . . . Grundmann, M. (2003). Infrared dielectric functions and phonon modes of high-quality ZnO films. *Journal of Applied Physics, 93*(1), 126-133.

Bagnall, D., Chen, Y., Zhu, Z., Yao, T., Shen, M., & Goto, T. (1998). High temperature excitonic stimulated emission from ZnO epitaxial layers. *Applied Physics Letters, 73*(8), 1038-1040.

Banerjee, D., Lao, J., Wang, D., Huang, J., Steeves, D., Kimball, B., & Ren, Z. (2004). Synthesis and photoluminescence studies on ZnO nanowires. *Nanotechnology, 15*(3), 404-409.

Baruah, S., & Dutta, J. (2009). Hydrothermal growth of ZnO nanostructures. *Science and Technology of Advanced Materials, 10*(1), 013001-1-18.

Baskoutas, S., Giabouranis, P., Yannopoulos, S. N., Dracopoulos, V., Toth, L., Chrissanthopoulos, A., & Bouropoulos, N. (2007). Preparation of ZnO nanoparticles by thermal decomposition of zinc alginate. *Thin Solid Films, 515*(24), 8461-8464.

Biju, V., Sugathan, N., Vrinda, V., & Salini, S. (2008). Estimation of lattice strain in nanocrystalline silver from X-ray diffraction line broadening. *Journal of Materials Science, 43*(4), 1175-1179.

Biswas, M., McGlynn, E., & Henry, M. (2009). Carbothermal reduction growth of ZnO nanostructures on sapphire—comparisons between graphite and activated charcoal powders. *Microelectronics Journal, 40*(2), 259-261.

Børseth, T. M., Svensson, B., Kuznetsov, A. Y., Klason, P., Zhao, Q., & Willander, M. (2006). Identification of oxygen and zinc vacancy optical signals in ZnO. *Applied Physics Letters, 89*(26), 262112-1-3.

Bruice, P. Y. (2006). Organic Chemistry, 2006: Prentice Hall.

Bundesmann, C., Ashkenov, N., Schubert, M., Spemann, D., Butz, T., Kaidashev, E., . . . Grundmann, M. (2003). Raman scattering in ZnO thin films doped with Fe, Sb, Al, Ga, and Li. *Applied Physics Letters, 83*(10), 1974-1976.

Byeon, J. H., & Kim, J.-W. (2013). Aerosol assisted fabrication of carbon nanotube/zinc oxide arrays for a field emission device. *Journal of Colloid and Interface Science, 393*, 397-401.

Bylander, E. (1978). Surface effects on the low-energy cathodoluminescence of zinc oxide. *Journal of Applied Physics, 49*(3), 1188-1195.

Cai, X., Han, B., Deng, S., Wang, Y., Dong, C., Wang, Y., & Djerdj, I. (2014). Hydrothermal growth of ZnO nanorods on Zn substrates and their application in degradation of azo dyes under ambient conditions. *CrystEngComm, 16*(33), 7761-7770.

Calleja, J., & Cardona, M. (1977). Resonant Raman scattering in ZnO. *Physical Review B, 16*(8), 3753-3761.

Cammarata, R., Trimble, T., & Srolovitz, D. (2000). Surface stress model for intrinsic stresses in thin films. *Journal of Materials Research, 15*(11), 2468-2474.

Chandrappa, K. G., Venkatesha, T. V., Vathsala, K., & Shivakumara, C. (2010). A hybrid electrochemical–thermal method for the preparation of large ZnO nanoparticles. *Journal of Nanoparticle Research, 12*(7), 2667-2678.

Chang, C., & Sze, S. M. (1996). *ULSI technology*: McGraw-Hill Book Co Ltd.

Chao, L.-C., & Yang, S.-H. (2007). Growth and Auger electron spectroscopy characterization of donut-shaped ZnO nanostructures. *Applied Surface Science, 253*(17), 7162-7165.

Chen, A., & Masel, R. (1995). Direct conversion of methanol to formaldehyde in the absence of oxygen on Cu (210). *Surface Science, 343*(1), 17-23.

Chen, B., Sun, X., & Xu, C. (2004). Fabrication of zinc oxide nanostructures on gold-coated silicon substrate by thermal chemical reactions vapor transport deposition in air. *Ceramics International, 30*(7), 1725-1729.

Chen, X.-L., Geng, X.-H., Xue, J., Zhang, D., Hou, G., & Zhao, Y. (2006). Temperature-dependent growth of zinc oxide thin films grown by metal organic chemical vapor deposition. *Journal of Crystal Growth, 296*(1), 43-50.

Chen, Y., Schneider, P., Liu, B.-J., Borodin, S., Ren, B., & Erbe, A. (2013). Electronic structure and morphology of dark oxides on zinc generated by electrochemical treatment. *Physical Chemistry Chemical Physics, 15*(24), 9812-9822.

Chey, C. O., Nur, O., & Willander, M. (2013). Low temperature aqueous chemical growth, structural, and optical properties of Mn-doped ZnO nanowires. *Journal of Crystal Growth, 375*, 125-130.

Chrissanthopoulos, A., Baskoutas, S., Bouropoulos, N., Dracopoulos, V., Poulopoulos, P., & Yannopoulos, S. (2011). Synthesis and characterization of ZnO/NiO p–n heterojunctions: ZnO nanorods grown on NiO thin film by thermal evaporation. *Photonics and Nanostructures-Fundamentals and Applications, 9*(2), 132-139.

Cimitan, S., Albonetti, S., Forni, L., Peri, F., & Lazzari, D. (2009). Solvothermal synthesis and properties control of doped ZnO nanoparticles. *Journal of Colloid and Interface Science, 329*(1), 73-80.

Cross, R., De Souza, M., & Narayanan, E. S. (2005). A low temperature combination method for the production of ZnO nanowires. *Nanotechnology, 16*(10), 2188-2192.

Cuscó, R., Alarcón-Lladó, E., Ibanez, J., Artús, L., Jiménez, J., Wang, B., & Callahan, M. J. (2007). Temperature dependence of Raman scattering in ZnO. *Physical Review B, 75*(16), 165202-1-11.

Damen, T. C., Porto, S., & Tell, B. (1966). Raman effect in zinc oxide. *Physical Review, 142*(2), 570-574.

Das, J., Pradhan, S., Sahu, D., Mishra, D., Sarangi, S., Nayak, B., . . . Roul, B. (2010). Micro-Raman and XPS studies of pure ZnO ceramics. *Physica B: Condensed Matter, 405*(10), 2492-2497.

Deka, S., & Joy, P. (2007). Synthesis and magnetic properties of Mn doped ZnO nanowires. *Solid State Communications, 142*(4), 190-194.

Derycke, V., Martel, R., Appenzeller, J., & Avouris, P. (2001). Carbon nanotube inter- and intramolecular logic gates. *Nano letters, 1*(9), 453-456.

Dinesha, M., Prasanna, G., Naveen, C., & Jayanna, H. (2013). Structural and dielectric properties of Fe doped ZnO nanoparticles. *Indian Journal of Physics, 87*(2), 147-153.

Ding, S., Li, C., Lei, W., Zhang, Y., Qasim, K., Cui, H., . . . Wang, B. (2012). Stable and uniform field emission from zinc oxide nanowires grown on carbon nanotube mesh template. *Thin Solid Films, 524*, 245-248.

Dingle, R. (1969). Luminescent transitions associated with divalent copper impurities and the green emission from semiconducting zinc oxide. *Physical Review Letters, 23*(11), 579-581.

Dodson, E., & Savage, J. (1968). Vapour growth of single-crystal zinc oxide. *Journal of Materials Science, 3*(1), 19-25.

Drexler, K. E. (1981). Molecular engineering: An approach to the development of general capabilities for molecular manipulation. *Proceedings of the National Academy of Sciences, 78*(9), 5275-5278.

Fan, Z., & Lu, J. G. (2005). Zinc oxide nanostructures: synthesis and properties. *Journal of Nanoscience and Nanotechnology, 5*(10), 1561-1573.

Fang, X., Bando, Y., Gautam, U. K., Zhai, T., Zeng, H., Xu, X., . . . Golberg, D. (2009). ZnO and ZnS nanostructures: ultraviolet-light emitters, lasers, and sensors. *Critical Reviews in Solid State and Materials Sciences, 34*(3-4), 190-223.

Fang, Y., Wong, K. M., & Lei, Y. (2012). Synthesis and field emission properties of different ZnO nanostructure arrays. *Nanoscale Research Letters, 7*(1), 1-11.

Feng, Q., Hu, L., Liang, H., Feng, Y., Wang, J., Sun, J., . . . Dong, L. (2010). Catalyst-free growth of well-aligned arsenic-doped ZnO nanowires by chemical vapor deposition method. *Applied Surface Science, 257*(3), 1084-1087.

Forrest, S. R. (2004). The path to ubiquitous and low-cost organic electronic appliances on plastic. *Nature, 428*(6986), 911-918.

Fowler, R. H., & Nordheim, L. (1928). Electron emission in intense electric fields. *Proceedings of the Royal Society of London. Series A, Containing Papers of a Mathematical and Physical Character*, 173-181.

Freund, L., & Chason, E. (2001). Model for stress generated upon contact of neighboring islands on the surface of a substrate. *Journal of Applied Physics, 89*(9), 4866-4873.

Fukumura, T., Jin, Z., Ohtomo, A., Koinuma, H., & Kawasaki, M. (1999). An oxide-diluted magnetic semiconductor: Mn-doped ZnO. *Applied Physics Letters, 75*(21), 3366-3368.

Gao, X., Li, X., & Yu, W. (2005). Rapid preparation, characterization, and photoluminescence of ZnO films by a novel chemical method. *Materials Research Bulletin, 40*(7), 1104-1111.

Gedamu, D., Paulowicz, I., Kaps, S., Lupan, O., Wille, S., Haidarschin, G., . . . Adelung, R. (2014). Rapid Fabrication Technique for Interpenetrated ZnO Nanotetrapod Networks for Fast UV Sensors. *Advanced Materials, 26*(10), 1541-1550.

Geis, M., Twichell, J., Macaulay, J., & Okano, K. (1995). Electron field emission from diamond and other carbon materials after H2, O2, and Cs treatment. *Applied Physics Letters, 67*(9), 1328-1330.

Gilliland, G. (1997). Photoluminescence spectroscopy of crystalline semiconductors. *Materials Science and Engineering: R: Reports, 18*(3), 99-399.

Gossling, B. (1926). The emission of electrons under the influence of intense electric fields. *Phil. Mag. Bd, 1*, 609-635.

Grundhauser, F. J. (1966). Vacuum arc x-ray tube: Google Patents.

Gu, Y., Kuskovsky, I. L., Yin, M., Obrien, S., & Neumark, G. (2004). Quantum confinement in ZnO nanorods. *Applied Physics Letters, 85*(17), 3833-3835.

Guo, M., Diao, P., & Cai, S. M. (2004). Photoelectrochemical properties of highly oriented ZnO nanotube array films on ITO substrates. *Chinese Chemical Letters, 15*(9), 1113-1116.

Halliburton, L., Giles, N., Garces, N., Luo, M., Xu, C., Bai, L., & Boatner, L. A. (2005). Production of native donors in ZnO by annealing at high temperature in Zn vapor. *Applied Physics Letters, 87*(17), 172108-1-3.

Han, N., Wu, X., Chai, L., Liu, H., & Chen, Y. (2010). Counterintuitive sensing mechanism of ZnO nanoparticle based gas sensors. *Sensors and Actuators B: Chemical, 150*(1), 230-238.

Harikumar, K., & Rao, C. (1999). Role of oxygen transients in the facile scission of C–O bonds of alcohols on Zn surfaces. *Chemical Communications*(4), 341-342.

Hasuike, N., Fukumura, H., Harima, H., Kisoda, K., Matsui, H., Saeki, H., & Tabata, H. (2004). Raman scattering studies on ZnO doped with Ga and N (codoping), and magnetic impurities. *Journal of Physics: Condensed Matter, 16*(48), S5807-S5810.

Hatch, S., Briscoe, J., Sapelkin, A., Gillin, W., Gilchrist, J., Ryan, M., . . . Dunn, S. (2013). Influence of anneal atmosphere on ZnO-nanorod photoluminescent and morphological properties with self-powered photodetector performance. *Journal of Applied Physics, 113*(20), 204501-1-9.

Hearle, J. W. S., Sparrow, J. T., & Cross, P. M. (1972). *Use of the scanning electron microscope*: Pergamon Press Inc.

Henley, S., Ashfold, M., & Cherns, D. (2004). The growth of transparent conducting ZnO films by pulsed laser ablation. *Surface and Coatings Technology, 177*, 271-276.

Hrkac, V., Kienle, L., Kaps, S., Lotnyk, A., Mishra, Y. K., Schuermann, U., . . . Adelung, R. (2013). Superposition twinning supported by texture in ZnO nanospikes. *Journal of Applied Crystallography, 46*(2), 396-403.

Hsieh, C.-T., Chen, J.-M., Lin, H.-H., & Shih, H.-C. (2003). Field emission from various CuO nanostructures. *Applied Physics Letters, 83*(16), 3383-3385.

Hu, J., Ma, X., Xie, Z., Wong, N., Lee, C., & Lee, S. (2001). Characterization of zinc oxide crystal whiskers grown by thermal evaporation. *Chemical Physics Letters, 344*(1), 97-100.

Huang, B.-R., Lin, T.-C., Chu, K.-T., Yang, Y.-K., & Lin, J.-C. (2013). Field emission properties of zinc oxide/zinc tungstate (ZnO/ZnWO< sub> 4</sub>) composite nanorods. *Surface and Coatings Technology, 231*, 289-292.

Huang, M. H., Wu, Y., Feick, H., Tran, N., Weber, E., & Yang, P. (2001). Catalytic growth of zinc oxide nanowires by vapor transport. *Advanced Materials, 13*(2), 113-116.

Huo, K., Hu, Y., Fu, J., Wang, X., Chu, P. K., Hu, Z., & Chen, Y. (2007). Direct and large-area growth of one-dimensional ZnO nanostructures from and on a brass substrate. *The Journal of Physical Chemistry C, 111*(16), 5876-5881.

Jagadish, C., & Pearton, S. (2006). ZnO bulk, thin films, and nanostructures: Elsevier Maryland Heights, MA.

Jang, M., Ryu, M., Yoon, M., Lee, S., Kim, H., Onodera, A., & Kojima, S. (2009). A study on the Raman spectra of Al-doped and Ga-doped ZnO ceramics. *Current Applied Physics, 9*(3), 651-657.

Jeong, C., Kim, H.-S., Chang, D.-R., & Kamisako, K. (2008). Effect on Al2O3 doping concentration of RF magnetron sputtered ZnO: Al films for solar cell applications. *Japanese Journal of Applied Physics, 47*(7R), 5656-5658.

Jia, C., Chen, Y., Liu, G., Liu, X., Yang, S., & Wang, Z. (2008). Growth of< i> c</i>-oriented ZnO films on (001) SrTiO3 substrates by MOCVD. *Journal of Crystal Growth, 311*(1), 200-204.

Kasai, P. H. (1963). Electron spin resonance studies of donors and acceptors in ZnO. *Physical Review, 130*(3), 989-995.

Kaschner, A., Haboeck, U., Strassburg, M., Strassburg, M., Kaczmarczyk, G., Hoffmann, A., . . . Hofmann, D. (2002). Nitrogen-related local vibrational modes in ZnO: N. *Applied Physics Letters, 80*(11), 1909-1911.

Khanderi, J., Hoffmann, R. C., Gurlo, A., & Schneider, J. J. (2009). Synthesis and sensoric response of ZnO decorated carbon nanotubes. *Journal of Materials Chemistry, 19*(28), 5039-5046.

Khorsand Zak, A., Abd Majid, W., Abrishami, M., & Yousefi, R. (2011). X-ray analysis of ZnO nanoparticles by Williamson–Hall and size–strain plot methods. *Solid State Sciences, 13*(1), 251-256.

Kim, H. W., Kebede, M. A., & Kim, H. S. (2010). Structural, Raman, and photoluminescence characteristics of ZnO nanowires coated with Al-doped ZnO shell layers. *Current Applied Physics, 10*(1), 60-63.

Kim, S., Jeong, M.-C., Oh, B.-Y., Lee, W., & Myoung, J.-M. (2006). Fabrication of Zn/ZnO nanocables through thermal oxidation of Zn nanowires grown by RF magnetron sputtering. *Journal of Crystal Growth, 290*(2), 485-489.

Klason, P., Moe Børseth, T., Zhao, Q. X., Svensson, B. G., Kuznetsov, A. Y., Bergman, P. J., & Willander, M. (2008). Temperature dependence and decay times of zinc and oxygen vacancy related photoluminescence bands in zinc oxide. *Solid State Communications, 145*(5), 321-326.

Kong, Y., Yu, D., Zhang, B., Fang, W., & Feng, S. (2001). Ultraviolet-emitting ZnO nanowires synthesized by a physical vapor deposition approach. *Applied Physics Letters, 78*(4), 407-409.

Kumar, K., Arun, P., Ravi Kant, C., Mehra, N., Makinistian, L., & Albanesi, E. (2010). Effect of residual stress on the optical properties of CsCl thin films. *Journal of Physics and Chemistry of Solids, 71*(3), 163-169.

Lao, C. S., Liu, J., Gao, P., Zhang, L., Davidovic, D., Tummala, R., & Wang, Z. L. (2006). ZnO nanobelt/nanowire Schottky diodes formed by dielectrophoresis alignment across Au electrodes. *Nano Letters, 6*(2), 263-266.

Lee, C., Lee, T., Lyu, S., Zhang, Y., Ruh, H., & Lee, H. (2002). Field emission from well-aligned zinc oxide nanowires grown at low temperature. *Applied Physics Letters, 81*(19), 3648-3650.

Lee, J.-S., Kang, M.-I., Kim, S., Lee, M.-S., & Lee, Y.-K. (2003). Growth of zinc oxide nanowires by thermal evaporation on vicinal Si (100) substrate. *Journal of Crystal Growth, 249*(1), 201-207.

Levis, R. J., Zhicheng, J., & Winograd, N. (1989). Thermal decomposition of methanol absorbed on palladium {111}. A new reaction pathway involving methyl formation. *Journal of the American Chemical Society, 111*(13), 4605-4612.

Li, F., Li, Z., & Jin, F. (2008). Fabrication and characterization of ZnO micro and nanostructures prepared by thermal evaporation. *Physica B: Condensed Matter, 403*(4), 664-669.

Li, J., Zhuang, H., Wang, J., & Xu, P. (2011). Synthesis and characterization of ZnO columns grown on MgO-coated silicon substrates by carbon-thermal evaporation. *Superlattices and Microstructures, 49*(2), 117-123.

Liao, L., Liu, D., Li, J., Liu, C., Fu, Q., & Ye, M. (2005). Synthesis and Raman analysis of 1D-ZnO nanostructure via vapor phase growth. *Applied Surface Science, 240*(1), 175-179.

Lieber, C. M. (1998). *One-dimensional nanostructures: chemistry, physics & applications.* (107). (11)

Lim, Y., Park, J., Hong, S.-T., & Kim, J. (2006). Carbothermal synthesis of ZnO nanocomb structure. *Materials Science and Engineering: B, 129*(1), 100-103.

Lin, J.-H., Patil, R. A., Devan, R. S., Liu, Z.-A., Wang, Y.-P., Ho, C.-H., . . . Ma, Y.-R. (2014). Photoluminescence mechanisms of metallic Zn nanospheres, semiconducting ZnO nanoballoons, and metal-semiconductor Zn/ZnO nanospheres. *Scientific Reports, 4*, 1-8.

Liu, K., Chen, R., Xing, G., Wu, T., & Sun, H. (2010). Photoluminescence characteristics of high quality ZnO nanowires and its enhancement by polymer covering. *Applied Physics Letters, 96*(2), 023111-1-3.

Liu, M., Kitai, A., & Mascher, P. (1992). Point defects and luminescence centres in zinc oxide and zinc oxide doped with manganese. *Journal of luminescence, 54*(1), 35-42.

Liu, W.-c., Wei, C., & Meng, X.-l. (2006a). Effects of temperature and pressure on morphologies of quasi-one-dimensional ZnO nanostructures fabricated via

thermal evaporation. *Transactions of Nonferrous Metals Society of China, 16*, s337-s340.

Liu, W., Gu, S., Ye, J., Zhu, S., Liu, S., Zhou, X., . . . Hang, Y. (2006b). Blue-yellow ZnO homostructural light-emitting diode realized by metalorganic chemical vapor deposition technique. *Applied Physics Letters, 88*(9), 092101-1-3.

Liu, Y., Li, Q., & Shao, H. (2009). Optical and photoluminescent properties of Al-doped zinc oxide thin films by pulsed laser deposition. *Journal of Alloys and Compounds, 485*(1), 529-531.

Lockman, Z., Pet Fong, Y., Wai Kian, T., Ibrahim, K., & Razak, K. A. (2010). Formation of self-aligned ZnO nanorods in aqueous solution. *Journal of Alloys and Compounds, 493*(1), 699-706.

Look, D. C., Farlow, G. C., Reunchan, P., Limpijumnong, S., Zhang, S., & Nordlund, K. (2005). Evidence for native-defect donors in n-type ZnO. *Physical Review Letters, 95*(22), 225502-1-4.

Louhichi, M., Romdhane, S., Fkiri, A., Smiri, L. S., & Bouchriha, H. (2015). Structural and photoluminescence properties of Al-doped zinc oxide nanoparticles synthesized in polyol. *Applied Surface Science, 356*, 998-1004.

Lü, C., Zou, Q., Zhang, R., & Ma, J. (2011). Tunable Visible Emission of Novel Zinc Oxide Nanocrystals. *Photonics Technology Letters, IEEE, 23*(9), 561-563.

Lübbe, M., Bressler, P., Drews, D., Braun, W., & Zahn, D. (1998). Study of hydrogen and methane modification of CVD diamond by XAS at the carbon K-edge. *Diamond and Related Materials, 7*(2), 247-249.

Luo, J., Liang, J., Liu, Q., Liu, F., Zhang, Y., Sun, B., & Rao, G. (2005). Structure and magnetic properties of Mn-doped ZnO nanoparticles. *Journal of Applied Physics, 97*(8), 086106-1-3.

Lupan, O., Shishiyanu, S., Chow, L., & Shishiyanu, T. (2008). Nanostructured zinc oxide gas sensors by successive ionic layer adsorption and reaction method and rapid photothermal processing. *Thin Solid Films, 516*(10), 3338-3345.

Lupan, O., Shishiyanu, S., Ursaki, V., Khallaf, H., Chow, L., Shishiyanu, T., . . . Railean, S. (2009). Synthesis of nanostructured Al-doped zinc oxide films on Si for solar cells applications. *Solar Energy Materials and Solar Cells, 93*(8), 1417-1422.

Lv, H., Sang, D., Li, H., Du, X., Li, D., & Zou, G. (2010). Thermal evaporation synthesis and properties of ZnO nano/microstructures using carbon group elements as the reducing agents. *Nanoscale Research Letters, 5*(3), 620-624.

Madou, M. J. (2011). *Manufacturing techniques for microfabrication and nanotechnology* (Vol. 2): CRC Press.

Mal, S., Narayan, J., Nori, S., Prater, J., & Kumar, D. (2010). Defect-mediated room temperature ferromagnetism in zinc oxide. *Solid State Communications, 150*(35), 1660-1664.

Manouni, A. E., Manjón, F., Mollar, M., Marí, B., Gómez, R., López, M., & Ramos-Barrado, J. (2006). Effect of aluminium doping on zinc oxide thin films grown by spray pyrolysis. *Superlattices and Microstructures, 39*(1), 185-192.

Mendelsberg, R., Kennedy, J., Durbin, S., & Reeves, R. (2008). Carbon enhanced blue–violet luminescence in ZnO films grown by pulsed laser deposition. *Current Applied Physics, 8*(3), 283-286.

Meyer, B., Alves, H., Hofmann, D., Kriegseis, W., Forster, D., Bertram, F., . . . Dworzak, M. (2004). Bound exciton and donor–acceptor pair recombinations in ZnO. *Physica Status Solidi (b), 241*(2), 231-260.

Millikan, R. A., & Lauritsen, C. C. (1929). Dependence of electron emission from metals upon field strengths and temperatures. *Physical Review, 33*(4), 598-604.

Mishra, Y. K., Kaps, S., Schuchardt, A., Paulowicz, I., Jin, X., Gedamu, D., . . . Adelung, R. (2014). Versatile Fabrication of Complex Shaped Metal Oxide Nano-Microstructures and Their Interconnected Networks for Multifunctional Applications. *KONA Powder and Particle Journal, 31*(0), 92-110.

Morkoç, H., Chyi, J.-I., Krost, A., Nanishi, Y., & Silversmith, D. J. (2010). Challenges and opportunities in GaN and ZnO Devices and materials. *Proceedings of the IEEE, 98(7)*, 1113-1117.

Morkoç, H., & Özgür, Ü. (2009). General properties of ZnO. *Zinc Oxide: Fundamentals, Materials and Device Technology*, 1-76.

Mote, V., Dargad, J., & Dole, B. (2013). Effect of Mn Doping Concentration on Structural, Morphological and Optical Studies of ZnO Nano-particles. *Nanoscience and Nanoengineering, 1*(2), 116-122.

Nishii, J., Hossain, F. M., Takagi, S., Aita, T., Saikusa, K., Ohmaki, Y., . . . Fukumura, T. (2003). High mobility thin film transistors with transparent ZnO channels. *Japanese journal of Applied Physics, 42*(4A), L347-L349.

Oo, W. H., Saraf, L. V., Engelhard, M. H., Shutthanandan, V., Bergman, L., Huso, J., & Mccluskey, M. D. (2009). Suppression of conductivity in Mn-doped ZnO thin films. *Journal of Applied Physics, 105*(1), 013715-1-4.

Ouyang, W., & Zhu, J. (2008). Catalyst-free synthesis of macro-scale ZnO nanonail arrays on Si substrate by simple physical vapor deposition. *Materials Letters, 62*(17), 2557-2560.

Özgür, Ü., Alivov, Y. I., Liu, C., Teke, A., Reshchikov, M., Doğan, S., . . . Morkoc, H. (2005). A comprehensive review of ZnO materials and devices. *Journal of Applied Physics, 98*(4), 041301-1-103.

Panchakarla, L., Govindaraj, A., & Rao, C. (2007). Formation of ZnO nanoparticles by the reaction of zinc metal with aliphatic alcohols. *Journal of Cluster Science, 18*(3), 660-670.

Patterson, C. (2006). Role of defects in ferromagnetism in Zn 1− x Co x O: a hybrid density-functional study. *Physical Review B, 74*(14), 144432-1-13.

Pawar, R. C., Kim, H.-s., & Lee, C. S. (2013). Improved field emission and photocatalysis properties of cacti-like zinc oxide nanostructures. *Scripta Materialia, 68*(2), 142-145.

Phillips, J. (2012). *Bonds and bands in semiconductors*: Elsevier.

Piner, R. D., Zhu, J., Xu, F., Hong, S., & Mirkin, C. A. (1999). " Dip-pen" nanolithography. *Science, 283*(5402), 661-663.

Quiroga-González, E., Carstensen, J., Glynn, C., O'Dwyer, C., & Föll, H. (2014). Pore size modulation in electrochemically etched macroporous p-type silicon monitored by FFT impedance spectroscopy and Raman scattering. *Physical Chemistry Chemical Physics, 16*(1), 255-263.

Raju, A., & Rao, C. (1991). Gas-sensing characteristics of ZnO and copper-impregnated ZnO. *Sensors and Actuators B: Chemical, 3*(4), 305-310.

Reimer, T., Paulowicz, I., Röder, R., Kaps, S. r., Lupan, O., Chemnitz, S., . . . Mishra, Y. K. (2014). Single step integration of ZnO nano-and microneedles in Si trenches by novel flame transport approach: whispering gallery modes and photocatalytic properties. *ACS Applied Materials & Interfaces, 6*(10), 7806-7815.

Rekha, K., Nirmala, M., Nair, M. G., & Anukaliani, A. (2010). Structural, optical, photocatalytic and antibacterial activity of zinc oxide and manganese doped zinc oxide nanoparticles. *Physica B: Condensed Matter, 405*(15), 3180-3185.

Rogers, K., & Daniels, P. (2002). An X-ray diffraction study of the effects of heat treatment on bone mineral microstructure. *Biomaterials, 23*(12), 2577-2585.

Ruan, H., Fang, L., Li, D., Saleem, M., Qin, G., & Kong, C. (2011). Effect of dopant concentration on the structural, electrical and optical properties of Mn-doped ZnO films. *Thin Solid Films, 519*(15), 5078-5081.

Rufael, T. S., Batteas, J. D., & Friend, C. (1997). The influence of surface oxidation on the reactions of methanol on Fe (110). *Surface Science, 384*(1), 156-167.

Russo, V., Ghidelli, M., Gondoni, P., Casari, C., & Bassi, A. L. (2014). Multi-wavelength Raman scattering of nanostructured Al-doped zinc oxide. *Journal of Applied Physics, 115*(7), 073508-1-27.

Ryu, Y., Lee, T.-S., Lubguban, J. A., White, H. W., Kim, B.-J., Park, Y.-S., & Youn, C.-J. (2006). Next generation of oxide photonic devices: ZnO-based ultraviolet light emitting diodes. *Applied Physics Letters, 88*(24), 241108-1-3.

Saha, D., Das, A. K., Ajimsha, R., Misra, P., & Kukreja, L. (2013). Effect of disorder on carrier transport in ZnO thin films grown by atomic layer deposition at different temperatures. *Journal of Applied Physics, 114*(4), 043703-1-6.

Samanta, P., Patra, S., Ghosh, A., & Chaudhuri, P. R. (2009). Visible emission from ZnO nanorods synthesized by a simple wet chemical method. *International Journal of Nanoscience and Nanotechnology, 1*(1-2), 81-90.

Schneck, H., & Helbig, R. (1975). Characterization of ZnO epitaxial films by their optical properties in the exciton region. *Thin Solid Films, 27*(1), 101-109.

Schottky, W. (1923). Cold and hot electron discharge. *Z. Phys, 14*, 63.

Scott, J. (1970). UV resonant Raman scattering in ZnO. *Physical Review B, 2*(4), 1209-1211.

Seghier, D., & Gislason, H. (2008). Shallow and deep donors in n-type ZnO characterized by admittance spectroscopy. *Journal of Materials Science: Materials in Electronics, 19*(8-9), 687-691.

Sen, S., Banerjee, A., & Acharjee, A. (2013). Nanotechnology: Shaping the world atom by atom. *International Journal of Modern Engineering Research, 3*(4), 2219-2225.

Serrano, J., Romero, A., Manjon, F., Lauck, R., Cardona, M., & Rubio, A. (2004). Pressure dependence of the lattice dynamics of ZnO: An ab initio approach. *Physical Review B, 69*(9), 094306-1-14.

Shalish, I., Temkin, H., & Narayanamurti, V. (2004). Size-dependent surface luminescence in ZnO nanowires. *Physical Review B, 69*(24), 245401-1-4.

Shan, F., Shin, B., Kim, S., & Yu, Y. (2003). Characterizations of Al doped zinc oxide thin films fabricated by pulsed laser deposition. *Journal of the Korean Physical Society, 42*, 1374-1377.

Sharma, R., Patel, S., & Pargaien, K. (2012). Synthesis, characterization and properties of Mn-doped ZnO nanocrystals. *Advances in Natural Sciences: Nanoscience and Nanotechnology, 3*(3), 035005-1-5.

Shinde, D. R., Chavan, P. G., Sen, S., Joag, D. S., More, M. A., Gadkari, S., & Gupta, S. (2011). Enhanced Field-Emission from SnO2: WO2. 72 Nanowire Heterostructures. *ACS Applied Materials & Interfaces, 3*(12), 4730-4735.

Smith, G. D., & Clark, R. J. (2004). Raman microscopy in archaeological science. *Journal of Archaeological Science, 31*(8), 1137-1160.

Sreenivas, K., Kumar, S., Choudhary, J., & Gupta, V. (2005). Growth of zinc oxide nanostructures. *Pramana, 65*(5), 809-814.

Srinivasan, G., & Kumar, J. (2008). Effect of Mn doping on the microstructures and optical properties of sol–gel derived ZnO thin films. *Journal of Crystal Growth, 310*(7), 1841-1846.

Studenikin, S., Cocivera, M., Kellner, W., & Pascher, H. (2000). Band-edge photoluminescence in polycrystalline ZnO films at 1.7 K. *Journal of Luminescence, 91*(3), 223-232.

Subramanyam, T., Srinivasulu Naidu, B., & Uthanna, S. (2000). Physical properties of zinc oxide films prepared by dc reactive magnetron sputtering at different sputtering pressures. *Crystal Research and Technology, 35*(10), 1193-1202.

Sun, X. (2006). Designing efficient field emission into ZnO. *SPIE Newsroom, The International Society for Optical Engineering. s.* 1-4.

Szymanski, H. A. (1967). *Raman spectroscopy: theory and practice.* Paper presented at the Raman Spectroscopy: Theory and Practice.

Tagliente, M., & Massaro, M. (2008). Strain-driven (002) preferred orientation of ZnO nanoparticles in ion-implanted silica. *Nuclear Instruments and Methods in Physics Research Section B: Beam Interactions with Materials and Atoms, 266*(7), 1055-1061.

Takahashi, N., Kaiya, K., Omichi, K., Nakamura, T., Okamoto, S., & Yamamoto, H. (2000). Atmospheric pressure vapor-phase growth of ZnO using a chloride source. *Journal of Crystal Growth, 209*(4), 822-827.

Tanaka, M., Qi, J., & Masumoto, Y. (2000). Comparison of energy levels of Mn< sup> 2+</sup> in nanosized-and bulk-ZnS crystals. *Journal of Luminescence, 87*, 472-474.

Taunk, P., Das, R., Bisen, D., & kumar Tamrakar, R. (2015). Structural characterization and photoluminescence properties of zinc oxide nano particles synthesized by chemical route method. *Journal of Radiation Research and Applied Sciences, 8*(3), 433-438.

Teke, A., Özgür, Ü., Doğan, S., Gu, X., Morkoç, H., Nemeth, B., . . . Everitt, H. (2004). Excitonic fine structure and recombination dynamics in single-crystalline ZnO. *Physical Review B, 70*(19), 195207-1-10.

Terakawa, M., Tanaka, Y., Obara, G., Sakano, T., & Obara, M. (2011). Randomly-grown high-dielectric-constant ZnO nanorods for near-field enhanced Raman scattering. *Applied Physics A, 102*(3), 661-665.

Terasako, T., Yamanaka, T., Yura, S., Yagi, M., & Shirakata, S. (2010). Photoluminescence, photoacoustic and Raman spectra of zinc oxide films grown by LP-MOCVD using diethylzinc and water as precursors. *Thin Solid Films, 519*(5), 1546-1551.

Thomas, D. (1960). The exciton spectrum of zinc oxide. *Journal of Physics and Chemistry of Solids, 15*(1), 86-96.

Tonto, P., Mekasuwandumrong, O., Phatanasri, S., Pavarajarn, V., & Praserthdam, P. (2008). Preparation of ZnO nanorod by solvothermal reaction of zinc acetate in various alcohols. *Ceramics International, 34*(1), 57-62.

Tseng, Y.-K., Lin, I.-N., Liu, K.-S., Lin, T.-S., & Chen, I. (2003). Low-temperature growth of ZnO nanowires. *Journal of Materials Research, 18*(03), 714-718.

Tzeng, Y. (2003). Method of hot-filament chemical vapor deposition of diamond: Google Patents.

Van, L., Hong, M., & Ding, J. (2008). Structural and magnetic property of Co-doped–ZnO thin films prepared by pulsed laser deposition. *Journal of Alloys and Compounds, 449*(1), 207-209.

Vanheusden, K., Seager, C., Warren, W. t., Tallant, D., & Voigt, J. (1996a). Correlation between photoluminescence and oxygen vacancies in ZnO phosphors. *Applied Physics Letters, 68*(3), 403-405.

Vanheusden, K., Warren, W., Seager, C., Tallant, D., Voigt, J., & Gnade, B. (1996b). Mechanisms behind green photoluminescence in ZnO phosphor powders. *Journal of Applied Physics, 79*(10), 7983-7990.

Vasil'ev, P. P., & Smetanin, I. V. (2006). Condensation of electron-hole pairs in a degenerate semiconductor at room temperature. *Physical Review B, 74*(12), 125206-1-8.

Vempati, S., Mitra, J., & Dawson, P. (2012a). One-step synthesis of ZnO nanosheets: a blue-white fluorophore. *Nanoscale Research Letters, 7*(1), 1-10.

Vempati, S., Shetty, A., Dawson, P., Nanda, K., & Krupanidhi, S. (2012b). Cobalt-doped ZnO nanowires on quartz: synthesis by simple chemical method and characterization. *Journal of Crystal Growth, 343*(1), 7-12.

Wagner, A., Behrends, A., Waag, A., & Bakin, A. (2012). Two step deposition method with a high growth rate for ZnO nanowire arrays and its application in photovoltaics. *Thin Solid Films, 520*(14), 4637-4641.

Wagner, P., & Helbig, R. (1977). The Hall effect and the anisotropy of the mobility of the electrons in ZnO. *The Hall effect and the anisotropy of the mobility of the electrons in ZnO Transl. into ENGLISH from J. Phys. Chem. Solids (England), v. 35, 1974 p 327-335, 1*, 327-335.

Wang, C., Cai, R. S., Diao, F. Y., Yuan, L., Zhou, G. W., & Wang, Y. Q. (2014). Growth and Epitaxy of ZnO Nanowires on Brass Substrates. *Advanced Materials Research, 850*, 3-6.

Wang, G., Chu, S., Zhan, N., Lin, Y., Chernyak, L., & Liu, J. (2011). ZnO homojunction photodiodes based on Sb-doped p-type nanowire array and n-type film for ultraviolet detection. *Applied Physics Letters, 98*(4), 041107-1-3.

Wang, L., Chen, K., & Dong, L. (2010a). Synthesis of exotic zigzag ZnO nanoribbons and their optical, electrical properties. *The Journal of Physical Chemistry C, 114*(41), 17358-17361.

Wang, M., Lee, K. E., Hahn, S. H., Kim, E. J., Kim, S., Chung, J. S., . . . Park, C. (2007). Optical and photoluminescent properties of sol-gel Al-doped ZnO thin films. *Materials Letters, 61*(4), 1118-1121.

Wang, M., Zhou, Y., Zhang, Y., Kim, E. J., Hahn, S. H., & Seong, S. G. (2012). Near-infrared photoluminescence from ZnO. *Applied Physics Letters, 100*(10), 101906-1-4.

Wang, S., Jia, X., Jiang, P., Fang, H., & Tang, W. (2010b). Large-scale preparation of chestnut-like ZnO and Zn–ZnO hollow nanostructures by chemical vapor deposition. *Journal of Alloys and Compounds, 502*(1), 118-122.

Wang, Z. L. (2004a). Nanostructures of zinc oxide. *Materials Today, 7*(6), 26-33.

Wang, Z. L. (2004b). Zinc oxide nanostructures: growth, properties and applications. *Journal of Physics: Condensed Matter, 16*(25), R829-R858.

Wang, Z. L., & Kang, Z. C. (1998). *Functional and smart materials: structural evolution and structure analysis*: Springer.

Warule, S. S., Chaudhari, N. S., Ambekar, J. D., Kale, B. B., & More, M. A. (2011). Hierarchical nanostructured ZnO with nanorods engendered to nanopencils and pin-cushion cactus with its field emission study. *ACS Applied Materials & Interfaces, 3*(9), 3454-3462.

Weber, W. H., & Merlin, R. (2000). *Raman scattering in materials science* (Vol. 42): Springer.

Willander, M., Nur, O., Zhao, Q., Yang, L., Lorenz, M., Cao, B., . . . Grundmann, M. (2009). Zinc oxide nanorod based photonic devices: recent progress in growth, light emitting diodes and lasers. *Nanotechnology, 20*(33), 332001-1-40.

Williamson, G., & Hall, W. (1953). X-ray line broadening from filed aluminium and wolfram. *Acta Metallurgica, 1*(1), 22-31.

Winkler, J. H. (1744). *Gedanken von den Eigenschaften, Wirkungen und Ursachen der Electricität: nebst einer Beschreibung zwo neuer electrischen Maschinen*: In Verlag Bernhard Christoph Breitkopfs.

Winkler, T., Schmidt, H., Flügge, H., Nikolayzik, F., Baumann, I., Schmale, S., . . . Riedl, T. (2012). Realization of ultrathin silver layers in highly conductive and transparent zinc tin oxide/silver/zinc tin oxide multilayer electrodes deposited at room temperature for transparent organic devices. *Thin Solid Films, 520*(14), 4669-4673.

Wood, R. W. (1897). A new form of cathode discharge and the production of X-rays, together with some notes on diffraction. Preliminary communication. *Physical Review (Series I), 5*(1), 1-10.

Wu, C., Li, F., Zhang, Y., Wang, L., & Guo, T. (2013). Formation and field emission of patterned zinc oxide-adhering graphene cathodes. *Vacuum, 89*, 57-61.

Wu, X., Siu, G., Fu, C., & Ong, H. (2001). Photoluminescence and cathodoluminescence studies of stoichiometric and oxygen-deficient ZnO films. *Applied Physics Letters, 78*(16), 2285-2287.

Xiang, B., Wang, P., Zhang, X., Dayeh, S. A., Aplin, D. P., Soci, C., . . . Wang, D. (2007). Rational synthesis of p-type zinc oxide nanowire arrays using simple chemical vapor deposition. *Nano Letters, 7*(2), 323-328.

Xu, C., Sun, X. W., Dong, Z., Tan, S. T., Cui, Y., & Wang, B. (2005). Manganese-doped zinc oxide tetratubes and their photoluminescent properties. *Journal of Applied Physics, 98*(11), 113513-1-5.

Xu, S., Qin, Y., Xu, C., Wei, Y., Yang, R., & Wang, Z. L. (2010). Self-powered nanowire devices. *Nature Nanotechnology, 5*(5), 366-373.

Yamauchi, S., Goto, Y., & Hariu, T. (2004). Photoluminescence studies of undoped and nitrogen-doped ZnO layers grown by plasma-assisted epitaxy. *Journal of Crystal Growth, 260*(1), 1-6.

Yang, L., Wu, X., Xiong, Y., Yang, Y., Huang, G., Chu, P. K., & Siu, G. (2005). Formation of zinc oxide micro-disks via layer-by-layer growth and growth mechanism of ZnO nanostructures. *Journal of Crystal Growth, 283*(3), 332-338.

Yang, X., Du, G., Wang, X., Wang, J., Liu, B., Zhang, Y., . . . Yang, S. (2003). Effect of post-thermal annealing on properties of ZnO thin film grown on c-Al< sub> 2</sub> O< sub> 3</sub> by metal-organic chemical vapor deposition. *Journal of Crystal Growth, 252*(1), 275-278.

Ye, J., Tripathy, S., Ren, F.-F., Sun, X., Lo, G., & Teo, K. (2009). Raman-active Fröhlich optical phonon mode in arsenic implanted ZnO. *Applied Physics Letters, 94*(1), 011913-1-3.

Yi, G.-C., Wang, C., & Park, W. I. (2005). ZnO nanorods: synthesis, characterization and applications. *Semiconductor Science and Technology, 20*(4), S22-S34.

Yogamalar, R., & Bose, A. C. (2013). Synthesis, Dopant Study and Device Fabrication of Zinc Oxide Nanostructures: Mini Review. *Progress in Nanotechnology and Nanomaterials, 2*, 1-20.

Yogamalar, R., Srinivasan, R., Vinu, A., Ariga, K., & Bose, A. C. (2009). X-ray peak broadening analysis in ZnO nanoparticles. *Solid State Communications, 149*(43), 1919-1923.

Yu, D., Trad, T., McLeskey Jr, J. T., Craciun, V., & Taylor, C. R. (2010). ZnO nanowires synthesized by vapor phase transport deposition on transparent oxide substrates. *Nanoscale Research Letters, 5*(8), 1333-1339.

Yuan, H., Xie, S., Liu, D., Yan, X., Zhou, Z., Ci, L., . . . Liu, L. (2003). Characterization of zinc oxide crystal nanowires grown by thermal evaporation of ZnS powders. *Chemical Physics Letters, 371*(3), 337-341.

Zaier, A., Meftah, A., Jaber, A., Abdelaziz, A., & Aida, M. (2015). Annealing effects on the structural, electrical and optical properties of ZnO thin films prepared by thermal evaporation technique. *Journal of King Saud University-Science, 27*(4), 356-360.

Zeng, H., Duan, G., Li, Y., Yang, S., Xu, X., & Cai, W. (2010). Blue Luminescence of ZnO Nanoparticles Based on Non-Equilibrium Processes: Defect Origins and Emission Controls. *Advanced Functional Materials, 20*(4), 561-572.

Zhang, G., Zhang, Q., Pei, Y., & Chen, L. (2004). Field emission from nonaligned zinc oxide nanowires. *Vacuum, 77*(1), 53-56.

Zhang, J.-M., Zhang, Y., Xu, K.-W., & Ji, V. (2006). General compliance transformation relation and applications for anisotropic hexagonal metals. *Solid State Communications, 139*(3), 87-91.

Zhang, J., Yang, Y., Xu, B., Jiang, F., & Li, J. (2005). Shape-controlled synthesis of ZnO nano-and micro-structures. *Journal of Crystal Growth, 280*(3), 509-515.

Zhang, S., Wei, S.-H., & Zunger, A. (2001). Intrinsic n-type versus p-type doping asymmetry and the defect physics of ZnO. *Physical Review B, 63*(7), 075205-1-7.

Zhang, W., He, D., Liu, Z., Sun, L., & Fu, Z. (2010). Preparation of transparent conducting Al-doped ZnO thin films by single source chemical vapor deposition. *Optoelectron Adv Mater-Rapid Commun, 4*(11), 1651-1654.

Zhang, Z.-K., Zhang, Y.-Z., Bian, J.-M., Sun, J.-C., Qin, F.-W., Liu, W.-F., & Luo, Y.-M. (2014). Growth of Low-dimensional ZnO Materials on Graphite Substrate. *无机材料学报, 29*(1), 103-107.

Zhao, Q., Klason, P., Willander, M., Zhong, H., Lu, W., & Yang, J. (2005). Deep-level emissions influenced by O and Zn implantations in ZnO. *Applied Physics Letters, 87*(21), 211912-1-3.

Zheng, Z. (2012). Synthesis and optical properties of ZnO nanostructures. *Journal of Nanoengineering and Nanomanufacturing, 2*(1), 60-64.

Zhong, J., Kitai, A. H., Mascher, P., & Puff, W. (1993). The influence of processing conditions on point defects and luminescence centers in ZnO. *Journal of the Electrochemical Society, 140*(12), 3644-3649.

Zhou, H.-m., Yi, D.-q., Yu, Z.-m., Xiao, L.-r., & Li, J. (2007). Preparation of aluminum doped zinc oxide films and the study of their microstructure, electrical and optical properties. *Thin Solid Films, 515*(17), 6909-6914.

Zhou, J., Wang, Y., Zhao, F., Wang, Y., Zhang, Y., & Yang, L. (2006). Photoluminescence of ZnO nanoparticles prepared by a novel gel-template combustion process. *Journal of Luminescence, 119*, 248-252.

Zhou, W., & Wang, Z. L. (2007). *Scanning microscopy for nanotechnology: techniques and applications*: Springer.

Zhu, Q., Xie, C., Li, H., Yang, C., Zhang, S., & Zeng, D. (2014). Selectively enhanced UV and NIR photoluminescence from a degenerate ZnO nanorod array film. *Journal of Materials Chemistry C, 2*(23), 4566-4580.

Zhu, Z., Chen, T.-L., Gu, Y., Warren, J., & Osgood, R. M. (2005). Zinc oxide nanowires grown by vapor-phase transport using selected metal catalysts: a comparative study. *Chemistry of Materials, 17*(16), 4227-4234.

Zhuang, H., Li, J., Wang, J., Xu, P., & An, N. (2011). Novel zinc oxide hexagonal prisms induced by polar surfaces. *Materials Characterization, 62*(6), 593-598.

Zu, P., Tang, Z., Wong, G. K., Kawasaki, M., Ohtomo, A., Koinuma, H., & Segawa, Y. (1997). Ultraviolet spontaneous and stimulated emissions from ZnO microcrystallite thin films at room temperature. *Solid State Communications, 103*(8), 459-463.

LIST OF PUBLICATIONS AND PAPERS PRESENTED

Publication of Papers

Thandavan, T. M. K., et al. (2015). "Enhanced Photoluminescence and raman properties of Al-Doped ZnO nanostructures prepared using thermal chemical vapor deposition of methanol assisted with heated brass." PloS one **10**(3): e0121756.

Thandavan, T. M. K., Gani, S. M. A., San Wong, C., & Nor, R. M. **(2015)**. Evaluation of Williamson–Hall Strain and Stress Distribution in ZnO Nanowires Prepared Using Aliphatic Alcohol. *Journal of Nondestructive Evaluation*, *34*(2), 1-9.

Thandavan, T. M. K., et al. (2014). "Synthesis of ZnO nanowires via hotwire thermal evaporation of brass (CuZn) assisted by vapor phase transport of methanol." Journal of Nanomaterials **2014**: 55.

Thandavan, T. M. K., Wong, C. S., Gani, S. M. A., & Nor, R. M. **(2014)**. Photoluminescence properties of un-doped and Mn-doped ZnO nanostructures. *Materials Express*, *4*(6), 475-482.

Thandavan, T. M. K., San Wong, C., Gani, S. M. A., & Nor, R. M. **(2012)**. [O][H] functionalization on carbon nanotube using (O_2–H_2) gas mixture DC glow discharge. *Applied Nanoscience*, *2*(1), 47-53.

Publications of Book Chapters

Nor, R. M., Bakar, S. A., Thandavan, T. M. K, & Rusop, M. **(2011)**. Diamond: synthesis, characterisation and applications *Carbon and Oxide Nanostructures* (pp. 195-217): Springer.

Thandavan, T. M. K., NOR, R. M., MERIAM, S., GHANI, A., & SAN, W. C. **(2012)** Surface Functionalization of Carbon Nano-tube using Direct Current Glow Discharge: Preparation and Characterization.

Conferences Attended

8th April 2013 4th International Conference on Functional Materials and Devices (ICFMD) Penang, Malaysia. (Paper).